


5-2011

# Symmetry-Based Techniques for Qualitative Understanding of Rovibrational Effects in Spherical-Top Molecular Spectra and Dynamics

Justin Chadwick Mitchell  
*University of Arkansas*

Follow this and additional works at: <http://scholarworks.uark.edu/etd>

 Part of the [Atomic, Molecular and Optical Physics Commons](#), and the [Physical Chemistry Commons](#)

---

## Recommended Citation

Mitchell, Justin Chadwick, "Symmetry-Based Techniques for Qualitative Understanding of Rovibrational Effects in Spherical-Top Molecular Spectra and Dynamics" (2011). *Theses and Dissertations*. 199.  
<http://scholarworks.uark.edu/etd/199>

This Dissertation is brought to you for free and open access by ScholarWorks@UARK. It has been accepted for inclusion in Theses and Dissertations by an authorized administrator of ScholarWorks@UARK. For more information, please contact [scholar@uark.edu](mailto:scholar@uark.edu), [ccmiddle@uark.edu](mailto:ccmiddle@uark.edu).

Symmetry-Based Techniques for Qualitative Understanding of Rovibrational Effects  
in Spherical-Top Molecular Spectra and Dynamics

Symmetry-Based Techniques for Qualitative Understanding of Rovibrational Effects  
in Spherical-Top Molecular Spectra and Dynamics

A dissertation submitted in partial fulfillment  
of the requirements for the degree of  
Doctor of Philosophy in Physics

By

Justin Chadwick Mitchell  
University of Tulsa  
Bachelor of Science in Physics, 2003  
University of Arkansas  
Master of Science in Physics, 2007

May 2011  
University of Arkansas

## Abstract

Using light to probe the structure of matter is as natural as opening our eyes. Modern physics and chemistry have turned this art into a rich science, measuring the delicate interactions possible at the molecular level.

Perhaps the most commonly used tool in computational spectroscopy is that of matrix diagonalization. While this is invaluable for calculating everything from molecular structure and energy levels to dipole moments and dynamics, the process of numerical diagonalization is an opaque one. This work applies symmetry and semi-classical techniques to elucidate numerical spectral analysis for high-symmetry molecules.

Semi-classical techniques, such as the Potential Energy Surfaces, have long been used to help understand molecular vibronic and rovibronic spectra and dynamics. This investigation focuses on newer semi-classical techniques that apply Rotational Energy Surfaces (RES) to rotational energy level clustering effects in high-symmetry molecules. Such clusters exist in rigid rotor molecules as well as deformable spherical tops. This study begins by using the simplicity of rigid symmetric top molecules to clarify the classical-quantum correspondence of RES semi-classical analysis and then extends it to a more precise and complete theory of modern high-resolution spectra.

RES analysis is extended to molecules having more complex and higher rank tensorial rotational and rovibrational Hamiltonians than were possible to understand before. Such molecules are shown to produce an extraordinary range of rotational level clusters, corresponding to a panoply of symmetries ranging from  $C_{4v}$  to  $C_2$  and  $C_1$  (no symmetry) with a corresponding range of new angular momentum localization and  $J$ -tunneling effects.

Using RES topography analysis and the commutation duality relations between symmetry group operators in the lab-frame to those in the body-frame, it is shown how to better describe and catalog complex splittings found in rotational level clus-

ters. Symmetry character analysis is generalized to give analytic eigensolutions. An appendix provides vibrational analogies.

For the first time, interactions between molecular vibrations (polyads) are described semi-classically by multiple RES. This is done for the  $\nu_3/2\nu_4$  dyad of  $\text{CF}_4$ . The nine-surface RES topology of the  $U(9)$ -dyad agrees with both computational and experimental work. A connection between this and a simpler  $U(2)$  example is detailed in an Appendix.

This dissertation is approved for  
Recommendation to the  
Graduate Council

Dissertation Director:

---

William Harter, Ph.D.

Dissertation Committee:

---

Daniel Kennefick, Ph.D.

---

Peter Pulay, Ph.D.

---

Gregory Salamo, Ph.D.

---

Reeta Vyas, Ph.D.

## Dissertation Duplication Release

I hereby authorize the University of Arkansas Libraries to duplicate this dissertation when needed for research and/or scholarship.

Agreed

---

Justin C. Mitchell

## **Acknowledgements**

I give particular thanks to Dr William Harter for his years of helpful guidance during this work. Also, both Dr Gay Stewart and Dr John Stewart have been steadfast advocates, giving much needed support. Finally, I am grateful to my wife, Amy, for her patience and encouragement.



## Contents

<b>1</b>	<b>Introduction to Semi-Classical Analysis and the Rotational Energy Surface</b>	<b>3</b>
1.1	Background . . . . .	4
1.1.1	Symmetry-based Clustering of Rotational Energy Levels . . . . .	4
1.1.2	Computer Graphical Techniques . . . . .	5
1.1.3	Lab-frame coupling vs. Body frame constriction . . . . .	8
1.1.4	Creating and Using Rotational Energy Surfaces . . . . .	11
	Bibliography . . . . .	19
<b>2</b>	<b>Tensor Geometry and Spectral Fine Structure: Symmetric and Asymmetric Top Molecules</b>	<b>22</b>
2.1	Chapter Summary . . . . .	23
2.2	Mathematical Background . . . . .	23
2.2.1	Unitary Multipole functions and operators . . . . .	23
2.2.2	Tensor and Elementary Matrix Operators . . . . .	28
2.2.3	Fano-Racah tensor algebra . . . . .	30
2.3	Tensor eigensolution and Legendre function RE surfaces . . . . .	31
2.3.1	Angular Momentum Cone and RES Paths . . . . .	34
2.3.2	Asymmetric Top and Rank-2 RES . . . . .	42
2.3.3	Symmetry Labeling of Asymmetric Top Eigenstates . . . . .	45
2.3.4	Tunneling Between RES-Path States . . . . .	49
2.4	Conclusion . . . . .	49
	Bibliography . . . . .	50
<b>3</b>	<b>Spectral Fine Structure of Octahedral Spherical Top Molecules</b>	<b>51</b>
3.1	Chapter Summary . . . . .	52
3.2	Tensor Eigensolutions for Octahedral Molecules . . . . .	52
3.2.1	Symmetry Considerations . . . . .	52
3.2.2	Assigning Symmetry Labels to Eigenlevels . . . . .	55
3.2.3	Octahedral Results . . . . .	56
3.2.4	$C_1$ Level Clustering . . . . .	66
3.3	Conclusion . . . . .	68
	Bibliography . . . . .	68
<b>4</b>	<b>Local Symmetry Tunneling Eigensolutions</b>	<b>70</b>
4.1	Chapter Summary . . . . .	71
4.2	Introduction . . . . .	71
4.3	Abelian symmetry analysis . . . . .	73
4.3.1	Operator expansion of $C_n$ symmetric Hamiltonian . . . . .	73
4.3.2	Spectral resolution of $C_n$ symmetry operators . . . . .	77
4.3.3	Spectral resolution of $C_n$ symmetric Hamiltonian . . . . .	82
4.4	Non-Abelian symmetry analysis . . . . .	85

4.4.1	Operator expansion of $D_3$ symmetric Hamiltonian . . . . .	85
4.4.2	Spectral resolution of $D_3$ symmetry operators . . . . .	89
4.4.3	Spectral resolution of dual groups $D_3$ and $\bar{D}_3$ . . . . .	97
4.4.4	Spectral resolution of $D_3$ Hamiltonian . . . . .	100
4.4.5	Global-lab-relative $G$ <i>versus</i> local-body-relative $\bar{G}$ base state definition . . . . .	102
4.4.6	Global <i>versus</i> local eigenstate symmetry . . . . .	105
4.4.7	Symmetry correlation and Frobenius reciprocity . . . . .	107
4.5	Conclusion . . . . .	116
	Bibliography . . . . .	117
4.A	Classical $D_3$ Vibrational Modes . . . . .	119
4.A.1	Classical $D_3$ modes: Local $C_2$ and $C_3$ symmetry examples . . .	120
<b>5</b>	<b>Local Symmetry Tunneling In Octahedral Molecules</b>	<b>131</b>
5.1	Chapter Summary . . . . .	132
5.2	Octahedral symmetry analysis . . . . .	132
5.2.1	Octahedral characters and subgroup correlations . . . . .	136
5.3	Spectral resolution of full $O_h$ symmetry . . . . .	152
5.3.1	Resolving Hamiltonians with $C_{2v}$ local symmetry . . . . .	154
5.4	Conclusion . . . . .	159
	Bibliography . . . . .	160
<b>6</b>	<b>Rotational Energy Surfaces Analysis for the <math>\nu_3/2\nu_4</math> Polyad of <math>\text{CF}_4</math></b>	<b>162</b>
6.1	Chapter Summary . . . . .	163
6.2	Polyad Formalism . . . . .	163
6.3	Development . . . . .	165
6.4	3D Oscillator Example . . . . .	167
6.5	Analysis . . . . .	169
6.5.1	Experimental and Computational Details . . . . .	169
6.5.2	Rotational Band Boundaries . . . . .	171
6.5.3	Rotational Level Clustering . . . . .	172
6.6	Conclusion . . . . .	175
	Bibliography . . . . .	177
6.A	Multiple Rotors and Rotor-2D Vibration Hamiltonians . . . . .	179
6.A.1	Constrained Molecular Double Rotators . . . . .	180
6.A.2	2D Oscillation - 3D Rotation Analogy . . . . .	181
6.A.3	Rovibrational Multi-surface RES Plots . . . . .	184
	Bibliography . . . . .	186
<b>7</b>	<b>Conclusions</b>	<b>187</b>
	Bibliography . . . . .	188

## List of Figures

1.1	Symmetric Top RES $J = 10$ . $K$ values are marked on the plot. . . . .	14
1.2	Rotational Energy Surface for $\text{SF}_6$ at $J = 30$ in the vibrational ground state. Quantum contours labeled by $K$ -values are shown with colors matching the symmetry of the topmost level in the $K$ -cluster. (Color code: $A_1$ is red, $A_2$ is orange, $E$ is green, $T_1$ is blue and $T_2$ is light blue.) Black clusters are too tight for the graphic routine to distinguish symmetry. The highest- $K$ ( $K = 30 = J$ ) uncertainty cone is protruding from the RES at the top. . . . .	15
1.3	Local symmetry axes of globally octahedral RES plots. The two plots are built of the same operators, but show different local symmetry features because of different fitting related to the rotational Hamiltonian. . . . .	17
2.1	Symmetric top RES showing angular momentum cone with minimum uncertainty. The cone intersects with one of the allowed paths. . . . .	35
2.2	Quantum solutions (blue) compared to semi-classical ones (orange) for two different multipoles. Semi-classical energies are also seen as the intersection of uncertainty cones with the RES. Inner circle represents zero-energy centroid. . . . .	39
2.3	Asymmetric Top RES $J = 10$ . . . . .	43
2.4	Asymmetric Top Energy Levels with Corresponding RES . . . . .	44
3.1	Symmetry Axes of $T^{[4,6]}$ RES for differing contributions of $T^{[4]}$ and $T^{[6]}$ . . . . .	58
3.2	Quantum spectrum of octahedral Hamiltonian (Eq (3.3)) with changing $\theta$ . Bold lines are the energy of the classical symmetry axis labeled. . . . .	59
3.3	Spectrum of Octahedral Rotor Showing Semi-Classical Boundaries Given Eq (3.6) . . . . .	61

3.4	Both Energy Levels and RES Plots for $T^{[4,6]}$ . Horizontal Axis goes from all $T^{[4]}$ on the left to all $T^{[6]}$ on the right . . . . .	62
3.5	RES with $C_1$ local symmetry regions visible . . . . .	63
3.6	Level Diagrams of Energy vs $\theta$ for given $\phi$ with RES Plots at Selected Positions . . . . .	65
3.7	$C_1$ Features on different parts of the parameter-space. All plots are done for $J = 30$ . . . . .	67
4.1	Three classes of tunneling paths and parameters . . . . .	77
4.2	$C_6$ Characters (a) Numerical table (b) Wave phasor table . . . . .	78
4.3	Energy level dispersion for archetypical tunneling parameters: B1: $r_1 = -r$ , B2: $r_2 = -s$ , B3: $r_3 = -t$ . . . . .	84
4.4	Zeeman shifted Bloch dispersion for complex parameter in ZB1(6) model: $r_1 = -re^{i\phi}$ with $\phi = \pi/12$ . . . . .	85
4.5	Rotation operators $[\mathbf{1}, \mathbf{r}^1, \mathbf{r}^2, \mathbf{i}_1, \mathbf{i}_2, \mathbf{i}_3]$ for a $D_3$ symmetric square-well potential. . . . .	86
4.6	$D_3$ -operator defined states and tunneling paths . . . . .	100
4.7	$D_3$ -operators compared (a) Global $\mathbf{i}_2$ (b) Local $\bar{\mathbf{i}}_2$ (c) $\bar{\mathbf{i}}_2$ followed by $\bar{\mathbf{i}}_1$ .	104
4.8	$D_3$ -symmetry waves (a) Sketch of projection (b) 3-Well wave simulation	108
4.9	$C_2 \uparrow D_3$ waves at vertex points $p = 0, 1, 2$ . (a) $0_2 \uparrow D_3$ bases $\mathbf{P}^x  \mathbf{r}^p\rangle \sqrt{2}$ (b) $1_2 \uparrow D_3$ bases $\mathbf{P}^y  \mathbf{r}^p\rangle \sqrt{2}$ . . . . .	115
4.10	$D_3 \supset C_2(i_3)$ -local symmetry modes of $X_3$ molecule . . . . .	121
4.11	$X_3$ spring models with local symmetry: (a) $D_3 \supset C_2(i_3)$ (b) Mixed . . .	124
4.12	Mixed-local symmetry modes of direct- $k_1$ -coupled $X_3$ model in Fig.4.11(b).	128
4.13	$D_3 \supset C_3$ -local symmetry modes of $X_3$ molecule. . . . .	130
5.1	$O$ operators distributed in cosets of $C_4 \supset C_2$ . . . . .	134
5.2	$O_h$ operators distributed in cosets of $C_{4v} \supset C_{2v}$ . . . . .	135
5.3	$O_h$ local symmetry (a) $C_{4v}$ (b) $C_{3v}$ (c) $C_{2v}$ . . . . .	136

5.4	$O$ $i$ -class level clusters of $C_4$ local symmetry (a) $0_4$ (b) $1_4$ (c) $2_4$ (d) $3_4$ .	144
5.5	Tiny excerpt of $SF_6$ $\nu_4P(88)$ superfine spectral cluster structure in $16\mu m$ region . . . . .	146
5.6	$O$ $i$ -class and $\rho$ -class level clusters of $C_3$ local symmetry given different tunneling parameters . . . . .	149
5.7	$O \subset L$ -local symmetry eigenmatrix parameters (a-e) $L=C_4, \dots, C_1$ (f-j) $L=O, D_4, \dots, D_2$ . . . . .	150
5.8	$J=30$ Energy levels and RES plots for $T^{[4,6]}vs.[4,6]$ mix-angle $\theta$ with $T^{[4]}$ levels above $\phi=0^\circ$ (extreme left), $T^{[6]}$ levels at $\theta=90^\circ$ (center), and $-T^{[4]}$ levels at $\theta=180^\circ$ (extreme right). $C_4$ local symmetry and 6-fold level clusters dominate at $\theta=17^\circ$ while $C_3$ type 8-fold level clusters dominate at $\theta=132^\circ$ . In between these extremes are $C_2$ type 12-fold level clusters particularly around $\theta=80^\circ$ where a $C_3 - C_4$ level-cluster-crossing of the top 14 levels occurs. . . . .	157
5.9	The plot focuses on the lowest cluster in the previous energy plot (Fig. 5.8) of the $T^{[4,6]}$ Hecht Hamiltonian for $J = 30$ . The inside plot has been magnified 100 times. The inside diagram also centers the levels around their center of mass, showing only the splittings and ignoring the shifts of the cluster. As before, color indicates the symmetry of each level. The vertical lines on inside plot draw attention to specific clustering patterns described in the text. . . . .	158
6.1	All 9 interacting Rotational Energy Eigenvalue Surfaces for $\nu_3/2\nu_4$ of $CF_4$ with $J = 60$ . Minimum uncertainty cone is also shown for this value of $J$ . Surfaces are also dissected show those of lower energy beneath. Outer RES also tend to be more spherical, making contours challenging and causing them to be slightly dappled. . . . .	167

6.2	Reduced Energy plots may show different types of interactions depending on the model Hamiltonian used. . . . .	170
6.3	Semi-quantum outlines show band boundaries for the rotational levels of $\nu_3/2\nu_4$ . Reduced energy is defined as the quantum energy subtracted by all scalar fully rotational terms. In this way, the reduced energy shows the energy splittings without the energy shifts related only to increasing $J$ . . . . .	173
6.4	$C_1$ local symmetry structures are rare, but we see some at $J = 57$ on the fifth surface from the bottom. Others do exist, but this one is amongst the clearest at this range of $J$ . . . . .	174
6.5	$CF_4$ $\nu_3/2\nu_4$ REES plots. Surfaces are labeled starting from the center going out. Looking at surfaces one by one shows their individual geometry and indicates how the level clusters (contours) must arrange themselves. We include only 4 surfaces as examples, but many are examined in the analysis. . . . .	176
6.6	Multi-rotor RES formed from different types of rotors will make RES with varying topographies. Unlike other RES, the contours here do not indicate quantum energies. They exist only to show changes in topography. . . . .	182
6.7	Classical and quantum spin treatment will result in different RES. Contours show topography and do not indicate quantum energy. Surfaces are sliced open to show the surface inside. . . . .	185

## List of Tables

2.1	Tabulated $\mathbf{v}_q^k$ values for $J=1$ . . . . .	25
2.2	Tabulated $\mathbf{v}_q^k$ values and relation to quaternions . . . . .	26
2.3	Unit Tensor Representations . . . . .	27
2.4	Forming $\langle \mathbf{v}_0^k \rangle$ from powers of $J$ and $m$ . . . . .	32
2.5	Forming $\langle \mathbf{v}_0^k \rangle$ from powers of $J$ and $m$ , expanded . . . . .	33
2.6	Quantum values are similar to their semiclassical counterparts. Shown are $\langle \mathbf{v}_q^k \rangle$ and $ J ^2 P_k(\cos \theta_m^J)$ at $J = 4, 6$ for changing $m$ . Agreement is exact for both $k = 2$ cases and improves with increasing $J$ for $k = 4$ . Values are normalized and reported in arbitrary energy units. . . . .	40
2.7	Orthorhombic 4-group $D_2 = C_2 \times C_2$ character table construction . . .	49
2.8	Group character tables for cyclic groups of symmetry order $N$ . . . . .	49
2.9	Symmetry correlation table between species of $D_2$ and its axial subgroups.	50
3.1	Correlation tables between octahedral symmetric, $O$ and various cyclic subgroups . . . . .	56
3.2	RES plots exploring the 2D parameter space . . . . .	64
5.1	Key commutation number for group $O$ are listed using Eq 4.43. . . . .	138
5.2	Splittings of $O \supset C_4$ given sub-class structure. . . . .	144
5.3	Splittings of $O \supset C_3$ given sub-class structure. . . . .	148
5.4	Splittings of $O \supset C_2(i_4)$ given sub-class structure. . . . .	154
5.5	Matrix that converts tunneling strengths to cluster splitting energies . .	155
5.6	Matrix that converts cluster splitting energies to tunneling strengths . .	156

## Introduction

Light is the only tool humanity has to glean information from the stars. It may be the only tool humanity will ever have. The details of interactions between light and molecules provides more than inspiring images from telescopes, but also a window into the chemistry, physics and perhaps biology of the universe. Moreover, high-resolution spectroscopy is not only responsible for our understanding of the very distant, but also the very small. The foundations of quantum mechanics are tested time and time again by spectroscopy.

Molecular spectroscopy is unique for providing a test bed for perfect molecular symmetry to dominate physical interactions. Symmetry and its slight perturbation create an array of effects that exist on wide energy range. The phenomena studied here are particular to high-resolution spectroscopy of highly symmetric molecules, but the same effects of symmetry play analogous roles in myriad physical systems from coupled oscillators to the electronic structure of crystals.

Physicists and chemists consider symmetry and group theory to be work saving tools. This undervalues the quantitative understanding that theoretical work can provide. Symmetry offers new avenues to explore, new phenomena to expect and way of mathematical story telling. While the quantum mechanical world is invisible to our massive bodies, symmetry analysis provides a qualitative understanding that lists of eigenvalues cannot.

A key mathematical technique for atomic or molecular physics and quantum chemistry is matrix diagonalization for quantum eigensolution. As computers become faster and more available, more problems of chemical physics are framed in terms of choosing bases for eigensolution of time evolution operators or Hamiltonian generator matrices. The resulting eigenvectors and eigenvalues are Fourier amplitudes and frequencies that combine to give all possible dynamics in a given basis choice.



Despite the ease and power of computer diagonalization, it remains a “black box” of processes quite unlike the complex natural selection by wave interference that we imagine nature uses to arrive at its quantum states. Diagonalization uses numerical tricks to reduce each  $N$ -by- $N$  matrix to  $N$  values and  $N$  stationary eigenstates, but the artificial processes may seem as opaque as nature itself with little or no physical insight provided by  $N^2 - N$  eigenvector components. We are thus motivated to seek ways to visualize more of the physics of molecular eigensolutions and their spectra. This leads one to explore digital graphical visualization techniques that provide insight as well as increased computational power.

Before describing tensor eigensolution techniques, a brief review is given of related methods that may help to put this particular technique in a historical and methodological context. Chapter 1 gives this context and a background of graphical techniques used to evaluate rotational level clustering and tensor algebra used to create these graphical tools. Chapter 2 expounds further on tensor algebra and uses these tools to evaluate symmetric and asymmetric top molecules. Much of this analysis is then shown for more complicated octahedral molecules in Chapter 3. The graphical analysis in Section 3.2 shows a type of rotational level clustering not previously known. Chapter 4 offers a Semi-Classical explanation of inter-cluster spectral structure. Finally, Chapter 6 shows how this analysis can work be used for measured or calculate spectra, particularly spectra with significant rotation-vibration coupling.

## Chapter 1

### Introduction to Semi-Classical Analysis and the Rotational Energy Surface

## 1.1 Background

### 1.1.1 Symmetry-based Clustering of Rotational Energy Levels

Clustering of rotational energy levels was first reported in 1972 by Dorney and Watson[1]. Their calculations of tetrahedral ( $XY_4$ ) molecules posited that anharmonic or high-order rotational Hamiltonians ( $J^k$  where  $k > 2$ ) could cause, rather than split degeneracy.

Harter and Patterson expanded this theoretical observation[2] which was also confirmed experimentally[3]. Their semi-classical study demonstrated that molecular symmetry can create an entirely new sort of effect: one where internally motivated symmetry-reduction could cause, rather than split degeneracy. In this case, internally motivated symmetry breaking is that which the molecule does to itself by a centrifugally induced interaction (anharmonic rotational Hamiltonian terms), rather than symmetry breaking from an external agent or field. Highly excited rotational states induce the molecule to deform its shape and also its rotational phase-space. As the  $2J + 1$  eigensolutions redistribute themselves in the deformed phase-space, they cluster themselves in ways dependent on the old symmetry (spherical) and the reduced symmetry (tetrahedral). This redistribution is explained in detail in Section 1.1.4 and ref [4].

Symmetry and semi-classical analysis were used to show the formation and splitting of clusters as well as line strength[4]. This work focuses on spectroscopic cluster formation and splitting as a testbed for exploring symmetry and semi-classical analysis as qualitative tools to evaluate classical-quantum correspondence, dynamical tunneling, vibrational mode localization and other topics central to chemical physics. Moreover, the effects outlined in this work are dominant in molecular species of current interest. Notable among these is methane ( $CH_4$ ), well known as a greenhouse gas on Earth as well as a molecule present in planetary and lunar atmospheres.

### 1.1.2 Computer Graphical Techniques

Several graphical techniques and procedures exist for gaining spectral insight. One of the oldest is the Born-Oppenheimer approximate (BOA) potential energy surface (PES) that is a well-established tool for disentangling vibrational-electronic (vibronic) dynamics. While BOA-PES predate the digital age by decades, their calculation and display is made practical by computer. More recent are studies of phase portraits and wavepacket propagation techniques to follow high- $\nu$  vibrational dynamics and chemical pathways for dissociation or re-association[5, 6]. This includes BOA-breakdown states in which a system evolves on multiple PES paths that interfere with each other. Dynamic Jahn-Teller-Renner effects are the earliest examples of multi-BOA-PES states in molecules and solids.

Visualizing eigensolutions and spectra in crystalline solids is helped by bands of dispersion functions in reciprocal frequency-versus-wavevector space. An analogy with band theory of solids in B-fields and molecular rovibronic bands is one of the ideas explored below.

Visualization of molecular rotational, rovibrational, and rovibronic eigensolutions and spectra is the subject of this work. Key techniques for achieving this goal involve the rotational energy surface (RES). As described below, an RES is a multipole expansion plot of an effective Hamiltonian in rotational momentum space. High sensitivity of vibronic states to rotation lets the RES expose intricate and unexpected physics.

The RES was introduced about twenty-five years ago[7] to analyze spectral fine structure of high resolution spectral bands in molecules of high symmetry. Among these are  $\text{PH}_3$ [8],  $\text{XDH}_3$  and  $\text{XD}_2\text{H}$  molecules[9], tetrahedral ( $\text{P}_4$ )[10], tetrafluorides ( $\text{CF}_4$  and  $\text{SiF}_4$ )[11], hexafluorides ( $\text{SF}_6$ ,  $\text{Mo}(\text{CO})_6$  and  $\text{UF}_6$ )[12, 13, 14, 15], cubane ( $\text{C}_8\text{H}_8$ ), and buckyball ( $\text{C}_{60}$ )[14, 15]. Several effects were predicted using RES techniques, including major hyperfine mixing of Herzberg rovibronic species[16]. Recently RES have been extended to help understand the dynamics and spectra of fluxional

rotors[17] or “floppy” molecules such as methyl-complexes[18].

Each of the techniques and particularly the RES-based ones described below depend upon the key wave functional properties of stationary phase, adiabatic invariance, and the spacetime symmetry underlying quantum theory. Additional symmetry (point group, space group, exchange, gauge, etc.) of a molecular system makes it prone to additional resonance, but that also makes graphical techniques even more useful to expose and analyze resonant phenomenal dynamics.

### **Vibronic Born-Openheimer Approximate potential energy surfaces (BOA-PES)**

A BOA-PES depends on an adiabatic invariance of each electronic wavefunction to nuclear vibration. It is often said that the electrons are so much faster than nuclei that the system “sticks” to a particular PES that electrons provide. Perhaps a better criterion would be that the spectrum associated with nuclear motion does not overlap that of an electronic transition to another energy level. Nuclei often provide stable configurations that quantize electronic energy into levels separated by gaps much wider than that of low lying vibrational “phonon” states.

A BOA wavefunction is a peculiarly entangled outer product  $\Psi = \eta\psi$  of a nuclear factor wavefunction  $\eta_{\nu(\epsilon)}(X \dots)$  in (1.1a) whose quantum labels  $\nu(\epsilon)$  depend on electronic quantum labels  $\epsilon = nlm$ , etc. while the electronic factor wave  $\psi(x_{(X\dots)} \dots)$  is a function whose electron coordinates  $x_{(X\dots)} \dots$  depend adiabatically on nuclear vibrational coordinates  $(X \dots)$  of the PES  $V_\epsilon(X \dots)$  belonging to one electron bonding state  $\epsilon$ .

The adiabatic convenience of a single product Eq (1.1a) with a vibration eigenfunction  $\eta_{\nu(\epsilon)}(X \dots)$  on a single PES function  $V_\epsilon(X \dots)$  is welcome but comes at the price of more complicated symmetry operator product algebra. A BOA-entangled coordinate-state is not a simple bra-ket wavefunction product in Eq (1.1b) of bra-bra

$\langle x \dots | \langle X \dots |$  position and ket-ket  $|\psi_\epsilon\rangle|\eta_\nu\rangle$  state.

$$\begin{aligned} \Psi_{\nu(\epsilon)}(x^{electron} \dots X^{nuclei} \dots) = \\ \psi_\epsilon(x_{(X\dots)} \dots) \cdot \eta_{\nu(\epsilon)}(X \dots) \quad \text{BOA-Entangled Product} \end{aligned} \quad (1.1a)$$

$$\begin{aligned} \Psi_{\nu,\epsilon}(x^{electron} \dots X^{nuclei} \dots) = \\ \psi_\epsilon(x \dots) \cdot \eta_\nu(X \dots) \quad \text{Unentangled Product} \\ = \langle x \dots | \psi_\epsilon \rangle \langle X \dots | \eta_\nu \rangle = \langle x \dots; X \dots | \psi_\epsilon; \eta_\nu \rangle \end{aligned} \quad (1.1b)$$

Elementary symmetry operators that operate on Eq (1.1b) are well known, but the symmetry transformation of BOA product Eq (1.1a) depends on rotational BOA-relativity of its parts. If one includes rotational effects as well, then the vibronic BOA-PES generalize to rovibronic RES that involve rotational frame symmetry relations described below.

### Rovibronic BOA rotational energy surfaces (BOA-RES)

The rotational energy surface (RES) can be seen as a generalization of adiabatic vibrational-electronic(vibronic) BOA wave Eq (1.1a) to a rovibronic wave in Eq (1.2) below that includes rotational motion. Here one treats vibronic motion as having the “fast” degrees of freedom while rotational coordinates  $\Theta$  (e.g., Euler angle  $(\alpha\beta\gamma)$  for semi-rigid molecules) play the “slow” semi-classical role vis-a-vis the “faster” adiabatic vibration or vibronic states.

$$\begin{aligned} \Phi_{J[\nu(\epsilon)]}(x^{elec} \dots Q^{vib} \dots \Theta^{rot}) = \\ \psi_\epsilon(x_{(Q\dots\Theta\dots)} \dots) \cdot \eta_{\nu(\epsilon)}(Q \dots [\Theta \dots]) \cdot \rho_{J[\nu(\epsilon)]}(\Theta^{rot} \dots) \end{aligned} \quad (1.2)$$

In Eq (1.2), the wave factors of each motion are ordered fast-to-slow going left-to-right. As in Eq (1.1a) each wave-factor quantum number depends on quanta in “faster” wave-factors written to its left, but each coordinate has adiabatic dependence on coordinates in “slower” factors written to its right.

Notation  $Q$  in Eq (1.2) stands for vibrational normal coordinates  $(q_1, q_2, \dots, q_m)$  and  $\nu$  stands for their quanta  $(\nu_1, \nu_2, \dots, \nu_m)$ . The number  $m = 3N - 6$  of modes of an  $N$ -atom semi-rigid molecule has subtracted 3 translational and 3 rotational coordinates. Each mode  $q_k$  assumes an adiabatic BOA dependency on overall translation and rotation  $\Theta$ . Such dependency involves well known Eckart conditions that underlie the Watson Hamiltonian[19, 20, 21]. (Here we ignore translation.)

RES are multipole expansion plots of effective BOA energy tensors for each quantum value of vibronic quanta  $\nu(\epsilon)$  and conserved total angular momentum  $J$ . Choices of effective energy tensors depend on the level of adiabatic approximation. So do the choices of spaces in which RES are plotted. Elementary examples of model BOA waves, tensors, and RES for rigid or semi-rigid molecules are discussed below.

### 1.1.3 Lab-frame coupling vs. Body frame constriction

Wave  $\rho_J(\Theta^{rotation})$  for a bare rigid symmetric-top ( $\psi = 1 = \eta$ ) molecule is a Wigner  $D^J$ -function.

$$\rho_J(\Theta) = \rho_{J,M,K}(\alpha\beta\gamma) = D_{M,K}^{J*}(\alpha\beta\gamma)\sqrt{\text{norm}}$$

$$\text{norm}=[J]=2J+1 \quad (1.3)$$

Total angular momentum  $J$  is  $J = R$  for a bare rotor. Bare lab-frame z-component is labeled  $M = m$ . Its body-frame  $\bar{z}$ -component is labeled  $K = \bar{M} = n$ . Both  $m$  and  $n$  range between  $+R$  and  $-R$  in integral steps.

An entangled BOA product Eq (1.2) mates vibronic factor Eq (1.1a) with a rotor factor  $\rho_J = \rho_{J,M,K}$  like Eq (1.3). Now  $J$  and  $K = \bar{M}$  depend on total vibronic

momentum  $l$  and its body  $\bar{z}$ -component  $\bar{\mu}$  in  $\Psi_{\nu(\epsilon)} = \Psi_{\bar{\mu}}^l$ .

$$\Phi_{J[\nu(\epsilon)]} = \Psi_{\nu(\epsilon)}^l \cdot \rho_{J[\nu(\epsilon)]} = \Psi_{\bar{\mu}}^l \cdot \rho_{J,M,K} = \Psi_{\bar{\mu}}^l \cdot \mathcal{D}_{M,K}^{J*} \sqrt{[J]} \quad (1.4)$$

A disentangled product  $\Psi_\rho$  like Eq (1.1b) of lab-based vibronic wave  $\Psi_\mu^l$  and bare rotor  $\rho_{R,m,n}$  Eq (1.3) is coupled by Clebsch-Gordan Coefficients  $C_{\mu m M}^{l R J}$  into a wave  $\Phi_M^J$  of total  $J = R + l, R + l - 1, \dots$  or  $|R - l|$  and  $M = \mu + m$  by the following sum over lab  $z$ -angular bare rotor momenta  $m$  and lab vibronic  $\mu$  bases.

$$\Phi_M^J = \sum_{\mu, m} C_{\mu m M}^{l R J} \psi_\mu^l \cdot \rho_m^R = \sum_{\mu, m} C_{\mu m M}^{l R J} \psi_\mu^l \cdot \mathcal{D}_{m,n}^{R*} \sqrt{[R]} \quad (1.5)$$

(M= $\mu+m$ =const.)

A BOA-entangled wave like Eq (1.1a) or Eq (1.4) requires more serious surgery in order to survive as a viable theoretical entity. BOA vibronic wave are not merely *coupled* like Eq (1.5) to a rotor, they are adiabatically “glued” or *constricted* to the intrinsic molecular rotor frame. (We say a rotor is “BOA-constricted” by its vibronic wave much as a boa-constrictor rides its writhing prey as the two rotate together.)

A remarkable property of quantum rotor operator algebra is that Wigner  $D^l$ -waves in Eq (1.3) are also transformation matrices that relate rotating body-fixed BOA  $\Psi_{\bar{\mu}}^l(\textit{body})$  into the lab-fixed  $\Psi_\mu^l(\textit{lab})$ .

$$\Psi_{\bar{\mu}}^l(\textit{body}) = \sum_{\mu} \Psi_\mu^l(\textit{lab}) \mathcal{D}_{\bar{\mu}\mu}^l(\alpha\beta\gamma) \quad (1.6a)$$

$$\Psi_\mu^l(\textit{lab}) = \sum_{\bar{\mu}} \Psi_{\bar{\mu}}^l(\textit{body}) \mathcal{D}_{\mu\bar{\mu}}^{l*}(\alpha\beta\gamma) \quad (1.6b)$$

D-matrices underlie all tensor operators, their eigenfunctions and their eigenvalues and are a non-Abelian (non-commutative) generalization of plane waves  $d^{k*}(r) = \langle r|k \rangle = e^{ikr}$  underlying Fourier operator analysis. Details of this connection are explored in Chapter 2.



Of particular importance to RES theory is the Wigner-Eckart factorization lemma, Eq 1.7a, that relates Clebsch-Gordan  $C_{\mu m M}^{lR J}$  to Wigner- $D$ 's and transforms coupled wave Eq (1.5) to BOA-constricted wave Eq (1.4).

$$\int d(\alpha\beta\gamma) \mathcal{D}_{\mu\bar{\mu}}^{l*}(\alpha\beta\gamma) \mathcal{D}_{mn}^{R*}(\alpha\beta\gamma) \mathcal{D}_{MK}^J(\alpha\beta\gamma) = \frac{1}{[J]} C_{\mu m M}^{lR J} C_{\bar{\mu} n K}^{lR J} \quad (1.7a)$$

$$\sum_{\mu} \sum_{\bar{\mu}} C_{\mu m M}^{lR J'} \mathcal{D}_{\mu\bar{\mu}}^{l*}(\alpha\beta\gamma) \mathcal{D}_{mn}^{R*}(\alpha\beta\gamma) C_{\bar{\mu} n K}^{lR J} = \delta^{J J'} \mathcal{D}_{MK}^{J*}(\alpha\beta\gamma) \quad (1.7b)$$

$$\sum_{\mu} C_{\mu m M}^{lR J'} \mathcal{D}_{\mu\bar{\mu}}^{l*}(\alpha\beta\gamma) \mathcal{D}_{mn}^{R*}(\alpha\beta\gamma) = \sum_{\bar{\mu}} C_{\bar{\mu} n K}^{lR J} \mathcal{D}_{MK}^{J*}(\alpha\beta\gamma) \quad (1.7c)$$

A more familiar form of this is the Kronecker relation of product reduction  $\mathcal{D}^l \otimes \mathcal{D}^R \approx \mathcal{D}^J \oplus \mathcal{D}^{J'} \oplus \dots$ . Another form is a body-to-lab coupling relation with  $M = \mu + m$  and  $n = K - \bar{\mu}$  fixed in the  $\mu$  or  $\bar{\mu}$  sums. The latter yields a sum over  $\bar{\mu} = K - n$  of body-fixed BOA waves Eq (1.4) giving lab-based  $\Phi_M^J$  wave Eq (1.5).

$$\Phi_M^J = \sum_{\mu} C_{\mu m M}^{lR J} \Psi_{\mu}^l(lab) \mathcal{D}_{m,n}^{R*} \sqrt{[R]} \quad (1.8)$$

$$\begin{aligned} \Phi_M^J &= \sum_{\mu} C_{\mu m M}^{lR J} \sum_{\bar{\mu}} \Psi_{\mu}^l(body) \mathcal{D}_{\mu\bar{\mu}}^{l*} \mathcal{D}_{m,n}^{R*}(\alpha\beta\gamma) \sqrt{[R]} \\ &= \sum_{\mu} C_{\bar{\mu} n K}^{lR J} \Psi_{\bar{\mu}}^l(body) \mathcal{D}_{MK}^{J*}(\alpha\beta\gamma) \sqrt{[R]} \\ &= \sum_{\bar{\mu}} C_{-K\bar{\mu} n}^{JlR} \Psi_{\bar{\mu}}^l(body) \mathcal{D}_{MK}^{J*}(\alpha\beta\gamma) \sqrt{[J]} \end{aligned} \quad (1.9)$$

The coupling relation  $\bar{\mu} = K - n$  also simplifies Eq 1.5 into Eq 1.8, or reorganized into Eq 1.9.

$$\Phi_M^J = \sum_{\bar{\mu}} C_{-K\bar{\mu} n}^{JlR} \Psi_{\bar{\mu}}^l \rho_{J,M,K} = \sum_{\bar{\mu}} C_{-K\bar{\mu} n}^{JlR} \Phi_{J[K\nu(\epsilon)]} \quad (1.10a)$$

$$\Phi_{J[K\nu(\epsilon)]} = \sum_R C_{-K\bar{\mu} n}^{JlR} \Phi_M^J \quad (1.10b)$$

Body-(un)coupling Eq (1.10a) is an undoing of BOA-constriction by subtracting

vibronic  $(l, \bar{\mu})$  from  $(J, K)$  of BOA-wave  $\Phi_{J[\nu(\epsilon)]}$  Eq (1.10b) to make lab-fixed  $\Phi_M^J$  Eq (1.10a) with sharp rotor quanta  $R = J - l, J - l + 1 \dots$  or  $J + l$ . In a lab-fixed wave  $\Phi_M^J$  of Eq (1.5) or Eq (1.10a), rotor  $R$  is conserved, but  $K$  and  $\bar{\mu}$  that are not. A BOA wave  $\Phi_{J[\nu(\epsilon)]}$  of Eq (1.4) or Eq (1.10b) has body-fixed vibronic  $K$  and  $\bar{\mu}$  that are conserved, but rotor  $R$  that is not.

It is important to note the following for Eqs (1.8) - (1.10b). For Eq (1.8),  $(M = \mu + m)$  equals a constant. Eq (1.9) is derived from Eqs (1.6b) and (1.7c), while  $(n = K - \bar{\mu})$  is a constant. Finally, in Eqs (1.10a) and (1.10b)  $K = \bar{\mu} + n$  and  $M = \mu + m$  respectively.

However, in both Eq (1.10a) and Eq (1.10b) the internal bare-rotor body component  $n = K - \bar{\mu}$  is conserved due to a symmetric rotor's azimuthal isotropy. This  $n$  is a basic rovibronic-species quantum number invariant to all lab based perturbation or transition operators. Like a gyro in a suitcase, no amount of external kicking of the case will slow its spin. Only internal body operations can "brake" its  $n$ .

The duality of lab vs body quantum state labels and external vs internal operators is an important feature of molecular and nuclear physics, and it is to be respected if we hope to take full advantage of symmetry group algebra of eigensolutions. The duality is related to that of bra-&-ket. For every group of symmetry operations such as a 3D rotation group  $R(3)_{lab} = \{\dots \mathbf{R}(\alpha\beta\gamma) \dots\}$  there is a dual body group  $R(3)_{body} = \{\dots \bar{\mathbf{R}}(\alpha\beta\gamma) \dots\}$  having identical group structure, but commuting with the lab group. Tensor multipole operators, discussed in detail in Chapter 2, come in dual and inter-commuting sets as well. Duality is discussed further in Chapter 4.

#### 1.1.4 Creating and Using Rotational Energy Surfaces

The Rotational Energy Surface (RES) is a semi-classical phase-space surface used to analyze various effects in rovibrational spectra. The Poinsot Ellipsoid, as well as other classical and semi-classical rotational phase-space surfaces, have been used in the past[22]. The Poinsot Ellipsoid is a surface of constant energy, plotting changing

angular velocity. The RES is useful spectroscopically because it describes rotational energy for a constant angular momentum. Therefore, the RES defines the energy level structure for a given angular momentum.

The RES tools used here were first developed by Harter et al [13, 2] to evaluate rotational level clusters in tetrahedral and octahedral molecules. This analysis was first done for ground and singly excited vibrational states and was expanded to deal with higher vibrational states, which are treated quantum mechanically [23, 24]. Other groups have used Rotational Energy Surfaces (RES) to evaluate the rotational clusters inside vibrational triplets [10, 12] and internal rotations [17]. In each of these cases there are three main uses of the RES.

1. To explain the boundaries of the rotational bands for a given angular momentum.
2. To explain rotational clusters in terms of symmetry reduction [2].
3. To explain the splittings of the rotational clusters in terms of phase-space tunneling [25].

Most of this work will employ the first two of these uses, while Chapter 4 focuses on the third.

While theorists typically use quantum rotational or rovibronic Hamiltonians written as polynomial functions of  $\hat{J}$ , converting to a unit-tensor formalism allows for a variety of semi-quantum, semi-classical and classical analyses. By rewriting the molecular Hamiltonian, one is able to use a well parameterized Hamiltonian that is written in terms of the symmetry reduction from the rotational Lie symmetry,  $SO(2)$ , to the molecular symmetry,  $SO(2) \supset \mathcal{G} \times \mathcal{T}$ , where  $\mathcal{G}$  is the point symmetry group of the molecule. Much of the effort in Chapters 3, 4 and 6 deals with octahedral and tetrahedral molecules where  $SO(2) \supset T_d \times \mathcal{T}$ . This Hamiltonian may also be written as an outer product of rotational and vibrational operators.

The semi-classical analysis done here will keep rotation a classical function of body

frame angles  $\theta$  and  $\phi$ . One may then create surfaces of constant angular momentum called Rotational Energy Surfaces.

The RES is built by first rewriting the rotational Hamiltonian as classical polynomial functions of  $\vec{J}$ , rather than of quantum operators  $J$  and  $K$ . By also making  $|J|$  a discrete value, the rotational Hamiltonian can be plotted for constant total angular momentum and varying direction of  $\vec{J}$  in the body frame. Thus, the semi-classical form of the rotational Hamiltonian can be called  $E^J(\theta, \phi)$ , or a RES.

Symmetric-top molecules have a simple Hamiltonian that can be quickly converted to  $E^J(\theta, \phi)$  form. The Hamiltonian polynomial and  $E^J(\theta, \phi)$  are expressed in Eq (1.11a). Fig 1.1 plots the RES for this Hamiltonian, given that  $A = B < C$ . Such Hamiltonians will be discussed in chapter 2.

$$H = A(J_x)^2 + B(J_y)^2 + C(J_z)^2 \quad (1.11a)$$

$$E^J = \frac{1}{3}(A + B + C)|J|^2 + \frac{1}{3}(2C - A - B)|J|^2 \left( \frac{3}{2} \cos^2 \theta - \frac{1}{2} \right) + \frac{1}{\sqrt{6}}(A - B) \sqrt{\frac{3}{2}} |J|^2 \sin^2 \theta \cos 2\phi \quad (1.11b)$$

A more complicated example of RES is one for SF<sub>6</sub> at  $J = 30$  is shown in Fig 1.2. SF<sub>6</sub> has a more complicated structure which requires a fourth order polynomial Hamiltonian  $H = BJ^2 + D(J_x^4 + J_y^4 + J_z^4)$ . Importantly, the RES and the molecule share octahedral symmetry. Fig 1.2 is given here as an example only and will be explained in detail in chapter 3.

Contours on RES in Fig 1.2 correspond to exact quantum levels. The radius of all RES at a particular location is the rotational energy for that  $J$  direction in the body-frame. The contour through that point is a precession path that  $J$  could follow without changing total energy. Contours are intersections of a constant energy (constant radius) sphere and the RES.

Contours show two important properties. The first is property is local-symmetry

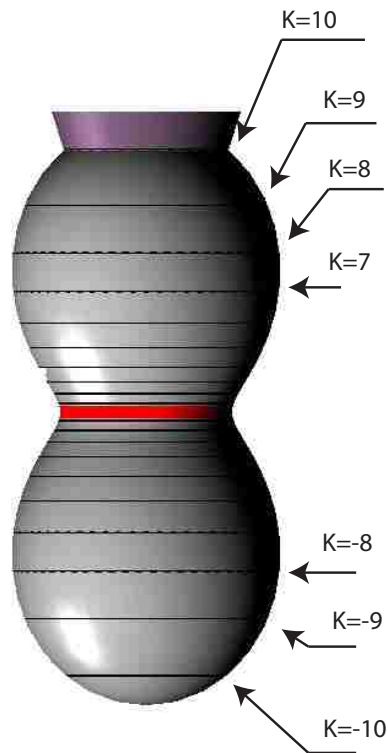


Figure 1.1: Symmetric Top RES  $J = 10$ .  $K$  values are marked on the plot.

of the cluster states in the rotational phase-space and is related to the molecular symmetry group[4, 25].

The second property of RES energy contours involves their relation with cones of angular momentum uncertainty. These cones are graphical manifestations of the uncertainty in  $J_x$  and  $J_y$  for a given  $J$  and  $J_z$ . Uncertainty cones have an opening angle defined by Eq (1.12).

$$\theta_{\text{uncertainty}} = \arccos \left( \frac{J_z}{\sqrt{J(J+1)}} \right) \quad (1.12)$$

Eq (1.12) comes from the known magnitude of  $J_z$  and  $\vec{J}$  for a given rotational angular momentum. An example of such an intersection with an RES is shown in Fig 1.2. Fig 1.2 is an RES describing a ground vibrational state and matches the behavior of  $\text{SF}_6$  at  $J = 30$  and shows a  $J_z = 30$  cone (shown in purple) protruding from the top

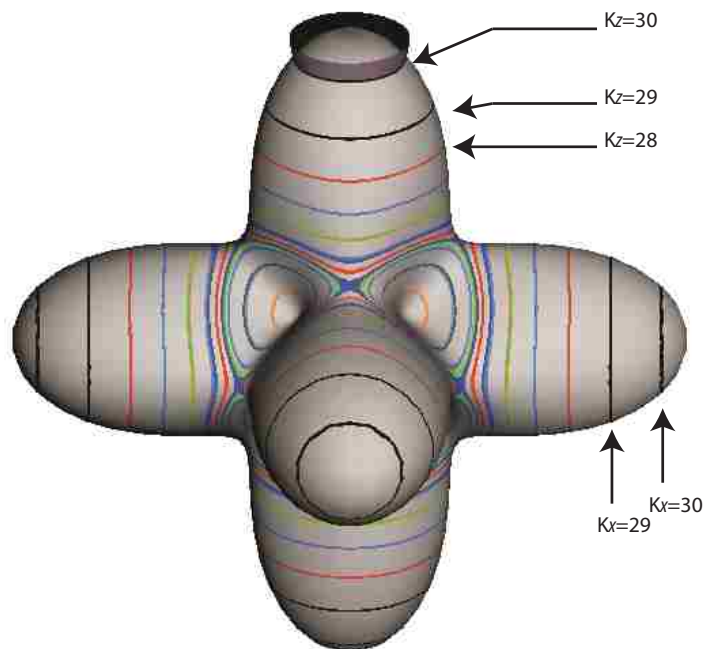


Figure 1.2: Rotational Energy Surface for  $\text{SF}_6$  at  $J = 30$  in the vibrational ground state. Quantum contours labeled by  $K$ -values are shown with colors matching the symmetry of the topmost level in the  $K$ -cluster. (Color code:  $A_1$  is red,  $A_2$  is orange,  $E$  is green,  $T_1$  is blue and  $T_2$  is light blue.) Black clusters are too tight for the graphic routine to distinguish symmetry. The highest- $K$  ( $K = 30 = J$ ) uncertainty cone is protruding from the RES at the top.

of the RES.

The uncertainty cone may be placed at any of the surface's symmetry axes and may vary in angle so long as  $J_z$  is an integer,  $|J_z| \leq J$  and the cone does not cross a separatrix.

Uncertainty cones and energy contours relate classical and quantum attributes of the RES. The RES itself is a classical phase-space that is shown to only allow certain quantized paths corresponding to quantum mechanically calculated energies. Likewise, the uncertainty cones are a graphical manifestation of angular quantization that relates to classical rotation intersection with the RES.

The uncertainty cones are useful for several analytical tasks. For example, it has been shown that non-circular cone intersections (semi-classical trajectories) have varying  $k$ -projection indicative of  $k$ -mixing. The RES and uncertainty cones can

also be used to determine how rotational levels may cluster together. The origins of clustering by symmetry reduction are discussed in section 1.1.4. More detail about uncertainty cones and their use can be found in ref [4].

RES plots in this document are created by computer programs written by the author, specifically for this purpose. High-level languages, such as Mathematica and Matlab, could be used to similar effect, but the hand written Objective-C code proved fast enough to be interactive for the user. Interactivity was a fundamental goal. This allowed the user to take full advantage of the qualitative analysis possible with phase-space plots.

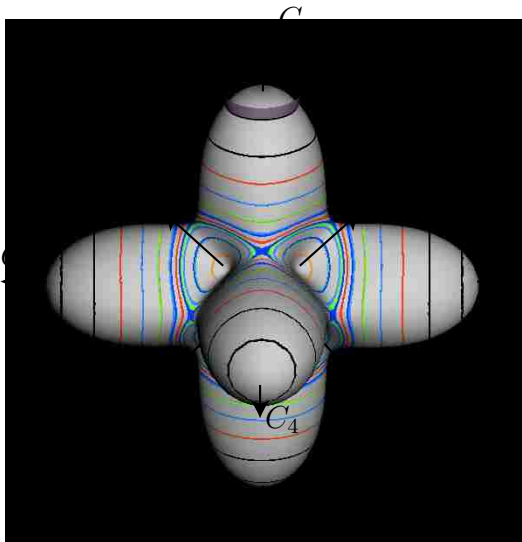
Three dimensional plotting was done using OpenGL while corresponding two dimensional energy level plots were made using a variety of tools.

## **RES Global and Local Symmetry**

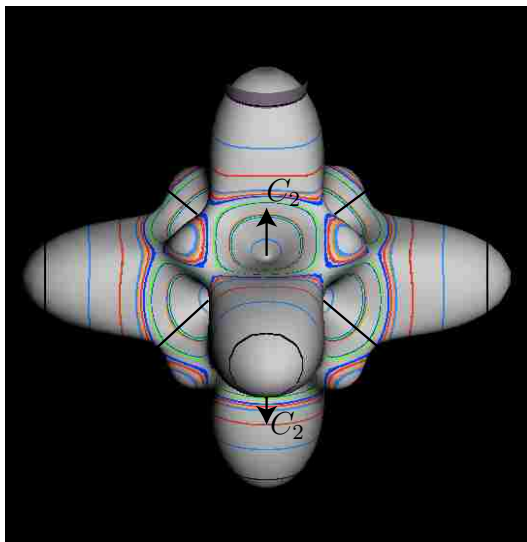
As mentioned in earlier, the placement of quantum contours in the RES determines possible clustering and cluster splitting within the molecule's energy level structure. Rotationally or vibrationally induced molecular distortions deform the RES away from a sphere. As long as these distortions are written in terms of operators sharing the molecular symmetry, the RES will also share that symmetry. Convex parts of the RES that protrude radially to elevated energy, correspond to rotational axes of reduced distortion. Concave portions of the RES at reduced energy, indicate rotational axes along which the molecule tends to flatten, and raise its moment of inertia. Generally the rotational axes with the greater structural distortion have the lowest rotational energy.

Though the entire RES must show the overall or global symmetry of the molecule, local pockets of an RES represent subgroups of the molecular symmetry group.

Subgroup sections are identified by the local shape of the base or separatrix contour that divides the RES into locales belonging to a particular subgroup chain. Fig 1.3 shows two different RES plots with slightly different local geometries, but both with



(a) RES contains 8  $C_3$  and 6  $C_4$  axes. All visible axes are indicated.



(b) RES contains 12  $C_2$  axes along with 8  $C_3$  and 6  $C_4$  axes. Only visible  $C_2$  axes are shown

Figure 1.3: Local symmetry axes of globally octahedral RES plots. The two plots are built of the same operators, but show different local symmetry features because of different fitting related to the rotational Hamiltonian.



globally octahedral symmetry, created by using different Hamiltonian fitting terms. Fig 1.3(a) shows six locally  $C_4$  sections protruding from their square bases as well as eight locally  $C_3$  concave sections with triangular bases. Both the  $C_4$  and  $C_3$  sections are marked by a labeled symmetry axis. Fig 1.3(b) relates to a slightly different Hamiltonian which includes both fourth and sixth order polynomial terms. Because of the new contribution, the RES contains  $C_4$  and  $C_3$  structures (both now protruding), but also 12 concave  $C_2$  sections, each with a rectangular base and a  $C_2$  symmetry axis.

How many such regions exist is found from the ratio of the order,  ${}^\circ\mathcal{G}$ , of the group to the order,  ${}^\circ\mathcal{H}$ , of the local subgroup. As is shown in Fig 1.3,  $({}^\circ\mathcal{G}/{}^\circ\mathcal{H})$  gives a smaller number of identical phase-space regions for higher symmetry subgroups. Without considering inversions the total order is  ${}^\circ\mathcal{G} = 24$  for our octahedral systems.

The level structure within each cluster will also be affected by the local geometry of the RES. Rotational level clustering has been well known for decades and well explained by internal symmetry breaking[25]. This is most easily understood in terms of the RES. For a molecule of point symmetry  $\mathcal{G}$ , a RES will have a global symmetry of  $\mathcal{G}$ , but rotational energy levels will sit in local sections of the RES with a symmetry corresponding to a subgroup  $\mathcal{H} \subset \mathcal{G}$  and generally there will be two or more equivalent copies of each  $\mathcal{H}$  locale. Each energy level will be able to tunnel to the corresponding level (contour) at the same altitude (energy) on all the other equivalent  $\mathcal{H}$  regions. The symmetry breaking  $\mathcal{G} \downarrow \mathcal{H}$  forces rotational levels to cluster in patterns described by the restricted representation or symmetry correlation table. The  $O \supset C_4$ ,  $O \supset C_3$  and  $O \supset C_2$  correlation tables are shown later in chapter 3.

Tunneling between equivalent local subgroup regions causes the rotational clusters to split slightly. A detailed description of these effects is in Chapter 4.

## Bibliography

- [1] A. J. Dorney and J. K. G. Watson. Forbidden rotational spectra of polyatomic molecules: Stark effects and  $\Delta J = 0$  transitions of  $T_d$  molecules. *Journal of Molecular Spectroscopy*, 42:135–148, 1972.
- [2] W. G. Harter and Chris W. Patterson. Simple model for asymptotic level clusters in  $\text{SF}_6$  rotational spectra. *Physical Review Letters*, 38(5):224–227, January 1977.
- [3] Jacques Bordé and Christian J. Bordé. Superfine and hyperfine structures in the  $\nu_3$  band of  $^{32}\text{SF}_6$ . *Chemical Physics*, 71:417–441, 1982.
- [4] William G. Harter. Computer graphical and simiclassical approaches to molecular rotations and vibrations. *Computer Physics Reports*, 8:319–394, 1988.
- [5] Joel M. Bowman. Beyond Born-Oppenheimer. *Science*, 319:40–41, 2008.
- [6] Etienne Garand, Jia Zhou, David E. Manolopoulos, Millard H. Alexander, and Daniel M. Neumark. Nonadiabatic interactions in the  $\text{Cl}+\text{H}_2$  reaction probed by  $\text{ClH}_2^-$  and  $\text{ClD}_2^-$  photoelectron imaging. *Science*, 319:72–75, 2008.
- [7] William G. Harter. Theory of hyperfine and superfine levels in symmetric polyatomic molecules. ii. elementary cases in octahedral hexafluoride molecules. *Physical Review A*, 24(1):192–263, July 1981.
- [8] Sergei N. Yurchenko, Walter Thiel, Serguei Patchkovskii, and Per Jensen. Theoretical evidence for the formation of rotational energy level clusters in the vibrational ground state of  $\text{PH}_3$ . *Physical Chemistry Chemical Physics*, 7:573–582, 2005.
- [9] Sergei N. Yurchenko, Roman I. Ovsyannikov, Walter Thiel, and Per Jensen. Rotation-vibration energy cluster formation in  $\text{XH}_2\text{D}$  and  $\text{XHD}_2$  molecules ( $\text{X}=\text{Bi}, \text{P}, \text{and Sb}$ ). *Journal of Molecular Spectroscopy*, 256:119–127, 2009.

- [10] Ch. van Hecke, D. A. Sadovskii, B. I. Zhilinskiĭ, and V. Boudon. Rotational-vibrational relative equilibria and the structure of quantum energy spectrum of the tetrahedral molecule  $P_4$ . *European Physical Journal D*, 17:13, 2001.
- [11] H. T. Crogman, V. Boudon, and D. A. Sadovskii. Local modes of silane within the framework of stretching vibrational polyads. *The European Physical Journal D*, 42:61–72, 2007.
- [12] G. Dhont, D. Sadovskii, B. Zhilinskiĭ, and V. Boudon. Analysis of the "unusual" vibrational components of triply degenerate vibrational mode  $\nu_6$  of  $Mo(CO)_6$  based on the classical interpretation of the effective rotation-vibration hamiltonian. *Journal of Molecular Spectroscopy*, 201:95–108, 2000.
- [13] William G. Harter and Chris W. Patterson. Asymptotic eigensolutions of fourth and sixth rank octahedral tensor operators. *Journal of Mathematical Physics*, 20(7):1453–1459, July 1979.
- [14] William G. Harter and David E. Weeks. Rotation-vibration spectra of icosahedral molecules. i. icosahedral symmetry analysis and fine structure. *Journal of Chemical Physics*, 90(9):4727, May 1988.
- [15] William G. Harter and David E. Weeks. Rovibrational spectral fine structure of icosahedral molecules. *Chemical Physics Letters*, 132(4,5):387, December 1986.
- [16] Juan Ortigoso, Isabelle Kleiner, and Jon T. Hougen. The k-rotational labeling problem for eigenvectors from internal rotor calculations: Application of energy levels of acetaldehyde below the barrier. *Journal of Chemical Physics*, 110(24):1688–11699, June 1999.
- [17] Juan Ortigoso and Jon T. Hougen. Rotational energy surfaces of molecules exhibiting internal rotation. *Journal of Chemical Physics*, 101(4):2710–2719, August 1994.

- [18] H. T. Crogman, V. Boudon, W. G. Harter, and J. Mitchell. Deformation of sulfur hexafluoride and floppiness of trifluoromethyl sulfur pentafluoride. *Molecular Physics*, 104(16-17):2781–2790, 20 August - 10 September 2006.
- [19] James K. G. Watson. Simplification of the molecular vibration-rotation hamiltonian. *Molecular Physics*, 100(1):47–54, 2002.
- [20] James K. G. Watson. Determination of centrifugal distortion coefficients of asymmetric-top molecules. *The Journal of Chemical Physics*, 46(5):1935, March 1967.
- [21] Philip R. Bunker and Per Jensen. *Molecular Symmetry and Spectroscopy*. NRC Research Press, 2 edition, 1998.
- [22] H.C. Corben and Philip Stehle. *Classical Mechanics*. Dover Publications, 31 East 2nd Street, Mineola, N.Y. 11501, 2 edition, 1994.
- [23] William G. Harter, Harold W. Galbraith, and Chris W. Patterson. Energy level cluster analysis for  $e(\nu_2)$  vibration rotation spectrum of spherical top molecules. *Journal of Chemical Physics*, 69:4888, 1978.
- [24] William G. Harter, Chris W. Patterson, and Harold W. Galbraith. Centrifugal and coriolis effects on level cluster patterns for  $t(\nu_3)$  rovibrational bands in spherical top molecules. *Journal of Chemical Physics*, 69:4896, 1978.
- [25] William G. Harter and Chris W. Patterson. Orbital level splitting in octahedral symmetry and SF<sub>6</sub> rotational spectra. i. qualitative features of high J levels. *Journal of Chemical Physics*, 66(11):4872, June 1977.

## Chapter 2

### Tensor Geometry and Spectral Fine Structure: Symmetric and Asymmetric Top Molecules

## 2.1 Chapter Summary

Symmetry analysis of tensorial operator eigensolutions has provided insight into molecular rovibronic spectra and improved ways to calculate quantum levels and molecular dynamics. Complex fine structure is related to topography and topology in tensorial plots of rovibronic energy surfaces (RES) and shows how level cluster-formation and avoided-crossing relates to selection rules and state mixing.

A critical review of RES analysis and technique is done here to show possibilities for more general application to quantum eigensolution analysis as well as its limitations. Also presented in this chapter is the classical-quantum correspondence possible for symmetric top molecules as well as the limitation of semi-classical approximation.

## 2.2 Mathematical Background

### 2.2.1 Unitary Multipole functions and operators

The semi-classical analysis and symmetry considerations presented here rely on rewriting a rovibronic Hamiltonian in terms of unitary multipole functions. Since unitary multipole functions and their related algebra are not well known and since many equivalent versions of these functions exist, this section describes the definitions used by the work presented later. The work here is based on earlier studies found in ref. [1, 2].

Spherical harmonic functions  $Y_{lm}(\phi\theta)$  are well known orbital angular factors in atomic and molecular physics. They are special ( $n = 0$ )-cases of Wigner- $D^l$  functions Eq (1.3) as follows. Here they will be used to symmetrize the Watson Hamiltonian[3].

$$Y_m^l(\phi\theta) = \mathcal{D}_{m,0}^{l*}(\phi\theta) \sqrt{\frac{[l]}{4\pi}} \quad \text{where: } [l] = 2l + 1 \quad (2.1)$$

A diatomic or linear rotor must have zero body quanta ( $n = 0$ ) and has a  $Y_{lm}(\phi\theta)$  rotor wave.  $Y_{lm}$ -matrix elements or expectation values of a multipole potential  $Y_{kq}$

are proportional to Clebsch forms of Eq (1.7a).

$$\int d(\phi\theta\theta) \mathcal{D}_{m'0}^{J'}(\phi\theta\theta) \mathcal{D}_{q0}^{k*}(\phi\theta\theta) \mathcal{D}_{m0}^{J*}(\phi\theta\theta) = \sqrt{\frac{(4\pi)^3}{[J'][k][J]}} \int d(\phi\theta) Y_{m'}^{J*} Y_q^k Y_m^J = \frac{1}{[J]} C_{qmm'}^{kJJ'} C_{000}^{kJJ'} \quad (2.2)$$

A multipole function  $X_{kq}(x, y, z)$ , an  $xyz$ -polynomial of degree  $k$ , is  $Y_{kq}(\phi\theta)$  multiplied by  $(r)^k$ . A generic multipole  $\mathbf{v}_q^k$  matrix equals Eq (2.2) up to a factor  $\langle J' || k || J \rangle$  depending only on  $\{J', k, J\}$ , but not  $\{m', q, m\}$ .

$$\left\langle \begin{matrix} J' \\ m' \end{matrix} \middle| \mathbf{v}_q^k \middle| \begin{matrix} J \\ m \end{matrix} \right\rangle = C_{qmm'}^{kJJ'} \langle J || k || J \rangle \quad (2.3a)$$

Factor  $\langle J' || \mathbf{v}_q^k || J \rangle$  is the reduced matrix element of  $\mathbf{v}_q^k$  and chosen by a somewhat arbitrary convention.

$$\langle J' || \mathbf{v}_q^k || J \rangle = (-1)^{k+J'-J} \sqrt{\frac{[J']}{[k]}} \quad (2.3b)$$

This particular choice is made to simplify bra-ket coupling and creation-destruction operator expressions for  $\mathbf{v}_q^k$ .

$$\begin{aligned} \mathbf{v}_q^k &= (-1)^{2J'} \sum_{\substack{m, m' \\ =q-m}} C_{m'mq}^{J'Jk} \left| \begin{matrix} J' \\ m' \end{matrix} \right\rangle \left| \begin{matrix} J^* \\ m \end{matrix} \right\rangle^\dagger \\ &= (-1)^{2J'} \sum_{\substack{m, m' \\ =q-m}} C_{m'mq}^{J'Jk} \left| \begin{matrix} J' \\ m' \end{matrix} \right\rangle \left\langle \begin{matrix} J \\ -m \end{matrix} \right| (-1)^{J-m} \\ &= \sum_{\substack{m, m' \\ =q+m}} (-1)^{J'-m'} \sqrt{[k]} \begin{pmatrix} k & J & J' \\ q & m & -m' \end{pmatrix} \bar{\mathbf{a}}_{m'}^{J'} \bar{\mathbf{a}}_m^J \end{aligned} \quad (2.3c)$$

In any case, other choices only rescale  $\mathbf{v}_q^k$  eigenvalues and do not affect eigenvectors of a tensor  $\mathbf{v}_q^k$  or alter its transformation behavior Eq (2.4). (By Eq (1.7c) and Eq

Table 2.1: Tabulated  $\mathbf{v}_q^k$  values for  $J=1$

$\langle \mathbf{v}_2^2 \rangle^{J=1} =$ $\begin{pmatrix} \cdot & \cdot & \cdot \\ \cdot & \cdot & \cdot \\ 1 & \cdot & \cdot \end{pmatrix}$	$\langle \mathbf{v}_1^2 \rangle^{J=1} =$ $\begin{pmatrix} \cdot & \cdot & \cdot \\ 1 & \cdot & \cdot \\ \cdot & -1 & \cdot \end{pmatrix} \frac{1}{\sqrt{2}}$	$\langle \mathbf{v}_0^2 \rangle^{J=1} =$ $\begin{pmatrix} 1 & \cdot & \cdot \\ \cdot & -2 & \cdot \\ \cdot & \cdot & 1 \end{pmatrix} \frac{1}{\sqrt{6}}$	$\langle \mathbf{v}_{-1}^2 \rangle^{J=1} =$ $\begin{pmatrix} \cdot & -1 & \cdot \\ \cdot & \cdot & 1 \\ \cdot & \cdot & \cdot \end{pmatrix} \frac{1}{2}$	$\langle \mathbf{v}_{-2}^2 \rangle^{J=1} =$ $\begin{pmatrix} \cdot & \cdot & 1 \\ \cdot & \cdot & \cdot \\ \cdot & \cdot & \cdot \end{pmatrix}$
	$\langle \mathbf{v}_1^1 \rangle^{J=1} =$ $\begin{pmatrix} \cdot & \cdot & \cdot \\ 1 & \cdot & \cdot \\ \cdot & 1 & \cdot \end{pmatrix} \frac{1}{\sqrt{2}}$	$\langle \mathbf{v}_0^1 \rangle^{J=1} =$ $\begin{pmatrix} 1 & \cdot & \cdot \\ \cdot & 0 & \cdot \\ \cdot & \cdot & -1 \end{pmatrix} \frac{1}{\sqrt{2}}$	$\langle \mathbf{v}_{-1}^1 \rangle^{J=1} =$ $\begin{pmatrix} \cdot & -1 & \cdot \\ \cdot & \cdot & -1 \\ \cdot & \cdot & \cdot \end{pmatrix} \frac{1}{\sqrt{2}}$	
		$\langle \mathbf{v}_0^0 \rangle^{J=1} =$ $\begin{pmatrix} 1 & \cdot & \cdot \\ \cdot & 1 & \cdot \\ \cdot & \cdot & 1 \end{pmatrix} \frac{1}{\sqrt{3}}$		

$\langle \mathbf{v}_{q=-2\dots 2}^2 \rangle^{J=1} =$ $\begin{pmatrix} 1 & -1 & 1 \\ 1 & -2 & 1 \\ 1 & -1 & 1 \end{pmatrix} \left  \begin{array}{l} 1 \\ \frac{1}{\sqrt{2}} \\ \frac{1}{\sqrt{6}} \end{array} \right.$
$\langle \mathbf{v}_{q=-1\dots 1}^1 \rangle^{J=1} =$ $\begin{pmatrix} 1 & -1 & \cdot \\ 1 & 0 & -1 \\ \cdot & 1 & -1 \end{pmatrix} \left  \begin{array}{l} \cdot \\ \frac{1}{\sqrt{3}} \\ \frac{1}{\sqrt{2}} \end{array} \right.$
$\langle \mathbf{v}_0^0 \rangle^{J=1} =$ $\begin{pmatrix} 1 & \cdot & \cdot \\ \cdot & 1 & \cdot \\ \cdot & \cdot & 1 \end{pmatrix} \left  \begin{array}{l} \cdot \\ \cdot \\ \frac{1}{\sqrt{3}} \end{array} \right.$

(2.3c),  $\mathbf{v}_q^k$  transforms like Eq (1.6a) for a wave state  $\left| \begin{smallmatrix} k \\ q \end{smallmatrix} \right\rangle$ .)

$$\bar{\mathbf{v}}_q^k = \mathbf{R}(\alpha\beta\gamma)\mathbf{v}_q^k\mathbf{R}^\dagger(\alpha\beta\gamma) = \sum_{q=-k}^k \mathbf{v}_{\bar{q}}^k \mathcal{D}_{\bar{q}q}^k(\alpha\beta\gamma) \quad (2.4)$$

Examples of  $\mathbf{v}_q^k$  tensor matrices for  $J' = J = 1$  to 3 are given in Table 2.1. The  $J = 2$  case is given in expanded form by Table 2.1. (Higher-J tables are  $q$ -folded to save space. Scalar  $\langle \mathbf{v}_0^0 \rangle^J = 1/\sqrt{[J]}$  is left off each  $J$ -table in Table 2.3)



Table 2.2: Tabulated  $\mathbf{v}_q^k$  values and relation to quaternions

(a) Tabulated  $\mathbf{v}_q^k$  values for  $J=1/2$

$\langle \mathbf{v}_{-1}^1 \rangle^{J=1/2} =$ $\begin{pmatrix} \cdot & \cdot \\ -1 & \cdot \end{pmatrix}$	$\langle \mathbf{v}_0^1 \rangle^{J=1/2} =$ $-\begin{pmatrix} 1 & \cdot \\ \cdot & -1 \end{pmatrix} \frac{1}{\sqrt{2}}$	$\langle \mathbf{v}_1^1 \rangle^{J=1/2} =$ $\begin{pmatrix} \cdot & 1 \\ \cdot & \cdot \end{pmatrix}$	$\langle \mathbf{v}_{-1\dots 1}^1 \rangle^{J=1/2} =$ $\begin{pmatrix} -1 & 1 \\ -1 & 1 \end{pmatrix} \Big _{\frac{1}{\sqrt{2}}}$
	$\langle \mathbf{v}_0^0 \rangle^{J=1/2} =$ $\begin{pmatrix} -1 & \cdot \\ \cdot & -1 \end{pmatrix} \frac{1}{\sqrt{2}}$		$\langle \mathbf{v}_0^0 \rangle^{J=1/2} =$ $-\begin{pmatrix} 1 & \cdot \\ \cdot & 1 \end{pmatrix} \frac{1}{\sqrt{2}}$

(b) Simple Conversion from  $\mathbf{v}$  to  $\sigma$

$\mathbf{v}_{-1}^1 = -\sigma_-$	$\mathbf{v}_0^1 = -\frac{1}{\sqrt{2}}\sigma_z$	$\mathbf{v}_{+1}^1 = +\sigma_+$	$\mathbf{v}_0^0 = +\sigma_0$
$\sigma_x = \sigma_+ + \sigma_-$ $= \begin{pmatrix} \cdot & 1 \\ 1 & \cdot \end{pmatrix}$	$\sigma_z = -\sqrt{2}\mathbf{v}_0^1$ $= \begin{pmatrix} +1 & \cdot \\ \cdot & -1 \end{pmatrix}$	$\sigma_y = -i\sigma_+ + i\sigma_-$ $= \begin{pmatrix} \cdot & -i \\ i & \cdot \end{pmatrix}$	$\sigma_0 = -\sqrt{2}\mathbf{v}_0^0$ $= \begin{pmatrix} 1 & 0 \\ 0 & 1 \end{pmatrix}$

(c) Conventional quaternion-spinor relations

$\mathbf{i} = i\sigma_x$ $= \begin{pmatrix} 0 & i \\ i & 0 \end{pmatrix}$	$\mathbf{k} = i\sigma_z$ $= \begin{pmatrix} +i & 0 \\ 0 & -i \end{pmatrix}$	$\mathbf{j} = i\sigma_y$ $= \begin{pmatrix} 0 & 1 \\ -1 & 0 \end{pmatrix}$	$\mathbf{1} = \sigma_0$ $= \begin{pmatrix} 1 & 0 \\ 0 & 1 \end{pmatrix}$
--	--	---	---

Historically, spinor  $J = 1/2$  tensors shown in Table 2.2(a) are related to four Pauli spinor matrices  $\sigma_\mu$  and Hamilton quaternions  $\{\mathbf{1}, \mathbf{i}, \mathbf{j}, \mathbf{k}\}$  in Table 2.2(b) or Table 2.2(c). The latter appear in 1843 and are used for Stokes' polarization theory in 1867. The  $\sigma_\mu$  are  $U(2)$  algebraic basis of quantum theory for physics ranging from sub-kHz NMR to TeV hadrons and also applies to special relativistic symmetry transformations of the Lorentz Group. General  $U(k)$  algebra has  $k^2$  generators  $\mathbf{v}_0^0, \mathbf{v}_q^1, \dots, \mathbf{v}_q^k$  with a subset of  $k$  mutually commuting diagonal ( $q = 0$ ) labeling operators  $\mathbf{v}_0^k$  of the  $U(k)$  tensor algebras. The  $\mathbf{v}_q^k$  are related to elementary creation( $\mathbf{a}^\dagger$ )-destruction( $\mathbf{a}$ ) operators, products  $\mathbf{a}_m^\dagger \mathbf{a}_{m'}$  and to their RES in the following sections.

The  $\mathbf{a}_m^\dagger \mathbf{a}_{m'}$  are also known a elementary matrix operators  $\mathbf{e}_m \mathbf{e}_{m'}$  which simply consist of unit-1 entry at the  $m$ - $m'$  position of an otherwise zero matrix.

Table 2.3: Unit Tensor Representations

$(\mathbf{v}_{q=-1\dots 1}^1)^{J=1} =$ $\begin{array}{ccc c} 1 & 1 & \cdot & \cdot \\ 1 & 0 & -1 & \frac{1}{\sqrt{3}} \\ \cdot & 1 & -1 & \frac{1}{\sqrt{2}} \end{array}$	$(\mathbf{v}_{q=-1\dots 1}^1)^{J=2} =$ $\begin{array}{cccc c} 2 & -\sqrt{2} & \cdot & \cdot & \cdot \\ \sqrt{2} & 1 & -\sqrt{3} & \cdot & \cdot \\ \cdot & \sqrt{3} & 0 & -\sqrt{3} & \cdot \\ \cdot & \cdot & \sqrt{3} & -1 & -\sqrt{2} \\ \cdot & \cdot & \cdot & \sqrt{2} & -2 \end{array}$	$(\mathbf{v}_{q=-1\dots 1}^1)^{J=3} =$ $\begin{array}{cccccc c} 3 & -\sqrt{3} & \cdot & \cdot & \cdot & \cdot & \cdot \\ \sqrt{3} & 2 & -\sqrt{5} & \cdot & \cdot & \cdot & \cdot \\ \cdot & \sqrt{5} & 1 & -\sqrt{6} & \cdot & \cdot & \cdot \\ \cdot & \cdot & \cdot & \sqrt{6} & -1 & -\sqrt{5} & \cdot \\ \cdot & \cdot & \cdot & \cdot & \sqrt{5} & -2 & -\sqrt{3} \\ \cdot & \cdot & \cdot & \cdot & \cdot & \sqrt{3} & -3 \end{array}$
$(\mathbf{v}_{q=-2\dots 2}^2)^{J=1} =$ $\begin{array}{ccc c} 1 & -1 & 1 & \frac{1}{\sqrt{2}} \\ 1 & -2 & 1 & \frac{1}{\sqrt{2}} \\ 1 & -1 & 1 & \frac{1}{\sqrt{6}} \end{array}$	$(\mathbf{v}_{q=-2\dots 2}^2)^{J=2} =$ $\begin{array}{cccc c} 2 & -\sqrt{6} & \sqrt{2} & \cdot & \cdot \\ \sqrt{6} & -1 & -1 & \sqrt{3} & \cdot \\ \sqrt{2} & 1 & -2 & 1 & \sqrt{6} \\ \cdot & \cdot & \sqrt{2} & -\sqrt{6} & 2 \end{array}$	$(\mathbf{v}_{q=-2\dots 2}^2)^{J=3} =$ $\begin{array}{cccccc c} 5 & -5 & \sqrt{5} & \cdot & \cdot & \cdot & \cdot \\ 5 & 0 & -\sqrt{15} & \sqrt{10} & \cdot & \cdot & \cdot \\ \sqrt{5} & \sqrt{15} & -3 & -\sqrt{2} & \sqrt{12} & \cdot & \cdot \\ \cdot & \sqrt{10} & \sqrt{2} & -4 & \sqrt{2} & \sqrt{10} & \cdot \\ \cdot & \cdot & \sqrt{12} & -\sqrt{2} & -3 & \sqrt{15} & 5 \\ \cdot & \cdot & \cdot & \sqrt{10} & -\sqrt{15} & 0 & 5 \\ \cdot & \cdot & \cdot & \cdot & \sqrt{5} & -5 & 5 \end{array}$
	$(\mathbf{v}_{q=-3\dots 3}^3)^{J=2} =$ $\begin{array}{cccc c} 1 & \sqrt{3} & 1 & -1 & \cdot \\ \sqrt{3} & -2 & \sqrt{2} & 0 & -1 \\ 1 & -\sqrt{2} & 0 & \sqrt{2} & -1 \\ 1 & 0 & -\sqrt{2} & 2 & -\sqrt{3} \\ \cdot & 1 & -1 & \sqrt{3} & -1 \end{array}$	$(\mathbf{v}_{q=-3\dots 3}^3)^{J=3} =$ $\begin{array}{cccccc c} 1 & -\sqrt{2} & \sqrt{2} & -1 & \cdot & \cdot & \cdot \\ \sqrt{2} & -1 & 0 & 1 & -\sqrt{2} & \cdot & \cdot \\ 1 & 1 & -1 & 0 & 1 & -1 & -1 \\ \cdot & \sqrt{2} & 0 & -1 & 1 & 0 & -\sqrt{2} \\ \cdot & \cdot & \sqrt{2} & -1 & 0 & 1 & -\sqrt{2} \\ \cdot & \cdot & \cdot & 1 & -\sqrt{2} & \sqrt{2} & -1 \end{array}$
	$(\mathbf{v}_{q=-4\dots 4}^4)^{J=2} =$ $\begin{array}{cccc c} 1 & -1 & \sqrt{3} & -1 & 1 \\ 1 & -4 & \sqrt{6} & -\sqrt{8} & 1 \\ \sqrt{3} & -\sqrt{6} & 6 & -\sqrt{6} & \sqrt{3} \\ 1 & -\sqrt{8} & \sqrt{6} & -4 & 1 \\ 1 & -1 & \sqrt{3} & -1 & 1 \end{array}$	$(\mathbf{v}_{q=-4\dots 4}^4)^{J=3} =$ $\begin{array}{cccccc c} 3 & -\sqrt{30} & \sqrt{54} & -3 & \sqrt{3} & \cdot & \cdot \\ \sqrt{30} & -7 & \sqrt{32} & -\sqrt{3} & -\sqrt{2} & \sqrt{5} & \cdot \\ \sqrt{54} & -\sqrt{32} & 1 & \sqrt{15} & -\sqrt{40} & \sqrt{2} & \sqrt{3} \\ 3 & -\sqrt{3} & -\sqrt{15} & 6 & -\sqrt{15} & -\sqrt{3} & 3 \\ \sqrt{3} & \sqrt{2} & -\sqrt{40} & \sqrt{15} & 1 & -\sqrt{32} & \sqrt{54} \\ \cdot & -\sqrt{2} & -\sqrt{3} & \sqrt{32} & -7 & -\sqrt{30} & \cdot \\ \cdot & \cdot & \sqrt{3} & -3 & \sqrt{54} & -\sqrt{30} & 3 \end{array}$
		$(\mathbf{v}_{q=-5\dots 5}^5)^{J=3} =$ $\begin{array}{cccccc c} 1 & -\sqrt{5} & 1 & -\sqrt{2} & 1 & -1 & \cdot \\ \sqrt{5} & -4 & \sqrt{27} & -\sqrt{2} & 1 & 0 & -1 \\ 1 & -\sqrt{27} & 5 & -\sqrt{10} & 0 & 1 & -1 \\ \sqrt{2} & -\sqrt{2} & \sqrt{10} & 0 & -\sqrt{10} & \sqrt{2} & -\sqrt{2} \\ 1 & -1 & 0 & \sqrt{10} & -5 & \sqrt{27} & -1 \\ 1 & 0 & -1 & \sqrt{2} & -\sqrt{27} & 4 & -\sqrt{5} \\ \cdot & 1 & -1 & \sqrt{2} & -1 & \sqrt{5} & -1 \end{array}$
		$(\mathbf{v}_{q=-6\dots 6}^6)^{J=3} =$ $\begin{array}{cccccc c} 1 & -\sqrt{2} & 1 & -\sqrt{2} & \sqrt{5} & -1 & 1 \\ \sqrt{2} & -6 & \sqrt{30} & -\sqrt{8} & 3 & -\sqrt{12} & 1 \\ 1 & -\sqrt{30} & 15 & -10 & \sqrt{15} & -3 & \sqrt{5} \\ \sqrt{2} & -\sqrt{8} & 10 & -20 & 10 & -\sqrt{8} & \sqrt{2} \\ \sqrt{5} & -3 & \sqrt{15} & -10 & 15 & -\sqrt{30} & 1 \\ 1 & -\sqrt{12} & 3 & -\sqrt{8} & \sqrt{30} & -6 & \sqrt{2} \\ 1 & -1 & \sqrt{5} & -\sqrt{2} & 1 & -\sqrt{2} & 1 \end{array}$

### 2.2.2 Tensor and Elementary Matrix Operators

Matrix Element  $\langle \begin{smallmatrix} J \\ m' \end{smallmatrix} | \mathbf{v}_q^k | \begin{smallmatrix} J \\ m \end{smallmatrix} \rangle$  for  $J' = J$  is a coefficient of elementary matrix operator

$$\mathbf{e}_{m',m} = \left| \begin{smallmatrix} J \\ m' \end{smallmatrix} \right\rangle \left\langle \begin{smallmatrix} J \\ m \end{smallmatrix} \right|.$$

$$\begin{aligned} \langle \mathbf{v}_q^k \rangle^J &= \sum_{m',m} \left| \begin{smallmatrix} J \\ m' \end{smallmatrix} \right\rangle \left\langle \begin{smallmatrix} J \\ m' \end{smallmatrix} | \mathbf{v}_q^k | \begin{smallmatrix} J \\ m \end{smallmatrix} \right\rangle \left\langle \begin{smallmatrix} J \\ m \end{smallmatrix} \right| = \\ &= \sum_{m',m} \left\langle \begin{smallmatrix} J \\ m' \end{smallmatrix} | \mathbf{v}_q^k | \begin{smallmatrix} J \\ m \end{smallmatrix} \right\rangle \left| \begin{smallmatrix} J \\ m' \end{smallmatrix} \right\rangle \left\langle \begin{smallmatrix} J \\ m \end{smallmatrix} \right| \\ &= \sum_{m',m} \left\langle \begin{smallmatrix} J \\ m' \end{smallmatrix} | \mathbf{v}_q^k | \begin{smallmatrix} J \\ m \end{smallmatrix} \right\rangle \langle \mathbf{e}_{m'm} \rangle^J \end{aligned} \quad (2.5a)$$

where:  $q = m' - m$

$$\left\langle \begin{smallmatrix} J' \\ m' \end{smallmatrix} | \mathbf{v}_q^k | \begin{smallmatrix} J \\ m \end{smallmatrix} \right\rangle = (-1)^{J'+m'} \sqrt{[k]} \begin{pmatrix} k & J & J' \\ q & m & -m' \end{pmatrix} = (-1)^{J'+J-k} \sqrt{\frac{[k]}{[J]}} C_{qmm'}^{kJJ'} \quad (2.5b)$$

This follows from (2.3c) and a CG to Wigner 3j coefficient definition in Eq (2.6).

$$\begin{pmatrix} k & J & J' \\ q & m & -m' \end{pmatrix} = (-1)^{k-J+m'} C_{qmm'}^{kJJ'} / \sqrt{[J']} \quad (2.6)$$

CG or 3j orthonormality makes  $\langle \mathbf{v}_q^k \rangle^J$  and  $\langle \mathbf{e}_{m',m} \rangle^J$  matrices convenient for analysis. Each has a unit vector of dimension  $d(J, q) = [J] - q = 2J - q + 1$  sitting on the  $q^{\text{th}}$ -diagonal of its  $[J]$ -by- $[J]$  matrix. For example, quadrupole  $\mathbf{v}_2^2$ , octopole  $\mathbf{v}_2^3$ , and



Any  $[J]$ -by- $[J]$  matrix is a combination of elementary  $\langle \mathbf{e}_{m',m} \rangle^J$  and thus also of  $\langle \mathbf{v}_q^k \rangle^J$ . From this we make RES maps to analyze  $[J]$ -by- $[J]$  matrix eigensolutions by plotting related combinations of  $Y_q^k(\theta, \phi)$ .

### 2.2.3 Fano-Racah tensor algebra

Diagonal dipole-vector (rank  $k = 1$ ) matrix  $\langle \mathbf{v}_0^1 \rangle^J$  is seen in top row of Table 2.3 to be proportional to the angular momentum  $z$ -component matrix  $\langle \mathbf{J}_z \rangle^J$ . Diagonal  $2^k$ -pole (rank- $k$ ) tensors  $\langle \mathbf{v}_0^k \rangle^J$  are linearly related to  $\mathbf{J}_z$  powers  $\mathbf{J}_z^2 = \mathbf{J}_z \mathbf{J}_z$ ,  $\mathbf{J}_z^3 = \mathbf{J}_z \mathbf{J}_z \mathbf{J}_z$ ,  $\dots$  up to the  $k^{\text{th}}$ -power  $\mathbf{J}_z^k$ . This relates  $\langle \mathbf{v}_0^k \rangle^J$ -eigenvalues to powers  $m^p$  of  $\langle \mathbf{J}_z \rangle$ -eigenvalues  $m$  and, in turn, leads to an RES scheme to analyze  $\langle \mathbf{v}_q^k \rangle^J$  eigensolutions.

For example, matrix diagonals in Table 2.3 give elementary representations for  $\mathbf{v}_0^k$  of  $J = 2$ . (Only diagonals are listed.)

$$\begin{aligned} \sqrt{5} \langle \mathbf{v}_0^0 \rangle^{(J=2)} &= \langle \mathbf{1} \rangle^{(2)} = \begin{pmatrix} 1 & 1 & 1 & 1 & 1 \end{pmatrix} \\ \sqrt{10} \langle \mathbf{v}_0^1 \rangle^{(J=2)} &= \langle \mathbf{J}_z \rangle^{(2)} = \begin{pmatrix} 2 & 1 & 0 & -1 & 2 \end{pmatrix} \end{aligned} \quad (2.8a)$$

$$\begin{aligned} \sqrt{14} \langle \mathbf{v}_0^2 \rangle^{(2)} &= \begin{pmatrix} 2 & -1 & -2 & -1 & 2 \end{pmatrix} \\ \sqrt{10} \langle \mathbf{v}_0^3 \rangle^{(2)} &= \begin{pmatrix} 1 & -2 & 0 & 2 & -1 \end{pmatrix} \\ \sqrt{70} \langle \mathbf{v}_0^4 \rangle^{(2)} &= \begin{pmatrix} 1 & -4 & 6 & -4 & 1 \end{pmatrix} \end{aligned} \quad (2.8b)$$

Powers of  $\langle \mathbf{J}_z \rangle^2$  in Eq (2.9) are combinations of  $\langle \mathbf{v}_q^k \rangle^2$  found by dot products with

vectors in Eq (2.8a) and (2.8b).

$$\begin{aligned}
\langle \mathbf{J}_z^0 \rangle^{(2)} &= \begin{pmatrix} 1 & 1 & 1 & 1 & 1 \end{pmatrix} = \frac{5}{\sqrt{5}} \langle \mathbf{v}_0^0 \rangle^{(2)} \\
\langle \mathbf{J}_z^1 \rangle^{(2)} &= \begin{pmatrix} 2 & 1 & 0 & -1 & -2 \end{pmatrix} = \frac{10}{\sqrt{10}} \langle \mathbf{v}_0^1 \rangle^{(2)} \\
\langle \mathbf{J}_z^2 \rangle^{(2)} &= \begin{pmatrix} 4 & 1 & 0 & 1 & 4 \end{pmatrix} = \frac{10}{\sqrt{5}} \langle \mathbf{v}_0^0 \rangle^{(2)} + \frac{14}{\sqrt{14}} \langle \mathbf{v}_0^2 \rangle^{(2)} \\
\langle \mathbf{J}_z^3 \rangle^{(2)} &= \begin{pmatrix} 8 & 1 & 0 & -1 & -8 \end{pmatrix} = \frac{34}{\sqrt{10}} \langle \mathbf{v}_0^1 \rangle^{(2)} + \frac{12}{\sqrt{10}} \langle \mathbf{v}_0^3 \rangle^{(2)} \\
\langle \mathbf{J}_z^4 \rangle^{(2)} &= \begin{pmatrix} 16 & 1 & 0 & 1 & 16 \end{pmatrix} = \frac{34}{\sqrt{5}} \langle \mathbf{v}_0^0 \rangle^{(2)} + \frac{62}{\sqrt{14}} \langle \mathbf{v}_0^2 \rangle^{(2)} + \frac{24}{\sqrt{70}} \langle \mathbf{v}_0^4 \rangle^{(2)}
\end{aligned} \tag{2.9}$$

Elementary triangular inversion of Eq (2.9) gives each  $\langle \mathbf{v}_0^k \rangle^2$  as a polynomial of  $\mathbf{J}_z$  powers  $\langle \mathbf{J}_z^p \rangle^2 = m^p$  in Eq (2.10).

$$\begin{aligned}
\langle \mathbf{v}_0^0 \rangle^{(2)} &= \frac{1}{\sqrt{5}} \langle \mathbf{J}_z^0 \rangle^{(2)} \\
\langle \mathbf{v}_0^1 \rangle^{(2)} &= \frac{1}{\sqrt{10}} \langle \mathbf{J}_z^1 \rangle^{(2)} \\
\langle \mathbf{v}_0^2 \rangle^{(2)} &= -\frac{2}{\sqrt{14}} \langle \mathbf{J}_z^0 \rangle^{(2)} + \frac{1}{\sqrt{14}} \langle \mathbf{J}_z^2 \rangle^{(2)} \\
\langle \mathbf{v}_0^3 \rangle^{(2)} &= -\frac{34\sqrt{10}}{120} \langle \mathbf{J}_z^1 \rangle^{(2)} + \frac{\sqrt{10}}{12} \langle \mathbf{J}_z^3 \rangle^{(2)} \\
\langle \mathbf{v}_0^4 \rangle^{(2)} &= \frac{3\sqrt{70}}{(5)(7)} \langle \mathbf{J}_z^0 \rangle^{(2)} - \frac{31\sqrt{70}}{(3)(7)(8)} \langle \mathbf{J}_z^2 \rangle^{(2)} + \frac{\sqrt{70}}{24} \langle \mathbf{J}_z^4 \rangle^{(2)}
\end{aligned} \tag{2.10}$$

Now RES plotting schemes arise by comparing  $\langle \mathbf{v}_0^k \rangle^J$  expansions in  $\mathbf{J}_z$  like Eq (2.10) with Wigner  $(J, m)$  polynomials  $(-1)^{J-m} \sqrt{[k]} \begin{pmatrix} k & J & J \\ 0 & m & -m \end{pmatrix}$  Eq (2.4), and Legendre polynomials  $\mathcal{D}_{00}^k(\cdot\theta) = P_k(\cos\theta)$  Eq (2.1) that are also polynomials of  $\mathbf{J}_z = |J| \cos\theta$ . By plotting the latter we hope to shed light on the eigensolutions of the former.

### 2.3 Tensor eigensolution and Legendre function RE surfaces

Legendre polynomials occupy the central (00)-component of a Wigner- $D^J$  matrix.

$$\mathcal{D}_{00}^k(\cdot\theta) = P_k(\cos\theta) \tag{2.11}$$

Table 2.4: Forming  $\langle \mathbf{v}_0^k \rangle$  from powers of  $J$  and  $m$

$$\langle \mathbf{v}_0^k \rangle_m^J = \left\langle \begin{matrix} J \\ m \end{matrix} \middle| \mathbf{v}_0^k \middle| \begin{matrix} J \\ m \end{matrix} \right\rangle = (-1)^{J-m} \sqrt{[k]} \begin{pmatrix} k & J & J \\ 0 & m & -m \end{pmatrix} = (-1)^k \sqrt{\frac{[k]}{[J]}} C_{0mm}^{kJJ}$$


---


$$\langle \mathbf{v}_0^0 \rangle_m^J = \frac{1}{\sqrt{2J+1}} \quad [1]$$

$$\langle \mathbf{v}_0^1 \rangle_m^J = \frac{2\sqrt{3}}{\sqrt{2J+2:0}} \quad [ \quad \quad \quad m ]$$

$$\langle \mathbf{v}_0^2 \rangle_m^J = \frac{2^2\sqrt{5}}{\sqrt{2J+3:-1}} \quad [-\frac{1}{2}J(J+1) \quad \quad \quad +\frac{3}{2}m^2]$$

$$\langle \mathbf{v}_0^3 \rangle_m^J = \frac{2^3\sqrt{7}}{\sqrt{2J+4:-2}} \quad [ \quad \quad \quad -\frac{3}{2}(J(J+1) - \frac{10}{3})m \quad \quad \quad +\frac{5}{2}m^3 ]$$

Examples of Legendre polynomials of  $\cos \theta = J_z/|J|$  and then of momenta  $J$  and  $J_z = |J| \cos \theta$  are given below, first in angular form, then in cartesian. Each set begins with  $P_0 = 1$ .

$$\begin{aligned} P_1(\cos \theta) &= \cos \theta \\ P_2(\cos \theta) &= -\frac{1}{2} + \frac{3}{2} \cos^2 \theta \\ P_3(\cos \theta) &= -\frac{3}{2} \cos \theta + \frac{5}{2} \cos^3 \theta \\ P_4(\cos \theta) &= \frac{3}{8} - \frac{30}{8} \cos^2 \theta + \frac{35}{8} \cos^4 \theta \end{aligned} \quad (2.12a)$$

$$\begin{aligned} |J|^1 P_1(\cos \theta) &= J_z \\ |J|^2 P_2(\cos \theta) &= -\frac{1}{2}|J|^2 + \frac{3}{2}J_z^2 \\ |J|^3 P_3(\cos \theta) &= -\frac{3}{2}|J|^2 J_z + \frac{5}{2}J_z^3 \\ |J|^4 P_4(\cos \theta) &= \frac{3}{8}|J|^4 - \frac{30}{8}|J|^2 J_z^2 + \frac{35}{8}J_z^4 \end{aligned} \quad (2.12b)$$

Classical  $P_k$  functions are to be compared to corresponding quantized  $\langle \mathbf{v}_0^k \rangle^J$  unit-tensor  $e$ -values in Table 2.4 that generalize examples of tensor matrix ( $J = 1 - 3$ )-eigenvalues in Table 2.3 and Eq (2.10) to any  $J$  and  $m = J, \dots, -J$ . The powers of  $m$  and  $J$  in  $\langle \mathbf{v}_0^k \rangle^J$ , shown in Table 2.4, are taken to higher order in Table 2.5.

Table 2.5: Forming  $\langle \mathbf{v}_0^k \rangle$  from powers of  $J$  and  $m$ , expanded

$k$	$m^0$	$m^1$	$m^2$	$m^3$	$m^4$	$m^5$	$m^6$	$m^7$
0	1							
1		1						
2	$\frac{-1}{2}J(J+1)$		$\frac{3}{2}$					
3		$\frac{-3}{2}(J(J+1) - \frac{2}{3})$		$\frac{5}{2}$				
4	$\frac{3}{8}(J+2 : -1)$		$\frac{-30}{8}(J(J+1) - \frac{5}{6})$		$\frac{35}{8}$			
5		$\frac{15}{8}(J+2 : -1) - \frac{4}{3}J(J+1) - \frac{4}{5}$		$\frac{-70}{8}(J(J+1) - \frac{3}{2})$		$\frac{63}{8}$		
6	$\frac{-5}{16}(J+3 : -2)$		$\frac{105}{16}(J+2 : -1) - 3J(J+1) + \frac{14}{5}$		$\frac{-315}{16}(J(J+1) - \frac{7}{3})$		$\frac{231}{16}$	
7		$\frac{-35}{16}(J+3 : -2) - 3(J+2 : -1) + \frac{36}{5}J(J+1) - \frac{36}{7}$		$\frac{315}{16}(J+2 : -1) - 5J(J+1) + \frac{61}{9}$		$\frac{-693}{16}(J(J+1) - \frac{10}{3})$		$\frac{429}{16}$
8	$35(J+4 : -3)$		$\frac{-1260}{128}(J+3 : -2) - \frac{13}{2}(J+2 : -1) + \frac{332}{15}J(J+1) - \frac{761}{35}$		$\frac{6930}{128}(J+2 : -1) - \frac{22}{3}J(J+1) - \frac{1871}{1386}$		$\frac{-12012}{128}(J(J+1) + \frac{9}{2})$	$\frac{6435}{128}$



Norm  $2^k \sqrt{[k]}/\sqrt{2J+k:-k+1}$  makes each  $\langle \mathbf{v}_0^k \rangle^J$  a unit vector. (Note shorthand definition:  $A+a:b = (A+a)(A+a-1)\dots(A+b)$ .) In contrast, normalized  $P_k$  have  $P_k(\cos 0) = 1$ . Coefficients  $c_p$  of  $\cos^p \theta$  sum to  $1 = \Sigma c_p$ . Square  $|c_p|^2$  usually do not sum to 1.

Tensor values  $\langle \mathbf{v}_0^0 \rangle^J$ ,  $\langle \mathbf{v}_0^1 \rangle^J$ , and  $\langle \mathbf{v}_0^2 \rangle^J$  in [...] -braces of Table 2.4 equal Legendre functions  $P_0$ ,  $P_1$ , and  $P_2$  in Eq (2.12b) exactly using  $J$ -expectation values Eq (2.13a) and (2.13b). However, for rank higher than  $k = 2$ ,  $P_k$  is only approximately equal to  $\langle \mathbf{v}_0^k \rangle_m^J$  though the approximation improves with higher  $J$ .

$$\langle \mathbf{J}_z \rangle_m^L = m = \langle |J| \rangle_m^J \cos \theta_m^J \quad (2.13a)$$

$$\langle |J| \rangle = \sqrt{J(J+1)} \cong J + \frac{1}{2} \quad (2.13b)$$

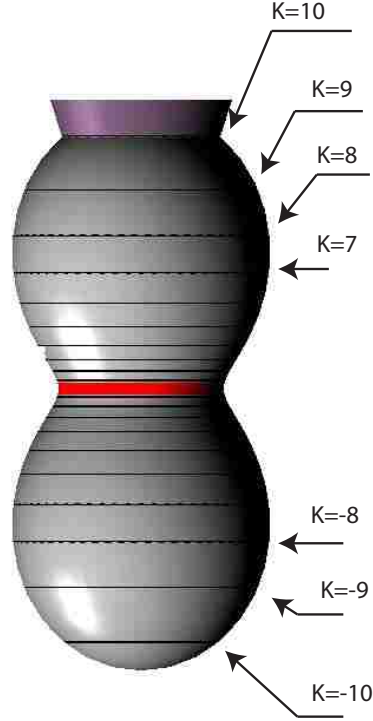
For large- $J$  values, the  $\langle \mathbf{v}_0^k \rangle_m^J$  in Table 2.4 approach the  $P_3, P_4, \dots$  of Eq (2.12b) according to  $\langle |J|^k \rangle_m^J \xrightarrow{J \gg k} [J(J+1)]^{k/2}$ . However,  $\langle \mathbf{v}_0^k \rangle_m^J$  differ significantly from  $P_k$  for low  $J$ .

The classical  $P_k$  in Eq (2.12b) lack the small terms ( $-2/3, -10/3$ , etc) that kill the  $\langle \mathbf{v}_0^k \rangle$  in Table 2.4 whenever  $J$  falls below strict quantum limits such as whenever  $J < |m|$  or  $J < k/2$ . However, the quantum “killer terms” become negligible for larger  $J$ -values ( $J > k$ ) and thus tensor eigenvalues converge to  $P_k$  and thus approach the RES plots.

### 2.3.1 Angular Momentum Cone and RES Paths

Quantum  $J$ -magnitude Eq (2.13b) introduces a quantum angular momentum cone geometry with quantized angles  $\theta_m^J$  given by Eq (2.13a) as summarized here in Eq

Figure 2.1: Symmetric top RES showing angular momentum cone with minimum uncertainty. The cone intersects with one of the allowed paths.



(2.14a) and (2.14b) for lab  $m = M$  and molecular body  $n = K$ .

$$\cos \theta_M^J = \frac{M}{\sqrt{J(J+1)}} \quad (2.14a)$$

$$\cos \theta_K^J = \frac{K}{\sqrt{J(J+1)}} \quad (2.14b)$$

An angular momentum eigenstate  $\left| \begin{matrix} J \\ m, n \end{matrix} \right\rangle$  has sharp (zero-uncertainty) eigenvalue  $m$  or  $n$  on the lab or body frame  $z$  or  $\bar{z}$  axis, respectively. This sharp altitude and magnitude in Eq (2.13b) constrain vector  $\mathbf{J}$  to base circles of cones making half-angle  $\theta_m^J$  or  $\theta_n^J$  with  $z$  or  $\bar{z}$  axes, respectively. Expected  $\mathbf{J}$ -values are shown in Fig 2.1 .

Elementary RES energy level analysis begins by writing a multipole  $T_q^k$  tensor expansion Eq (2.15a) of a general rigid rotor or asymmetric top Hamiltonian and

then plotting the resulting surface using Eq (2.15a)

$$\begin{aligned}
H &= A(J_{\bar{x}})^2 + B(J_{\bar{y}})^2 + C(J_{\bar{z}})^2 \\
&= \frac{1}{3}(A + B + C)T_0^0 + \frac{1}{3}(2C - A - B)T_0^2 \\
&\quad + \frac{1}{\sqrt{6}}(A - B)(T_2^2 + T_{-2}^2)
\end{aligned} \tag{2.15a}$$

The ( $k = 0$ ) and ( $k = 2$ ) tensorial components of  $T_q^k$  are listed in Eq (2.15b).

$$\begin{aligned}
T_0^0 &= (J_{\bar{x}})^2 + (J_{\bar{y}})^2 + (J_{\bar{z}})^2 = |\mathbf{J}|^2 \\
T_0^2 &= \frac{-1}{2}(J_{\bar{x}})^2 - \frac{1}{2}(J_{\bar{y}})^2 + (J_{\bar{z}})^2 = |\mathbf{J}|^2 \left( \frac{3}{2} \cos^2 \theta - \frac{1}{2} \right) \\
&= |\mathbf{J}|^2 P_2(\cos \theta) \\
T_2^2 + T_{-2}^2 &= -\sqrt{\frac{3}{2}}(J_{\bar{x}})^2 + \sqrt{\frac{3}{2}}(J_{\bar{y}})^2 \\
&= |\mathbf{J}|^2 \sqrt{\frac{3}{2}} \sin^2 \theta \cos 2\phi
\end{aligned} \tag{2.15b}$$

Inertial constants ( $A = 1/I_{\bar{x}}$ ,  $B = 1/I_{\bar{y}}$ ,  $C = 1/I_{\bar{z}}$ ) linearly combine in (2.15a) the  $J$ -tensor operators  $T_q^k$ . Exact relation of  $\langle \mathbf{v}_0^0 \rangle^J$  and  $\langle \mathbf{v}_0^2 \rangle^J$  in Table 2.4 to classical  $P_0$  and  $P_2$  in Eq (2.12b) is used in Eq (2.15b) for  $T_0^0$  and  $T_0^2$ .

A rigid spherical top ( $A = B = C$ ) has only the  $T_0^0$  term of Eq (2.15a). Rigid prolate ( $A = B > C$ ) or oblate ( $A = B < C$ ) symmetric tops have only  $T_0^0$  and  $T_0^2$

terms with the following quantum energy eigenvalues.

$$\begin{aligned}
\left\langle \begin{matrix} J \\ m, n \end{matrix} \left| \mathbf{H}^{\text{SymTop}} \right| \begin{matrix} J \\ m, n \end{matrix} \right\rangle &= \\
&= \left\langle \begin{matrix} J \\ m, n \end{matrix} \left| B(\mathbf{J}_{\bar{x}})^2 + B(J_{\bar{y}})^2 + C(J_{\bar{z}})^2 \right| \begin{matrix} J \\ m, n \end{matrix} \right\rangle \\
&= \frac{1}{3} \left\langle \begin{matrix} J \\ m, n \end{matrix} \left| (2B + C)T_0^0 + 2(C - B)T_0^2 \right| \begin{matrix} J \\ m, n \end{matrix} \right\rangle \quad (2.16) \\
&= \left\langle \begin{matrix} J \\ m, n \end{matrix} \left| B|J|^2 + (C - B)(J_{\bar{z}})^2 \right| \begin{matrix} J \\ m, n \end{matrix} \right\rangle \\
&= BJ(J + 1) + (C - B)n^2
\end{aligned}$$

Since a rigid symmetric-top involves only  $T_0^0$  and  $T_0^2$ , the  $\theta_n^J$ -cones define its eigenvalues exactly by  $\mathbf{J}$ -vector trajectories at angle- $\theta_n^J$  where  $\theta_n^J$ -cones intersect the following  $T_0^2$ -RES shown in Fig 2.1.

$$RE^{\text{SymTop}}(\theta) = \frac{1}{3}(2B + C)T_0^0(\theta) + \frac{2}{3}(C - B)T_0^2(\theta) \quad (2.17a)$$

Inserting quantized-body cone relation Eq (2.14b) yields desired eigenvalues Eq (2.16) exactly for all  $J$ . (This includes low  $J$ ).

$$\begin{aligned}
RE^{\text{SymTop}}(\theta_L^J) &= \frac{1}{3}(2B + C)J(J + 1) \\
&\quad + \frac{2}{3}(C - B)J(J + 1) \left( \frac{3}{2} \cos^2 \theta_K^J - \frac{1}{2} \right) \\
&= J(J + 1) \frac{1}{3} [(2B + C) + (C - B)(K^2 - 1)] \quad (2.17b) \\
&= J(J + 1)B + (C - B)K^2
\end{aligned}$$

Cone paths in Fig 2.1 are constant energy contours on symmetric top RES Eq

(2.17a) and (2.17b) of constant  $J$ . They may be viewed as  $J$ -phase paths on which the  $\mathbf{J}$ -vector may delocalize or “precess” on a circular  $\theta_n^J$ -cone around body  $\bar{z}$ -axis. Or else one might view paths on Fig 2.1 as coordinate space tracks of the lab  $z$ -axis around the  $\bar{z}$ -axis by assuming  $\mathbf{J}$  lies fixed on the former. Either view describes  $\mathbf{J}$  in the body-frame by Euler polar and azimuth angles  $-\beta, -\gamma$  with angle  $\beta = \theta_n^J$  and  $|J|^2 = J(J+1)$  fixed.

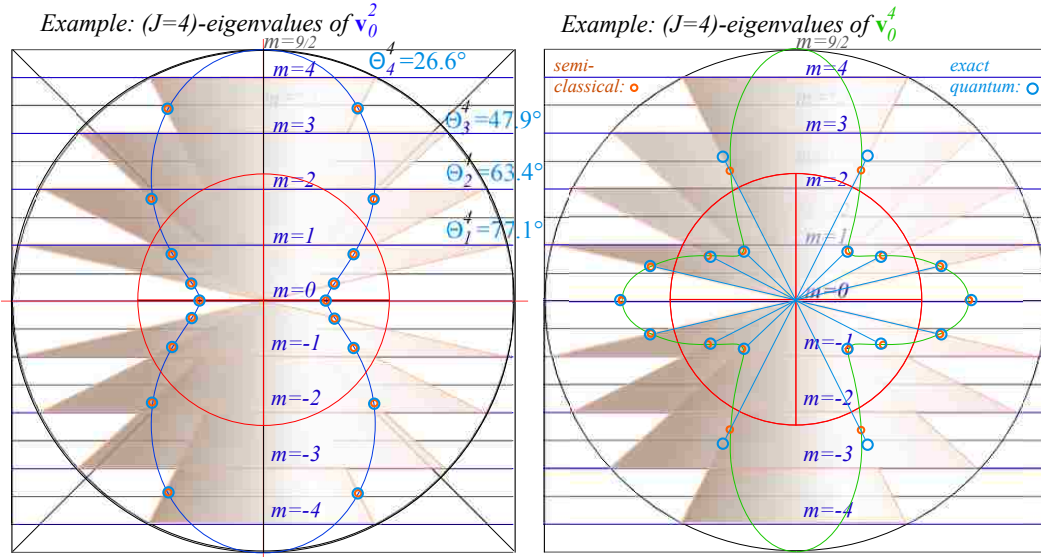
$$\mathbf{J} = (J_{\bar{x}}, J_{\bar{y}}, J_{\bar{z}}) = (-|\mathbf{J}| \cos \gamma \sin \beta, |\mathbf{J}| \sin \gamma \sin \beta, |\mathbf{J}| \cos \beta) \quad (2.18)$$

While  $P_2(\theta_M^J)$  functions fit tensor  $\mathbf{v}_0^2$  eigenvalues exactly, it is not the case for higher  $P_k$ , particularly for low  $J$ . The difference between quantum  $\mathbf{v}_0^k$  and semi-classical  $P_k$  functions can be easily plotted as in Fig 2.2 and tabulated in Table 2.6. The figure shows a slice of the semi-classical surface and the uncertainty cones for each  $m$  from  $J$  to  $-J$ . The orange circles indicate the intersection of the surface with the uncertainty cones and the blue circles indicate the energy of the quantum value,  $\langle \mathbf{v}_0^k \rangle_m^J$ , placed along the uncertainty cone. The fourth order plot in Fig 2.2 shows significant divergence between quantum  $J = 4$  and semi-classical energies for  $\langle \mathbf{v}_0^4 \rangle_m^4$ , while the second order version for  $\langle \mathbf{v}_0^2 \rangle_m^4$  is exact. The exact correspondence between  $\langle \mathbf{v}_0^2 \rangle_m^4$  and  $P_2(\theta_m^J)$  extends for all  $J \geq 2$ , though  $\langle \mathbf{v}_0^k \rangle_m^J$  are only fitted by  $P_k(\theta_m^J)$  by approximations that improve with higher  $J > k$ .

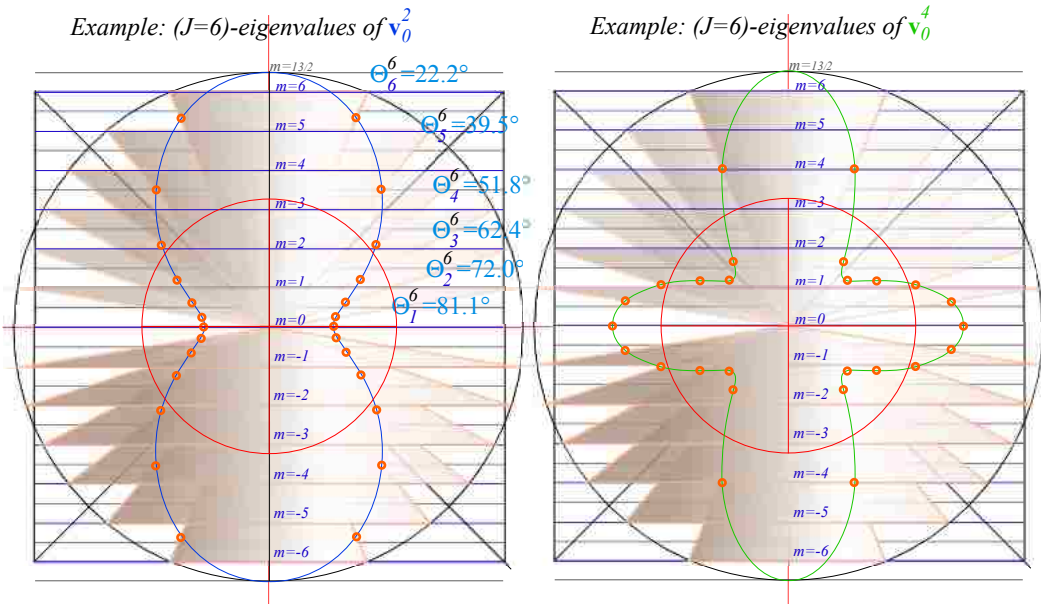
## Reduced Matrix and RES Scaling

An RES is a radial plot along  $\mathbf{J}$  direction  $-\beta, -\gamma$  that has hills where energy is high and valleys where it is low, but at all points the same magnitude  $|\mathbf{J}| = \sqrt{J(J+1)}$ . Origin-shift to keep RES radius positive and scaling to display hills, valleys, and saddles, may be needed to make useful RES plots.

A scalar term  $s \cdot \mathbf{v}_0^0$  added to a tensor combination  $\mathbf{T} = \sum_k t_k \mathbf{v}_0^k$  does not affect the  $\mathbf{T}$ -eigenvectors and neither does an overall scaling of  $\mathbf{T}$  to  $c\mathbf{T}$ . This is true since



(a) At low  $J$  semi-classical approximation may have significant error.



(b) As  $J$  becomes greater than  $k$ , semi-classical approximation improves.

Figure 2.2: Quantum solutions (blue) compared to semi-classical ones (orange) for two different multipoles. Semi-classical energies are also seen as the intersection of uncertainty cones with the RES. Inner circle represents zero-energy centroid.

(a) Semi-classical correspondence for  $k = 2, 4$  at  $J = 4$ . Correspondence degrades for increasing  $k$ .

$J = 4$	$m = 4$	3	2	1	0	-1	-2	-3	-4
$\langle \mathbf{v}_0^2 \rangle_m^{J=4}$	14	3.5	-4	-8.5	-10	-8.5	-4	3.5	14
$ J ^2 P_2(\cos \theta_m^J)$	14	3.5	-4	-8.5	-10	-8.5	-4	3.5	14
$\langle \mathbf{v}_0^4 \rangle_m^{J=4}$	14	-21	-11	9	18	9	-11	-21	14
$ J ^2 P_4(\cos \theta_m^J)$	9.3	-22.8	-10.7	10.6	20	10.6	-10.7	-22.8	9.

(b) Correspondence for  $k = 4$  improves by increasing  $J$ .

$J = 6$	$ m  = 6$	5	4	3	2	1	0
$\langle \mathbf{v}_0^2 \rangle_m^{J=6}$	22	11	2	-5	-10	-13	-14
$ J ^2 P_2(\cos \theta_m^J)$	22	11	2	-5	-10	-13	-14
$\langle \mathbf{v}_0^4 \rangle_m^{J=6}$	18.7	-12.5	-18.1	-10.2	2.1	12.1	15.9
$ J ^2 P_4(\cos \theta_m^J)$	16.7	-13.6	-18.6	-10.1	2.6	12.8	16.7

Table 2.6: Quantum values are similar to their semiclassical counterparts. Shown are  $\langle \mathbf{v}_q^k \rangle$  and  $|J|^2 P_k(\cos \theta_m^J)$  at  $J = 4, 6$  for changing  $m$ . Agreement is exact for both  $k = 2$  cases and improves with increasing  $J$  for  $k = 4$ . Values are normalized and reported in arbitrary energy units.

eigenvectors are invariant to adding a multiple  $s\mathbf{1}$  of unit matrix  $\mathbf{1}$  to  $\mathbf{T}$  or multiplying it by  $c\mathbf{1}$ . (Of course, eigenvalues would, respectively, be shifted by  $s$  or scaled by  $c$ .)

Wigner-Racah tensor algebra defines a reduced matrix element  $\langle J' \| T^k \| J \rangle$  to serve as a scale factor for each Clebsch-Gordan tensor matrix element having Wigner-Eckart form Eq (2.3a).

$$\left\langle \begin{matrix} J' \\ m' \end{matrix} \left| T_q^k \right| \begin{matrix} J \\ m \end{matrix} \right\rangle = C_{qmm'}^{kJJ'} \langle J' \| T^k \| J \rangle \quad (2.19)$$

Wigner-Eckart form for matrix  $\left\langle \begin{matrix} J \\ m \end{matrix} \left| T_0^2 \right| \begin{matrix} J \\ m \end{matrix} \right\rangle$  of quadratic- $J$ -tensor  $T_0^2 = \mathbf{J}_0^2$  Eq (2.15b) reveals some key points.

$$\begin{aligned} \left\langle \begin{matrix} J \\ m \end{matrix} \left| \left( \frac{3}{2} J_z^2 - \frac{1}{2} \mathbf{J}^2 \right) \right| \begin{matrix} J \\ m \end{matrix} \right\rangle &= \left\langle \begin{matrix} J \\ m \end{matrix} \left| T_0^2 \right| \begin{matrix} J \\ m \end{matrix} \right\rangle \\ &= (C_{0mm}^{2JJ}) \cdot \langle J \| T^2 \| J \rangle \end{aligned} \quad (2.20a)$$

$$\begin{aligned}
\frac{3}{2}m^2 - \frac{1}{2}J(J+1) &= \left\langle \begin{array}{c} J \\ m \end{array} \left| T_0^2 \right| \begin{array}{c} J \\ m \end{array} \right\rangle \\
&= \frac{4[J]}{\sqrt{2J+3:-1}} \left( \frac{3}{2}m^2 - \frac{1}{2}J(J+1) \right) \cdot \frac{\sqrt{2J+3:-1}}{4[J]} \quad (2.20b)
\end{aligned}$$

Reduced matrix element  $\langle J \| T^2 \| J \rangle$  cancels norm factor  $4\sqrt{[J]}/\sqrt{2J+3:-1}$  in  $C_{0mm}^{2JJ}$ . The result is the quadratic Legendre form  $|J|^2 P_2(m/|J|)$  found inside  $[\dots]$ -braces of Table 2.4 with norm  $4\sqrt{[k]}/\sqrt{2J+3:-1}$  outside the braces. (The latter is just a norm in Eq (2.20a) and (2.20b) multiplied by the factor  $\sqrt{[k]}/[J]$  from definition Eq (2.5b).)

Apparent conflicts in factors are due to having sum-of-*squared*-component normalization of unit  $\mathbf{v}^k$  on one hand and sum-of-component normalization of  $P_k$  on the other. Matrix elements  $\left\langle \begin{array}{c} J \\ m \end{array} \left| T \right| \begin{array}{c} J \\ m \end{array} \right\rangle$  or  $\left| \begin{array}{c} J \\ m \end{array} \right\rangle \left\langle \begin{array}{c} J \\ m \end{array} \right|$  use the former since amplitude squares give probability. However, it is *unsquared* amplitude sum  $\Sigma c_k$  that measures anisotropy of a tensor  $T = \Sigma c_k \cdot P_k$  since  $\Sigma c_k$  is a maximum  $T$ -amplitude. (Each  $P_k$  contributes  $P_k(0) = 1$ .) Expectation values  $\left\langle \begin{array}{c} J \\ m \end{array} \left| T \right| \begin{array}{c} J \\ m \end{array} \right\rangle$  scale linearly, too, but  $\mathbf{J}^2$  tensors may have extra scale factors.

Tensor  $T^2 = \mathbf{J}^2$  in Eq (2.20a) and (2.20b) scales as  $|J|^2 = J(J+1)$  and  $T^k = \mathbf{J}^k$  scale as  $|J|^k$ . Factor  $4\sqrt{[J]}/\sqrt{2J+3:-1}$  of  $C_{0mm}^{2JJ}$  reduces scale  $|J|^2$  to  $\sqrt{2J+1} = \sqrt{[J]}$ . Then the reduced factor  $\langle J \| T \| J \rangle$  brings it back to  $|J|^2$ .

$$\begin{aligned}
\frac{4[J]}{\sqrt{2J+3:-1}} &= \\
&= \frac{4(2J+1)}{\sqrt{(2J+3)(2J+2)(2J+1)(2J)(2J-1)}} \quad (2.21) \\
&= \frac{\sqrt{[J]}}{\sqrt{(J+\frac{3}{2})(J+1)(J-\frac{1}{2})}} \approx \frac{\sqrt{[J]}}{|J|^2}
\end{aligned}$$

Each rank- $k$  part has a factor  $|J|^k = |J(J+1)|^{k/2}$ . Anisotropy of mixed-rank  $\mathbf{J}$ -tensor



$\mathbf{T} = \Sigma c_k \cdot \mathbf{J}^k$  is  $\Sigma |J|^k c_k$ , and thus is quite sensitive to quantum number  $J$ . So also are the RES and related eigensolutions of  $\mathbf{T}$ .

### 2.3.2 Asymmetric Top and Rank-2 RES

Plotting RES of non-diagonal Hamiltonians for the asymmetric top Eq (2.15a) involves  $2^{nd}$ -rank tensors  $\mathbf{v}_q^2$  with reduced z-axial symmetry, nonzero  $q$ -values, and non-commuting  $J_a$  combinations. Each  $J_a$  in the quadratic expressions in Eq (2.15a) is replaced by its classical Euler-angle form in Eq (2.18).

$$\begin{aligned} H^{\text{AsymTop}} &= A (J_{\bar{x}})^2 + B (J_{\bar{y}})^2 + C (J_{\bar{z}})^2 \\ \Rightarrow RES^{\text{AsymTop}} &= A (|J| \cos \gamma \sin \beta)^2 + B (|J| \sin \gamma \sin \beta)^2 + C (|J| \cos \beta)^2 \end{aligned} \quad (2.22a)$$

Or else, each tensor  $T_q^k$  in Eq (2.15a) is replaced by a multipole function  $X_q^k = |J|^k \mathcal{D}_{0q}^{k*}(\cdot, \beta, \gamma)$ . (Recall Eq (2.15b).)

$$\begin{aligned} H^{\text{AsymTop}} &= \frac{A+B+C}{3} T_0^0 + \frac{2C-A-B}{3} T_0^2 + \frac{A-B}{\sqrt{6}} (T_2^2 + T_{-2}^2) \\ \Rightarrow RES^{\text{AsymTop}} &= \frac{A+B+C}{3} |J|^2 + \frac{2C-A-B}{3} X_0^2 + \frac{A-B}{\sqrt{6}} (X_2^2 + X_{-2}^2) \\ &= |J|^2 \left[ \frac{A+B}{2} + \frac{2C-A-B}{2} \cos^2 \beta + \frac{A-B}{2} \sin^2 \beta \cos 2\gamma \right] \end{aligned} \quad (2.22b)$$

Forms Eq (2.22a) and (2.22b) of rank- $(k=2)$ -RES are equal and give the same plots shown in Fig 2.3, but tensor form Eq (2.22b) reveals symmetry. Terms  $X_0^0$  and  $X_0^2$  (Fig 2.1) are  $z$ -symmetric and non-zero near  $z$ -axis while  $X_{\pm 2}^2$  terms are asymmetric and vary as  $\sin^2 \beta$  with polar angle  $\beta$  between the  $\mathbf{J}$  vector and the  $z$ -axis. As  $\beta$  approaches  $\pi/2$ ,  $X_{\pm 2}^2$  terms grow to give equatorial valleys and saddles in Fig 2.3 while  $X_0^2$  vanishes.

Asymmetric tensor operators  $T_{\pm q}^k$  are non-diagonal and do not commute with di-

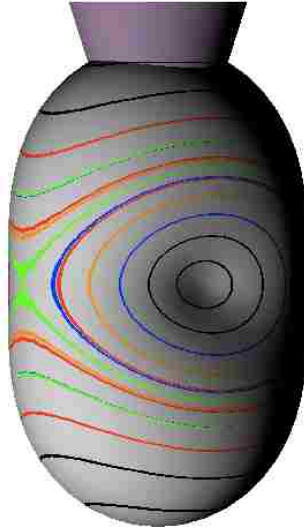


Figure 2.3: Asymmetric Top RES  $J = 10$

agonal  $T_0^k$  or with each other, and so  $H^{\text{AsymTop}}$  eigenstates as well as eigenvalues vary with coefficient  $(A - B)$  in (2.22b). As  $T_{\pm 2}^2$  mixes symmetric-top states  $\left| \begin{smallmatrix} J \\ K \end{smallmatrix} \right\rangle$  into asymmetric-top eigenstates,  $\theta_K^J$  cone circles around the  $z$ -axis of Fig 2.1 warp into oval-pairs and are squeezed by nascent oval pairs emerging around the  $x$ -axis and separated from them by a pair of separatrix circle-planes that meet at an angle  $\theta^{\text{sep}}$  on the  $y$ -axis. Fig 2.4 shows a range of RES and levels between symmetric-prolate top ( $B = A$  or  $\theta^{\text{sep}} = 0$ ) and oblate top ( $B = C$  or  $\theta^{\text{sep}} = \pi$ ). A most-asymmetric case ( $B = C$  or  $\theta^{\text{sep}} = \pi/2$ ) is midway between the symmetric cases.

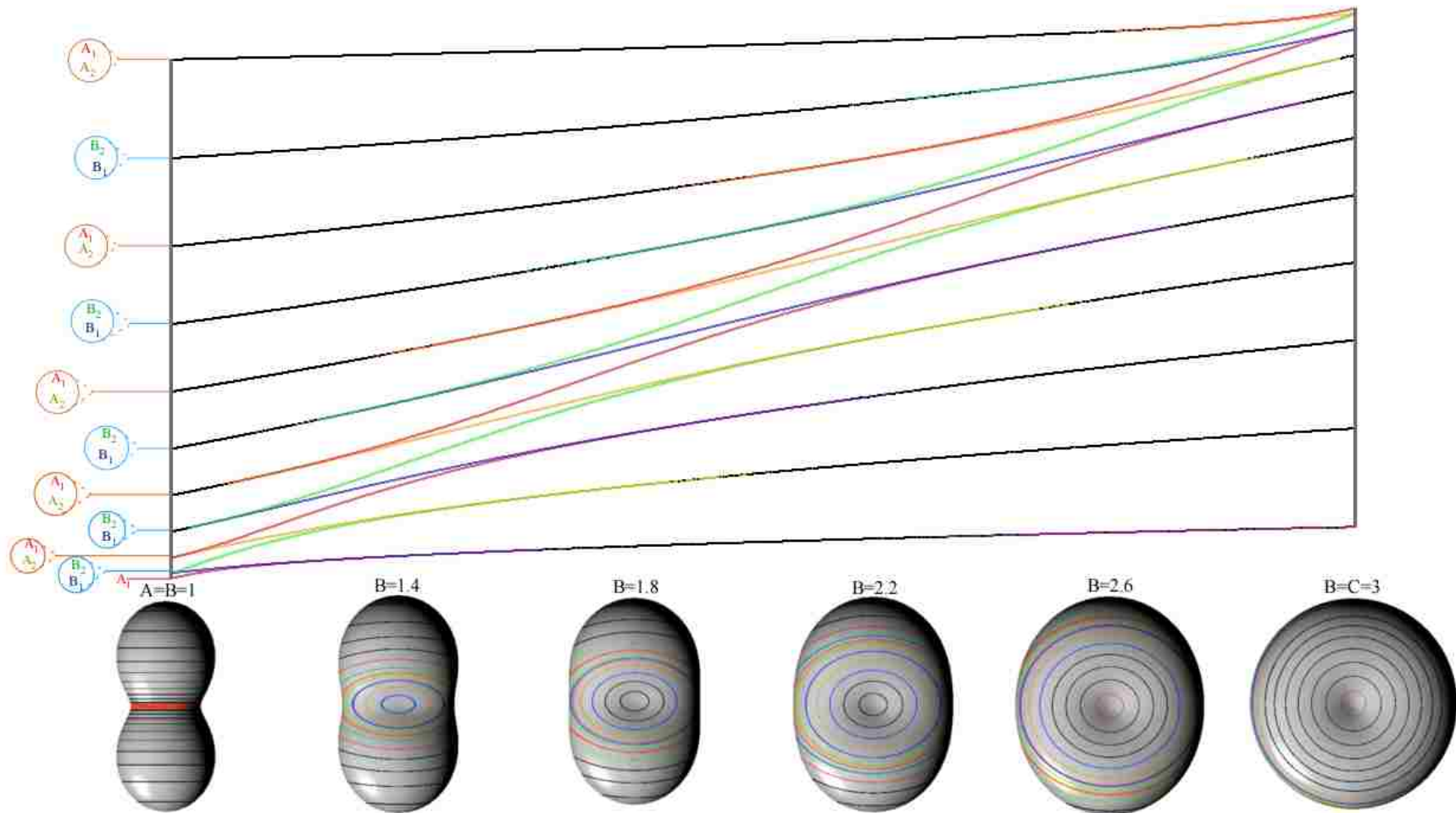


Figure 2.4: Asymmetric Top Energy Levels with Corresponding RES

$$\theta^{\text{sep}} = \tan^{-1} \frac{|A - B|}{|B - C|} = \begin{cases} 0 & \text{for } : B = A \\ \pi/2 & \text{for } : B = (A + C)/2 \\ \pi & \text{for } : B = C \end{cases} \quad (2.23)$$

As  $B$  first differs a little from  $A$ , off-diagonal  $T_{\pm 2}^2$  and asymmetric  $X_{\pm 2}^2$  first “quench” degenerate  $\pm K$ -momentum eigenstate pairs  $\left| \begin{matrix} J \\ \pm K \end{matrix} \right\rangle$  into non-degenerate standing cos or sin-wave pairs.

$$|c_K^J\rangle = \frac{1}{\sqrt{2}} \left( \left| \begin{matrix} J \\ +K \end{matrix} \right\rangle + \left| \begin{matrix} J \\ -K \end{matrix} \right\rangle \right) \quad (2.24a)$$

$$|s_K^J\rangle = \frac{-i}{\sqrt{2}} \left( \left| \begin{matrix} J \\ +K \end{matrix} \right\rangle - \left| \begin{matrix} J \\ -K \end{matrix} \right\rangle \right) \quad (2.24b)$$

These state have nodes or anti-nodes standing on hills, saddles, or valleys of the RES topography at the principal body axes. Whether a wave is cos-like or sin-like at an axial point depends on whether it is symmetric or antisymmetric at the point and thus whether that point is an anti-node or node. Nodal location can determine whether a cos-like or sin-like wave has higher energy.

As  $B$  differs more and more from  $A$ , off-diagonal  $T_{\pm 2}^2$  will mix standing waves like  $|c_K^J\rangle$  with others such as  $|c_{K\pm 2}^J\rangle$ ,  $|c_{K\pm 4}^J\rangle$ , and  $|c_{K\pm 6}^J\rangle$  that share the same  $H^{\text{AsymTop}}$  symmetry described below.

### 2.3.3 Symmetry Labeling of Asymmetric Top Eigenstates

Throughout the range of asymmetric cases in Fig 2.4 the symmetry of  $H^{\text{A Top}}$  in Eq (2.22a) and (2.22b) is described by orthorhombic group  $D_2$  made up of  $180^\circ$  rotations  $\mathbf{R}_x$ ,  $\mathbf{R}_y$ , and  $\mathbf{R}_z$  about inertial body axes that mutually commute ( $\mathbf{R}_x \mathbf{R}_y = \mathbf{R}_z = \mathbf{R}_y \mathbf{R}_x$ ), *etc.*). Unit square ( $\mathbf{R}_x^2 = \mathbf{1}$ , *etc.*)  $\mathbf{R}$ -eigenvalues  $\pm 1$  label nodal symmetry

(+1) or antisymmetry (−1) on each axis.  $D_2$  is an outer product of cyclic  $C_2$  groups for any two axes, say  $C_2(x)$  and  $C_2(y)$ .  $x$  and  $y$  values also label nodal symmetry for the  $z$  axis since  $\mathbf{R}_x\mathbf{R}_y = \mathbf{R}_z$ . A Cartesian 2-by-2 product of  $C_2(x)$  and  $C_2(y)$  symmetry character tables shown in Table 2.7 gives four sets of characters and four symmetry labels  $[A_1, B_1, A_2, B_2]$  for the outer product  $D_2 = C_2(x) \otimes C_2(y)$ .

Labels  $(A, B)$  or  $(1, 2)$  for  $(x)$  or  $(y)$  symmetric and anti-symmetric states follow ancient arcane conventions. We prefer a binary  $(0_2, 1_2)$  notation for  $C_2$  characters and N-ary notation  $(0_N, 1_N, 2_N, \dots, (N - 1)_N)$  for  $C_N$  characters  $\mathcal{D}^{m_N}(R^p)$  where each label  $m_N$  denotes “ $m$ -wave-quanta-modulo N” as in Table 2.8.

$$\mathcal{D}^{m_N}(\mathbf{R}^p) = e^{-im \cdot p(2\pi/N)} \quad (2.25)$$

This notation is used in correlation Table 2.9 between symmetry labels of  $D_2$  and its subgroups  $C_2(x)$ ,  $C_2(y)$ , and  $C_2(z)$ , respectively. Each row belongs to a  $D_2$  species and indicates which  $C_2$  symmetry, *even* ( $0_2$ ) or *odd* ( $1_2$ ), correlates to it. The Tables 2.9(a), 2.9(b) and 2.9(c) follow respectively from the columns  $\mathbf{R}_x$ ,  $\mathbf{R}_y$ , and  $\mathbf{R}_z$  of Table 2.7. An *odd* ( $0_2$ )  $D_2$  character is  $\mathcal{D}^{0_2}(\mathbf{R}) = +1$  and *odd* ( $1_2$ ) is  $\mathcal{D}^{1_2}(\mathbf{R}) = -1$ .

$J = 10$   $H^{\text{AsymTop}}$ -levels in Fig 2.3 consist of two sets of five pairs  $[(A_1, B_1) (A_2, B_2) (A_1, B_1) (A_2, B_2) (A_1, B_1)]$  and  $[(B_2, A_1) (B_1, A_2) (B_2, A_1) (B_1, A_2) (B_2, A_1)]$  separated by a single  $(A_2)$  level. Each is related to RES  $x$ -valley path pairs  $K_x \sim [\pm 10, \pm 9, \pm 8, \pm 7, \pm 6]$  or  $z$ -hill pairs  $K_z \sim [\pm 6, \pm 7, \pm 8, \pm 9, \pm 10]$  separated by a single  $y$ -path ( $A_2 : K_y \sim 5$ ). Even- $K$  belongs to a ( $0_2$ ) column and odd- $K$  belongs to a ( $1_2$ ) column of  $C_2(x)$  Table 2.9(a) or  $C_2(z)$  Table 2.9(c).

Valley-pair sequence  $(A_1, B_1), (A_2, B_2) \dots$  is consistent with ( $0_2$ ) and ( $1_2$ ) columns of the  $C_2(x)$  Table 2.9(a), and hill-pair sequence  $(B_2, A_1), (B_1, A_2) \dots$  is consistent with ( $0_2$ ) and ( $1_2$ ) column of the  $C_2(z)$  Table 2.9(c). This is because lower pairs correspond to  $x$ -axial RES loops of approximate momentum  $K_x \sim \pm 10, \pm 9 \dots \pm 6$  while upper pairs correspond to  $z$ -axial RES loops of approximate momentum  $K_z \sim$

$\pm 6, \pm 7 \dots \pm 10$  in Fig 2.3

Table 2.9(b) for  $C_2(y)$  is not used since  $\pm y$ -axes are hyperbolic saddle points on one separatrix path, unlike the disconnected *pairs* of elliptic RES paths that encircle  $\pm x$ -axes or  $\pm z$ -axes at hill or valley points. Only a single  $E$  level exists in Fig 2.3 at the energy  $E^{\text{Sep}}$  of the saddle points and their separatrix.

$$E^{\text{Sep}} = H^{\text{AsymTop}}(J_x, J_y, J_z) = BJ(J+1)$$

$$\text{for } \begin{cases} J_x &= 0 \\ J_y &= |J|^2 \\ J_z &= 0 \end{cases} \quad (2.26)$$

As symmetric  $H^{\text{Sym}}$  becomes a more asymmetric  $H^{\text{AsymTop}}$  in Fig 2.4, a hill or valley path bends away from its ideal single- $K$  symmetric-top cone circle at constant polar angle  $\theta_K^J$  Eq (2.14a) and (2.14b). Each  $H^{\text{Sym}}$  state  $\left| \begin{smallmatrix} J \\ K \end{smallmatrix} \right\rangle$  turns into an  $H^{\text{AsymTop}}$  eigenstate expansion of states  $\left| \begin{smallmatrix} J \\ K \pm 2p \end{smallmatrix} \right\rangle$  with  $K \pm 2p$  above and below  $K$ , and its RES path bends from constant  $\theta_K^J$  toward polar angles  $\theta_{K\pm 2}^J, \theta_{K\pm 4}^J, \theta_{K\pm 6}^J \dots$  above and below angle  $\theta_K^J$ . At energy near the separatrix  $E^{\text{Sep}}$ , bending of hill and valley paths become more severe as they approach separatrix asymptotes where the polar angle range Eq (2.23) expands to  $2\theta^{\text{Sep}}$  or  $\pi$  and the bend becomes a kink.

It is conventional to label  $H^{\text{Sep}}$  eigenstate  $|E\rangle$  by both  $K_x$  and  $K_z$  quantum values since  $|E\rangle$  may use either a  $K_x$  basis or else a  $K_z$  basis. However,  $\mathbf{J}_x$  and  $\mathbf{J}_z$  do not commute. For energy  $E$  above  $E^{\text{Sep}}$ , a  $|J, K_z\rangle$  expansion is more compact and a dominate  $|K_z|$  value may label  $|E\rangle$ . For  $E$  below  $E^{\text{Sep}}$ , a  $|J, K_x\rangle$  expansion may have a dominate  $|K_x|$  label that is meaningful. For  $E$  near  $E^{\text{Sep}}$ ,  $K$ -labels are meaningless.

Though a more general form of the symmetry identification process may be unfa-

miliar, it is easy to implement by computer. Group projectors (using Eq (2.27)) that can distinguish how each eigenvector splits with respect to subgroup operations are used. The product of these projectors and the calculated eigenvectors identifies the subgroup symmetry of each level.

$$P_{jk}^{\alpha} = \left( \frac{l^{\alpha}}{\circ\mathcal{G}} \right) \sum_g \mathcal{D}_{jk}^{\alpha*}(g)g \quad (2.27)$$

Only projectors in lower symmetry subgroups are used because they are easy to calculate and there are fewer in number. With the eigenvector projection lengths and knowledge of the correlation table between the molecular group itself and the subgroup one can start to deduce the eigenvector symmetry. As mentioned earlier, one correlation table is not enough to fully identify an eigenvector’s symmetry, but using several subgroups one can assign symmetry. This process tends to be quicker to implement than calculating projectors of the full group, particularly if one can use a  $C_n$  subgroup. In such a case  $\mathcal{D}_{jk}^{\alpha*}(g)$  from Eq (2.27) is calculated by Eq (2.25).

This method can be significantly simpler than a traditional block diagonalization. Block diagonalizing the Hamiltonian requires projectors of the entire molecular symmetry group rather than of the smaller subgroups.

The disadvantage of this method is that it becomes unstable when clusters are tightest. As the eigenvectors can become more mixed with tight clustering they become harder for the algorithm to distinguish. Thus, some of the RES paths in the figure (as in Fig 2.4) may appear black, meaning they are not distinguishable to the projector method alone. Symmetry definitions hold for asymmetric tops where  $J < 50$ . Spherical tops are particularly challenging, but octahedral or tetrahedral spherical top Hamiltonians often split clusters enough to allow symmetry assignment, even at high  $J$ .

Table 2.7: Orthorhombic 4-group  $D_2 = C_2 \times C_2$  character table construction

$C_2(x)$			<b>1</b>	$\mathbf{R}_x$	$\times$	$C_2(y)$			<b>1</b>	$\mathbf{R}_y$	$=$	$D_2 = C_2(x) \times C_2(y)$			
$A = (0_2)_x$	1	1	1	1		$1 = (0_2)_y$	1	1	$A_1 = (0_2 0_2)_{xy}$	1		1	$\mathbf{R}_x$	$\mathbf{R}_y$	$\mathbf{R}_z$
$B = (1_2)_x$	1	-1	1	-1	$2 = (1_2)_y$	1	-1	$A_2 = (0_2 1_2)_{xy}$	1	-1	1	1	-1		
								$B_1 = (1_2 0_2)_{xy}$	1	1	-1	-1	-1		
								$B_2 = (1_2 1_2)_{xy}$	1	-1	-1	1	1		

Table 2.8: Group character tables for cyclic groups of symmetry order N.

(a) N=2			(b) N=3: $\epsilon = e^{2\pi/3}$				(c) N=4				
$C_2$	<b>1</b>	$\mathbf{R}_x$	$C_3$	<b>1</b>	$\mathbf{R}^1$	$\mathbf{R}^2$	$C_4$	<b>1</b>	$\mathbf{R}^1$	$\mathbf{R}^2$	$\mathbf{R}^3$
$(0_2)$	1	1	$(0_3)$	1	1	1	$(0_4)$	1	1	1	1
$(1_2)$	1	-1	$(1_3)$	1	$\epsilon^*$	$\epsilon$	$(1_4)$	1	$-i$	-1	$i$
			$(2_3)$	1	$\epsilon$	$\epsilon^*$	$(2_4)$	1	-1	1	-1
							$(3)_4$	1	$i$	-1	$-i$

### 2.3.4 Tunneling Between RES-Path States

N-atom inversion in ammonia,  $\text{NH}_3$ , is an example of molecular tunneling modeled by a particle whose closely paired levels (inversion doublets) lie below the barrier of a double-well PES. An RES generalization, sketched in Fig 2.3, shows level pairs such as  $(A_1, B_1)$ ,  $(A_2, B_2)$ , *etc.* as rotational analogs of inversion doublets. Here tunneling between left and right positions on a PES is replaced by an RES inversion between left-handed and right-handed rotation of an entire molecule. Instead of oscillation of expected position values  $\langle \mathbf{r} \rangle$  between PES valleys there is oscillation of momentum  $\langle \mathbf{J} \rangle$  between pairs of  $x$ -paths ( $+K_x \leftrightarrow -K_x$ ) in RES valleys or else between pairs of  $z$ -paths ( $+K_z \leftrightarrow -K_z$ ) on RES hills. Chapters 4 and 5 describes this phenomenon in detail for molecules of octahedral symmetry.

## 2.4 Conclusion

This chapter has shown the function of unitary multipole functions and operators and how they are used in calculating rovibrational energy levels. Approximations can be made to many symmetric top molecular Hamiltonians making them classical, ignoring high rank contribution. We have shown both cases where this approximation works



Table 2.9: Symmetry correlation table between species of  $D_2$  and its axial subgroups.

(a) $C_2(x)$ subgroup			(b) $C_2(y)$ subgroup		
$D_2 \supset C_2(x)$	$(0_2)_x$	$(1_2)_x$	$D_2 \supset C_2(y)$	$(0_2)_y$	$(1_2)_y$
$A_1$	1	·	$A_1$	1	·
$A_2$	·	1	$A_2$	1	·
$B_1$	1	·	$B_1$	·	1
$B_2$	·	1	$B_2$	·	1

(c) $C_2(z)$ subgroup		
$D_2 \supset C_2(z)$	$(0_2)_z$	$(1_2)_z$
$A_1$	1	·
$A_2$	·	1
$B_1$	·	1
$B_2$	1	·

and where it fails.

For asymmetric top Hamiltonians, the RES is a more appropriate semi-classical approximation. This work is continued in Chapter 3 for  $D_3$  molecules and octahedral spherical top molecules.

## Bibliography

- [1] W. G. Harter. Alternative basis for the theory of complex spectra. *Physical Review A*, 8(6):2819, 1973.
- [2] William G. Harter. *Principles of symmetry, dynamics, and spectroscopy*. J. Wiley, 1993.
- [3] James K. G. Watson. Simplification of the molecular vibration-rotation hamiltonian. *Molecular Physics*, 100(1):47–54, 2002.

## Chapter 3

### Spectral Fine Structure of Octahedral Spherical Top Molecules

### 3.1 Chapter Summary

Extreme examples of high-rank tensor eigensolutions with high-degeneracy 12 and 24-fold level clusters are examined in this chapter. Details of degeneracy are examined using the semi-classical Rotational Energy Surface (RES). The RES is placed in context with other quantum visualization tools such as the potential energy surface (PES) of Born and Oppenheimer. Limits of the RES semi-classical approximation are also investigated.

### 3.2 Tensor Eigensolutions for Octahedral Molecules

Section 2.3 has shown that asymmetric top molecules may be treated semi-classically, using only tensor operators and RES plots, but that the separatrix between regions of local symmetry confounds the approximation. Spherical-top molecules experience this symmetry breaking, but with far more possible separatrices into far more possible regions of local symmetry. This chapter focuses on the added complication and convenience of higher symmetry as well as showing novel rotational level clustering patterns diagnosed by symmetry methods.

#### 3.2.1 Symmetry Considerations

Just as qualitative features of asymmetric top spectra was analyzed in Sec 2.3, similar theoretical machinery may be used to analyze nearly spherical molecules. This section will demonstrate semi-classical tools, including multipole tensor operators, for an octahedral or cubic molecule, such as  $\text{SF}_6$ . This analysis will show spectral structures and level clusterings that have not been previously considered or analyzed, but not altogether different from those seen by ref [1].

Up to fourth order, any such molecule may be treated using the Hecht Hamiltonian[2], which may be rewritten in terms of tensor operators, as shown in Eq (3.1a) and Eq

(3.1b).

$$H = BJ^2 + 10t_{004}(J_x^4 + J_y^4 + J_z^4 - \frac{3}{5}J^4) \quad (3.1a)$$

$$H = BT_0^0 + 4t_{044} \left[ T_0^4 + \sqrt{\frac{5}{14}}(T_4^4 + T_{-4}^4) \right] \quad (3.1b)$$

$$T^{[4]} = \sqrt{\frac{7}{12}} \left[ T_0^4 + \sqrt{\frac{5}{14}}(T_4^4 + T_{-4}^4) \right] \quad (3.1c)$$

Eq (3.1c) isolates the 4th order term from the rest of the Hamiltonian. This can be continued to the sixth order and show a more complicated structure[3]. Calculation of the the tensor coefficients requires the symmetry-adapted vector coupling coefficients,  $F_{A_1pp}^{kJJ}$ , developed by Moret-Bailly[4]. The  $F_{A_1pp}^{kJJ}$  coupling coefficient is used to find the coefficient for the  $T_p^k$  tensor. The vector coupling coefficients are tabulated in ref [4] and are derived from the symmetry subduction from  $R(3)$ , fully rotational invariant symmetry, to  $O_h$  or  $T_d$ , octahedral and tetrahedral symmetry.

For convenience, we normalize the sum of these coefficients. Written this way, the sixth order contribution to the Hamiltonian goes as follows.

$$T^{[6]} = \frac{1}{2\sqrt{2}}T_0^6 - \frac{\sqrt{7}}{4}(T_4^6 + T_{-4}^6) \quad (3.2)$$

Previous work has studied how both the RES and eigenvalue spectrum change with different contributions of 4th and 6th rank tensor operators[5]. The relative contributions of these operators may be expressed as a normalized parameter-space as in Eq (3.3).

$$T^{[4,6]} = \cos(\theta)T^{[4]} + \sin(\theta)T^{[6]} \quad (3.3)$$

Others[6] have looked at how 8th rank contributions change the eigenvalue spectrum. This added term greatly expands the parameter-space by making it 2 dimensional, as demonstrated in Eq (3.4). Later portions of Section 3.2 of this chapter demonstrate not only solutions to this Hamiltonian, but how to categorize the eigen-

vectors and effects particular to inclusion of 8th order Hamiltonian terms.

$$T^{[4,6,8]} = \cos(\phi) \left( \cos(\theta)T^{[4]} + \sin(\theta)T^{[6]} \right) + \sin(\phi)T^{[8]} \quad (3.4)$$

As with the asymmetric top Hamiltonian, the octahedral Hamiltonian uses non-axial operators shown in Eq (3.1b) and Eq (3.2). These operators are not simple  $P_k(\theta)$  Legendre functions, complicating purely semi-classical analysis. Thus, approximate solutions based on axially symmetric operators alone will work only asymptotically for high  $J$  and in regions of the RES far from any separatrix. In these cases, diagonalization must be taken seriously as it becomes impossible to simply use combinations of  $J$  and  $J_z$  for calculating spectra. Though full numerical diagonalization is required, the use of tensor operators simplify the Hamiltonian matrix to a sparse, banded one.

In ref. [6], Gulacsi and coworkers explore the splitting of eigenvalues from varying the  $T^{[4]}$  and  $T^{[8]}$  for fixed  $T^{[6]}$ . They do this for  $J \leq 10$  and small contributions of  $T^{[6]}$ . Below, we show agreement with these results and extend them by greatly increasing  $J$  and also describing the topology of these manifolds using RES diagrams.

While the asymmetric top systems show clustering related to symmetry subduction from  $D_2$  to a related  $C_2$  subgroup, octahedral molecules may experience clustering related to subgroups subgroup  $D_4$ ,  $D_3$ ,  $D_2$ ,  $C_4$ ,  $C_3$  or  $C_2$ .  $O_h$  has  $D_{2d}$ ,  $C_{4v}$ ,  $C_{3v}$  and  $C_{2v}$  related to these by vertical reflection or inversion.

For simplicity, the discussion here will focus on  $O$  rather than  $O_h$  molecules. The slightly lower symmetry equations and tables that are easier to display and easier for the reader to interpret.

For a symmetric molecules, all possible clustering patterns could be described in terms of correlations found in Table 2.9. Correlations in Table 3.1 are for octahedral ( $O$ ) symmetry and  $C_4$ ,  $C_3$  and  $C_2$ . The columns of Table 3.1 represent the different clusters of rotational levels found within the spectra. These clusterings are identified by their degeneracy as well as their location in the RES of that rotational transition.

In the RES, rotationally induced deformation or symmetry breaking is seen from the shape of local regions of the RES involving a specific contour. Fig 3.1 shows two examples of RES plots, both globally octahedral, but with local regions that correspond to a subgroup symmetry of the octahedron. Fig 3.1(a) is the most common RES of an octahedral molecule with a fourth rank Hamiltonian. It has  $C_4$  and  $C_3$  local symmetry regions. The  $C_4$  regions are identified by their location on  $[100]$ ,  $[010]$ ,  $[001]$ ,  $(x, y, z)$  axes and by their square base. Similarly, the  $C_3$  regions are identified by their location on  $[111]$  axes and triangular base. In this case  $C_4$  symmetric regions are concave while  $C_3$  regions are convex. This depends on Hamiltonian fitting terms which change the relative contributions of  $T^{[4]}$  and  $T^{[6]}$ . Fig 3.1(b) shows the  $C_2$  regions due to higher rank tensors, which are located on  $[101]$  axes and have rectangular bases.

Cluster degeneracy is a hallmark of a specific symmetry breaking. While a symmetric-top spectra may be resolved into a set of  $m_J$  levels, a rotational symmetry-reduced spherical-top has multiple identical  $z$ -axes and  $m_J$  level-sets localized in symmetry-reduced- $\mathcal{H}$  regions. The number of these  $\mathcal{H}$ -regions must equal the degeneracy,  $d_{\mathcal{H}}$  of the cluster for that  $\mathcal{H}$ -region.

$$d_{\mathcal{H}} = \frac{^{\circ}\mathcal{G}}{^{\circ}\mathcal{H}} \quad (3.5)$$

This degeneracy,  $d_{\mathcal{H}}$ , is also found using the sum of the numbers in the columns of Table 3.1 or by (3.5) given  $^{\circ}\mathcal{G}$  is the order of the molecular symmetry group and  $^{\circ}\mathcal{H}$  is the order of the subgroup. In the cases shown here cluster degeneracy  $d_{\mathcal{H}}$  becomes 6, 8 and 12 for  $C_4$ ,  $C_3$  and  $C_2$  respectively.

### 3.2.2 Assigning Symmetry Labels to Eigenlevels

It is possible to diagonalize the Hamiltonian and organize symmetry species by the order of each block, yet this alone will not distinguish all levels. For Hamiltonians defined by  $T^{[4]}$  as Eq (3.1a) it is possible to analytically determine the symmetry of

Table 3.1: Correlation tables between octahedral symmetric,  $O$  and various cyclic subgroups

(a)					(b)				(c)		
$O \supset C_4$	$0_4$	$1_4$	$2_4$	$3_4$	$O \supset C_3$	$0_3$	$1_3$	$2_3$	$O \supset C_2(\mathbf{i}_1)$	$0_2$	$1_2$
$A_1 \downarrow C_4$	1	·	·	·	$A_1 \downarrow C_3$	1	·	·	$A_1 \downarrow C_2$	1	·
$A_2 \downarrow C_4$	·	·	1	·	$A_2 \downarrow C_3$	1	·	·	$A_2 \downarrow C_2$	·	1
$E \downarrow C_4$	1	·	1	·	$E \downarrow C_3$	·	1	1	$E \downarrow C_2$	1	1
$T_1 \downarrow C_4$	1	1	·	1	$T_1 \downarrow C_3$	1	1	1	$T_1 \downarrow C_2$	1	2
$T_2 \downarrow C_4$	·	1	1	1	$T_2 \downarrow C_3$	1	1	1	$T_2 \downarrow C_2$	2	1

(d)		
$O \supset C_2(\rho_z)$	$0_2$	$1_2$
$A_1 \downarrow C_2$	1	·
$A_2 \downarrow C_2$	1	·
$E \downarrow C_2$	2	·
$T_1 \downarrow C_2$	1	2
$T_2 \downarrow C_2$	1	2

each level[5]. Once  $T^{[6]}$  or  $T^{[8]}$  terms are present, a numerical examination of eigenvectors is required to assign the symmetry of each level. Subgroup projectors are used here where the cluster degeneracy increases and the symmetry becomes challenging to distinguish. These projectors represent a simplification of the symmetry analysis of an octahedral molecule into projections onto  $C_4$  symmetric projectors. The correlation table for  $O \supset C_4$ , shown in Table 3.1, and (2.27) give the information necessary for the assignment. Moreover, when using the subgroup  $C_4$  there are only four projectors to create and a clever choice of axis can force several of these projectors to be entirely real or entirely imaginary. Conveniently, the  $C_4$  projectors can be used to diagnose level symmetry for clusters in any subgroup region.

### 3.2.3 Octahedral Results

#### Demonstration of Topological Changes in $T^{[4,6]}$

The Hecht Hamiltonian, Eq (3.1a), and its higher order analogues are generic Hamiltonians. Such Hamiltonians have numerous fitting constants specific to a given molecule

and a given vibronic species. To better understand all such octahedral systems, we consider changes in the level spectrum and RES plots with varying contributions of  $T^{[4]}$ ,  $T^{[6]}$  and  $T^{[8]}$ .

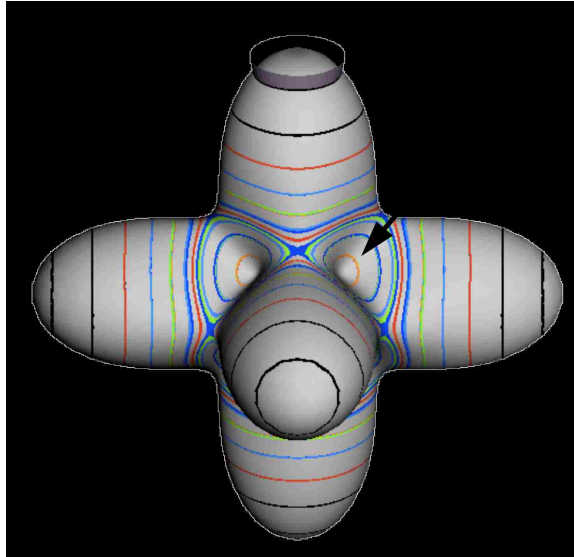
Eq (3.4) has two angular parameters,  $\theta$  and  $\phi$ . Several plots may be required to show slices in this parameter space. If  $T^{[8]}$  contributions are zero (as is usually the case), the eigenvalue spectrum for Eq (3.3) can be plotted versus  $\theta$ , changing relative contributions of 4<sup>th</sup> and 6<sup>th</sup> order Hamiltonian terms. Fig 3.4 plots such an eigenvalue spectrum for  $\phi = 0$  and places RES plots for important parts of the level diagram. The RES plots show the minimum-uncertainty cone (highest  $m$ ) on an axis that has the majority of level clusters. Fig 3.4 also points out what spots on the level diagram correspond to important changes in the RES plot.

To understand the behavior of the level diagram in Fig 3.4 it is critical to inspect the changing shape of the RES plots. In particular, the clustering of levels in the eigenvalue diagram is dependent on the localized symmetry regions of the RES at each value of  $\theta$ . Locally, the RES forms hills and valleys of a lower symmetry than that of the molecule. The local symmetry must also be a sub-group of the molecular symmetry. Fig 3.1 identifies the various local symmetry regions. The center of each local symmetry region defines the local symmetry axis. In the case of  $C_4$ ,  $C_3$  and  $C_2$  axes shown in Fig 3.1(a) and Fig 3.1(b), these axes are fixed on the RES as  $\theta$  changes. In some cases a  $C_4$ ,  $C_3$  or  $C_2$  region may not be visible or present at all.

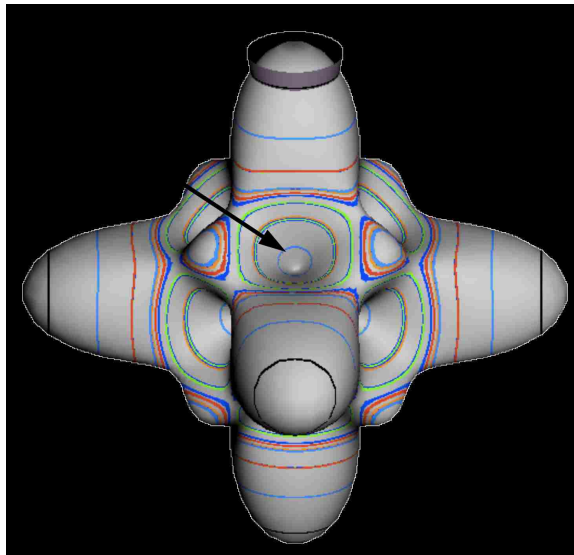
### **Semi-classical Outlines and Quantum Behavior**

By understanding local subgroup regions, it is possible to discuss more detail of Fig 3.4. The correspondence between the RES plots and the level diagram can also be seen by appending the eigenvalue spectrum in Fig 3.4 with the height of the  $C_4$ ,  $C_3$  and  $C_2$  axes. This confirms that the quantum spectrum sits inside the semi-classical boundaries and tracks the change in the eigenvalue spectrum corresponding to changes in RES topology. Fig 3.2 shows the same quantum spectrum as Fig 3.4,





(a)  $C_3$  and  $C_4$  local regions



(b)  $C_2$  local region

Figure 3.1: Symmetry Axes of  $T^{[4,6]}$  RES for differing contributions of  $T^{[4]}$  and  $T^{[6]}$

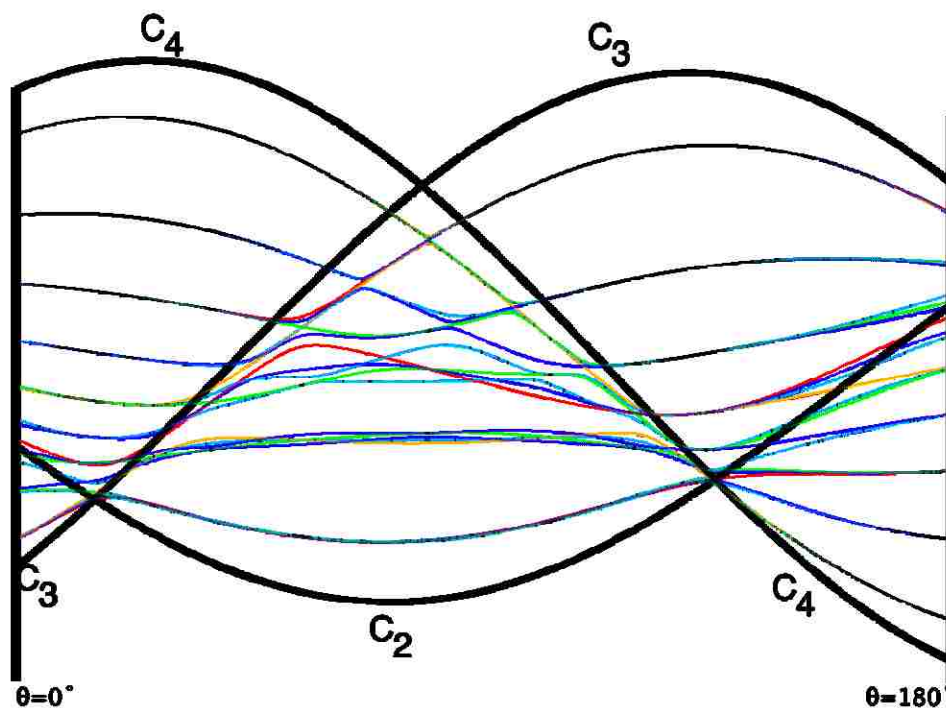


Figure 3.2: Quantum spectrum of octahedral Hamiltonian (Eq (3.3)) with changing  $\theta$ . Bold lines are the energy of the classical symmetry axis labeled.

but also includes the height (energy) of each symmetry axis. The outlines are printed in bold and are labeled for which  $C_n$  axis they each belong.

The separation of the extreme (highest or lowest) level clusters and the classical boundaries corresponds to a generalized “zero point” energy gap or Maslov index. No such gap appears for internal clusters around the  $C_2$  classical boundary when it becomes a separatrix.

Section 2.3 described how to predict the error between a fully quantum mechanical calculation and a semi-classical approximation of the symmetric rotor rotational spectra. For the symmetric rotor this could be done analytically. It is difficult to be as exact in calculating error for an octahedrally symmetric Hamiltonian, but a simple plot can show to what extent an RES plot fails to describe quantum mechanical behavior.

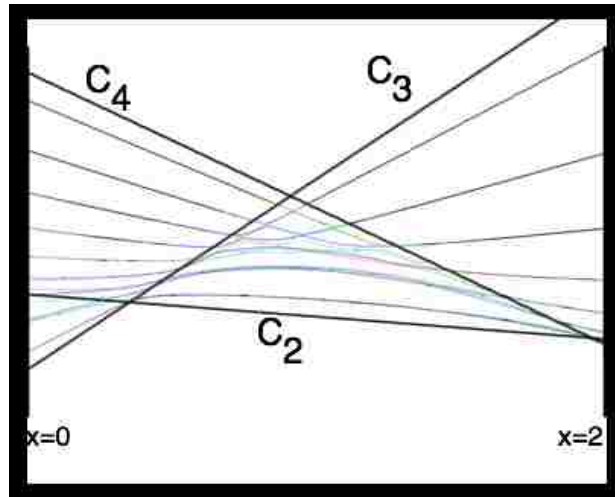
Rather than plotting the Hamiltonian as Eq (3.3) we will arrange it as

$$T^{[4,6]} = (1 - x)T^{[4]} + xT^{[6]}. \quad (3.6)$$

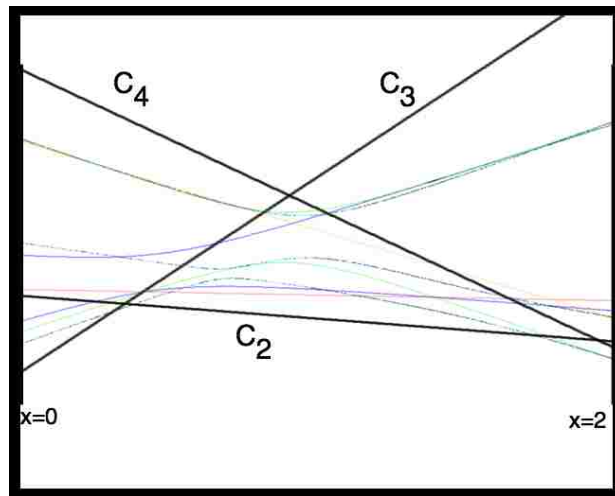
By doing so the semi-classical outlines will go from being cosine-like to linear. This rescaling helps to visually detect where quantum mechanical levels go outside the semi-classical bounds and see cases where a RES plot can be trusted as a valid approximation.

The three plots in Fig 3.3 show spectra and semi-classical outlines for  $J = 30$ ,  $J = 10$  and  $J = 4$ . Fig 3.3(a) shows that the quantum levels fit for all values of  $x$  at  $J = 30$ , while Fig 3.3(b) shows some small disagreement near  $x = 2$  for  $J = 10$ . Fig 3.3(c) shows that for low  $J = 4$  there is strong disagreement between quantum calculations and semi-classical approximations.

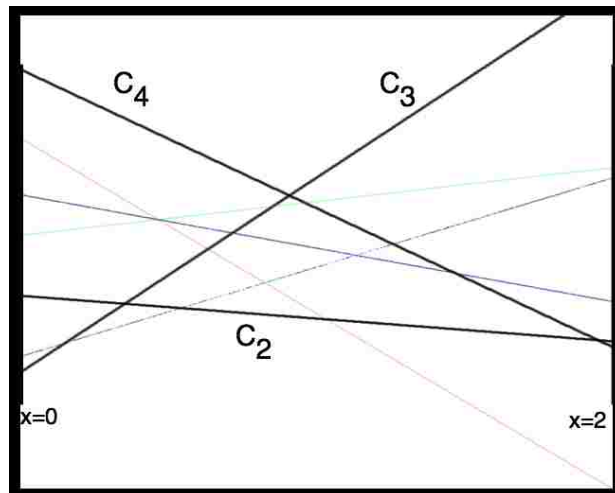
Next, an analysis of  $T^{[4,6,8]}$  demonstrates how such a Hamiltonian gives a different type of topology than previously reported, that of  $C_1$  symmetry.



(a)  $J=30$



(b)  $J=10$



(c)  $J=4$

Figure 3.3: Spectrum of Octahedral Rotor Showing Semi-Classical Boundaries Given Eq (3.6)

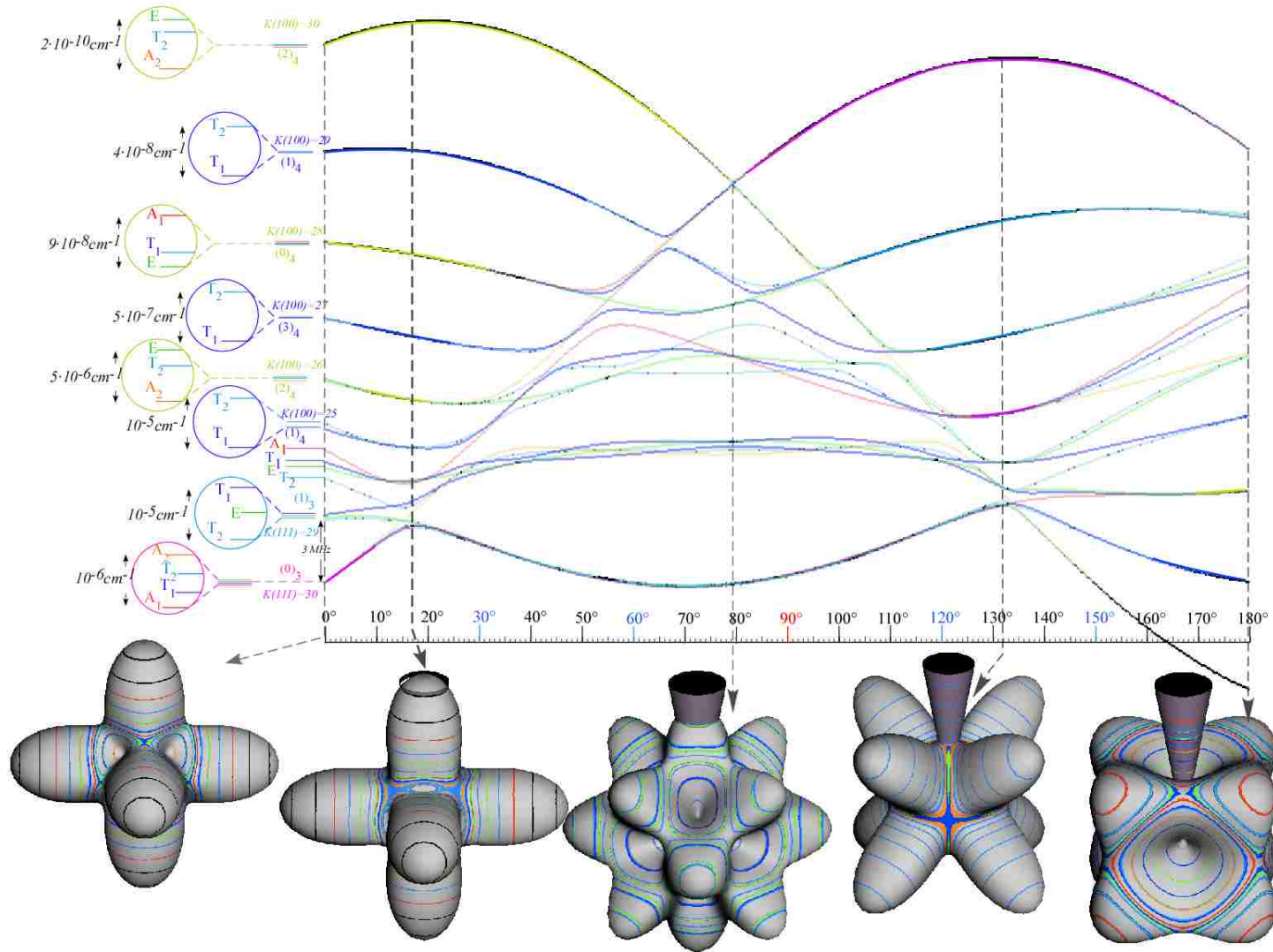


Figure 3.4: Both Energy Levels and RES Plots for  $T^{[4,6]}$ . Horizontal Axis goes from all  $T^{[4]}$  on the left to all  $T^{[6]}$  on the right

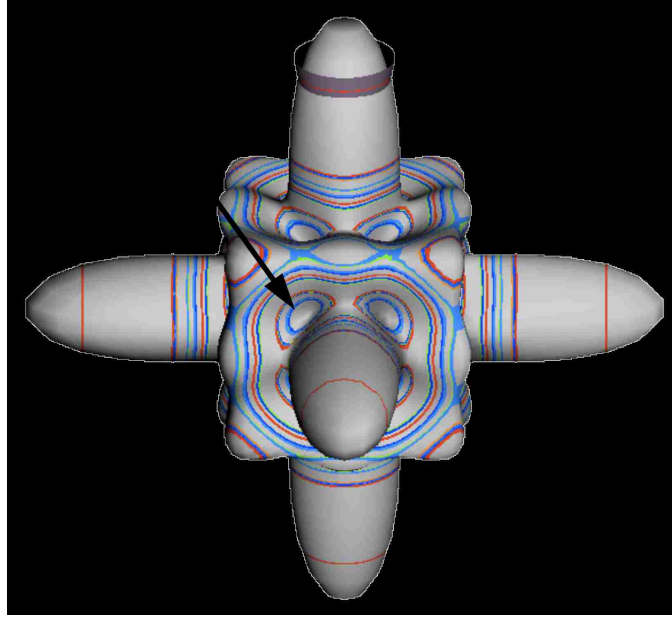


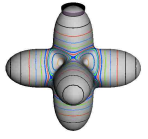
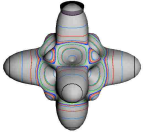
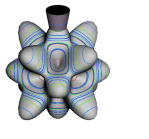
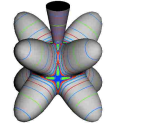
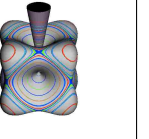
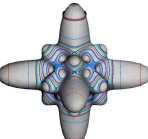
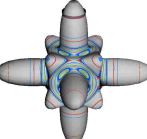
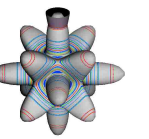
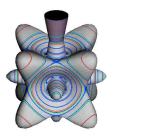
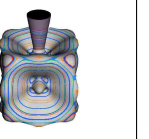
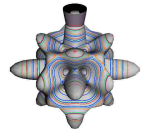
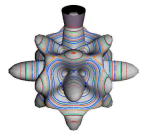
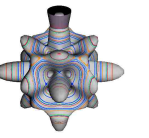
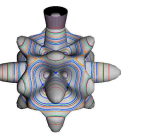
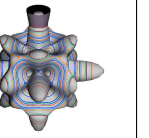
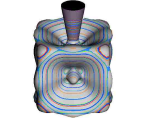
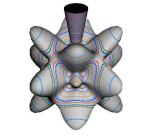
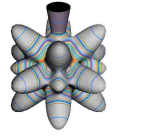
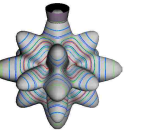
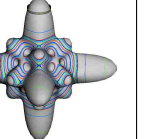
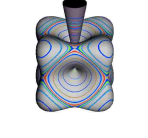
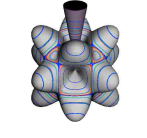
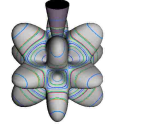
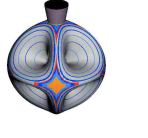
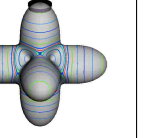
Figure 3.5: RES with  $C_1$  local symmetry regions visible

### Topological and Clustering Changes in the $T^{[4,6,8]}$ Parameter Space

The inclusion of eighth rank operators to the Hamiltonian dramatically changes the possible types of RES local symmetry and the related level clustering. While Fig 3.1 demonstrated  $C_4$ ,  $C_3$  and  $C_2$  symmetric local structures for RES plots for  $T^{[4,6]}$  Hamiltonians, Fig 3.5 demonstrates previously unseen local structures in a  $T^{[4,6,8]}$  Hamiltonian. This new level cluster structure contains all 24 levels of an entire regular representation. The local RES region pointed to in Fig 3.5 is asymmetric, that is,  $C_1$  symmetric and is repeated 24 times.

To demonstrate details of the two-dimensional  $T^{[4,6,8]}$  parameter space, several slices of the phase-space are shown by Table 3.2, which plots RES at select points in the  $(\theta, \phi)$ -parameter-space. To be consistent with Eq (3.4), the plots range  $(0$  to  $\pi)$  in  $\theta$  as they go from left to right and from  $(0$  to  $\pi)$  in  $\phi$  as they go from top to bottom. Since the symmetry labeling of the octahedral group is different from the asymmetric top, a new coloring convention for the octahedral levels is defined. For all octahedral RES plots in this chapter  $A_1$  is red,  $A_2$  is orange,  $E_2$  is green,  $T_1$  is dark blue and  $T_2$

Table 3.2: RES plots exploring the 2D parameter space

	$\theta = 0$	$\theta = \pi/4$	$\theta = \pi/2$	$\theta = 3\pi/4$	$\theta = \pi$
$\phi = 0$					
$\phi = \pi/4$					
$\phi = \pi/2$					
$\phi = 3\pi/4$					
$\phi = \pi$					

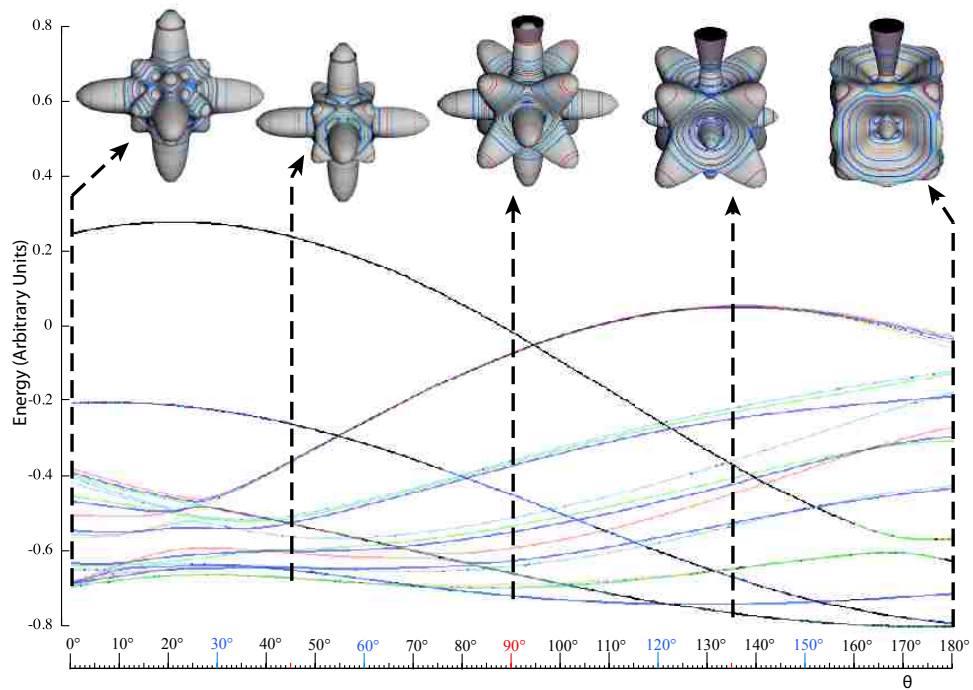
is light blue.

Due to Eq (3.4), the top and bottom rows are opposites of one another. That is, where one RES is convex (shifts to higher energy), the other is concave (shifts to lower energy). The RES at  $\theta = 0, \phi = 0$  has convex  $C_4$  and concave  $C_3$  structure as does the RES at  $\theta = \pi, \phi = \pi$ , but opposite the shape of the RES at either  $\theta = 0, \phi = \pi$  or  $\theta = \pi, \phi = 0$ . The ordering of the levels is also inverted. These two extremal rows also have no eighth order contribution, so they produce simple shapes, like Fig 3.1, and nn  $C_1$  local symmetry regions.

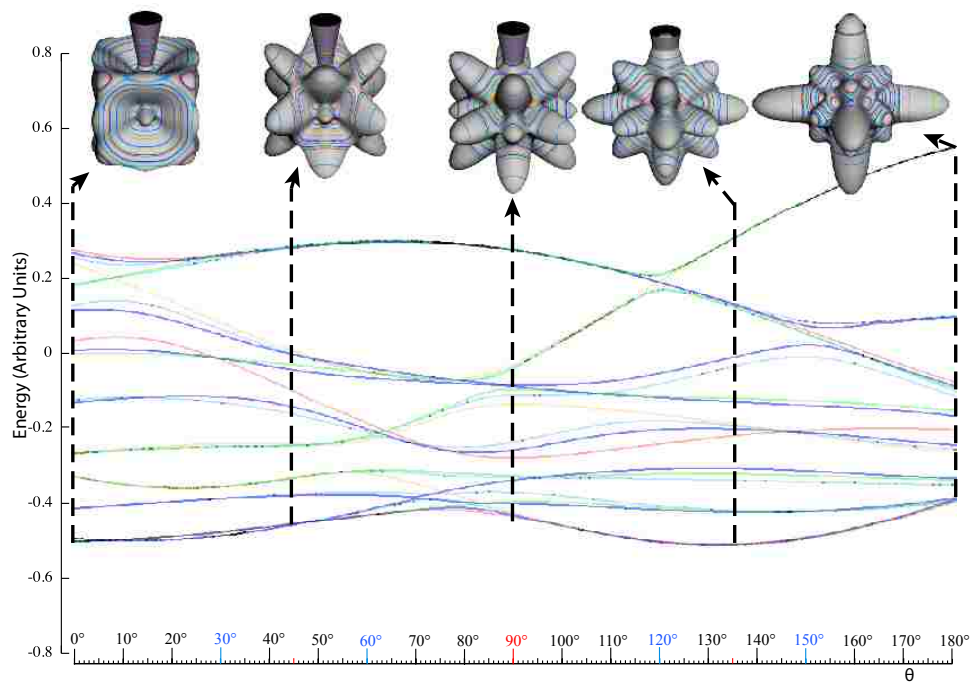
Note, in the middle row all the RES are identical as required by Eq (3.4) for any case where  $\phi = \pi/2$ .

Figure 3.6 shows level diagrams with select RES plots that exhibit symmetry and





(a)  $\phi = \pi/4$



(b)  $\phi = 3\pi/4$

Figure 3.6: Level Diagrams of Energy vs  $\theta$  for given  $\phi$  with RES Plots at Selected Positions



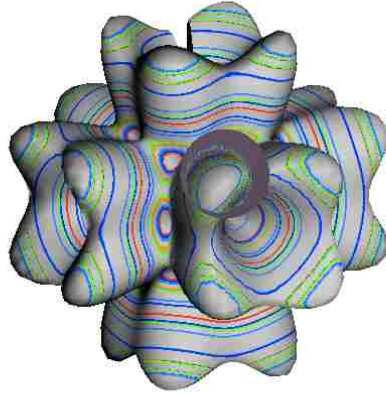
topology at each  $\theta$ -point in the space. The bold vertical lines next to the RES plots locate the spot in the level diagram or that particular RES. The  $\theta = \pi/2$  case is unchanged, so it is not shown. The  $\theta = \pi$  case is neglected as it is a mirror image of the  $\theta = 0$  case.

### 3.2.4 $C_1$ Level Clustering

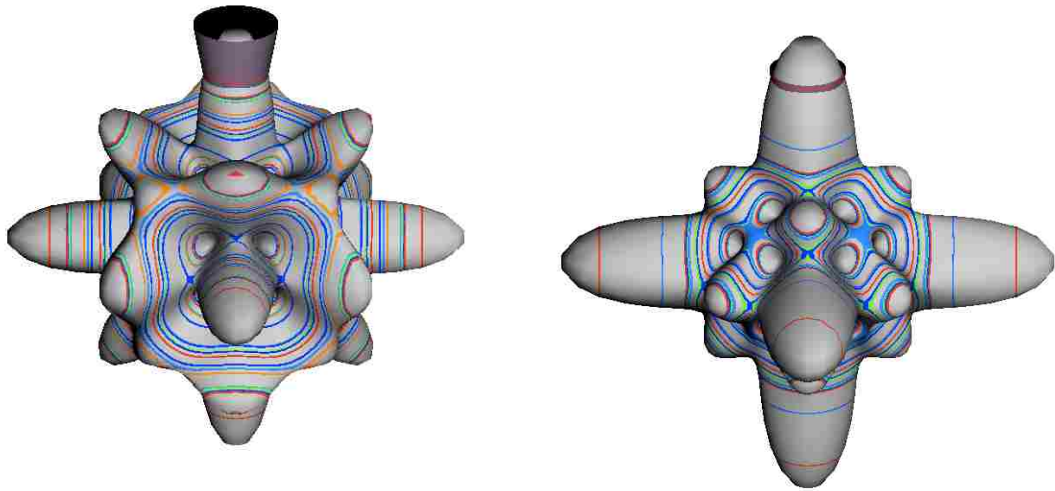
Fig 3.5 shows where  $C_1$  local regions are located on the RES. Unlike the  $C_2$ ,  $C_3$  and  $C_4$  local symmetry regions, the local  $C_1$  structures are not constrained to an axis and may be at different locations about the RES given different values of parameter  $\theta$  and  $\phi$ . RES plots with these local symmetries are also visible in parts of second, third and fourth rows of Table 3.2 as well as parts of Figures 3.6(a) and 3.6(b) that show concave  $C_1$  features. Fig 3.7 shows convex and concave  $C_1$  features arranged in either a square or triangular pattern.

The  $C_1$  features are not always present for two reasons. First, only certain parts of the parameter space allow them. In particular, there must be a non-zero  $T^{[8]}$  contribution. That is,  $\phi$  must not be any multiple of  $\pi$  (including 0), but  $\theta$  may have any value. Second,  $J$  must be large enough for an energy level to actually exist at that point on the surface. Thus, higher values of  $J$  make  $C_1$  clusters more likely since there are then more eigenvalues and more ways to fit  $J$  cones on the surface. RES with angular momenta as low as  $J = 4$  may show  $C_1$  clusters, since they cannot have 24 levels and do not meet minimum uncertainty relationships.

From our studies, we see that no  $C_1$  clusters are uncertainty-allowed until around  $J = 20$ . Their number does not grow quickly with  $J$ . Even for  $J = 30$ ,  $C_1$  levels are still barely allowed. This is indicated by the minimum ( $J = 30$ ) uncertainty cone that barely fits the the  $C_1$  portion of the RES in Fig 3.7(a). There is room for only one cluster, at the least uncertain ( $J = 30 = k$ ) cone.



(a) RES with convex  $C_1$  in a square arrangement. Note the figure is rotated slightly and the angular momentum cone has rotated to point in a  $C_1$  symmetric direction.



(b) RES with concave  $C_1$  structures in a tetragonal arrangement. (c) RES with concave, trigonal arrangement of  $C_1$  pockets

Figure 3.7:  $C_1$  Features on different parts of the parameter-space. All plots are done for  $J = 30$ .

### 3.3 Conclusion

In this chapter we have used the lowest parts of a Wigner multipole expansion of a Watson-Hecht rovibrational Hamiltonian to analyze purely geometric approximations to diagonalization. The RES approximations are often good and deviations can be accounted for analytically for axially symmetric systems. Predictably, deviations are large at low angular momentum and vanish with increasing  $J$ .

The Wigner  $D$ -functions that make up the multipole expansion tensors can also create the projectors that assist in identifying the symmetry of each eigenvector to come from a Hamiltonian matrix diagonalization. This process is simplified by using  $C_n$  subgroups of a given molecule's point symmetry.

The RES analysis shows a new complexity in the topological analysis of high order rotational Hamiltonians of octahedral  $O$  symmetry spherical-top molecules. A Hecht Hamiltonian terms of eighth order has new types of level clusters that have only  $C_1$  symmetric (asymmetric) RES regions that repeat 24 times along the RES. The possibility emerges of having 48 such asymmetric regions in a  $O_h$  Hamiltonian RES with a "monster" cluster of 48 rovibrational levels.

### Bibliography

- [1] A. J. Dorney and J. K. G. Watson. Forbidden rotational spectra of polyatomic molecules: Stark effects and  $\Delta J = 0$  transitions of  $T_d$  molecules. *Journal of Molecular Spectroscopy*, 42:135–148, 1972.
- [2] Karl T. Hecht. The vibration-rotation energies of tetrahedral  $XY_4$  molecules: Part i. theory of spherical top molecules. *Journal of Molecular Spectroscopy*, 5:355–389, 1961.
- [3] William G. Harter and Chris W. Patterson. Asymptotic eigensolutions of fourth and sixth rank octahedral tensor operators. *Journal of Mathematical Physics*,

- 20(7):1453–1459, July 1979.
- [4] Jacques Moret-Bailly, Lucienne Gautier, and Jean Montagutelli. Clebsch-gordan coefficients adapted to cubic symmetry. *Journal of Molecular Spectroscopy*, 15:355–377, 1965.
- [5] William G. Harter. Computer graphical and simiclassical approaches to molecular rotations and vibrations. *Computer Physics Reports*, 8:319–394, 1988.
- [6] M. Gulacsi, Zs. Gulacsi, and V. Tosa. The eigenvalue spectra of octahedral invariant tensor operator combinations up to eighth rank. *Journal of Molecular Spectroscopy*, 118(2):424–433, 1986.

## Chapter 4

### Local Symmetry Tunneling Eigensolutions

## 4.1 Chapter Summary

High-resolution rovibronic spectra of spherical top molecules may cluster and exhibit superfine structure. Superfine splittings depend on both the symmetry and geometry of phase-space tunneling paths. These paths are elucidated by rovibronic energy surfaces (RES). The relevant tunneling is that found between equivalent contours (energy levels) regions showing similar “local” symmetry. This chapter offers a method of labeling tunneling paths with molecular symmetry group labels. This allows for convenient labeling, but, more importantly, offers ways to simplify projection algebra to analyze tunneling dynamics and superfine energy splittings.

Rotational energy level cluster degeneracy or dimension increases as local symmetry is reduced. This is quite the opposite of extrinsic or “global” symmetry degeneracy, which splits with global symmetry reduction or “breaking”. An important duality exists between “un-splitting” or clustering due to local symmetry reduction and level splitting due to global symmetry reduction. The latter has been called “applied symmetry breaking” while the former may be known as “spontaneous symmetry breaking” in a number of areas of physics and chemistry.

A critical reformulation of quantum eigensolution analysis by exploiting the global-local duality improves its insight and computational efficiency. Here the parameter formation is introduced using an Abelian  $C_6$  example of Fourier group projection. This is extended to the most elementary non-Abelian  $D_3$  symmetry example in order to demonstrate dual symmetry analysis subsequent chapters follow with examples of  $O_h$  tensor eigensolutions having 12-fold and 24-fold level cluster superfine structure.

## 4.2 Introduction

For a system to have symmetry means two or more of its parts are the same or similar and therefore subject to resonance. This can make a system particularly sensitive to internal parameters and external perturbations and give rise to interesting and useful

effects. However, resonances can make it more difficult to analyze and understand a system's eigensolutions. The tensor level cluster states discussed in the preceding chapter 3 have examples of complex superfine structure due to  $J$ -tunneling that is the focus of this chapter and the following chapter 5.

Fortunately, the presence of symmetry in a physical system allows algebraic or group theoretical analysis of quantum eigensolutions and their dynamics. Groups of operators  $(g, g', g'', \dots)$  leave a Hamiltonian operator  $H$  invariant ( $g^\dagger H g = H$ ) if and only if each  $g$  commutes with it ( $gH = Hg$ ). Then each  $g$  in the group shares a set of eigenfunctions with  $H$ . However, if  $(g')$  and  $(g)$  do not commute then the  $(g')$  and  $(g)$  sets will differ.

Hamiltonians may themselves be symmetry operators or linear expansions thereof. Multipole tensor expansions used in chapters 1 through 3 are examples. Expanding  $H$  into operators with symmetry properties, such as  $(a^\dagger a)$  or  $(T_q^k)$ , helps to analyze its eigensolutions since, in some sense, a symmetry algebra “knows” its spectral resolutions. The underlying isometry of a system's variables and states contains all the sub-algebras that are possible  $H$ -symmetries.

If  $H$ -symmetry operators  $(g, g', \dots)$  also commute with each other ( $gg' = g'g, \text{etc.}$ ) then all  $g$  share with  $H$  a single set of eigenvectors as discussed in Sec. 4.3. Such commutative or *Abelian* symmetry analysis is just a Fourier analysis where all  $H$  are linear expansion of its symmetry elements  $(g, g', g'', \dots)$  and simultaneously diagonalized with  $H$ . Such  $g$  expansions define both Hamiltonians  $H$  and their states as described in Sec. 4.3.

However, non-commuting (non-Abelian) symmetry operators  $(g, g', g'', \dots)$  of  $H$  cannot both expand  $H$  and commute with  $H$ . This impasse is resolved in Sec. 4.4 by using a dual *local* operator group  $(\bar{g}, \bar{g}', \bar{g}'', \dots)$  that mutually commutes with the original *global* group. Then local  $(\bar{g})$  expand any  $H$  that commutes with global  $g$ , while the global  $g$  define base states and their combinations define symmetry projected

states.

In Sec. 4.4, the dual group ( $\bar{D}_3 \sim \bar{C}_{3v}$ ) of the smallest non-Abelian group ( $D_3 \sim C_{3v}$ ) is defined and applied. Dual symmetry-analysis is demonstrated for a trigonal tunneling system by group parametrization of all possible ( $D_3$ )-symmetric  $\mathbf{H}$  matrices and all possible eigensolutions for each. The example shows how global ( $g$ ) label states while the local ( $\bar{g}$ ) label tunneling paths. In this way symmetry labels processes as well as states.

In chapter 5, the local symmetry expansion is applied to octahedral tensor superfine structure. Local symmetry conditions are used to relate tunneling paths to RES topography in chapter 3 and predict specific energy level patterns.

### 4.3 Abelian symmetry analysis

This introduction to analysis of tunneling using symmetry begins with the very simplest cases that involve just cyclic  $C_n$  symmetry of  $n$ -fold polygonal structure. But, it also applies to Abelian (mutually commuting) groups  $A$  since they may be shown to reduce to outer products  $C_m \times C_n \times \dots$  of cyclic groups of prime order.

#### 4.3.1 Operator expansion of $C_n$ symmetric Hamiltonian

The analysis described here and in Sec. 4.4 deviates from standard procedure[1, 2, 3, 4, 5]. Instead of beginning with a given quantum Hamiltonian  $\mathbf{H}$ -matrix, we start with a  $C_n$  symmetry matrix ( $\mathbf{r}$ ) and build all possible  $C_n$  symmetric ( $\mathbf{H}$ )-matrices by combining  $n$  powers ( $\mathbf{r}^p$ ) = ( $\mathbf{r}$ ) <sup>$p$</sup>  of ( $\mathbf{r}$ ) ranging from identity  $\mathbf{r}^0 = \mathbf{1} = \mathbf{r}^n$  to inverse  $\mathbf{r}^{n-1} = \mathbf{r}^{-1}$  [6].

$$\begin{aligned} \mathbf{H} &= r_0\mathbf{r}^0 + r_1\mathbf{r}^1 + r_2\mathbf{r}^2 + \dots + r_{n-2}\mathbf{r}^{n-2} + r_{n-1}\mathbf{r}^{n-1} \\ &= r_0\mathbf{1} + r_1\mathbf{r}^1 + r_2\mathbf{r}^2 + \dots + r_{-2}\mathbf{r}^{-2} + r_{-1}\mathbf{r}^{-1} \end{aligned} \quad (4.1)$$

In (4.1) the rotation  $\mathbf{r}$  is by angle  $2\pi/n$  so rotation  $\mathbf{r}^n$  is by angle  $n2\pi/n = 2\pi$ ,



that is, the identity operator  $\mathbf{r}^0 = \mathbf{1} = \mathbf{r}^n$ . Thus power- $p$  indices label *modulo- $n$*  or base- $n$  algebras. If  $n=2$ , it is a *Boolean* algebra  $C_1 \subset C_2$  of *parity*  $[+1,-1]$  or classical *bits*  $[0,1]$ . ( $U(2)$  spin-algebras of  $q$ -bits have  $4\pi$  identity but are not considered here.)

$$\text{Sum rule: } p + p' = (p + p') \bmod (n)$$

$$\text{Product rule: } p \cdot p' = (p \cdot p') \bmod (n) \quad (4.2)$$

We construct the general  $\mathbf{H}$ -matrix using  $C_n$  group-product tables shown below in a  $\mathbf{g}^{-1}\mathbf{g}$ -form and a  $\mathbf{g}^\dagger\mathbf{g}$ -form that is equivalent for unitary operators  $\mathbf{g}^\dagger = \mathbf{g}^{-1}$ . In each table the  $k^{\text{th}}$ -row label  $\mathbf{g}^{-1}$  matches  $k^{\text{th}}$ -column label  $\mathbf{g}$  so that the identity operator  $\mathbf{1} = \mathbf{g}^{-1}\mathbf{g}$  resides only on the diagonal. This example is for hexagonal symmetry  $C_6$  for which  $\mathbf{r}^{-6} = \mathbf{r}^0 = \mathbf{1} = \mathbf{r}^6 = \mathbf{r}^{6\dagger}$ ,  $\mathbf{r}^{-5} = \mathbf{r}^1 = \mathbf{r}^{5\dagger}$ ,  $\mathbf{r}^{-4} = \mathbf{r}^2 = \mathbf{r}^{4\dagger}$ ,  $\mathbf{r}^{-3} = \mathbf{r}^3 = \mathbf{r}^{3\dagger}$ , and so forth.

$\mathbf{g}^{-1}\mathbf{g}$ <i>form</i>	$\mathbf{r}^0$ $\mathbf{r}^1$ $\mathbf{r}^2$ $\mathbf{r}^3$ $\mathbf{r}^4$ $\mathbf{r}^5$	$\mathbf{g}^\dagger\mathbf{g}$ <i>form</i>	$\mathbf{1}$ $\mathbf{r}^{+1}$ $\mathbf{r}^{+2}$ $\mathbf{r}^{+3}$ $\mathbf{r}^{-2}$ $\mathbf{r}^{-1}$
$\mathbf{r}^0$	$\mathbf{r}^0$ $\mathbf{r}^1$ $\mathbf{r}^2$ $\mathbf{r}^3$ $\mathbf{r}^4$ $\mathbf{r}^5$	$\mathbf{1}$	$\mathbf{1}$ $\mathbf{r}^{+1}$ $\mathbf{r}^{+2}$ $\mathbf{r}^{+3}$ $\mathbf{r}^{-2}$ $\mathbf{r}^{-1}$
$\mathbf{r}^5$	$\mathbf{r}^5$ $\mathbf{r}^0$ $\mathbf{r}^1$ $\mathbf{r}^2$ $\mathbf{r}^3$ $\mathbf{r}^4$	$\mathbf{r}^{-1}$	$\mathbf{r}^{-1}$ $\mathbf{1}$ $\mathbf{r}^{+1}$ $\mathbf{r}^{+2}$ $\mathbf{r}^{+3}$ $\mathbf{r}^{-2}$
$\mathbf{r}^4$	$\mathbf{r}^4$ $\mathbf{r}^5$ $\mathbf{r}^0$ $\mathbf{r}^1$ $\mathbf{r}^2$ $\mathbf{r}^3$	$\mathbf{r}^{-2}$	$\mathbf{r}^{-2}$ $\mathbf{r}^{-1}$ $\mathbf{1}$ $\mathbf{r}^{+1}$ $\mathbf{r}^{+2}$ $\mathbf{r}^{+3}$
$\mathbf{r}^3$	$\mathbf{r}^3$ $\mathbf{r}^4$ $\mathbf{r}^5$ $\mathbf{r}^0$ $\mathbf{r}^1$ $\mathbf{r}^2$	$\mathbf{r}^{+3}$	$\mathbf{r}^{+3}$ $\mathbf{r}^{-2}$ $\mathbf{r}^{-1}$ $\mathbf{1}$ $\mathbf{r}^{+1}$ $\mathbf{r}^{+2}$
$\mathbf{r}^2$	$\mathbf{r}^2$ $\mathbf{r}^3$ $\mathbf{r}^4$ $\mathbf{r}^5$ $\mathbf{r}^0$ $\mathbf{r}^1$	$\mathbf{r}^{+2}$	$\mathbf{r}^{+2}$ $\mathbf{r}^{+3}$ $\mathbf{r}^{-2}$ $\mathbf{r}^{-1}$ $\mathbf{1}$ $\mathbf{r}^{+1}$
$\mathbf{r}^1$	$\mathbf{r}^1$ $\mathbf{r}^2$ $\mathbf{r}^3$ $\mathbf{r}^4$ $\mathbf{r}^5$ $\mathbf{r}^0$	$\mathbf{r}^{+1}$	$\mathbf{r}^{+1}$ $\mathbf{r}^{+2}$ $\mathbf{r}^{+3}$ $\mathbf{r}^{-2}$ $\mathbf{r}^{-1}$ $\mathbf{1}$

(4.3)

The  $\mathbf{g}^\dagger\mathbf{g}$ -form produces a *regular representation*  $R(\mathbf{g}) = (\mathbf{g})$  of each operator  $\mathbf{g}$  as indicated by examples below. Each  $R(\mathbf{r}^p)$  is a zero-matrix with a  $1$  inserted at any

matrix position where a  $\mathbf{r}^p$  appears in the  $\mathbf{g}^\dagger\mathbf{g}$ -table.

$$\begin{aligned}
 R(\mathbf{1}) = & \quad R(\mathbf{r}^1) = & (4.4) \\
 \begin{pmatrix} 1 & \cdot & \cdot & \cdot & \cdot & \cdot \\ \cdot & 1 & \cdot & \cdot & \cdot & \cdot \\ \cdot & \cdot & 1 & \cdot & \cdot & \cdot \\ \cdot & \cdot & \cdot & 1 & \cdot & \cdot \\ \cdot & \cdot & \cdot & \cdot & 1 & \cdot \\ \cdot & \cdot & \cdot & \cdot & \cdot & 1 \end{pmatrix}, & \begin{pmatrix} \cdot & 1 & \cdot & \cdot & \cdot & \cdot \\ \cdot & \cdot & 1 & \cdot & \cdot & \cdot \\ \cdot & \cdot & \cdot & 1 & \cdot & \cdot \\ \cdot & \cdot & \cdot & \cdot & 1 & \cdot \\ \cdot & \cdot & \cdot & \cdot & \cdot & 1 \\ 1 & \cdot & \cdot & \cdot & \cdot & \cdot \end{pmatrix},
 \end{aligned}$$

$$\begin{aligned}
 R(\mathbf{r}^2) = & \quad R(\mathbf{r}^3) = & (4.5) \\
 \begin{pmatrix} \cdot & \cdot & 1 & \cdot & \cdot & \cdot \\ \cdot & \cdot & \cdot & 1 & \cdot & \cdot \\ \cdot & \cdot & \cdot & \cdot & 1 & \cdot \\ \cdot & \cdot & \cdot & \cdot & \cdot & 1 \\ 1 & \cdot & \cdot & \cdot & \cdot & \cdot \\ \cdot & 1 & \cdot & \cdot & \cdot & \cdot \end{pmatrix}, & \begin{pmatrix} \cdot & \cdot & \cdot & 1 & \cdot & \cdot \\ \cdot & \cdot & \cdot & \cdot & 1 & \cdot \\ \cdot & \cdot & \cdot & \cdot & \cdot & 1 \\ 1 & \cdot & \cdot & \cdot & \cdot & \cdot \\ \cdot & 1 & \cdot & \cdot & \cdot & \cdot \\ \cdot & \cdot & 1 & \cdot & \cdot & \cdot \end{pmatrix}, \dots
 \end{aligned}$$

$$(4.7)$$

A general  $C_n$  Hamiltonian ( $\mathbf{H}$ ) matrix results by inserting matrices from (4.4) above

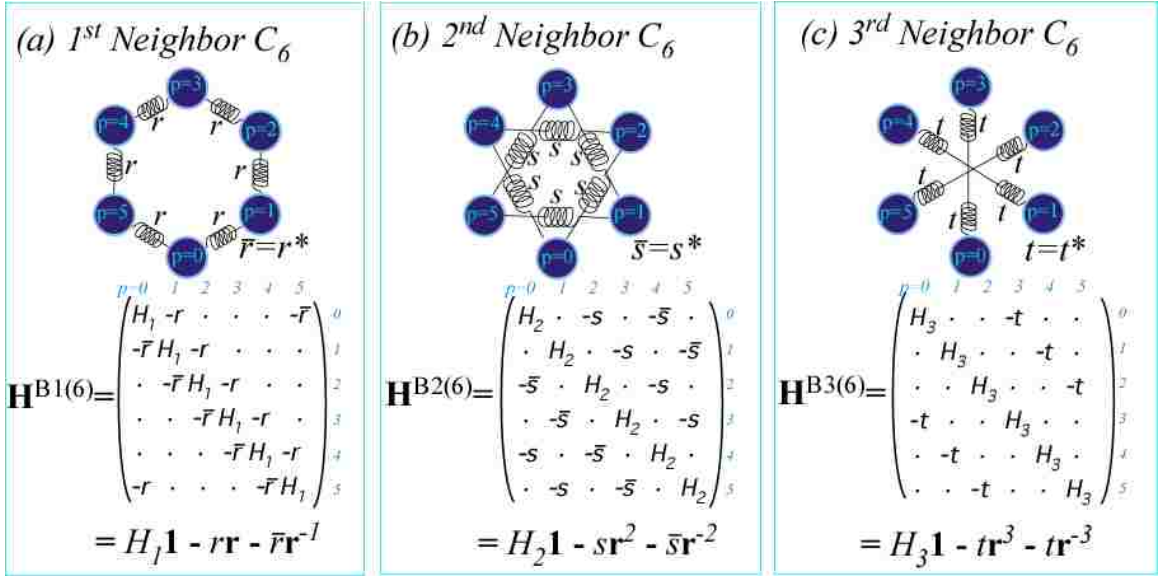
into expansion (4.1) of operator  $\mathbf{H}$ .

$$\begin{aligned}
(\mathbf{H}) &= \sum_{p=0}^{n-1} r_p (\mathbf{r}^p) = \begin{pmatrix} r_0 & r_1 & r_2 & r_3 & r_4 & r_5 \\ r_5 & r_0 & r_1 & r_2 & r_3 & r_4 \\ r_4 & r_5 & r_0 & r_1 & r_2 & r_3 \\ r_3 & r_4 & r_5 & r_0 & r_1 & r_2 \\ r_2 & r_3 & r_4 & r_5 & r_0 & r_1 \\ r_1 & r_2 & r_3 & r_4 & r_5 & r_0 \end{pmatrix} \\
&= \begin{pmatrix} r_0 & r_1 & r_2 & r_3 & r_{-2} & r_{-1} \\ r_{-1} & r_0 & r_1 & r_2 & r_3 & r_{-2} \\ r_{-2} & r_{-1} & r_0 & r_1 & r_2 & r_3 \\ r_3 & r_{-2} & r_{-1} & r_0 & r_1 & r_2 \\ r_2 & r_3 & r_{-2} & r_{-1} & r_0 & r_1 \\ r_1 & r_2 & r_3 & r_{-2} & r_{-1} & r_0 \end{pmatrix} \tag{4.8}
\end{aligned}$$

The matrices in (4.8) are simply group tables (4.3) with each operator  $\mathbf{r}^p$  replaced by a complex amplitude parameter  $r_p$ . Parameters  $r_0 = (r_0)^*$  and  $r_3 = (r_3)^*$  belong to self-conjugate elements of binary subgroups  $C_1 \subset C_2 = (\mathbf{1}, \mathbf{r}^3)$  related by  $\mathbf{1} = (\mathbf{r}^3)^2$ , and they must be real so that matrix  $(\mathbf{H})$  is Hermitian self-conjugate ( $H_{ab} = H_{ba}^*$ ), as well.

Three distinct classes of tunneling or coupling parameters are depicted in Fig. 4.1 using classical spring-mass analogs for quantum systems[7]. They are similar to those presented in ref [8, 9, 10] and many others using tunneling Hamiltonians. The 1<sup>st</sup>-neighbor class has non-zero parameters  $r_1=-r$  and conjugate  $r_{-1}=-r^*=-\bar{r}$  coupling only nearest neighbors each with self-energy  $r_0=H_1$ . The 2<sup>nd</sup>-neighbor class has non-zero parameters  $r_2=-s$  and conjugate  $r_{-2}=-s^*=-\bar{s}$  coupling only next-nearest neighbors with self-energy  $r_0=H_2$ . Finally, 3<sup>rd</sup>-neighbor coupling  $r_3=-t=-t^*$  is real as required for binary self-conjugacy  $\mathbf{r}^3=(\mathbf{r}^3)^\dagger$ .

Figure 4.1: Three classes of tunneling paths and parameters



### 4.3.2 Spectral resolution of $C_n$ symmetry operators

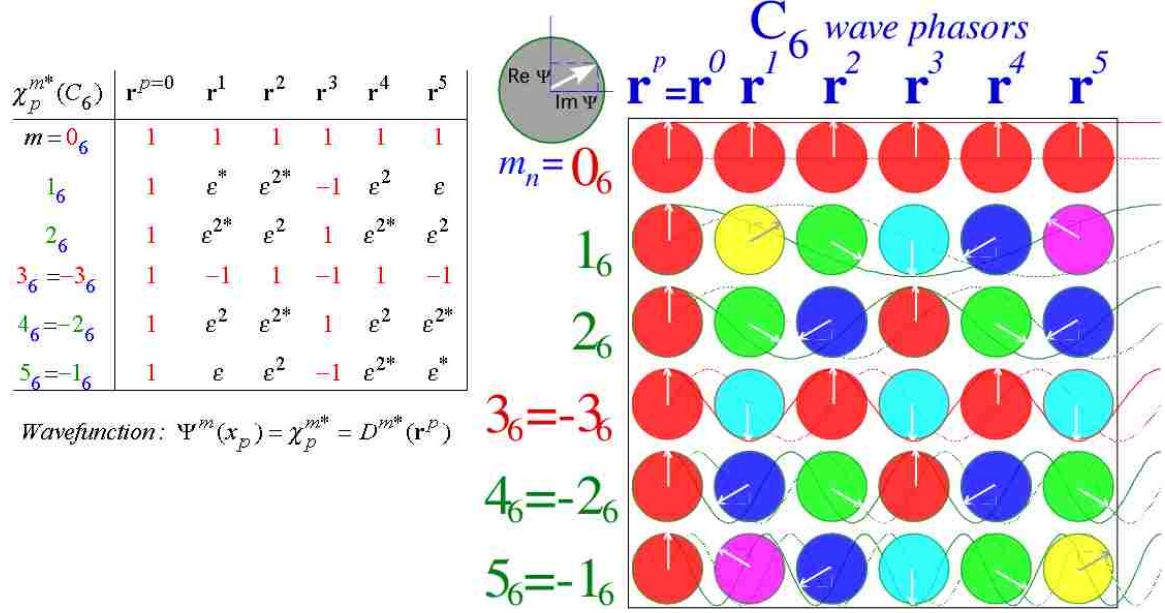
Eigenvalues  $\chi_p^m$  of each operator  $\mathbf{r}^p$  are  $m^{\text{th}}$  multiples of  $n^{\text{th}}$ -roots of unity since all  $C_n$  symmetry operators  $\mathbf{g} = \mathbf{r}^p$  satisfy  $\mathbf{g}^n = \mathbf{1}$  and are *characters* of  $C_n$  symmetry operators. Magnetic or *mode*-wavenumber indices  $m$  label a base- $n$  algebra as do the power or position-*point* indices  $p$  in (4.2). Spatial lattice points  $x_p = L \cdot p(\text{meters})$  are indexed by  $p$  while reciprocal- $(k)$ -wavevector space  $k_m = 2\pi m/L(\text{per meter})$  is indexed by integer  $m$ .

$$\langle \mathbf{r}^p \rangle_m = \chi_p^m = e^{-i(m \cdot p)2\pi/n} = e^{-ik_m x_p} = D^{(m)}(\mathbf{r}^p) \quad (4.9)$$

The  $\chi_p^m$  are  $C_n$  irreducible representations  $D^{(m)}(\mathbf{r}^p)$  as well as  $C_n$  characters. General group characters are traces (diagonal sums) of D-matrices ( $\chi^{(m)}(\mathbf{g}) = \text{trace} D^{(m)}(\mathbf{g})$ ). Abelian group irreducible representations are 1-dimensional due to their commutativity, and so for them characters and representations are identical. ( $\chi^{(m)}(\mathbf{g}) = D^{(m)}(\mathbf{g})$ )

Any number of mutually commuting unitary matrices may be diagonalized by a single unitary transformation matrix. The characters in (4.9) form a unitary trans-

Figure 4.2:  $C_6$  Characters (a) Numerical table (b) Wave phasor table



formation matrix  $T_{m,p}$  that diagonalizes each  $C_n$  matrix ( $\mathbf{r}^p$ ).

$$T_{m,p} = \chi_p^m / \sqrt{n} \quad (4.10)$$

This  $T$  is a discrete ( $n$ -by- $n$ ) Fourier transformation. A 6-by-6 example that diagonalizes all matrices in (4.4) and (4.8) and in Fig. 4.1 is shown in Fig. 4.2 by a character table of wave phasors based on  $D^{(m)}(\mathbf{r}^p)$  in eq.(4.9) or (4.10). The irreducible representations  $D^{(m)}(\mathbf{r}^p)$  or *irreps* play multiple roles. They are variously eigenvalues, eigenvectors, eigenfunctions, transformation components, and Fourier components of dispersion relations. This hyper-utility centers on their role as coefficients in *spectral resolution* of operators  $\mathbf{r}^p$  into idempotent projection operators  $\mathbf{P}^{(m)}$ .

$$\begin{aligned} \mathbf{r}^p &= \sum_{m=0}^{n-1} \chi_p^m \mathbf{P}^{(m)} \\ &= \chi_p^0 \mathbf{P}^{(0)} + \chi_p^1 \mathbf{P}^{(1)} + \chi_p^2 \mathbf{P}^{(2)} + \chi_p^3 \mathbf{P}^{(3)} + \chi_p^4 \mathbf{P}^{(4)} + \chi_p^5 \mathbf{P}^{(5)} \end{aligned} \quad (4.11)$$

$\mathbf{P}^{(m)}$  are irrep *placeholders*. Eq (4.11) is column- $p$  of Fig. 4.2. Column-0 is a

completeness or identity resolution relation.

$$\mathbf{r}^0 = \sum_{m=0}^{n-1} \mathbf{P}^{(m)} = \mathbf{1} = \mathbf{P}^{(0)} + \mathbf{P}^{(1)} + \mathbf{P}^{(2)} + \mathbf{P}^{(3)} + \mathbf{P}^{(4)} + \mathbf{P}^{(5)} \quad (4.12)$$

Dirac notation for  $\mathbf{P}^{(m)}$  is  $|(m)\rangle\langle(m)|$ . Its representation in its own basis (*eigenbasis*) is simply a zero matrix with a single 1 at the  $(m, m)$ -diagonal component.  $\mathbf{P}^{(m)}$ -product table in (4.13) is equivalent through (4.11) to  $\mathbf{g}$ -product table in Eq (4.3) but the  $\mathbf{P}^{(m)}$ -table given below has an orthogonal (*e.g.*  $\mathbf{P}^{(1)}\mathbf{P}^{(2)} = \mathbf{0}$ ) idempotent (*e.g.*  $\mathbf{P}^{(1)}\mathbf{P}^{(1)} = \mathbf{P}^{(1)}$ ) form.

$\mathbf{P}^\dagger \mathbf{P}$ <i>form</i>	$\mathbf{P}^{(0)}$	$\mathbf{P}^{(1)}$	$\mathbf{P}^{(2)}$	$\mathbf{P}^{(3)}$	$\mathbf{P}^{(4)}$	$\mathbf{P}^{(5)}$
$\mathbf{P}^{(0)}$	$\mathbf{P}^{(0)}$	.	.	.	.	.
$\mathbf{P}^{(1)}$	.	$\mathbf{P}^{(1)}$	.	.	.	.
$\mathbf{P}^{(2)}$	.	.	$\mathbf{P}^{(2)}$	.	.	.
$\mathbf{P}^{(3)}$	.	.	.	$\mathbf{P}^{(3)}$	.	.
$\mathbf{P}^{(4)}$	.	.	.	.	$\mathbf{P}^{(4)}$	.
$\mathbf{P}^{(5)}$	.	.	.	.	.	$\mathbf{P}^{(5)}$

$$\mathbf{P}^{(m)}\mathbf{P}^{(n)} = \delta^{mn}\mathbf{P}^{(n)} \rightarrow (\mathbf{P}^{(2)})_{\mathbf{P}} = \begin{pmatrix} \cdot & \cdot & \cdot & \cdot & \cdot & \cdot & \cdot \\ \cdot & \cdot & \cdot & \cdot & \cdot & \cdot & \cdot \\ \cdot & \cdot & 1 & \cdot & \cdot & \cdot & \cdot \\ \cdot & \cdot & \cdot & \cdot & \cdot & \cdot & \cdot \\ \cdot & \cdot & \cdot & \cdot & \cdot & \cdot & \cdot \\ \cdot & \cdot & \cdot & \cdot & \cdot & \cdot & \cdot \end{pmatrix} \quad (4.13)$$

The location of each  $\mathbf{P}^{(m)}$  in the  $\mathbf{P}$ -table is a location of a 1 in its representation as indicated in the right hand side of (4.13) in the same way that locations in  $\mathbf{g}$ -table (4.3) place 1's in representations (4.4). However, idempotent self-conjugacy ( $\mathbf{P}^\dagger = \mathbf{P}$ ) makes row labels of  $\mathbf{P}$ -table (4.13) identical to its column labels, whereas only  $\mathbf{g} = \mathbf{1}$

and  $\mathbf{g} = \mathbf{r}^3$  are self-conjugate in  $\mathbf{g}$ -table (4.3).

We may view character arrays such as Fig. 4.2 as representing operator eigen-products between  $\mathbf{r}^p$  and  $\mathbf{P}^{(m)}$ .

$$\mathbf{r}^p \mathbf{P}^{(m)} = \chi_p^m \mathbf{P}^{(m)} = \mathbf{P}^{(m)} \mathbf{r}^p \quad (4.14)$$

We may also view character  $\chi_p^m$  as scalar product *overlap* of position state bra or ket with momentum ket or bra.

$$\begin{aligned} \text{Position bra: } \langle x_p | &= \langle p | = \langle 0 | \mathbf{r}^{-p} \\ \text{Position ket: } |x_p \rangle &= |p \rangle = \mathbf{r}^p |0 \rangle \end{aligned} \quad (4.15a)$$

$$\begin{aligned} \text{Momentum bra: } \langle k_m | &= \langle (m) | = \langle 0 | \mathbf{P}^{(m)} \sqrt{\bar{n}} \\ \text{Momentum ket: } |k_m \rangle &= |(m) \rangle = \mathbf{P}^{(m)} |0 \rangle \sqrt{\bar{n}} \end{aligned} \quad (4.15b)$$

Plane wave momentum eigenfunction  $\psi_{k_m}(x_p)$  equals character (4.9) conjugated to  $e^{ik_m x_p}$  and normalized by  $\sqrt{\bar{n}}$ .

$$\begin{aligned} \psi_{k_m}(x_p) &= \langle x_p | k_m \rangle = \langle p | (m) \rangle = (\chi_p^m / \sqrt{\bar{n}})^* \\ &= (\langle (m) | p \rangle)^* = e^{ik_m x_p} / \sqrt{\bar{n}} \end{aligned} \quad (4.16)$$

The effect of  $\mathbf{r}^p$  on a state ket  $|(m) \rangle = |k_m \rangle$  is conjugate and inverse to its effect on coordinate bra  $\langle x_q | = \langle q |$ .

$$\begin{aligned} \psi_{k_m}(x_q - p \cdot L) &= \langle x_q | \mathbf{r}^p | k_m \rangle = \langle q | \mathbf{r}^p | (m) \rangle \\ &= \langle q - p | (m) \rangle = e^{-ik_m x_p} \langle q | (m) \rangle \end{aligned} \quad (4.17)$$

The same overlap results whether  $\mathbf{r}^p$  moves a  $(m)$ -wave  $p$ -points forward or moves the coordinate grid  $p$ -points backward. This  $C_n$  relativity-duality principle is generalized

below in the discussion of higher symmetry and is a key part of the operator labeling of coordinates, base states, Hamiltonians, and their eigensolutions.

$\mathbf{P}^{(m)}$  operators project momentum states using conjugate characters  $\phi_p^m = (\chi_p^m)^*$  normalized by  $1/n$  to be idempotent and sum to  $\mathbf{1}$ . ( $\sum_p \mathbf{P}^{(m)} = \mathbf{1}$ ) States  $|k_m\rangle$  use  $\phi_p^m$  normalized by  $1/\sqrt{n}$  to be orthonormal so a sum of *squares* is 1. ( $\sum_p |\langle x_p | k_m \rangle|^2 = 1$ ) This gives rise to a factor  $\sqrt{n}$  in projection eq.(4.15b) of  $|k_m\rangle$  by  $\mathbf{P}^{(m)}$ .

More explicitly, the inverse of spectral resolution in (4.11) sums over column points  $p$  using  $\phi_p^m$  from each row- $(m)$  of Fig. 4.2. Factor  $1/n$  makes  $\mathbf{P}^{(m)}$  complete ( $\sum_m \mathbf{P}^{(m)} = \mathbf{1}$  in (4.12)) and idempotent ( $\mathbf{P}^{(m)}\mathbf{P}^{(m)} = \mathbf{P}^{(m)}$ ) in (4.13)).

$$\begin{aligned} \mathbf{P}^{(m)} &= \left( \sum_{p=0}^{n-1} \phi_p^m \mathbf{r}^p \right) / n \\ &= (\phi_0^m \mathbf{r}^0 + \phi_1^m \mathbf{r}^1 + \phi_2^m \mathbf{r}^2 + \phi_3^m \mathbf{r}^3 + \phi_4^m \mathbf{r}^4 + \phi_5^m \mathbf{r}^5) / 6 \end{aligned} \quad (4.18)$$

The first row (The  $(m)=(0)$ -row) of Fig. 4.2 is the average or a sum of all symmetry operators weighted by  $1/n$ .

$$\mathbf{P}^{(0)} = \left( \sum_{p=0}^{n-1} \mathbf{r}^p \right) / n = (\mathbf{r}^0 + \mathbf{r}^1 + \mathbf{r}^2 + \mathbf{r}^3 + \mathbf{r}^4 + \mathbf{r}^5) / 6 \quad (4.19)$$

The preceding shows how factors  $\sqrt{n} = \sqrt{6}$  in state projections in (4.15b) gives state norms  $\sqrt{n}/n = 1/\sqrt{n}$  in (4.16).

$$\begin{aligned} \mathbf{P}^{(m)}|0\rangle\sqrt{n} &= \left( \sum_{p=0}^{n-1} \phi_p^m |p\rangle \right) / \sqrt{n} \\ &= (\phi_0^m |0\rangle + \phi_1^m |1\rangle + \phi_2^m |2\rangle + \phi_3^m |3\rangle + \phi_4^m |4\rangle + \phi_5^m |5\rangle) / \sqrt{6} \end{aligned} \quad (4.20)$$

The  $(0)$ -momentum or *scalar* state is a sum over the  $(m)=(0)$ -row of Fig. 4.2 normal-



ized by  $1/\sqrt{n}$ .

$$\mathbf{P}^{(0)}|0\rangle\sqrt{n} = \left( \sum_{p=0}^{n-1} |p\rangle \right) / \sqrt{n} = (|0\rangle + |1\rangle + |2\rangle + |3\rangle + |4\rangle + |5\rangle) / \sqrt{6} \quad (4.21)$$

### 4.3.3 Spectral resolution of $C_n$ symmetric Hamiltonian

Given Hamiltonian  $\mathbf{H}$  expansion in (4.1) in operators  $\mathbf{r}^p$  and the spectral resolution in (4.11) of  $\mathbf{r}^p$ , there follows the desired spectral resolution of  $\mathbf{H}$ . The eigenvalue coefficients  $\omega^{(m)}$  of  $\mathbf{P}^{(m)}$  define the dispersion function  $\omega(k_m)$  of  $\mathbf{H}$ .

$$\mathbf{H} = \sum_{p=0}^{n-1} r_p \mathbf{r}^p = \sum_{p=0}^{n-1} r_p \sum_{m=0}^{n-1} \chi_p^m \mathbf{P}^{(m)} = \sum_{m=0}^{n-1} \omega^{(m)} \mathbf{P}^{(m)} \quad \text{where : } \omega^{(m)} = \sum_{p=0}^{n-1} r_p \chi_p^m = \omega(k_m) \quad (4.22)$$

It is conventional to center scalar origin  $(m)=0$ . Positive  $k_m$ -axis  $C_6$  array [...(0), (1), (2), (3), (4), (5), ...] of Eq (4.13) shifts to a zone-centered array *mod-6*: [...(4), (5), (0), (1), (2), (3), ...]=[...(-2), (-1), (0), (1), (2), (3), ...] using (4.2).

Examples of dispersion relations for three classes of tunneling paths in Fig. 4.1 are shown in Fig. 4.3. Dispersion  $\omega(k_m)$  for  $C_6$  symmetry depends sensitively on the Hamiltonian tunneling amplitudes  $r_p$  for  $-3 < p \leq 3$  (or  $0 \leq p < 6$ ) in Eq (4.8), and for any set of eigenvalues  $\omega(k_m)$  there is a unique set of  $r_p$  found by inverting (4.22).

$$r_p = \sum_{m=0}^{n-1} \phi_p^m \omega^{(m)} / n \quad \text{where : } \phi_p^m = (\chi_p^m)^* \quad (4.23)$$

A common tunneling spectral model is the elementary Bloch 1<sup>st</sup>-neighbor  $B1(6)$ -model shown in Fig. 4.3a, much like that developed in ref [8]. For negative values of  $r_1=-r$ , a  $B1(6)$  spectra for  $C_6$  consist of six points on a single inverted cosine-wave curve centered at  $m=0$  with its maxima at the *Brillouin-band boundaries*  $(m)=\pm 3$ . This curve applies to  $B1(n)$  spectra for  $C_n$  where  $n$  equally spaced  $(m)$  points lie on the

dispersion curve between  $m=\pm n/2$  for even- $n$ . The  $n$  energy eigenvalues  $\omega^{(m)}$  are projections of an  $n$ -polygon. For  $n=6$  that is the hexagon shown in Fig. 4.3a projecting two doublet levels  $\omega^{(\pm 1)}$  and  $\omega^{(\pm 2)}$  between singlet  $\omega^{(0)}$  and singlet  $\omega^{(3)}$  at lowest and highest hexagonal vertices as follows from (4.22).

$$\omega^{B1(n)}(k_m) = r_0\chi_0^m + r_1\chi_1^m + r_{-1}\chi_{-1}^m = H_1 - 2r \cos(2\pi m/6) \quad (4.24)$$

The  $2^{nd}$ -neighbor  $B2$ -model (Fig. 4.3b) has a two-cosine-wave dispersion curve. An equilateral triangle projects energy doublet levels  $[\omega^{(0)}, \omega^{(3)}]$  from its lowest vertex and a quartet  $[\omega^{(\pm 1)}, \omega^{(\pm 2)}]$  from its upper vertices.

$$\omega^{B2(n)}(k_m) = r_0\chi_0^m + r_2\chi_2^m + r_{-2}\chi_{-2}^m = H_2 - 2s \cos(4\pi m/6) \quad (4.25)$$

The  $3^{rd}$ -neighbor  $B3$ -model (Fig. 4.3c) has a three-cosine-wave dispersion, which for  $n=6$  and  $r_3=-t$ , separates levels into an even- $m$  triplet  $[\omega^{(0)}, \omega^{(\pm 2)}]$  below an odd- $m$  triplet  $[\omega^{(3)}, \omega^{(\pm 1)}]$ .

$$\omega^{B3(n)}(k_m) = r_0\chi_0^m + r_3\chi_3^m + r_{-3}\chi_{-3}^m = H_3 - 2t(-1)^m \quad (4.26)$$

Combining of  $k^{th}$ -neighbor  $r_k$ -terms gives dispersion  $\omega^{(m)}$  as a  $k$ -term Fourier cosine series that is, for real  $r_k$ , a sum of the preceding three equations (4.24), (4.25), and (4.26). However, real  $r_k$  imply symmetry that is higher than  $C_6$ , namely non-Abelian reflection-rotation symmetry such as  $C_{6v}$  or  $D_{6h}$  and a corresponding degeneracy between  $\omega^{(\pm m)}$  levels that will be treated shortly. Simple  $C_6$  symmetry allows six real parameters with complex  $r_1$  and  $r_2$ . Then eq. (4.22) implies six levels that are generally non-degenerate as shown in Fig. 4.4. Complex  $r_1 = |r|e^{i\phi}$  of a ZB1 model describes chiral magnetic or rotational effects that include Zeeman-like splitting of  $m$ -doublets. The projecting hexagon tilts by the “gauge” phase angle  $\phi = \pi/12$  as the ZB1(6) dispersion  $\omega(m)$  shifts. Then  $m$  doublets  $(\pm 1)$  and  $(\pm 2)$  suffer splittings

Figure 4.3: Energy level dispersion for archetypical tunneling parameters: B1: $r_1 = -r$ , B2: $r_2 = -s$ , B3: $r_3 = -t$

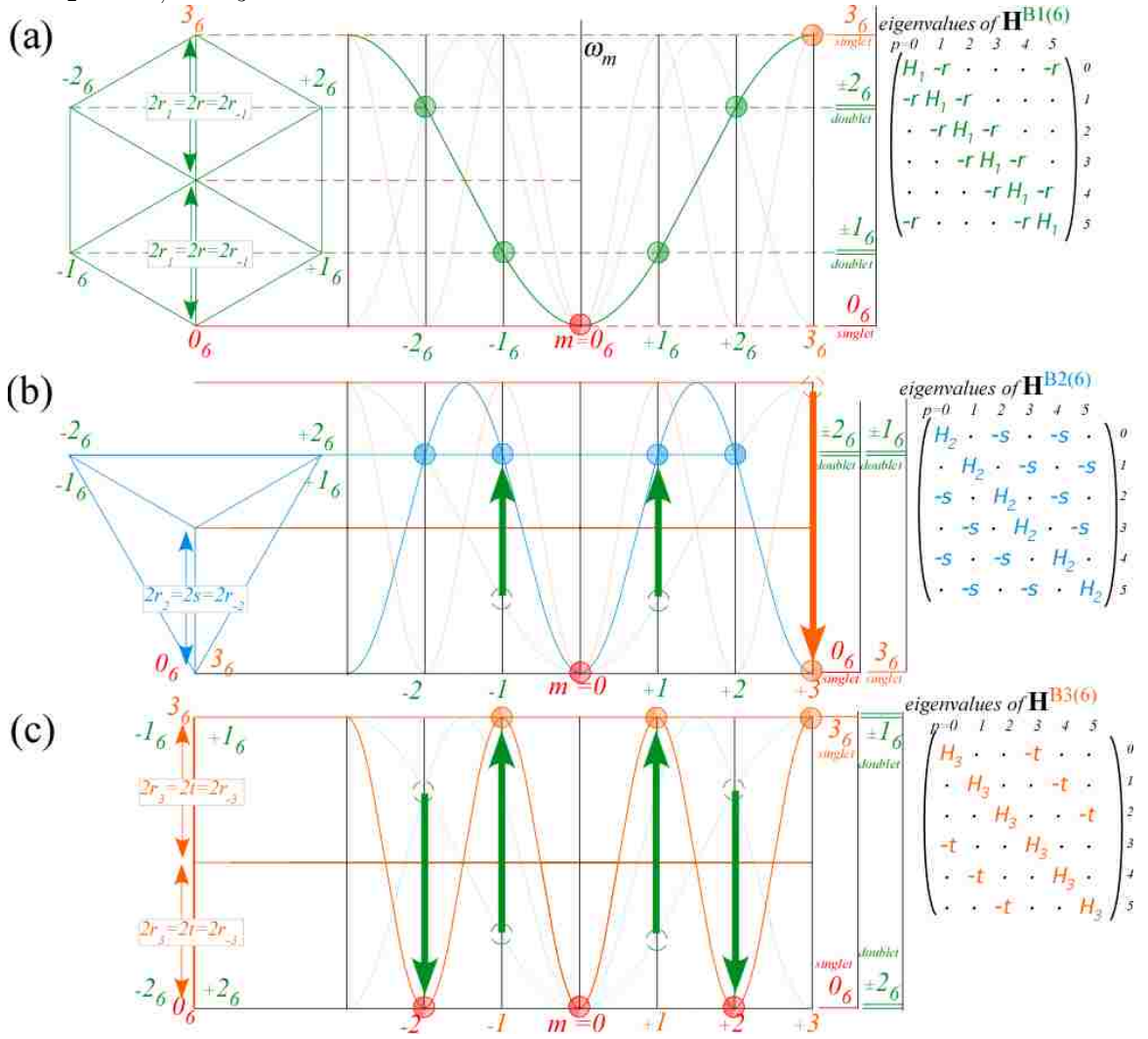
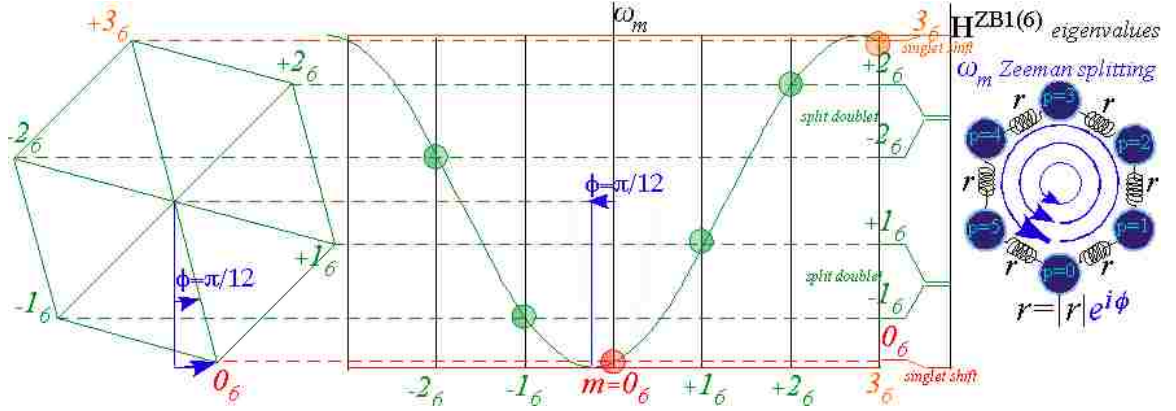


Figure 4.4: Zeeman shifted Bloch dispersion for complex parameter in ZB1(6) model:  $r_1 = -re^{i\phi}$  with  $\phi = \pi/12$



that are 1<sup>st</sup>-order in  $\phi$  while singlets (0) and (3) undergo shifts that are 2<sup>nd</sup>-order in  $\phi$ .

#### 4.4 Non-Abelian symmetry analysis

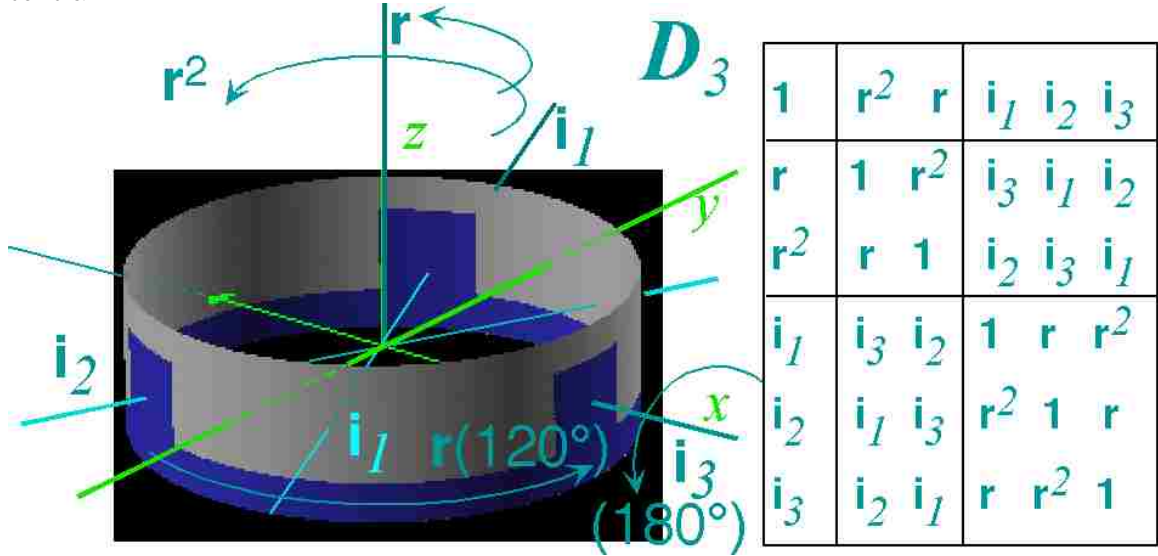
Characterization and spectral resolution in (4.22) of a Hamiltonian  $\mathbf{H}^{Bk(6)}$  uses its expansion in (4.1) in Abelian group  $C_6$ . Similar spectral resolution of a Hamiltonian  $\mathbf{H}$  by a non-Abelian group  $G = [\dots \mathbf{g}_1, \mathbf{g}_2 \dots]$  of non-commuting symmetry operators might seem impossible. To be symmetry operators of  $\mathbf{H}$ , elements  $\mathbf{g}_1$  and  $\mathbf{g}_2$  must commute with  $\mathbf{H}$ , but that cannot be if  $\mathbf{H}$  is a linear expansion of them like (4.1). The impasse is broken by introducing operator *relativity-duality* detailed below. A  $D_3$ -symmetric tunneling  $\mathbf{H}$  with a 3-well potential sketched in Fig. 4.5 is used as an example.

Though examples in this section are for rotational states and Hamiltonians, appendix 4.A demonstrates similar structure for vibrational states.

##### 4.4.1 Operator expansion of $D_3$ symmetric Hamiltonian

The simplest non-Abelian group is the rotational symmetry  $D_3 = [\mathbf{1}, \mathbf{r}^1, \mathbf{r}^2, \mathbf{i}_1, \mathbf{i}_2, \mathbf{i}_3]$  of an equilateral triangle.  $D_3$  is used to show how to generalize  $C_6$  operator analysis of the preceding section to any symmetry group. The  $D_3$  analysis begins with a  $\mathbf{g}^\dagger \mathbf{g}$ -form

Figure 4.5: Rotation operators  $[1, \mathbf{r}^1, \mathbf{r}^2, \mathbf{i}_1, \mathbf{i}_2, \mathbf{i}_3]$  for a  $D_3$  symmetric square-well potential.



of group product table like (4.3) for  $C_6$ . However,  $D_3$  also requires a  $\mathbf{g}\mathbf{g}^\dagger$ -form giving the same product rules but using inverse  $\mathbf{g}^\dagger$  ordering  $|\dots\mathbf{r}^2, \mathbf{r}^1, \dots| = |\dots\mathbf{r}^{1\dagger}, \mathbf{r}^{2\dagger}, \dots|$  along the top instead of down the left side as is done for the  $\mathbf{g}^\dagger\mathbf{g}$ -form of table. (The two  $\pm 120^\circ$  rotations  $\mathbf{r}^1$  and  $\mathbf{r}^2$  are the only pair ( $\mathbf{r}^{1\dagger} = \mathbf{r}^2$ ) to be switched by conjugation). The three  $\pm 180^\circ$  rotations are each self-conjugate ( $\mathbf{i}_p^\dagger = \mathbf{i}_p$ ) as is (always) the identity  $\mathbf{1}^\dagger = \mathbf{1}$ .)

$\mathbf{g}^\dagger\mathbf{g}$ form	<b>1</b>	$\mathbf{r}^1$	$\mathbf{r}^2$	$\mathbf{i}_1$	$\mathbf{i}_2$	$\mathbf{i}_3$	$\mathbf{g}\mathbf{g}^\dagger$ form	$\bar{\mathbf{1}}$	$\bar{\mathbf{r}}^2$	$\bar{\mathbf{r}}^1$	$\bar{\mathbf{i}}_1$	$\bar{\mathbf{i}}_2$	$\bar{\mathbf{i}}_3$	(4.27)
<b>1</b>	<b>1</b>	$\mathbf{r}^1$	$\mathbf{r}^2$	$\mathbf{i}_1$	$\mathbf{i}_2$	$\mathbf{i}_3$	$\bar{\mathbf{1}}$	$\bar{\mathbf{1}}$	$\bar{\mathbf{r}}^2$	$\bar{\mathbf{r}}^1$	$\bar{\mathbf{i}}_1$	$\bar{\mathbf{i}}_2$	$\bar{\mathbf{i}}_3$	
$\mathbf{r}^2$	$\mathbf{r}^2$	<b>1</b>	$\mathbf{r}^1$	$\mathbf{i}_2$	$\mathbf{i}_3$	$\mathbf{i}_1$	$\bar{\mathbf{r}}^1$	$\bar{\mathbf{r}}^1$	$\bar{\mathbf{1}}$	$\bar{\mathbf{r}}^2$	$\bar{\mathbf{i}}_3$	$\bar{\mathbf{i}}_1$	$\bar{\mathbf{i}}_2$	
$\mathbf{r}^1$	$\mathbf{r}^1$	$\mathbf{r}^2$	<b>1</b>	$\mathbf{i}_3$	$\mathbf{i}_1$	$\mathbf{i}_2$	$\bar{\mathbf{r}}^2$	$\bar{\mathbf{r}}^2$	$\bar{\mathbf{r}}^1$	$\bar{\mathbf{1}}$	$\bar{\mathbf{i}}_2$	$\bar{\mathbf{i}}_3$	$\bar{\mathbf{i}}_1$	
$\mathbf{i}_1$	$\mathbf{i}_1$	$\mathbf{i}_2$	$\mathbf{i}_3$	<b>1</b>	$\mathbf{r}^1$	$\mathbf{r}^2$	$\bar{\mathbf{i}}_1$	$\bar{\mathbf{i}}_1$	$\bar{\mathbf{i}}_3$	$\bar{\mathbf{i}}_2$	$\bar{\mathbf{1}}$	$\bar{\mathbf{r}}^1$	$\bar{\mathbf{r}}^2$	
$\mathbf{i}_2$	$\mathbf{i}_2$	$\mathbf{i}_3$	$\mathbf{i}_1$	$\mathbf{r}^2$	<b>1</b>	$\mathbf{r}^1$	$\bar{\mathbf{i}}_2$	$\bar{\mathbf{i}}_2$	$\bar{\mathbf{i}}_1$	$\bar{\mathbf{i}}_3$	$\bar{\mathbf{r}}^2$	$\bar{\mathbf{1}}$	$\bar{\mathbf{r}}^1$	
$\mathbf{i}_3$	$\mathbf{i}_3$	$\mathbf{i}_1$	$\mathbf{i}_2$	$\mathbf{r}^1$	$\mathbf{r}^2$	<b>1</b>	$\bar{\mathbf{i}}_3$	$\bar{\mathbf{i}}_3$	$\bar{\mathbf{i}}_2$	$\bar{\mathbf{i}}_1$	$\bar{\mathbf{r}}^1$	$\bar{\mathbf{r}}^2$	$\bar{\mathbf{1}}$	

The over-bar notation is used for a *dual-group*  $\bar{D}_3 = [\bar{\mathbf{1}}, \bar{\mathbf{r}}^1, \bar{\mathbf{r}}^2, \bar{\mathbf{i}}_1, \bar{\mathbf{i}}_2, \bar{\mathbf{i}}_3]$  of “body”-based operators isomorphic to the usual “lab”-based group. Matrix representations

(4.28a) for  $D_3$  or matrices (4.28b) for  $\bar{D}_3$  are given, respectively, by  $\mathbf{g}^\dagger \mathbf{g}$  or  $\mathbf{g} \mathbf{g}^\dagger$ -forms



Most pairs of resulting  $D_3$  matrices in (4.28a) do not commute. (For example  $(\mathbf{r}^1)(\mathbf{i}_1)=(\mathbf{i}_3)$  does not equal  $(\mathbf{i}_1)(\mathbf{r}^1)=(\mathbf{i}_2)$ .) Identical non-commutative product rules apply to the dual bar group  $\bar{D}_3$  matrices in (4.28b). However, all matrices of the latter  $\bar{D}_3$  commute with all matrices of the former  $D_3$ . This suggests that the Hamiltonian matrix, in order to commute with its symmetry group  $D_3$ , is constructed by linear combination of bar group operators of  $\bar{D}_3$  [6].

$$\mathbf{H} = r_0\bar{\mathbf{I}} + r_1\bar{\mathbf{r}}^1 + r_2\bar{\mathbf{r}}^2 + i_1\bar{\mathbf{i}}_1 + i_2\bar{\mathbf{i}}_2 + i_3\bar{\mathbf{i}}_3 \quad (4.29)$$

The resulting  $D_3$  symmetric ( $\mathbf{H}$ ) matrix generalizes the  $C_6$  symmetric ( $\mathbf{H}$ ) matrix in (4.8) to non-Abelian symmetry.

$$(\mathbf{H}) = \sum_{g=1}^{\circ G} r_g(\bar{\mathbf{g}}) = \begin{pmatrix} r_0 & r_2 & r_1 & i_1 & i_2 & i_3 \\ r_1 & r_0 & r_2 & i_3 & i_1 & i_2 \\ r_2 & r_1 & r_0 & i_2 & i_3 & i_1 \\ i_i & i_3 & i_2 & r_0 & r_1 & r_2 \\ i_2 & i_1 & i_3 & r_2 & r_0 & r_1 \\ i_3 & i_2 & i_1 & r_1 & r_2 & r_0 \end{pmatrix} \quad (4.30)$$

#### 4.4.2 Spectral resolution of $D_3$ symmetry operators

Spectral resolution of  $D_3$  or any non-Abelian group  $G = [\dots\mathbf{g}_1, \mathbf{g}_2\dots]$  entails more than the  $C_6$  expansion into a unique combination of idempotent operators  $\mathbf{P}^\alpha = |\alpha\rangle\langle\alpha|$  multiplied by eigenvalue  $D^{(\alpha)}(g)$  coefficients as in (4.11). It is not possible to diagonalize two non-commuting  $\mathbf{g}_1$  and  $\mathbf{g}_2$  in one basis since numbers (eigenvalues) always commute. If  $\mathbf{g}_1$  and  $\mathbf{g}_2$  do not commute, their collective resolution must include eigenmatrix coefficients  $D_{m,n}^\alpha$  involving *nilpotent* ( $\mathbf{N}^2 = \mathbf{0}$ ) operators  $\mathbf{P}_{m,n}^\alpha = |\alpha_m\rangle\langle\alpha_n|$  as well as idempotent ( $\mathbf{I}^2 = \mathbf{I}$ ) operators  $\mathbf{P}_{m,m}^\alpha = |\alpha_m\rangle\langle\alpha_m|$  seen in (4.11).

Unlike a commutative algebra of  $C_n$  idempotents, which are shown in (4.13) and



uniquely defined by (4.18), a non-Abelian algebra yields a panoply of equivalent choices of  $\mathbf{P}$  operators that resolve it. The number and types of these  $\mathbf{P}$ 's is uniquely determined by size and structure of certain key commuting sub-algebras. The key to symmetry analysis of quantum physics is to first sort out the operators and algebras that commute from those that do not. It amounts to a kind of symmetry analysis of symmetry and leads to a far greater diversity than is found in commutative Abelian systems.

### Sorting commuting subalgebras: Rank and commuting observables

The *rank*  $\rho(G)$  of a  $G$ -algebra is the maximal number of *mutually-commuting* operators available by linearly combining the  ${}^oG$  operators  $\mathbf{g}_k$  of symmetry group  $G$ .  $\rho(G)$  is also the greatest number of orthogonal idempotents  $\mathbf{P}^m$  that can resolve the  $G$ -identity  $\mathbf{1}$  as in Eq (4.12). ( ${}^oG$  is total number or *order* of  $G$ . Here  ${}^oD_3$  and  ${}^oC_6$  both equal 6.)

$C_6$  rank is obviously equal to its order ( $\rho(C_6) = 6$ ), but the rank of  $D_3$  turns out to be only four ( $\rho(D_3) = 4$ ). As shown below,  $D_3$  can have no more than four  $\mathbf{P}$ -operators that *mutually* commute though there exist quite different sets of them. On the other hand,  $D_3$  has just *three* linearly independent  $\mathbf{P}^\alpha$ -operators that commute with *all* of  $D_3$ , and there is but *one* invariant set of them just as there is but one set of  $\mathbf{P}^{(m)}$  for  $C_6$  in Eq (4.18).

Rank is a key quantum concept since it is the total number of commuting observables, the operators that label and define eigenstates. Of primary importance are  $G$ -invariant labeling operators  $\mathbf{I}_G$  that commute with *all*  $\mathbf{g}$  and not just with other labeling operators.  $\mathbf{I}_G$  are uniquely defined within their group  $G$  and invariant to all  $\mathbf{g}$ . ( $\mathbf{g}\mathbf{I}_G\mathbf{g}^{-1}=\mathbf{I}_G$ ) For example, total angular momentum  $\mathbf{J}^2$  and e-values  $J(J+1)$  are  $R(3)$ -invariant .

Next in importance are labeling operators  $[\mathbf{I}_{H_{n-1}}, \mathbf{I}_{H_{n-2}}, \dots, \mathbf{I}_{H_1}]$  belonging to nested subgroups of  $G=H_n$  in a *subgroup chain*  $G \supset H_{n-1} \supset H_{n-2} \supset \dots H_1$ . Multiple choices of

chains exists since each subgroup link  $H_k$  is not uniquely determined by the  $H_{k+1}$  that contains it, but each  $\mathbf{I}_{H_k}$  is invariant to all possible  $H_{j \leq k}$  at level- $k$  or below.

For example, the  $z$ -axial momentum  $\mathbf{J}_z$  and its e-values  $m_z$  belong to a  $2^{nd}$  link in chain- $R(3) \supset R(2_z) \supset C_6(z)$ . Given  $R(3)$  there are an infinity of  $R(2)$  subgroups besides the one for  $z$ -axis of quantization.  $\mathbf{J}_x$  or  $\mathbf{J}_y$  are just two of an infinite number of possible alternatives to  $\mathbf{J}_z$ . Each  $R(2_\zeta)$  has an infinite number of cyclic  $C_n(\zeta)$  sub-subgroups.

### Sorting commuting subalgebras: Centrum and class invariants

The *centrum*  $\kappa(G)$  of a  $G$ -algebra is the number of *all-commuting* operators available by combining  $\mathbf{g}_k$ . It is also the number of  $G$ -invariant  $\mathbf{P}^\alpha$ -operators. Students of group theory know  $\kappa(G)$  as the number of equivalence *classes* of group  $G$ .  $D_3$  elements in Fig. 4.5 are separated into three classes of elements  $[\mathbf{1}], [\mathbf{r}^1, \mathbf{r}^2]$ , and  $[\mathbf{i}_1, \mathbf{i}_2, \mathbf{i}_3]$ . ( $\kappa(D_3) = 3$ )

Elements in each class are related through transformation  $\mathbf{g}_1 = \mathbf{g}_t \mathbf{g}_2 \mathbf{g}_t^{-1}$  by  $\mathbf{g}_t$  in group  $G$ . Sum  $\kappa_{\mathbf{k}}$  of  ${}^o c_k$  elements in  $\mathbf{g}_k$ 's class is invariant to  $\mathbf{g}_t$  transformation. (It only permutes  $\mathbf{g}_k$ -terms in  $\kappa_{\mathbf{k}}$  thus  $\kappa_{\mathbf{k}}$  commutes with all  $\mathbf{g}_t$  in  $G$ .)

$$\mathbf{g}_t \kappa_{\mathbf{k}} \mathbf{g}_t^{-1} = \kappa_{\mathbf{k}} \text{ where: } \kappa_{\mathbf{k}} = \sum_{j=1}^{j={}^o c_k} \mathbf{g}_j = 1/{}^o s_k \sum_{t=1}^{t={}^o G} \mathbf{g}_t \mathbf{g}_k \mathbf{g}_t^{-1} \quad (4.31)$$

The product table for  $D_3$  class algebra  $[\kappa_1 = \mathbf{1}, \kappa_2 = \mathbf{r}^1 + \mathbf{r}^2, \kappa_3 = \mathbf{i}_1 + \mathbf{i}_2 + \mathbf{i}_3]$  in Eq (4.32) below follows by inspecting  $D_3$  group product tables in Fig. 4.5 or (4.27). It is a commutative algebra since each  $\kappa_j$  commutes with each  $\kappa_{\mathbf{k}}$  as well as with each

$\mathbf{g}_t$ . This guarantees a class algebra has a unique and invariant spectral resolution.

$\mathbf{1}$	$\mathbf{r}^1$	$\mathbf{r}^2$	$\mathbf{i}_1$	$\mathbf{i}_2$	$\mathbf{i}_3$
$\mathbf{r}^2$	$\mathbf{1}$	$\mathbf{r}^1$	$\mathbf{i}_2$	$\mathbf{i}_3$	$\mathbf{i}_1$
$\mathbf{r}^1$	$\mathbf{r}^2$	$\mathbf{1}$	$\mathbf{i}_3$	$\mathbf{i}_1$	$\mathbf{i}_2$
$\mathbf{i}_1$	$\mathbf{i}_2$	$\mathbf{i}_3$	$\mathbf{1}$	$\mathbf{r}^1$	$\mathbf{r}^2$
$\mathbf{i}_2$	$\mathbf{i}_3$	$\mathbf{i}_1$	$\mathbf{r}^2$	$\mathbf{1}$	$\mathbf{r}^1$
$\mathbf{i}_3$	$\mathbf{i}_1$	$\mathbf{i}_2$	$\mathbf{r}^1$	$\mathbf{r}^2$	$\mathbf{1}$

 $\rightarrow$ 

$\kappa_1 = \mathbf{1}$	$\kappa_2 = \mathbf{r}^1 + \mathbf{r}^2$	$\kappa_3 = \mathbf{i}_1 + \mathbf{i}_2 + \mathbf{i}_3$
$\kappa_2$	$2\kappa_1 + \kappa_2$	$2\kappa_3$
$\kappa_3$	$2\kappa_3$	$3\kappa_1 + 3\kappa_2$

(4.32)

The first sum in Eq (4.31) is over the  ${}^o c_k$  elements in  $\mathbf{g}_k$ 's class. ( ${}^o c_k$  is order of  $\kappa_k$ .) The second sum is over all  ${}^o G$  group elements. The number of elements  $\mathbf{g}_t$  that commute with  $\mathbf{g}_k$  is  ${}^o s_k$ , the order of  $\mathbf{g}_k$ 's self-symmetry  $s_k$ . Each group operator  $\mathbf{g}_k$  has a self-symmetry group consisting of (at least) the identity  $\mathbf{1}$  and powers  $(\mathbf{g}_k)^p$  of itself. The order of class- $k$  is the (integer) fraction  ${}^o c_k = {}^o G / {}^o s_k$ .

**Resolving all-commuting class subalgebra: centrum= $\kappa(D_3) = 3$**

Spectral resolution gives class-sum operators  $\kappa_1$ ,  $\kappa_2$ , and  $\kappa_3$  as combinations of three  $D_3$ -invariant  $\mathbf{P}^\alpha$ -operators with each of the  $\kappa_k$  eigenvalues as coefficients. The  $\kappa_3$  characteristic equation found by (4.32) gives three  $\mathbf{P}^\alpha$  directly.

$$\begin{aligned}
0 &= \kappa_3^3 - 9\kappa_3 = (\kappa_3 - 3 \cdot \mathbf{1})(\kappa_3 + 3 \cdot \mathbf{1})(\kappa_3 + 0 \cdot \mathbf{1}) \\
&= (\kappa_3 - 3 \cdot \mathbf{1})\mathbf{P}^{A_1} = (\kappa_3 + 3 \cdot \mathbf{1})\mathbf{P}^{A_2} = (\kappa_3 - 0 \cdot \mathbf{1})\mathbf{P}^E
\end{aligned}
\tag{4.33}$$

Standard notation  $A_1$ ,  $A_2$ , and  $E$  is used for the three invariant idempotents  $\mathbf{P}^\alpha$ .

$$\begin{aligned}
\kappa_1 &= 1 \cdot \mathbf{P}^{A_1} + 1 \cdot \mathbf{P}^{A_2} + 1 \cdot \mathbf{P}^E \\
\kappa_2 &= 2 \cdot \mathbf{P}^{A_1} - 2 \cdot \mathbf{P}^{A_2} - 1 \cdot \mathbf{P}^E \\
\kappa_3 &= 3 \cdot \mathbf{P}^{A_1} - 3 \cdot \mathbf{P}^{A_2} + 0 \cdot \mathbf{P}^E \\
\mathbf{P}^{A_1} &= (\kappa_1 + \kappa_2 + \kappa_3)/6 = (\mathbf{1} + \mathbf{r}^1 + \mathbf{r}^2 + \mathbf{i}_1 + \mathbf{i}_2 + \mathbf{i}_3)/6 \\
\mathbf{P}^{A_2} &= (\kappa_1 + \kappa_2 - \kappa_3)/6 = (\mathbf{1} + \mathbf{r}^1 + \mathbf{r}^2 - \mathbf{i}_1 - \mathbf{i}_2 - \mathbf{i}_3)/6 \\
\mathbf{P}^E &= (2\kappa_1 - \kappa_2)/3 = (2\mathbf{1} - \mathbf{r}^1 - \mathbf{r}^2)/3
\end{aligned} \tag{4.34}$$

Traces of  $D_3$  matrices ( $\mathbf{g}_k$ ) in (4.28a) are zero excepting  $Trace(\mathbf{1}) = 6$ . Traces of ( $\mathbf{P}^\alpha$ ) then follow.

$$trace\mathbf{P}^{A_1} = 1, \quad trace\mathbf{P}^{A_2} = 1, \quad trace\mathbf{P}^E = 4. \tag{4.35}$$

This means ( $\mathbf{P}^{A_1}$ ) and ( $\mathbf{P}^{A_2}$ ) are each 1-by-1 projectors while ( $\mathbf{P}^E$ ) splits into two 2-by-2 projectors. The latter splitting is not uniquely defined until subgroup chain  $D_3 \supset C_3$  or a particular  $D_3 \supset C_2$  chain is chosen, but relations in (4.34) are invariant and unique. The  $\kappa_k$  coefficients inside parentheses of  $\mathbf{P}^\alpha$  expansion give the  $D_3$  character table for traces of irreducible representations (irreps). Irrep dimension  $\ell^\alpha$  is trace of the  $\alpha^{th}$ -irrep of identity  $\mathbf{g}_1 = \mathbf{1}$ .

$D_3$	$\kappa_1$	$\kappa_2$	$\kappa_3$
$A_1$	1	1	1
$A_2$	1	1	-1
$E$	2	-1	0

$$\chi_k^\alpha = Trace D^\alpha(\mathbf{g}_k), \quad \ell^\alpha = \chi_1^\alpha = Trace D^\alpha(\mathbf{1})$$

(4.36)

**Resolving maximal mutually commuting subalgebra: rank= $\rho(D_3) = 4$**

Completing resolution of  $D_3$  uses a product of two completeness relations, the resolution of class identity  $\kappa_1 = \mathbf{1}$  in Eq (4.34) with the identity resolution of a  $D_3$  subgroup  $C_3 = [\mathbf{1}, \mathbf{r}^1, \mathbf{r}^2]$  or else  $C_2 = [\mathbf{1}, \mathbf{i}_3]$ . In either case invariant  $\mathbf{P}^E$  splits but  $\mathbf{P}^{A_1}$  and  $\mathbf{P}^{A_2}$  do not. In Eq (4.37)  $\mathbf{P}^E$  is split by  $C_2$  into plane-polarizing projectors  $\mathbf{P}_{x,x}^E + \mathbf{P}_{y,y}^E = \mathbf{P}_{0_2 0_2}^E + \mathbf{P}_{1_2 1_2}^E$ .

$$\left[ \begin{array}{c} D_3 \left( \begin{array}{l} \text{class algebra} \\ \text{completeness} \end{array} \right) \\ \mathbf{1} = \mathbf{P}^{A_1} + \mathbf{P}^{A_2} + \mathbf{P}^E \end{array} \right] \cdot \left[ \begin{array}{c} C_2 \left( \begin{array}{l} \text{subgroup} \\ \text{completeness} \end{array} \right) \\ \mathbf{1} = \mathbf{P}^{0_2} + \mathbf{P}^{1_2} \end{array} \right] = \left[ \begin{array}{c} D_3 \left( \begin{array}{l} \text{group} \\ \text{completeness} \end{array} \right) \\ \mathbf{1} = \mathbf{P}_{0_2 0_2}^{A_1} + \mathbf{P}_{1_2 1_2}^{A_2} \\ + \mathbf{P}_{0_2 0_2}^E + \mathbf{P}_{1_2 1_2}^E \end{array} \right]$$

where :

$$\begin{aligned} \mathbf{P}^{A_1} &= \mathbf{P}_{0_2 0_2}^{A_1} = (\mathbf{1} + \mathbf{r}^1 + \mathbf{r}^2 + \mathbf{i}_1 + \mathbf{i}_2 + \mathbf{i}_3)/6 = \mathbf{P}^{A_1} \mathbf{P}^{0_2} \\ \mathbf{P}^{A_2} &= \mathbf{P}_{1_2 1_2}^{A_2} = (\mathbf{1} + \mathbf{r}^1 + \mathbf{r}^2 - \mathbf{i}_1 - \mathbf{i}_2 - \mathbf{i}_3)/6 = \mathbf{P}^{A_2} \mathbf{P}^{1_2} \quad (\text{All other} \\ \mathbf{P}_{x,x}^E &= \mathbf{P}_{0_2 0_2}^E = (2\mathbf{1} - \mathbf{r}^1 - \mathbf{r}^2 - \mathbf{i}_1 - \mathbf{i}_2 + 2\mathbf{i}_3)/6 = \mathbf{P}^E \mathbf{P}^{0_2} \quad \mathbf{P}^\alpha \mathbf{P}^{m_2} = \mathbf{0}) \\ \mathbf{P}_{y,y}^E &= \mathbf{P}_{1_2 1_2}^E = (2\mathbf{1} - \mathbf{r}^1 - \mathbf{r}^2 + \mathbf{i}_1 + \mathbf{i}_2 - 2\mathbf{i}_3)/6 = \mathbf{P}^E \mathbf{P}^{1_2} \end{aligned} \tag{4.37}$$

In (4.38)  $\mathbf{P}^E$  is split by  $C_3$  into Right and Left circular-polarized projectors  $\mathbf{P}_{R,R}^E + \mathbf{P}_{L,L}^E = \mathbf{P}_{1_3 1_3}^E + \mathbf{P}_{2_3 2_3}^E$ .

$$\left[ \begin{array}{c} D_3 \left( \begin{array}{l} \text{class algebra} \\ \text{completeness} \end{array} \right) \\ \mathbf{1} = \mathbf{P}^{A_1} + \mathbf{P}^{A_2} + \mathbf{P}^E \end{array} \right] \cdot \left[ \begin{array}{c} C_3 \left( \begin{array}{l} \text{subgroup} \\ \text{completeness} \end{array} \right) \\ \mathbf{1} = \mathbf{P}^{0_3} + \mathbf{P}^{1_3} + \mathbf{P}^{2_3} \end{array} \right] = \left[ \begin{array}{c} D_3 \left( \begin{array}{l} \text{group} \\ \text{completeness} \end{array} \right) \\ \mathbf{1} = \mathbf{P}_{0_3 0_3}^{A_1} + \mathbf{P}_{0_3 0_3}^{A_2} \\ + \mathbf{P}_{1_3 1_3}^E + \mathbf{P}_{2_3 2_3}^E \end{array} \right]$$

where :

$$\begin{aligned} \mathbf{P}^{A_1} &= \mathbf{P}_{0_3 0_3}^{A_1} = (\mathbf{1} + \mathbf{r}^1 + \mathbf{r}^2 + \mathbf{i}_1 + \mathbf{i}_2 + \mathbf{i}_3)/6 = \mathbf{P}^{A_1} \mathbf{P}^{0_3} \\ \mathbf{P}^{A_2} &= \mathbf{P}_{0_3 0_3}^{A_2} = (\mathbf{1} + \mathbf{r}^1 + \mathbf{r}^2 - \mathbf{i}_1 - \mathbf{i}_2 - \mathbf{i}_3)/6 = \mathbf{P}^{A_2} \mathbf{P}^{0_3} \\ \mathbf{P}_{R,R}^E &= \mathbf{P}_{1_3 1_3}^E = (\mathbf{1} + \varepsilon \mathbf{r}^1 + \varepsilon^* \mathbf{r}^2) / 3 = \mathbf{P}^E \mathbf{P}^{1_3} \\ \mathbf{P}_{L,L}^E &= \mathbf{P}_{2_3 2_3}^E = (\mathbf{1} + \varepsilon^* \mathbf{r}^1 + \varepsilon \mathbf{r}^2) / 3 = \mathbf{P}^E \mathbf{P}^{2_3} \end{aligned} \quad \begin{array}{l} \text{(All other} \\ \mathbf{P}^\alpha \mathbf{P}^{m_3} = \mathbf{0}) \\ \varepsilon = e^{i2\pi/3} \end{array} \quad (4.38)$$

In (4.37) and (4.38), neither  $\mathbf{P}^{A_1}$  nor  $\mathbf{P}^{A_2}$  split or change except to acquire some  $C_2$  or  $C_3$  labels. The total number (four) of irreducible idempotents after either complete splitting is the same group rank noted before:  $\rho(D_3)=4$ . But, the  $RL$ -circularly polarized pairs  $\mathbf{P}_{R,R}^E$  and  $\mathbf{P}_{L,L}^E$  split-out by  $C_3=[\mathbf{1}, \mathbf{r}^1, \mathbf{r}^2]$  differ from the linear  $xy$ -polarized pairs  $\mathbf{P}_{x,x}^E$  and  $\mathbf{P}_{y,y}^E$  split-out by  $C_2=[\mathbf{1}, \mathbf{i}_3]$ .  $\mathbf{P}_{x,x}^E$  and  $\mathbf{P}_{y,y}^E$  are, respectively, parallel (symmetric  $\mathbf{i}_3 \mathbf{P}_x^E = +\mathbf{P}_x^E$ ) and anti-parallel (anti-symmetric  $\mathbf{i}_3 \mathbf{P}_y^E = -\mathbf{P}_y^E$ ) to  $x$ -axial  $180^\circ$  rotation  $\mathbf{i}_3$  in Fig. 4.5 and will be used in examples.

### Final resolutions of non-commuting algebra: ${}^o(D_3) = 6$

Mutually commuting algebras resolve into ( $\mathbf{I}^2 = \mathbf{I}$ ) operators  $\mathbf{P}_{m,m}^\alpha = |\alpha_m\rangle \langle \alpha_m|$  that sum to identity operator  $\mathbf{1}$ . They are split using the “one-equals-one-times-one” ( $\mathbf{1}=\mathbf{1}\cdot\mathbf{1}$ ) trick in (4.37) and (4.38).

Non-commuting algebras resolve into idempotents and nilpotent ( $\mathbf{N}^2 = \mathbf{0}$ ) operators  $\mathbf{P}_{m,n}^\alpha = |\alpha_m\rangle \langle \alpha_n|$  that are split out using the following “operator-equals-one-times-operator-times-one” ( $\mathbf{g}=\mathbf{1}\cdot\mathbf{g}\cdot\mathbf{1}$ ) trick. It is only necessary that  $\mathbf{1}$  be resolved into

rank-number  $\rho$  of irreducible idempotents as in Eq (4.37) or (4.38). (Here  $\rho(D_3) = 4$ .)

$$\mathbf{g} = \mathbf{1} \cdot \mathbf{g} \cdot \mathbf{1} = (\mathbf{P}_{x,x}^{A_1} + \mathbf{P}_{y,y}^{A_2} + \mathbf{P}_{x,x}^E + \mathbf{P}_{y,y}^E) \cdot \mathbf{g} \cdot (\mathbf{P}_{x,x}^{A_1} + \mathbf{P}_{y,y}^{A_2} + \mathbf{P}_{x,x}^E + \mathbf{P}_{y,y}^E) \quad (4.39)$$

The product in (4.39) could have sixteen terms, but only six survive due to idempotent orthogonality  $\mathbf{P}_{j,j}^\alpha \mathbf{P}_{k,k}^\beta = \delta^{\alpha,\beta} \delta_{j,k} \mathbf{P}_{j,j}^\alpha$ , and the fact that both  $\mathbf{P}^{A_1}$  and  $\mathbf{P}^{A_2}$  remain invariant and commute with all  $\mathbf{P}_{j,j}^\alpha$  and all  $\mathbf{g}$ .

$$\begin{aligned} \mathbf{g} = & \mathbf{P}^{A_1} \cdot \mathbf{g} \cdot \mathbf{P}^{A_1} + \mathbf{P}^{A_2} \cdot \mathbf{g} \cdot \mathbf{P}^{A_2} + \mathbf{P}_{x,x}^E \cdot \mathbf{g} \cdot \mathbf{P}_{x,x}^E + \mathbf{P}_{x,x}^E \cdot \mathbf{g} \cdot \mathbf{P}_{y,y}^E \\ & + \mathbf{P}_{y,y}^E \cdot \mathbf{g} \cdot \mathbf{P}_{x,x}^E + \mathbf{P}_{y,y}^E \cdot \mathbf{g} \cdot \mathbf{P}_{y,y}^E \end{aligned} \quad (4.40)$$

This reduces to a non-Abelian spectral resolution of  $D_3$  that generalizes resolution (4.11) of Abelian  $C_6$  and includes two nilpotent projectors  $\mathbf{P}_{j,k}^\alpha$  multiplied by off-diagonal irrep matrix components  $D_{j,k}^\alpha$  as well as the four idempotents  $\mathbf{P}_{j,j}^\alpha$  with their diagonal irrep matrix coefficients  $D_{j,j}^\alpha$  that are not altogether unlike the  $D^{(m)}(\mathbf{r}^p) \mathbf{P}^{(m)}$  terms in (4.11).

$$\mathbf{g} = \sum_{\text{irreps } (\alpha)} \sum_{j=1}^{\ell^\alpha} \sum_{k=1}^{\ell^\alpha} D_{j,k}^\alpha(g) \mathbf{P}_{j,k}^\alpha \quad (4.41a)$$

$$\begin{aligned} \mathbf{g} = & D^{A_1}(g) \mathbf{P}^{A_1} + D^{A_2}(g) \mathbf{P}^{A_2} + D_{x,x}^E(g) \mathbf{P}_{x,x}^E + D_{x,y}^E(g) \mathbf{P}_{x,y}^E \\ & + D_{y,x}^E(g) \mathbf{P}_{y,x}^E + D_{y,y}^E(g) \mathbf{P}_{y,y}^E \end{aligned} \quad (4.41b)$$

$$\text{where } \mathbf{P}_{j,j}^\alpha \cdot \mathbf{g} \cdot \mathbf{P}_{j,j}^\alpha = D_{j,j}^\alpha(g) \mathbf{P}_{j,j}^\alpha \quad \mathbf{P}_{j,j}^\alpha \cdot \mathbf{g} \cdot \mathbf{P}_{k,k}^\alpha = D_{j,k}^\alpha(g) \mathbf{P}_{j,k}^\alpha$$

Terms  $(1/n) D^{(m)*}(\mathbf{r}^p) \mathbf{r}^p$  in Eq (4.18) that give  $\mathbf{P}^{(m)}$  of  $C_n$  in Eq (4.11) generalize to non-Abelian  $\mathbf{P}_{j,k}^\alpha$  and invert (4.41a) to (4.42).

$$\mathbf{P}_{j,k}^\alpha = (\ell^\alpha / {}^oG) \sum_{g=1}^{{}^oG} D_{j,k}^{\alpha*}(g) \mathbf{g} \quad (4.42)$$

$D_3$  resolution in (4.41b) has two irreps  $D^{A_1}$  and  $D^{A_2}$  of dimension  $\ell^{A_1}=1=\ell^{A_2}$  and a third irrep  $D^E$  of dimension  $\ell^E=2$  as noted in the first column of the character array in (4.36). The irrep dimensions are related to the centrum  $\kappa(D_3)=3$ , rank  $\rho(D_3)=4$ , and order  $oD_3=6$ . The following power sums of  $\ell^\alpha$  apply to any finite group  $G$ .

$$\begin{aligned}
G - \text{centrum} : \quad \kappa(G) &= \sum_{\text{irrep}(\alpha)} (\ell^\alpha)^0 = \text{Number of classes, invariants or irrep types} \\
G - \text{rank} : \quad \rho(G) &= \sum_{\text{irrep}(\alpha)} (\ell^\alpha)^1 = \text{Number of mutually commuting observables} \\
G - \text{order} : \quad o(G) &= \sum_{\text{irrep}(\alpha)} (\ell^\alpha)^2 = \text{Number of symmetry operators}
\end{aligned} \tag{4.43}$$

#### 4.4.3 Spectral resolution of dual groups $D_3$ and $\bar{D}_3$

Spectral resolution shown in (4.41a) and (4.42) of non-Abelian group  $G$  reduce  $\mathbf{g}\cdot\mathbf{h}$ -product tables in (4.27) to  $P$ -projector algebra.

$$\mathbf{P}_{jk}^\alpha \mathbf{P}_{j'k'}^\beta = \delta^{\alpha\beta} \delta_{kj'} \mathbf{P}_{jk'}^\alpha \tag{4.44}$$

Product tables in Eq (4.45) for  $D_3$  projectors  $\mathbf{P}_{jk}^\alpha$  generalize the  $C_6$  idempotent table in (4.13). Non-commutativity entails a pair of tables like the  $\mathbf{g}^\dagger\mathbf{g}$  form and  $\mathbf{g}\mathbf{g}^\dagger$ -forms in (4.27) for “lab”  $\mathbf{g}$  and “body”  $\bar{\mathbf{g}}$  operators. Tables in (4.27) differ by switching conjugate pair  $\mathbf{r}^1$  and  $\mathbf{r}^2$  on side and top. ( $\mathbf{r}^{1\dagger} = \mathbf{r}^2$ ) The rest are self conjugate. ( $\mathbf{i}_1^\dagger = \mathbf{i}_1, \text{etc.}$ ) Similarly, tables in (4.45) differ by switching conjugate nilpotent pair  $\mathbf{P}_{xy}^E$  and  $\mathbf{P}_{yx}^E$ . ( $\mathbf{P}_{xy}^{E\dagger} = \mathbf{P}_{yx}^E$ ) The rest are self-conjugate. ( $\mathbf{P}_{jj}^{\alpha\dagger} = \mathbf{P}_{jj}^\alpha$ )



$\mathbf{p}^\dagger \mathbf{p}$ <i>form</i>	$\mathbf{P}^{A_1}_{xx}$	$\mathbf{P}^{A_2}_{yy}$	$\mathbf{P}^{E_1}_{xx}$	$\mathbf{P}^{E_1}_{xy}$	$\mathbf{P}^{E_1}_{yx}$	$\mathbf{P}^{E_1}_{yy}$
$\mathbf{P}^{A_1}_{xx}$	$\mathbf{P}^{A_1}_{xx}$	.	.	.	.	.
$\mathbf{P}^{A_2}_{yy}$	.	$\mathbf{P}^{A_2}_{yy}$	.	.	.	.
$\mathbf{P}^{E_1}_{xx}$	.	.	$\mathbf{P}^{E_1}_{xx}$	$\mathbf{P}^{E_1}_{xy}$	.	.
$\mathbf{P}^{E_1}_{yx}$	.	.	$\mathbf{P}^{E_1}_{yx}$	$\mathbf{P}^{E_1}_{yy}$	.	.
$\mathbf{P}^{E_1}_{xy}$	.	.	.	.	$\mathbf{P}^{E_1}_{xx}$	$\mathbf{P}^{E_1}_{xy}$
$\mathbf{P}^{E_1}_{yy}$	.	.	.	.	$\mathbf{P}^{E_1}_{yx}$	$\mathbf{P}^{E_1}_{yy}$

$\mathbf{p} \mathbf{p}^\dagger$ <i>form</i>	$\mathbf{P}^{A_1}_{xx}$	$\mathbf{P}^{A_2}_{yy}$	$\mathbf{P}^{E_1}_{xx}$	$\mathbf{P}^{E_1}_{yx}$	$\mathbf{P}^{E_1}_{xy}$	$\mathbf{P}^{E_1}_{yy}$
$\mathbf{P}^{A_1}_{xx}$	$\mathbf{P}^{A_1}_{xx}$	.	.	.	.	.
$\mathbf{P}^{A_2}_{yy}$	.	$\mathbf{P}^{A_2}_{yy}$	.	.	.	.
$\mathbf{P}^{E_1}_{xx}$	.	.	$\mathbf{P}^{E_1}_{xx}$	.	$\mathbf{P}^{E_1}_{xy}$	.
$\mathbf{P}^{E_1}_{xy}$	.	.	.	$\mathbf{P}^{E_1}_{xx}$	.	$\mathbf{P}^{E_1}_{xy}$
$\mathbf{P}^{E_1}_{yx}$	.	.	$\mathbf{P}^{E_1}_{yx}$	.	$\mathbf{P}^{E_1}_{yy}$	.
$\mathbf{P}^{E_1}_{yy}$	.	.	.	$\mathbf{P}^{E_1}_{yx}$	.	$\mathbf{P}^{E_1}_{yy}$

(4.45)

The  $\mathbf{p}^\dagger \mathbf{p}$  and  $\mathbf{p} \mathbf{p}^\dagger$  tables in (4.45) give commuting representations of projector  $\mathbf{P}^\alpha_{jk}$  just as  $\mathbf{g}^\dagger \mathbf{g}$  and  $\mathbf{g} \mathbf{g}^\dagger$  tables in (4.27) give commuting  $(\mathbf{g})_G$ -matrices in (4.28a). Wherever  $\mathbf{P}^\alpha_{jk}$  appears in a table, a “1” is put in its  $(\mathbf{p})$ -matrix. Putting “ $D^\alpha_{jk}(g)$ ” at each  $\mathbf{P}^\alpha_{jk}$  spot instead gives the following  $\mathbf{p}^\dagger \mathbf{p}$ -representation  $(\mathbf{g})_P$  of  $\mathbf{g}$  since it is a sum of

$D_{jk}^\alpha(g)\mathbf{P}_{jk}^\alpha$  in Eq (4.41a).

$$\begin{aligned}
(\mathbf{g})_P &= T(\mathbf{g})_G T^\dagger = \\
&\begin{pmatrix}
|\mathbf{P}_{xx}^{A_1}\rangle & |\mathbf{P}_{yy}^{A_2}\rangle & |\mathbf{P}_{xx}^{E_1}\rangle & |\mathbf{P}_{yx}^{E_1}\rangle & |\mathbf{P}_{xy}^{E_1}\rangle & |\mathbf{P}_{yy}^{E_1}\rangle \\
D^{A_1}(g) & \cdot & \cdot & \cdot & \cdot & \cdot \\
\cdot & D^{A_2}(g) & \cdot & \cdot & \cdot & \cdot \\
\cdot & \cdot & D_{xx}^{E_1}(g) & D_{xy}^{E_1}(g) & \cdot & \cdot \\
\cdot & \cdot & D_{yx}^{E_1}(g) & D_{yy}^{E_1}(g) & \cdot & \cdot \\
\cdot & \cdot & \cdot & \cdot & D_{xx}^{E_1}(g) & D_{xy}^{E_1}(g) \\
\cdot & \cdot & \cdot & \cdot & D_{yx}^{E_1}(g) & D_{yy}^{E_1}(g)
\end{pmatrix} \tag{4.46}
\end{aligned}$$

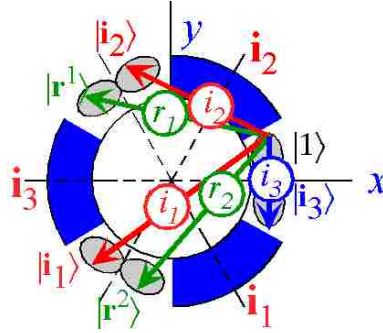
Conjugate  $\mathbf{pp}^\dagger$ -representation  $(\bar{\mathbf{g}})_P$  of  $\bar{\mathbf{g}}$  has complex conjugate “ $D_{jk}^{\alpha*}(g)$ ” put at each  $\mathbf{P}_{jk}^\alpha$  spot. The matrices in Eqs (4.46) and (4.47) are transformations  $(\mathbf{g})_P = T(\mathbf{g})_G T^\dagger$  and  $(\bar{\mathbf{g}})_P = T(\bar{\mathbf{g}})_G T^\dagger$  of the respective matrices in Eqs (4.28a) and (4.28b) by transformation  $T$  composed of  $D_{jk}^\alpha(g)$  components. The  $C_6$  analogy is Fourier transform (4.10) from (4.4) to (4.13).

$$\begin{aligned}
(\bar{\mathbf{g}})_P &= T(\bar{\mathbf{g}})_G T^\dagger = \\
&\begin{pmatrix}
|\mathbf{P}_{xx}^{A_1}\rangle & |\mathbf{P}_{yy}^{A_2}\rangle & |\mathbf{P}_{xx}^{E_1}\rangle & |\mathbf{P}_{yx}^{E_1}\rangle & |\mathbf{P}_{xy}^{E_1}\rangle & |\mathbf{P}_{yy}^{E_1}\rangle \\
D^{A_1*}(g) & \cdot & \cdot & \cdot & \cdot & \cdot \\
\cdot & D^{A_2*}(g) & \cdot & \cdot & \cdot & \cdot \\
\cdot & \cdot & D_{xx}^{E_1*}(g) & \cdot & D_{xy}^{E_1*}(g) & \cdot \\
\cdot & \cdot & \cdot & D_{xx}^{E_1*}(g) & \cdot & D_{xy}^{E_1*}(g) \\
\cdot & \cdot & D_{yx}^{E_1*}(g) & \cdot & D_{yy}^{E_1*}(g) & \cdot \\
\cdot & \cdot & \cdot & D_{yx}^{E_1*}(g) & \cdot & D_{yy}^{E_1*}(g)
\end{pmatrix} \tag{4.47}
\end{aligned}$$

Matrices  $\dots(\bar{\mathbf{r}}^2)_P, (\bar{\mathbf{i}}_1)_P, \dots$  defined by Eq (4.47) commute with every  $\dots(\mathbf{r}^2)_P, (\mathbf{i}_1)_P, \dots$  defined by Eq (4.46) while each represents identical *non*-commutative  $D_3$  product

Figure 4.6:  $D_3$ -operator defined states and tunneling paths

$$\begin{aligned}
 r_0 &= \langle 1 | \mathbf{H} | 1 \rangle = r_0^* \\
 r_1 &= \langle \mathbf{r} | \mathbf{H} | 1 \rangle = r_2^* \\
 r_1^* &= \langle \mathbf{r}^2 | \mathbf{H} | 1 \rangle = r_2^* \\
 i_1 &= \langle \mathbf{i}_1 | \mathbf{H} | 1 \rangle = i_1^* \\
 i_2 &= \langle \mathbf{i}_2 | \mathbf{H} | 1 \rangle = i_2^* \\
 i_3 &= \langle \mathbf{i}_3 | \mathbf{H} | 1 \rangle = i_3^*
 \end{aligned}$$



tables in (4.27). Both use real  $[x, y]$ -based  $\mathbf{i}_3$ -diagonal irreps  $D_{jk}^\alpha(g)$  given below.

$\mathbf{g} =$	$\mathbf{1}$	$\mathbf{r}$	$\mathbf{r}^2$	$\mathbf{i}_1$	$\mathbf{i}_2$	$\mathbf{i}_3$
$D^{A_1}(\mathbf{g}) =$	1	1	1	1	1	1
$D^{A_2}(\mathbf{g}) =$	1	1	1	-1	-1	-1
$D_{\substack{xx \ xy \\ yx \ yy}}^E(\mathbf{g}) =$	$\begin{pmatrix} 1 & \cdot \\ \cdot & 1 \end{pmatrix}$	$\begin{pmatrix} \frac{-1}{2} & \frac{-\sqrt{3}}{2} \\ \frac{\sqrt{3}}{2} & \frac{-1}{2} \end{pmatrix}$	$\begin{pmatrix} \frac{-1}{2} & \frac{\sqrt{3}}{2} \\ \frac{-\sqrt{3}}{2} & \frac{-1}{2} \end{pmatrix}$	$\begin{pmatrix} \frac{-1}{2} & \frac{-\sqrt{3}}{2} \\ \frac{-\sqrt{3}}{2} & \frac{1}{2} \end{pmatrix}$	$\begin{pmatrix} \frac{-1}{2} & \frac{\sqrt{3}}{2} \\ \frac{\sqrt{3}}{2} & \frac{1}{2} \end{pmatrix}$	$\begin{pmatrix} 1 & \cdot \\ \cdot & -1 \end{pmatrix}$

(4.48)

#### 4.4.4 Spectral resolution of $D_3$ Hamiltonian

Hamiltonian  $\mathbf{H}$ -matrix in (4.30) has six parameters  $[r_0, r_1, r_2, i_1, i_2, i_3]$  or coefficients of its expansion (4.29) in terms of intrinsic  $\bar{D}_3$  operators  $[\mathbf{1} = \bar{\mathbf{r}}^0, \bar{\mathbf{r}}^1, \bar{\mathbf{r}}^2, \bar{\mathbf{i}}_1, \bar{\mathbf{i}}_2, \bar{\mathbf{i}}_3]$ . The parameters are indicated in Fig. 4.6 by tunneling paths between the first  $D_3$  base state  $|1\rangle$  and other  $D_3$ -defined base states  $|\mathbf{g}\rangle = \mathbf{g}|1\rangle$  representing potential minima.

The resolution of  $\mathbf{H}$ -matrix then follows that of  $\bar{\mathbf{g}}$  and  $(\bar{\mathbf{g}})_P$ -matrices. Any reduction of all  $(\bar{\mathbf{g}})_P$ -matrices, such as the  $[x, y]$ -reduction in Eq (4.47), also reduces the  $(\mathbf{H})_P$ -matrix accordingly. Row-1 of  $(\mathbf{H}_P)$  in Eq (4.30) has all six parameters.

$$H_{ab}^\alpha = \sum_{g=1}^{\circ G} \langle \mathbf{1} | \mathbf{H} | \mathbf{g} \rangle D_{ab}^{\alpha*}(g) = \sum_{g=1}^{\circ G} r_g D_{ab}^{\alpha*}(g) \quad (4.49)$$

If the  $P$ -nilpotent pair are switched to  $\dots \mathbf{P}_{xy}^E, \mathbf{P}_{yx}^E \dots$ , then  $(\mathbf{H})_P$  and all  $(\bar{\mathbf{g}})_P$  (instead of

all  $(\mathbf{g})_P$  as in Eq (4.46)) are diagonal with eigenvalues  $H^{A_1}$  and  $H^{A_2}$  or block-diagonal with a pair of identical 2-by-2  $H^E$ -blocks.

$$(\mathbf{H})_P = \bar{T} (\mathbf{H})_G \bar{T}^\dagger = \begin{pmatrix} | \mathbf{P}_{xx}^{A_1} \rangle & | \mathbf{P}_{yy}^{A_2} \rangle & | \mathbf{P}_{xx}^{E_1} \rangle & | \mathbf{P}_{xy}^{E_1} \rangle & | \mathbf{P}_{yx}^{E_1} \rangle & | \mathbf{P}_{yy}^{E_1} \rangle \\ \hline H^{A_1} & \cdot & \cdot & \cdot & \cdot & \cdot \\ \hline \cdot & H^{A_2} & \cdot & \cdot & \cdot & \cdot \\ \hline \cdot & \cdot & H_{xx}^E & H_{xy}^E & \cdot & \cdot \\ \cdot & \cdot & H_{yx}^E & H_{yy}^E & \cdot & \cdot \\ \hline \cdot & \cdot & \cdot & \cdot & H_{xx}^E & H_{xy}^E \\ \cdot & \cdot & \cdot & \cdot & H_{yx}^E & H_{yy}^E \end{pmatrix} \quad (4.50)$$

The  $H$ -block matrix components follow by combing (4.48) with (4.49).

$$\begin{aligned} H^{A_1} &= r_0 D^{A_1^*}(1) + r_1 D^{A_1^*}(r^1) + r_1^* D^{A_1^*}(r^2) + i_1 D^{A_1^*}(i_1) + i_2 D^{A_1^*}(i_2) \\ &\quad + i_3 D^{A_1^*}(i_3) = r_0 + r_1 + r_1^* + i_1 + i_2 + i_3 \\ H^{A_2} &= r_0 D^{A_2^*}(1) + r_1 D^{A_2^*}(r^1) + r_1^* D^{A_2^*}(r^2) + i_1 D^{A_2^*}(i_1) + i_2 D^{A_2^*}(i_2) \\ &\quad + i_3 D^{A_2^*}(i_3) = r_0 + r_1 + r_1^* - i_1 - i_2 - i_3 \\ H_{xx}^E &= r_0 D_{xx}^{E^*}(1) + r_1 D_{xx}^{E^*}(r^1) + r_1^* D_{xx}^{E^*}(r^2) + i_1 D_{xx}^{E^*}(i_1) + i_2 D_{xx}^{E^*}(i_2) + i_3 D_{xx}^{E^*}(i_3) \\ &= (2r_0 - r_1 - r_1^* - i_1 - i_2 + 2i_3) / 2 \\ H_{xy}^E &= r_0 D_{xy}^{E^*}(1) + r_1 D_{xy}^{E^*}(r^1) + r_1^* D_{xy}^{E^*}(r^2) + i_1 D_{xy}^{E^*}(i_1) + i_2 D_{xy}^{E^*}(i_2) + i_3 D_{xy}^{E^*}(i_3) \\ &= \sqrt{3}(-r_1 + r_1^* - i_1 + i_2) / 2 = H_{yx}^{E^*} \\ H_{yy}^E &= r_0 D_{yy}^{E^*}(1) + r_1 D_{yy}^{E^*}(r^1) + r_1^* D_{yy}^{E^*}(r^2) + i_1 D_{yy}^{E^*}(i_1) + i_2 D_{yy}^{E^*}(i_2) + i_3 D_{yy}^{E^*}(i_3) \\ &= (2r_0 - r_1 - r_1^* + i_1 + i_2 - 2i_3) / 2 \end{aligned} \quad (4.51)$$

Irrep-dimension  $\ell^E = 2$  implies (at least) 2-fold degenerate  $E$ -level since eigenvalues of identical  $H^E$ -blocks must also be identical, but only certain parameter values give

diagonal  $H^E$ -blocks in (4.51), *i.e.*, real  $r_1 = r_2^*$  and equal  $i_1 = i_2$ .

$$\begin{aligned} \begin{pmatrix} H_{xx}^E & H_{xy}^E \\ H_{yx}^E & H_{yy}^E \end{pmatrix} &= \frac{1}{2} \begin{pmatrix} 2r_0 - r_1 - r_1^* - i_1 - i_2 + 2i_3 & \sqrt{3}(-r_1 + r_1^* - i_1 + i_2) \\ \sqrt{3}(-r_1^* + r_1 - i_1 + i_2) & 2r_0 - r_1 - r_1^* + i_1 + i_2 - 2i_3 \end{pmatrix} \\ &= \begin{pmatrix} r_0 - r_1 - i_{12} + i_3 & 0 \\ 0 & r_0 - r_1 + i_{12} - i_3 \end{pmatrix} \end{aligned} \quad (4.52)$$

For:  $r_1 = r_1^*$  and:  $i_1 = i_2 = i_3$

These are the values that respect the local  $D_3 \supset C_2[\mathbf{1}, \mathbf{i}_3]$  subgroup chain symmetry that gave  $(x, y)$ -plane polarized splitting in Eq (4.37). This is broken by a complex  $r_1$  or by unequal  $i_1$  and  $i_2$ . Complex  $r_1 = |r|e^{i\phi}$  gives rise to complex rotating-wave eigenstates similar to ones in Fig. 4.4 but, unlike that ZB1 model, cannot split  $E$ -degeneracy. Unequal  $i_1$  and  $i_2$  shift standing-wave nodes but cannot split  $E$ -doublets either.  $E$ -levels may split if  $\mathbf{H}$  contains *external* or *lab*-based operators  $\mathbf{g}$  in addition to its *internal* or *body*-based  $\bar{\mathbf{g}}$ , but it thereby loses its  $D_3$  symmetry.

#### 4.4.5 Global-lab-relative $G$ versus local-body-relative $\bar{G}$ base state definition

Non-Abelian symmetry analysis in general, and the present example of  $D_3$  resolution in particular, involves a dual-group relativity between an *extrinsic* or *global* “lab-based” group  $G=D_3$  on one hand, and an *intrinsic* or *local* “body-based” group  $\bar{G}=\bar{D}_3$  on the other hand. Each  $\bar{\mathbf{g}}$  in  $\bar{G}$  commutes with each  $\mathbf{g}$  in  $G$ .

In the present example, the *global* “lab-based” group  $G=D_3=[\mathbf{1}, \mathbf{r}^1, \mathbf{r}^2, \mathbf{i}_1, \mathbf{i}_2, \mathbf{i}_3]$  labels equivalent locations in a potential or lab-based field and is a reference frame for an excitation wave or “body” occupying lab locations.

On the other hand, the *local* “bod-based” group  $\bar{G}=\bar{D}_3=[\mathbf{1}, \bar{\mathbf{r}}^1, \bar{\mathbf{r}}^2, \bar{\mathbf{i}}_1, \bar{\mathbf{i}}_2, \bar{\mathbf{i}}_3]$  regards the excitation wave as a reference frame to define relative location of the potential or laboratory field.

Quantum waves provide the most precise space-time reference frames that are

possible in any situation due to the ultra-sensitive nature of wave interferometry. This is the case for optical coherent waves or electronic and nuclear matter waves. The latter derive their space-time symmetry properties from the former, and these are deep classical and quantum mechanical rules of engagement for currently accepted Hamiltonian quantum theory.

Interference and interaction of any two waves depends only on the relative position. This is reflected in the following equivalent definitions of base state kets for wave in a  $D_3$  potential in Fig. 4.5 as sketched by six localized wave bases  $[|\mathbf{1}\rangle, |\mathbf{r}^1\rangle, |\mathbf{r}^2\rangle, |\mathbf{i}_1\rangle, |\mathbf{i}_2\rangle, |\mathbf{i}_3\rangle]$  in Fig. 4.6.

$$|\mathbf{g}_k\rangle = \mathbf{g}_k|\mathbf{1}\rangle = \bar{\mathbf{g}}_k^{-1}|\mathbf{1}\rangle \quad (4.53)$$

Key to this definition is the principle of independence and mutual commutation of the dual sets in (4.28a) and (4.28b).

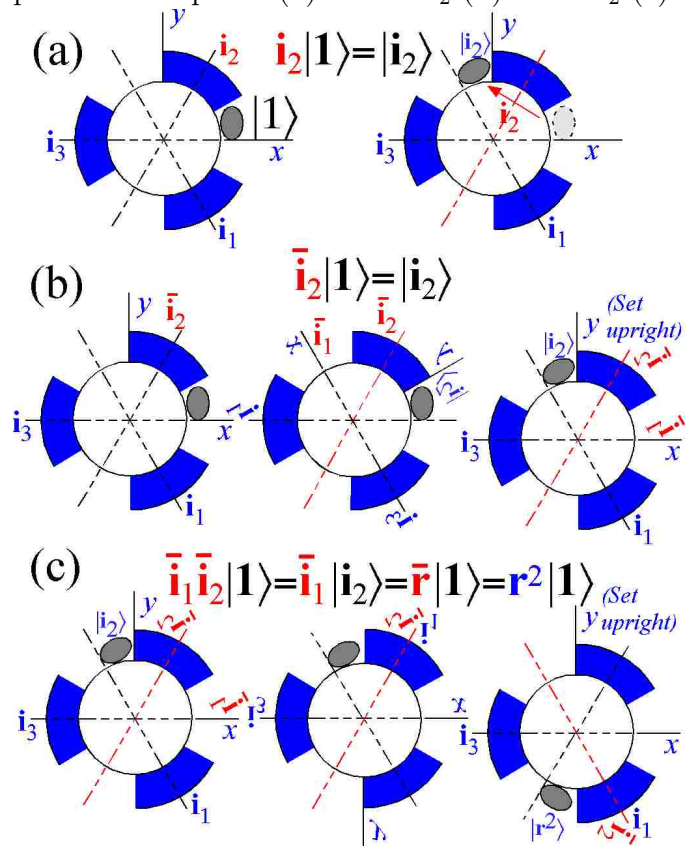
$$\mathbf{g}_j\bar{\mathbf{g}}_k = \bar{\mathbf{g}}_k\mathbf{g}_j \quad (4.54)$$

Neither relation makes sense if we were to equate  $\mathbf{g}_k$  with  $\bar{\mathbf{g}}_k^{-1}$ . The effect of  $\mathbf{g}_k$  is equal to that of  $\bar{\mathbf{g}}_k^{-1}$  *only* when acting on the origin-state  $|\mathbf{1}\rangle$ . The action of global  $\mathbf{i}_2$  in Fig. 4.7(a) is compared to local  $\bar{\mathbf{i}}_2$  in Fig. 4.7(b) that gives the same *relative* position of wave and wells. In Fig. 4.7(c) product  $\bar{\mathbf{i}}_1\bar{\mathbf{i}}_2=\bar{\mathbf{r}}$  has the same action as  $\mathbf{i}_2\mathbf{i}_1=\mathbf{r}^{-1}=\mathbf{r}^2$  on  $|\mathbf{1}\rangle$ .

Different points of view show how “body”  $\bar{\mathbf{g}}$  operations relate to the “lab”  $\mathbf{g}$ . Starting from state  $|\mathbf{1}\rangle$ ,  $\bar{\mathbf{r}}^1=\bar{\mathbf{r}}$  rotates lab potential clockwise ( $-120^\circ$ ) in a view where the body “stays put”. The body wave ends up in the same well as it would if, instead, the body rotates counter-clockwise ( $+120^\circ$ ) by  $\mathbf{r}=\mathbf{r}^1$  in a lab frame that “stays put.”

In a lab view, effects of body operation  $\bar{\mathbf{g}}_k$  and lab operation  $\mathbf{g}_k^{-1}$  on  $|\mathbf{1}\rangle$  are the same except that  $\bar{\mathbf{g}}_k^{-1}$  also moves each body operation  $\bar{\mathbf{g}}_j$  in the same way to  $\bar{\mathbf{g}}_k\bar{\mathbf{g}}_j\bar{\mathbf{g}}_k^{-1}$ .

Figure 4.7:  $D_3$ -operators compared (a) Global  $\mathbf{i}_2$  (b) Local  $\bar{\mathbf{i}}_2$  (c)  $\bar{\mathbf{i}}_2$  followed by  $\bar{\mathbf{i}}_1$



The lab view of a lab operation  $\mathbf{g}_k$  does not see any of lab  $\mathbf{g}_j$  axes change location.

The following generalization of lab-body relativity relation (4.53) using (4.54) shows how  $\bar{\mathbf{g}}_j$  affects arbitrary  $|\mathbf{g}_k\rangle$ .

$$\begin{aligned}\bar{\mathbf{g}}_j^{-1}|\mathbf{g}_k\rangle &= \bar{\mathbf{g}}_j^{-1}\mathbf{g}_k|\mathbf{1}\rangle = \mathbf{g}_k\bar{\mathbf{g}}_j^{-1}|\mathbf{1}\rangle \\ &= \mathbf{g}_k\mathbf{g}_j|\mathbf{1}\rangle = \mathbf{g}_k\mathbf{g}_j\mathbf{g}_k^{-1}\mathbf{g}_k|\mathbf{1}\rangle = \mathbf{g}_k\mathbf{g}_j\mathbf{g}_k^{-1}|\mathbf{g}_k\rangle\end{aligned}\quad (4.55)$$

#### 4.4.6 Global *versus* local eigenstate symmetry

Each projection operator  $\mathbf{P}_{jk}^\alpha$  in (4.42) applied to origin ket  $|\mathbf{1}\rangle$  gives a local-and-global symmetry-defined ket  $|\mathbf{j}k\rangle^\alpha$ .

$$|\mathbf{j}k\rangle^\alpha = \mathbf{P}_{jk}^\alpha|\mathbf{1}\rangle\sqrt{{}^oG/\ell^\alpha} = \sqrt{\ell^\alpha/{}^oG}\sum_{g=1}{{}^oG}D_{j,k}^{\alpha*}(g)|\mathbf{g}\rangle\quad (4.56)$$

The norm-factor  $N={}^oG/\ell^\alpha$  is a non-Abelian generalization of the integral norm  $N$  for Abelian  $C_N$  eigenket projection in (4.20). Interestingly, the non-Abelian norm is also an integer since irrep dimension  $\ell^\alpha$  is always a factor of its group's order  ${}^oG$ .

A non-Abelian projection ket in (4.56) has two independent symmetry labels  $j$  and  $k$  belonging to global-lab symmetry operators  $\mathbf{g}$  and local-body operators  $\bar{\mathbf{g}}$ , respectively. Application of  $\mathbf{g}$ -resolution Eq (4.41a) to ket Eq (4.56) is reduced by  $\mathbf{P}$ -product rules in (4.44) to the following global transformation.

$$\begin{aligned}\mathbf{g}|\mathbf{j}k\rangle^\alpha &= \mathbf{g}\mathbf{P}_{jk}^\alpha|\mathbf{1}\rangle\sqrt{N} = \sum_{j'=1}^{\ell^\alpha}\sum_{k'=1}^{\ell^\alpha}D_{j',k'}^\mu(g)\mathbf{P}_{j',k'}^\alpha\mathbf{P}_{jk}^\alpha|\mathbf{1}\rangle\sqrt{N} \\ &= \sum_{j'=1}^{\ell^\alpha}D_{j',j}^\alpha(g)\mathbf{P}_{j',k}^\alpha|\mathbf{1}\rangle\sqrt{N} \\ &= \sum_{j'=1}^{\ell^\alpha}D_{j',j}^\alpha(g)|\mathbf{j}'k\rangle^\alpha\end{aligned}\quad (4.57)$$

The corresponding local operator  $\bar{\mathbf{g}}$  first commutes through  $\mathbf{P}_{jk}^\alpha$  according to (4.54)



and is converted by Eq (4.53) to inverse global  $\mathbf{g}^{-1}$  on the right of  $\mathbf{P}_{jk}^\alpha$  using Eq (4.41a) again. Finally, unitary irreps  $D^\alpha(g^{-1}) = D^{\alpha\dagger}(g)$  are assumed.

$$\begin{aligned}
\bar{\mathbf{g}} \left| \begin{smallmatrix} \alpha \\ jk \end{smallmatrix} \right\rangle &= \bar{\mathbf{g}} \mathbf{P}_{jk}^\alpha |\mathbf{1}\rangle \sqrt{N} = \mathbf{P}_{jk}^\alpha \bar{\mathbf{g}} |\mathbf{1}\rangle \sqrt{N} = \mathbf{P}_{jk}^\alpha \mathbf{g}^{-1} |\mathbf{1}\rangle \sqrt{N} \\
&= \sum_{j'=1}^{\ell^\alpha} \sum_{k'=1}^{\ell^\alpha} D_{j'k'}^\mu(g^{-1}) \mathbf{P}_{jk}^\alpha \mathbf{P}_{j'k'}^\alpha |\mathbf{1}\rangle \sqrt{N} = \sum_{j'=1}^{\ell^\alpha} D_{kk'}^\alpha(g^{-1}) \mathbf{P}_{j'k'}^\alpha |\mathbf{1}\rangle \sqrt{N} \\
&= \sum_{j'=1}^{\ell^\alpha} D_{kk'}^\alpha(g^{-1}) \left| \begin{smallmatrix} \alpha \\ jk' \end{smallmatrix} \right\rangle = \sum_{j'=1}^{\ell^\alpha} D_{k'k}^{\alpha*}(g) \left| \begin{smallmatrix} \alpha \\ jk' \end{smallmatrix} \right\rangle
\end{aligned} \tag{4.58}$$

A summary of the results is consistent with the block matrix forms in (4.46) and (4.47).

$$\left\langle \begin{smallmatrix} \alpha \\ j'k \end{smallmatrix} \right| \mathbf{g} \left| \begin{smallmatrix} \alpha \\ jk \end{smallmatrix} \right\rangle = D_{j'j}^\alpha(g), \quad \left\langle \begin{smallmatrix} \alpha \\ jk' \end{smallmatrix} \right| \bar{\mathbf{g}} \left| \begin{smallmatrix} \alpha \\ jk \end{smallmatrix} \right\rangle = D_{k'k}^{\alpha*}(g). \tag{4.59}$$

Choice of subgroup  $C_2 = [\mathbf{1}, \mathbf{i}_3]$  in Eq (4.37) leads to  $(x, y)$ -polarized states  $(m)_2$  labeled by their  $\mathbf{i}_3$  eigenvalues  $(-1)^m$ .

$$\begin{aligned}
\left\langle \begin{smallmatrix} \alpha \\ j'k \end{smallmatrix} \right| \mathbf{i}_3 \left| \begin{smallmatrix} \alpha \\ jk \end{smallmatrix} \right\rangle &= D_{j'j}^\alpha(i_3), & \left\langle \begin{smallmatrix} \alpha \\ jk' \end{smallmatrix} \right| \bar{\mathbf{i}}_3 \left| \begin{smallmatrix} \alpha \\ jk \end{smallmatrix} \right\rangle &= D_{k'k}^{\alpha*}(i_3). \\
= \delta_{j'j} \begin{cases} +1 \text{ for } :j=x \\ -1 \text{ for } :j=y \end{cases}, & = \delta_{k'k} \begin{cases} +1 \text{ for } :k=x \\ -1 \text{ for } :k=y \end{cases}.
\end{aligned} \tag{4.60}$$

Significance of these global- $(j)$  and local- $(k)$  values are now discussed using Fig. 4.8.

Wherever the global  $j$  is  $x$  or  $\mathbf{i}_3$ -symmetric  $(0_2)$ , then the entire wave is symmetric to  $x$ -axial rotation by  $\pi$  in Fig. 4.8(a) or horizontal reflection thru the middle square-well in Fig. 4.8(b). Similarly, wherever the global  $j$  is  $y$  or  $\mathbf{i}_3$ -antisymmetric  $(1_2)$ , that is seen for each overall figure, too.

However, if the local  $k$  is  $x$  or  $\mathbf{i}_3$ -symmetric  $(0_2)$ , the local wave in *each* well has no node and is symmetric to its local axis of rotation by  $\pi$  in Fig. 4.8(a) or horizontal reflection of *each* square-well in Fig. 4.8(b). Similarly, wherever the local  $j$  is  $y$  or  $\mathbf{i}_3$ -antisymmetric  $(1_2)$ , that antisymmetry and one node is seen in *each* well, too.

Local and global symmetry clash along the  $\mathbf{i}_3$ -axis for states projected by nilpotent

$\mathbf{P}_{xy}^\alpha$  or  $\mathbf{P}_{yx}^\alpha$  and give  $x$ -axial wave nodes indicated by pairs of arrows in Fig. 4.8. The  $|E_{yx}\rangle$  wave in the lower right of Fig. 4.8(b) appears quite suppressed on the  $\mathbf{i}_3$ -axis. However, the  $|E_{xy}\rangle$  “node” in the upper left seems to be coming unglued.

The “unglued” level  $\omega_{xy}^E$  is higher than  $\omega_{yx}^E$  and enjoys more tunneling. If tunneling increases so do parameters such as  $r_1$  and  $r_2$  in (4.51) that do not respect  $x$ -axial local subgroup  $C_2 = [\mathbf{1}, \mathbf{i}_3]$ . This breaks  $x$ -axial nodes and  $\mathbf{i}_3$  local symmetry causing  $E$ -modes to be less  $C_2$ -local and more like current-carrying above-barrier  $C_3$ -local waves rotating on  $r$ -paths.  $D_3$  correlation arrays in (4.61) with  $C_2$  or  $C_3$  indicate level cluster structure for extremes of each case.

$$\begin{array}{c|cc|}
 D_3 \supset C_2 & 0_2 & 1_2 \\
 \hline
 A_1 & 1 & \cdot \\
 A_2 & \cdot & 1 \\
 E & 1 & 1 \\
 \hline
 \end{array}
 \qquad
 \begin{array}{c|ccc|}
 D_3 \supset C_3 & 0_3 & 1_3 & 2_3 \\
 \hline
 A_1 & 1 & \cdot & \cdot \\
 A_2 & 1 & \cdot & \cdot \\
 E & \cdot & 1 & 1 \\
 \hline
 \end{array}
 \tag{4.61}$$

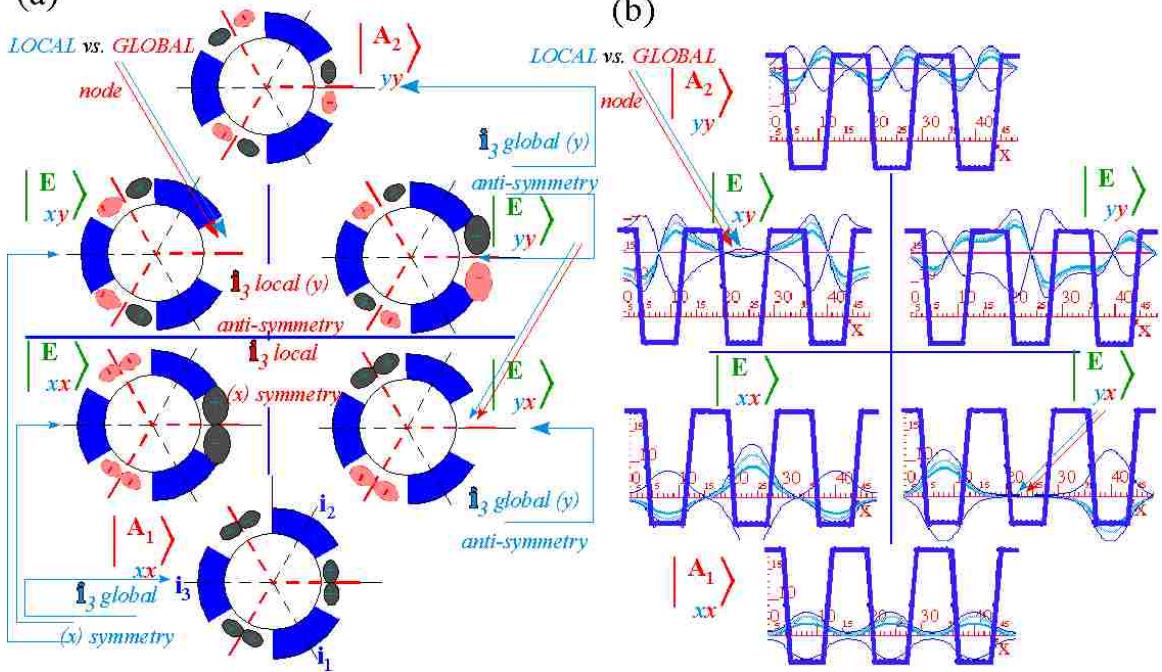
Column  $0_2$  of array  $D_3 \supset C_2$  in Eq (4.61) correlates to  $A_1$  and  $E$ . The lower  $(A_1, E)$ -level cluster in Fig. 4.8 has  $0_2$  local symmetry and lies below cluster- $(A_2, E)$  that has local  $1_2$  symmetry according to the  $1_2$  column of (4.61). Column  $0_3$  of table  $D_3 \supset C_3$  indicates that  $A_1$  and  $A_2$  levels cluster under extreme  $C_3$  localization, but columns  $1_3$  and  $2_3$  indicate that each  $E$  doublet level is unclustered under  $C_3$  with no extra degeneracy beyond its own ( $\ell^E = 2$ ).

#### 4.4.7 Symmetry correlation and Frobenius reciprocity

The mathematical basis of correlation arrays in (4.61) is a Frobenius reciprocity relation that exists between irreps of a group and its subgroups. This may be clarified by appealing to the physics of  $\mathbf{P}_{jk}^\alpha$ -projected states  $|_{jk}^\alpha\rangle$  such as are displayed in Fig. 4.8 and by exploiting the duality between their local and global symmetry and subgroups.

$D_3$ -symmetric Hamiltonian  $\mathbf{H}$  in (4.30) is made only of local  $\bar{\mathbf{g}}$  that couple  $|_{jk}^\alpha\rangle$ -

Figure 4.8:  $D_3$ -symmetry waves (a) Sketch of projection (b) 3-Well wave simulation



states thru local  $k$ -indices by (4.59) but leave all  $\ell^\alpha$  values of global  $j$ -indices unchanged. Thus  $\alpha$ -eigenstates of  $\mathbf{H}$  mix  $k$ -values to form  $\ell^\alpha$ -fold degenerate levels labeled by  $j$ -indices. (Recall  $\ell^E = 2$  equal sub-matrices Eqs (4.52) in (4.50).) Further degeneracy or near-degeneracy (“clustering”) occurs if inter-and-intra local tunneling coefficients vary exponentially with quantum numbers causing various types of local modes or “spontaneous” symmetry localization.

In contrast to the clustering or “un-splitting” associated with local  $\bar{\mathbf{g}}$  symmetry operators, global  $\mathbf{g}$  are associated with external or “applied” symmetry reduction that causes level splitting. Adding global  $\mathbf{g}_m$  to a Hamiltonian  $\mathbf{H}$  reduces its  $G$ -symmetry to a self-symmetry subgroup  $K=s_m$  consisting of operators that commute with  $\mathbf{g}_m$ . Adding a combination of  $\mathbf{g}_m$  and  $\mathbf{g}_n$  reduces  $K$  to an even smaller self-symmetry intersection group  $s_m \cap s_n$ .

Global  $\mathbf{g}$  couple  $|\alpha_{jk}\rangle$ -states thru global  $j$ -indices according to (4.57). The more global perturbations are added to a Hamiltonian  $\mathbf{H}$  the more likely it is to split  $\ell^\alpha$ -fold  $j$ -degeneracy (for  $\ell^\alpha \geq 2$ ) and/or alter eigenfunctions.

## Global “applied” symmetry reduction, subduction, and level splitting

In the  $G=D_3$  example, adding matrix  $(\mathbf{r}^1)$  from Eq (4.28a) to  $(\mathbf{H})$  in Eq (4.30) reduces its symmetry to  $K=C_3=[\mathbf{1}, \mathbf{r}^1, \mathbf{r}^2]$ , and adding  $(\mathbf{i}_3)$  reduces it to  $K=C_2=[\mathbf{1}, \mathbf{i}_3]$ . Adding a combination of  $(\mathbf{r}^1)$  and  $(\mathbf{i}_3)$  completely reduces  $(\mathbf{H})$ -symmetry to intersection  $C_3 \cap C_2=C_1=[\mathbf{1}]$ , which corresponds to having *no* global symmetry.

By reducing  $G$  to a subgroup  $K \subset G$ , each  $G$ -labeled  $\alpha$ -level becomes relabeled by that subgroup  $K$  and split (if  $\ell^\alpha \geq 2$ ) in precisely the way that central  $G$ -idempotent  $\mathbf{P}^\alpha$  is relabeled and/or split by unit resolution shown in (4.37) or Eq (4.38). The splitting in (4.38) of  $D_3$  idempotent  $\mathbf{P}^E$  into  $C_3$ -labeled  $\mathbf{P}_{1_3 1_3}^E$  plus  $\mathbf{P}_{2_3 2_3}^E$  implies the  $D_3$  doublet level  $\omega^E$  splits into  $C_3$ -labeled singlets  $\omega^{1_3}$  and  $\omega^{2_3}$ . Both  $D_3$  singlets  $A_1$  and  $A_2$  end up relabeled with  $C_3$  scalar  $0_3$  labels.

$$\begin{array}{llll}
 D_3 \supset C_3 & \underline{\mathbf{P}^\alpha \text{relabel/split}} & \underline{D^\alpha \text{relabel/reduce}} & \underline{\omega^\alpha \text{relabel/split}} \\
 A_1 & \mathbf{P}^{A_1} = \mathbf{P}^{A_1} \mathbf{P}^{0_3} = \mathbf{P}_{0_3 0_3}^{A_1} & \Rightarrow D^{A_1} \downarrow C_3 \sim D^{0_3} & \Rightarrow \omega^{A_1} \rightarrow \omega^{0_3} \\
 A_2 & \mathbf{P}^{A_2} = \mathbf{P}^{A_2} \mathbf{P}^{0_3} = \mathbf{P}_{0_3 0_3}^{A_2} & \Rightarrow D^{A_2} \downarrow C_3 \sim D^{0_3} & \Rightarrow \omega^{A_2} \rightarrow \omega^{0_3} \\
 E & \mathbf{P}^E = \mathbf{P}^E \mathbf{P}^{1_3} + \mathbf{P}^E \mathbf{P}^{2_3} & \Rightarrow D^E \downarrow C_3 \sim & \Rightarrow \omega^E \rightarrow \omega^{1_3} \\
 & = \mathbf{P}_{1_3 1_3}^E + \mathbf{P}_{2_3 2_3}^E & D^{1_3} \oplus D^{2_3} & \searrow \omega^{2_3}
 \end{array} \quad (4.62)$$

Global  $D_3 \supset C_2$  relabeling and/or splitting follows (4.37). Now  $D_3$  singlets end up with different labels  $0_2$  and  $1_2$  [6].

$$\begin{array}{llll}
 D_3 \supset C_2 & \underline{\mathbf{P}^\alpha \text{relabel/split}} & \underline{D^\alpha \text{relabel/reduce}} & \underline{\omega^\alpha \text{relabel/split}} \\
 A_1 & \mathbf{P}^{A_1} = \mathbf{P}^{A_1} \mathbf{P}^{0_2} = \mathbf{P}_{0_2 0_2}^{A_1} & \Rightarrow D^{A_1} \downarrow C_2 \sim D^{0_2} & \Rightarrow \omega^{A_1} \rightarrow \omega^{0_2} \\
 A_2 & \mathbf{P}^{A_2} = \mathbf{P}^{A_2} \mathbf{P}^{1_2} = \mathbf{P}_{1_2 1_2}^{A_2} & \Rightarrow D^{A_2} \downarrow C_2 \sim D^{1_2} & \Rightarrow \omega^{A_2} \rightarrow \omega^{1_2} \\
 E & \mathbf{P}^E = \mathbf{P}^E \mathbf{P}^{0_2} + \mathbf{P}^E \mathbf{P}^{1_2} & \Rightarrow D^E \downarrow C_2 \sim & \Rightarrow \omega^E \rightarrow \omega^{0_2} \\
 & = \mathbf{P}_{0_2 0_2}^E + \mathbf{P}_{1_2 1_2}^E & D^{0_2} \oplus D^{1_2} & \searrow \omega^{1_2}
 \end{array} \quad (4.63)$$

Center portions of splitting relations in Eqs (4.62) and (4.63) use *subduction* symbols ( $\downarrow$ ) to denote how each  $D_3$  irrep- $D^\alpha$  reduces to subgroup  $C_3$  or  $C_2$  irreps under

their respective global symmetry breaking. Earlier studies[11] have referred to these multiple subgroup splittings as multiple frameworks. Each  $\alpha$ -row of (4.62) and (4.63) corresponds to the row  $\alpha=A_1, A_2,$  or  $E,$  of correlation array  $D_3 \supset C_3$  or  $D_3 \supset C_2,$  respectively, in (4.61).

### Local “spontaneous” symmetry reduction, induction, and level clustering

Opposite to global  $G \supset K$  symmetry irrep subduction  $D^\alpha(G) \downarrow K = \dots \oplus d^a(K) \oplus d^b(K) \oplus \dots$  that predicts level-splitting is the reverse relation of local  $K \subset G$  symmetry irrep induction  $d^a(K) \uparrow G = \dots \oplus D^\alpha(G) \oplus D^\beta(G) \oplus \dots$  that predicts “unsplitting” or level-clustering. In the former, an  $\ell^\alpha$ -dimensional irrep  $D^\alpha(\mathbf{k})$  of global  $G$ -symmetry is reducible to smaller ( $\ell^a \leq \ell^\alpha$ ) block-diagonal irreps  $d^a(\mathbf{k})$  of a subgroup  $K$ . In the latter, a  $K$  irrep  $d^a$  is projected kaleidoscope-like onto coset bases of a larger induced representation  $d^a \uparrow G$  of  $G$  that is generally reducible to  $G$  irreps  $D^\alpha$ .

Base states  $|k \uparrow_j^\alpha\rangle$  of induced representation  $d^k \uparrow G$  are each made by a  $G$ -projector  $\mathbf{P}_{jk}^\alpha$  acting on local  $d^k$ -symmetry base state  $|k\rangle = \mathbf{P}^k |k\rangle$  defined by local  $K$ -projector  $\mathbf{P}^k$ .  $G$ -projection is simpler if  $\mathbf{P}_{jk}^\alpha$  is also based on  $K$ -projection.

Of all  $D_3 \supset C_2$ -projectors  $\mathbf{P}_{j_2 k_2}^\alpha$  based on Eq(4.37), only  $\mathbf{P}_{0_2 0_2}^{A_1}, \mathbf{P}_{0_2 0_2}^E,$  and  $\mathbf{P}_{1_2 0_2}^E$  have right index  $k_2 = 0_2$ . Only these can project induced states  $|0_2 \uparrow_{j_2}^\alpha\rangle$  from local base state  $|0_2\rangle$  corresponding to the  $0_2$ -column of  $D_3 \supset C_2$  array in (4.61) having  $A_1$  and  $E$ . Similarly,  $A_2$  and  $E$  in the  $1_2$ -column of Eq (4.61) correspond to  $\mathbf{P}_{1_2 1_2}^{A_2}, \mathbf{P}_{0_2 1_2}^E,$  and  $\mathbf{P}_{1_2 1_2}^E$  projecting states  $|1_2 \uparrow_{j_2}^\alpha\rangle$  from a local  $|1_2\rangle$  state. Each projector  $\mathbf{P}_{j_2 k_2}^\alpha$  in (4.63) has a  $C_2$ -subgroup projector  $\mathbf{P}^{k_2}$  “right-guarding” the side facing each local  $\ell_2$ -ket  $|\ell_2\rangle = \mathbf{P}^{\ell_2} |\ell_2\rangle$  that is similarly “guarded” by its own defining projector  $\mathbf{P}^{\ell_2}$ .  $C_2$ -subgroup projector orthogonality then allows only  $k_2 = \ell_2$ . This is the reason for projection selection rules just described.

$$\mathbf{P}_{j_2 k_2}^\alpha |\ell_2\rangle = \mathbf{P}_{j_2 k_2}^\alpha \mathbf{P}^{k_2} \mathbf{P}^{\ell_2} |\ell_2\rangle = \delta^{k_2 \ell_2} \mathbf{P}_{j_2 \ell_2}^\alpha |\ell_2\rangle = \delta^{k_2 \ell_2} |\ell_2 \uparrow_{j_2}^\alpha\rangle \quad (4.64)$$

Each “right guard” projector  $\mathbf{P}^k$  of  $\mathbf{P}_{jk}^\alpha$  is part of a  $G \supset K$  subgroup splitting or subduction splitting  $D^\alpha(G) \downarrow K = \dots \oplus d^k(K) \oplus \dots$  as shown by  $D_3 \downarrow C_2$  examples in Eq (4.63). (These go back to the original  $D_3 \supset C_2$  subgroup chain resolution in Eq (4.37).) In Eq (4.64) each  $\mathbf{P}^k$  selects which  $\alpha$ -type induced bases  $|k \uparrow_j^\alpha\rangle$  and block-diagonal  $\alpha$ -irreps can appear in a  $k$ -induced representation  $d^k(K) \uparrow G = \dots \oplus D^\alpha(G) \oplus \dots$ , and it implies a duality between induced ( $\uparrow$ ) level-clustering and subduced ( $\downarrow$ ) level-splitting as stated by the following *Frobenius reciprocity relation*.

$$\text{Number of } D^\alpha \text{ in } d^k(K) \uparrow G = \text{Number of } d^k \text{ in } D^\alpha(G) \downarrow K \quad (4.65)$$

The numbers on the left-hand side of (4.65) would reside in the  $k^{\text{th}}$ -column of a  $G \supset K$ -correlation array such as in (4.61) while the numbers on the right-hand side of (4.65) would reside in the  $\alpha^{\text{th}}$ -row of the *same* array. The examples in Eq (4.61) have only ones  $\{1\}$  and zeros  $\{\cdot\}$ . A deeper correlation  $D_3 \supset C_1$  to  $C_1$  symmetry, *i.e.*, to *no* symmetry is a conflation of either the array  $D_3 \supset C_2$  or the array  $D_3 \supset C_3$  in (4.61) since  $C_1 = C_2 \cap C_3$  is the intersection of  $C_2$  and  $C_3$ .

$D_3 \supset C_1$	$0_1 = 1_1$	
$A_1$	1	(4.66)
$A_2$	1	
$E$	2	

The  $C_1$  local symmetry base  $|0_1\rangle = |1_1\rangle$  is just the  $|\mathbf{1}\rangle$  in Fig. 4.6. Its projections give the scalar  $A_1$ , pseudo-scalar  $A_2$ , and two  $E$  wave states in Fig. 4.8. That is consistent with the single column of the  $D_3 \supset C_1$  correlation array in (4.66).

Reciprocity in (4.65) also holds for non-Abelian subgroup irreps  $d^k$ .  $D_3$  is the smallest non-Abelian group so it has no such subgroups, but octahedral symmetry has non-Abelian  $D_3$  and  $D_4$  subgroups that figure in its splitting and clustering that are described in chapter 5.

## Coset structure and factored eigensolutions

Three pairs of kets in Fig. 4.6 relate to *left cosets* [ $\mathbf{1}C_2 = (\mathbf{1}, \mathbf{i}_3)$ ,  $\mathbf{r}C_2 = (\mathbf{r}^1, \mathbf{i}_2)$ ,  $\mathbf{r}^2C_2 = (\mathbf{r}^2, \mathbf{i}_1)$ ] one at each site.

$$[(|\mathbf{1}\rangle, |\mathbf{i}_3\rangle), (|\mathbf{r}^1\rangle, |\mathbf{i}_2\rangle) = \mathbf{r}^1(|\mathbf{1}\rangle, |\mathbf{i}_3\rangle), (|\mathbf{r}^2\rangle, |\mathbf{i}_1\rangle) = \mathbf{r}^2(|\mathbf{1}\rangle, |\mathbf{i}_3\rangle)] \quad (4.67)$$

Conjugate bras  $\langle \mathbf{g}| = \langle \mathbf{1}|\mathbf{g}^\dagger$  relate to *right cosets* [ $C_2 = (\mathbf{1}, \mathbf{i}_3)$ ,  $C_2\mathbf{r}^2 = (\mathbf{r}^2, \mathbf{i}_2)$ ,  $C_2\mathbf{r} = (\mathbf{r}, \mathbf{i}_1)$ ], again, one per  $C_2$ -well site.

$$[(\langle \mathbf{1}|, \langle \mathbf{i}_3|), (\langle \mathbf{r}^1|, \langle \mathbf{i}_2|) = (\langle \mathbf{1}|, \langle \mathbf{i}_3|)\mathbf{r}^2, (\langle \mathbf{r}^2|, \langle \mathbf{i}_1|) = (\langle \mathbf{1}|, \langle \mathbf{i}_3|)\mathbf{r}^1] \quad (4.68)$$

$C_2$  projectors  $\mathbf{P}^{0z} = \frac{1}{2}(\mathbf{1} + \mathbf{i}_3) = \mathbf{P}^x$  and  $\mathbf{P}^{1z} = \frac{1}{2}(\mathbf{1} - \mathbf{i}_3) = \mathbf{P}^y$  split bra  $\langle \mathbf{g}|$  into  $\pm$ -sum of bras mapped by left coset  $\mathbf{g}^\dagger C_2$ .

$$[\langle \mathbf{1}| \mathbf{P}^{m_2} = \frac{1}{2} (\langle \mathbf{1}| \pm \langle \mathbf{i}_3|), \langle \mathbf{r}^1| \mathbf{P}^{m_2} = \frac{1}{2} (\langle \mathbf{r}^1| \pm \langle \mathbf{i}_2|), \langle \mathbf{r}^2| \mathbf{P}^{m_2} = \frac{1}{2} (\langle \mathbf{r}^2| \pm \langle \mathbf{i}_1|)] \quad (4.69)$$

The same projectors split ket  $|\mathbf{g}\rangle$  into bases  $\mathbf{P}^{m_2}|\mathbf{g}\rangle$  that are  $\pm$ -sum of kets mapped by right coset  $C_2\mathbf{g}$ .

$$[\mathbf{P}^{m_2} |\mathbf{1}\rangle = \frac{1}{2} (|\mathbf{1}\rangle \pm |\mathbf{i}_3\rangle), \mathbf{P}^{m_2} |\mathbf{r}^1\rangle = \frac{1}{2} (|\mathbf{r}^1\rangle \pm |\mathbf{i}_2\rangle), \mathbf{P}^{m_2} |\mathbf{r}^2\rangle = \frac{1}{2} (|\mathbf{r}^2\rangle \pm |\mathbf{i}_1\rangle)] \quad (4.70)$$

$g$ -coefficients in  $H$ -submatrix (4.52) track  $C_2$  cosets. Row-(bra)- $x$  terms in  $H_{x,\cdot}^E$  line up in (+)-right-coset  $\mathbf{1g} + \mathbf{i}_3\mathbf{g}$  order  $\dots(r_1 + i_1), (r_2 + i_2)$ . Row-(bra)- $y$  terms in  $H_{y,\cdot}^E$  line up in (-)-right-coset  $\mathbf{1g} - \mathbf{i}_3\mathbf{g}$  order  $(r_1 - i_1), (r_2 - i_2)$ . Column-(ket) ( $\pm$ )-forms  $H_{\cdot,x}^E$  and  $H_{\cdot,y}^E$  line up in *left-coset* order  $\dots(r_1 \pm i_2), (r_2 \pm i_1)$ . Either ordering gives the same matrix. Off-diagonal components  $H_{x,y}^E$  and  $H_{y,x}^E$  have  $x$  vs.  $y$  symmetry conflicts so

coset parameters  $(r^0 \pm i_3)$  vanish.

$$\begin{aligned}
& \begin{pmatrix} H_{[x]x}^E & H_{[x]y}^E \\ H_{[y]x}^E & H_{[y]y}^E \end{pmatrix} = \\
& \begin{pmatrix} (r_0 + i_3) - \frac{1}{2}(r_1 + i_1) - \frac{1}{2}(r_2 + i_2) & 0 \cdot (r_0 + i_3) - \frac{\sqrt{3}}{2}(r_1 + i_1) + \frac{\sqrt{3}}{2}(r_2 + i_2) \\ 0 \cdot (r_0 - i_3) + \frac{\sqrt{3}}{2}(r_1 - i_1) - \frac{\sqrt{3}}{2}(r_2 - i_2) & (r_0 - i_3) - \frac{1}{2}(r_1 - i_1) - \frac{1}{2}(r_2 - i_2) \end{pmatrix}_{bra} \\
& \begin{pmatrix} H_{x[x]}^E & H_{x[y]}^E \\ H_{y[x]}^E & H_{y[y]}^E \end{pmatrix} = \\
& \begin{pmatrix} (r_0 + i_3) - \frac{1}{2}(r_1 + i_2) - \frac{1}{2}(r_2 + i_1) & 0 \cdot (r_0 - i_3) - \frac{\sqrt{3}}{2}(r_1 - i_2) + \frac{\sqrt{3}}{2}(r_2 - i_1) \\ 0 \cdot (r_0 + i_3) + \frac{\sqrt{3}}{2}(r_1 + i_2) - \frac{\sqrt{3}}{2}(r_2 + i_1) & (r_0 - i_3) - \frac{1}{2}(r_1 - i_2) - \frac{1}{2}(r_2 - i_1) \end{pmatrix}_{ket} \\
& \hspace{15em} (4.71)
\end{aligned}$$

Kets  $\mathbf{P}^x|\mathbf{r}^p\rangle = [\mathbf{P}^x|\mathbf{1}\rangle, \mathbf{P}^x|\mathbf{r}^1\rangle, \mathbf{P}^x|\mathbf{r}^2\rangle$  span induced representation  $d^x(C_2)\uparrow D_3$ , and  $\mathbf{P}^y|\mathbf{r}^p\rangle$  span  $d^y(C_2)\uparrow D_3$ . Normalized states  $\mathbf{P}^x|\mathbf{r}^p\rangle/\sqrt{2}$  and  $\mathbf{P}^y|\mathbf{r}^p\rangle/\sqrt{2}$  correspond to  $\sigma$ -type and  $\pi$ -type orbitals at vertex positions  $p=0, 1$ , or  $2$  in Fig. 4.9.

$D_3$  table in (4.27) is reordered in (4.72) below to display  $C_2(\mathbf{i}_3)$  body-basis right-coset representation bra-defined by  $\langle \mathbf{g} | = \langle \mathbf{1} | \bar{\mathbf{g}}$  or ket-defined by  $\bar{\mathbf{g}}^\dagger | \mathbf{1} \rangle = | \mathbf{g} \rangle$ . The result-



ing  $H$ -matrix in (4.27) is (4.30) reordered for cosets of  $C_2$  instead of  $C_3$ .

$D_3$ body $gg^\dagger$ form	$ \mathbf{1}\rangle$	$ \mathbf{i}_3\rangle =$ $\bar{\mathbf{i}}_3  \mathbf{1}\rangle$	$ \mathbf{r}^1\rangle =$ $\bar{\mathbf{r}}^2  \mathbf{1}\rangle$	$ \mathbf{i}_2\rangle =$ $\bar{\mathbf{i}}_3 \bar{\mathbf{r}}^2  \mathbf{1}\rangle$	$ \mathbf{r}^2\rangle =$ $\bar{\mathbf{r}}^1  \mathbf{1}\rangle$	$ \mathbf{i}_1\rangle =$ $\bar{\mathbf{i}}_3 \bar{\mathbf{r}}^1  \mathbf{1}\rangle$
$\langle \mathbf{1}  $	$\mathbf{1}$	$\bar{\mathbf{i}}_3$	$\bar{\mathbf{r}}^2$	$\bar{\mathbf{i}}_2$	$\bar{\mathbf{r}}^1$	$\bar{\mathbf{i}}_1$
$\langle \mathbf{i}_3   = \langle \mathbf{1}   \bar{\mathbf{i}}_3$	$\bar{\mathbf{i}}_3$	$\mathbf{1}$	$\bar{\mathbf{i}}_2$	$\bar{\mathbf{r}}^2$	$\bar{\mathbf{i}}_1$	$\bar{\mathbf{r}}^1$
$\langle \mathbf{r}^1   = \langle \mathbf{1}   \bar{\mathbf{r}}^1$	$\bar{\mathbf{r}}^1$	$\bar{\mathbf{i}}_2$	$\mathbf{1}$	$\bar{\mathbf{i}}_1$	$\bar{\mathbf{r}}^2$	$\bar{\mathbf{i}}_3$
$\langle \mathbf{i}_2   = \langle \mathbf{1}   \bar{\mathbf{r}}^1 \bar{\mathbf{i}}_3$	$\bar{\mathbf{i}}_2$	$\bar{\mathbf{r}}^1$	$\bar{\mathbf{i}}_1$	$\mathbf{1}$	$\bar{\mathbf{i}}_3$	$\bar{\mathbf{r}}^2$
$\langle \mathbf{r}^2   = \langle \mathbf{1}   \bar{\mathbf{r}}^2$	$\bar{\mathbf{r}}^2$	$\bar{\mathbf{i}}_1$	$\bar{\mathbf{r}}^1$	$\bar{\mathbf{i}}_3$	$\mathbf{1}$	$\bar{\mathbf{i}}_2$
$\langle \mathbf{i}_1   = \langle \mathbf{1}   \bar{\mathbf{r}}^2 \bar{\mathbf{i}}_3$	$\bar{\mathbf{i}}_1$	$\bar{\mathbf{r}}^2$	$\bar{\mathbf{i}}_3$	$\bar{\mathbf{r}}^1$	$\bar{\mathbf{i}}_2$	$\mathbf{1}$

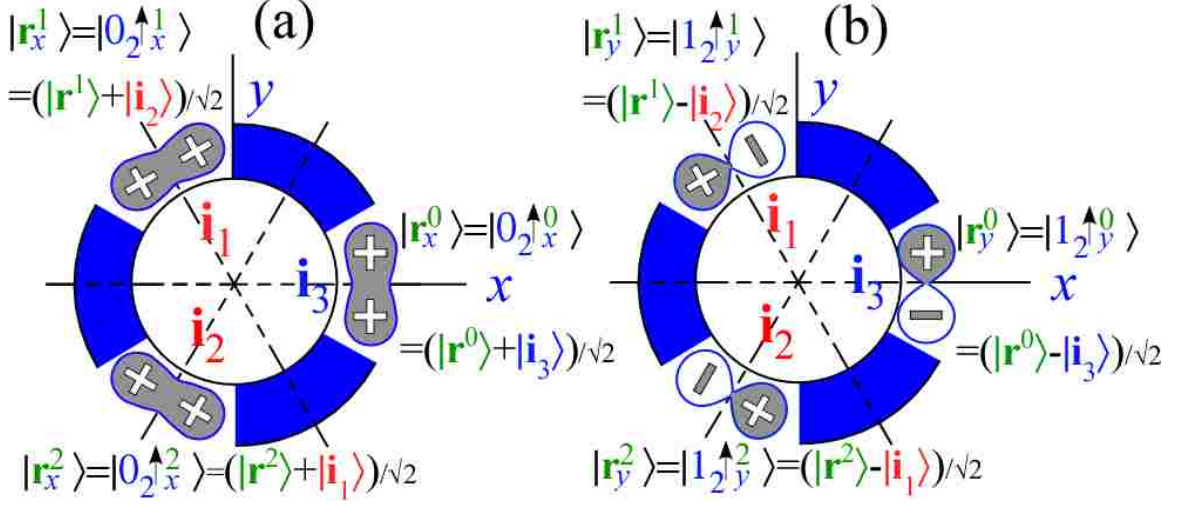
(4.72)

	$ \mathbf{1}\rangle$	$ \mathbf{i}_3\rangle$	$ \mathbf{r}^1\rangle$	$ \mathbf{i}_2\rangle$	$ \mathbf{r}^2\rangle$	$ \mathbf{i}_1\rangle$
$\langle \mathbf{1}  $	$r_0$	$i_3$	$r_2$	$i_2$	$r_1$	$i_1$
$\langle \mathbf{i}_3  $	$i_3$	$r_0$	$i_2$	$r_2$	$i_1$	$r_1$
$\langle \mathbf{r}^1  $	$r_1$	$i_2$	$r_0$	$i_1$	$r_2$	$i_3$
$\langle \mathbf{i}_2  $	$i_2$	$r_1$	$i_1$	$r_0$	$i_3$	$r_2$
$\langle \mathbf{r}^2  $	$r_2$	$i_1$	$r_1$	$i_3$	$r_0$	$i_2$
$\langle \mathbf{i}_1  $	$i_1$	$r_2$	$i_3$	$r_1$	$i_2$	$r_0$

$\Rightarrow \langle H \rangle =$

$C_2$  ordered products in (4.72) help reduce  $H$ -matrix in (4.30) to a direct sum of  $C_2$  induced reps  $(d^{0_2} \oplus d^{1_2}) \uparrow D_3$  in (4.73). Upper  $(0_2)$ -array in Eq (4.73) uses  $\sigma$ -orbital bases  $|\mathbf{r}_x^p\rangle$  in Fig. 4.9a while  $\pi$ -orbital bases  $|\mathbf{r}_y^p\rangle$  in Fig. 4.9b span the  $(1_2)$ -array.

Figure 4.9:  $C_2 \uparrow D_3$  waves at vertex points  $p = 0, 1, 2$ . (a)  $0_2 \uparrow D_3$  bases  $\mathbf{P}^x |\mathbf{r}^p\rangle \sqrt{2}$  (b)  $1_2 \uparrow D_3$  bases  $\mathbf{P}^y |\mathbf{r}^p\rangle \sqrt{2}$



	$ 0_2 \uparrow_x^0\rangle$	$ 0_2 \uparrow_x^1\rangle$	$ 0_2 \uparrow_x^2\rangle$	$ 1_2 \uparrow_y^0\rangle$	$ 1_2 \uparrow_y^1\rangle$	$ 1_2 \uparrow_y^2\rangle$	
$\langle x^0 $	$r_0 + i_3$	$r_2 + i_2$	$r_1 + i_1$	$\cdot$	$\cdot$	$\cdot$	(4.73)
$\langle x^1 $	$r_1 + i_2$	$r_0 + i_1$	$r_2 + i_3$	$\cdot$	$\cdot$	$\cdot$	
$\langle x^2 $	$r_2 + i_1$	$r_1 + i_3$	$r_0 + i_2$	$\cdot$	$\cdot$	$\cdot$	
$\langle y^0 $	$\cdot$	$\cdot$	$\cdot$	$r_0 - i_3$	$r_2 - i_2$	$r_1 - i_1$	
$\langle y^1 $	$\cdot$	$\cdot$	$\cdot$	$r_1 - i_2$	$r_0 - i_1$	$r_2 - i_3$	
$\langle y^2 $	$\cdot$	$\cdot$	$\cdot$	$r_2 - i_1$	$r_1 - i_3$	$r_0 - i_2$	

Any group component of (4.73) or combination thereof is a possible tunneling matrix.

Submatrices  $d^{0_2}(\mathbf{g}) \uparrow D_3$  shown for  $\mathbf{g}=\mathbf{r}^1$ ,  $\mathbf{i}_1$ , and  $\mathbf{i}_3$  reflect the effect of these operators

on states in Fig. 4.9a and similarly for  $d^{12}(\mathbf{g})\uparrow D_3$  in Fig. 4.9b.

$$\begin{aligned}
 \langle r_1 \bar{\mathbf{r}}^1 \rangle = r_1 & \left| \begin{array}{cc|cc} \cdot & \cdot & 1 & \cdot & \cdot & \cdot \\ 1 & \cdot & \cdot & \cdot & \cdot & \cdot \\ \cdot & 1 & \cdot & \cdot & \cdot & \cdot \\ \hline \cdot & \cdot & \cdot & \cdot & \cdot & 1 \\ \cdot & \cdot & \cdot & 1 & \cdot & \cdot \\ \cdot & \cdot & \cdot & \cdot & 1 & \cdot \end{array} \right|, & \quad \langle i_1 \bar{\mathbf{i}}_1 \rangle = i_1 & \left| \begin{array}{cc|cc} \cdot & \cdot & 1 & \cdot & \cdot & \cdot \\ \cdot & 1 & \cdot & \cdot & \cdot & \cdot \\ 1 & \cdot & \cdot & \cdot & \cdot & \cdot \\ \hline \cdot & \cdot & \cdot & \cdot & \cdot & -1 \\ \cdot & \cdot & \cdot & \cdot & -1 & \cdot \\ \cdot & \cdot & \cdot & -1 & \cdot & \cdot \end{array} \right|, \\
 \langle i_3 \bar{\mathbf{i}}_3 \rangle = i_3 & \left| \begin{array}{cc|cc} 1 & \cdot & \cdot & \cdot & \cdot & \cdot \\ \cdot & \cdot & 1 & \cdot & \cdot & \cdot \\ \cdot & 1 & \cdot & \cdot & \cdot & \cdot \\ \hline \cdot & \cdot & \cdot & -1 & \cdot & \cdot \\ \cdot & \cdot & \cdot & \cdot & \cdot & -1 \\ \cdot & \cdot & \cdot & \cdot & -1 & \cdot \end{array} \right| \tag{4.74}
 \end{aligned}$$

The  $O_2$  correlation in (4.61) implies  $d^{02}\uparrow D_3$  reduces further to  $D_3$  irreps  $A_1 \oplus E$  that label the lower band of Fig. 4.8. Meanwhile  $d^{12}\uparrow D_3$  reduces to irreps  $A_2 \oplus E$  that label the upper band of Fig. 4.8. Eq (4.50) shows  $A_1 \oplus A_2 \oplus E \oplus E$ .

## 4.5 Conclusion

This chapter uses dual sets of symmetry operator groups,  $\mathcal{G}$  and  $\bar{\mathcal{G}}$ , to define the most general  $\mathcal{G}$ -symmetric Hamiltonian and then to define general sets of eigenvectors that diagonalize the Hamiltonian. In this case, molecular symmetry operator combinations of  $g$  from the lab-frame are used to diagonalize a Hamiltonian written in terms of projection body-frame operators  $\bar{g}$ . Examples here involve ideal molecular models of  $D_3$  symmetry. The eigenstates that obey local symmetry, as shown in Eq 4.71, reduce the number of free parameters which govern the physical system and reduce the eigensolutions to analytic expressions for eigenvectors and eigenvalues.

This formalism or parameterization is shown for octahedral molecules in Chapter 5 where its power is more apparent. As molecule symmetry goes higher, parameterization typically becomes more cumbersome. The method described here reduces this difficulty by using the molecular symmetry to reduce the number of required parameters to exactly the number of physical coupling processes.

## Bibliography

- [1] Volker Heine. *Group Theory in Quantum Mechanics*. Number 9 in International Series of Monographs in Pure and Applied Mathematics. The MacMillan Company, 60 Fifth Avenue, New York 11, NY, 1960.
- [2] H. W. Kroto. *Molecular Rotation Spectra*. Dover Publications, Inc, 1992.
- [3] D. Papousek and M.R. Aliev. *Molecular Vibrational-Rotational Spectra*. Number 17 in Studies in Physical and Theoretical Chemistry. Elsevier Scientific Publishing Company, 1982.
- [4] E. Bright Wilson Jr., J. C. Decius, and Paul C. Cross. *Molecular Vibrations: The theory of infrared and Raman vibrational spectra*. McGraw-Hill Book Company, 1955.
- [5] Philip R. Bunker and Per Jensen. *Molecular Symmetry and Spectroscopy*. NRC Research Press, 2 edition, 1998.
- [6] William G. Harter. *Principles of symmetry, dynamics, and spectroscopy*. J. Wiley, 1993.
- [7] William G. Harter and Chris W. Patterson. Orbital level splitting in octahedral symmetry and SF<sub>6</sub> rotational spectra. i. qualitative features of high J levels. *Journal of Chemical Physics*, 66(11):4872, June 1977.

- [8] Arthur A. Frost and Boris Musulin. A mnemonic device for molecular orbital energies. *Journal of Chemical Physics*, 21(3):572–573, 1953.
- [9] Jon T. Hougen. Hydrogen migration tunneling effects in the rotational and vibrational spectrum of protonated acetylene  $C_2H_3^+$ . *Journal of Molecular Spectroscopy*, 123:197–227, 1987.
- [10] Jon T. Hougen. The calculation of rotational energy levels using tunneling hamiltonians. In *International Symposium on Molecular Spectroscopy*, Columbus OH, June 2009.
- [11] E. Bright Wilson Jr. Symmetry considerations concerning the splitting of vibration-rotation levels in polyatomic molecules. *Journal of Chemical Physics*, 3:818, December 1935.

## Appendix 4.A Classical $D_3$ Vibrational Modes

#### 4.A.1 Classical $D_3$ modes: Local $C_2$ and $C_3$ symmetry examples

Local symmetry theory applies to classical vibrational modes as well as to quantum tunneling. Examples of classical  $D_3$  modes given below help clarify global-*vs*-local symmetry and geometry of group projection. For example,  $D_3$  modes defined by local  $C_2(i_3)$  in Fig. 4.10 are to be compared with quantum waves in Fig. 4.8. Each mode ket  $|_{jk}^\alpha\rangle$  has the same coefficients  $D_{jk}^{\alpha*}(\mathbf{g})$  for projections in (4.37) as the waves do, but the mode shapes clearly display a vector geometry.

In particular, global  $x$ -vector modes  $|_{xx}^{E_1}\rangle$  and  $|_{xy}^{E_1}\rangle$  (left  $E_1$  column in figure) “point” along global  $x$ -direction while  $y$ -vector modes  $|_{yx}^{E_1}\rangle$  and  $|_{yy}^{E_1}\rangle$  (right  $E_1$  column) “point” along global  $y$ -direction. Each global pair  $[|_{x\ell}^{E_1}\rangle, |_{y\ell}^{E_1}\rangle](\ell = x, y)$  is projected to be an  $\mathbf{i}_3$ -symmetric-antisymmetric pair like lab unit vectors  $[|x\rangle, |y\rangle]$ . (Recall Eq (4.37).)

$$|x\rangle = \mathbf{P}^{03} |\mathbf{1}\rangle \sqrt{2} = (|\mathbf{1}\rangle + |\mathbf{i}_3\rangle) / \sqrt{2}, \quad |y\rangle = \mathbf{P}^{13} |\mathbf{1}\rangle \sqrt{2} = (|\mathbf{1}\rangle - |\mathbf{i}_3\rangle) / \sqrt{2} \quad (4.75)$$

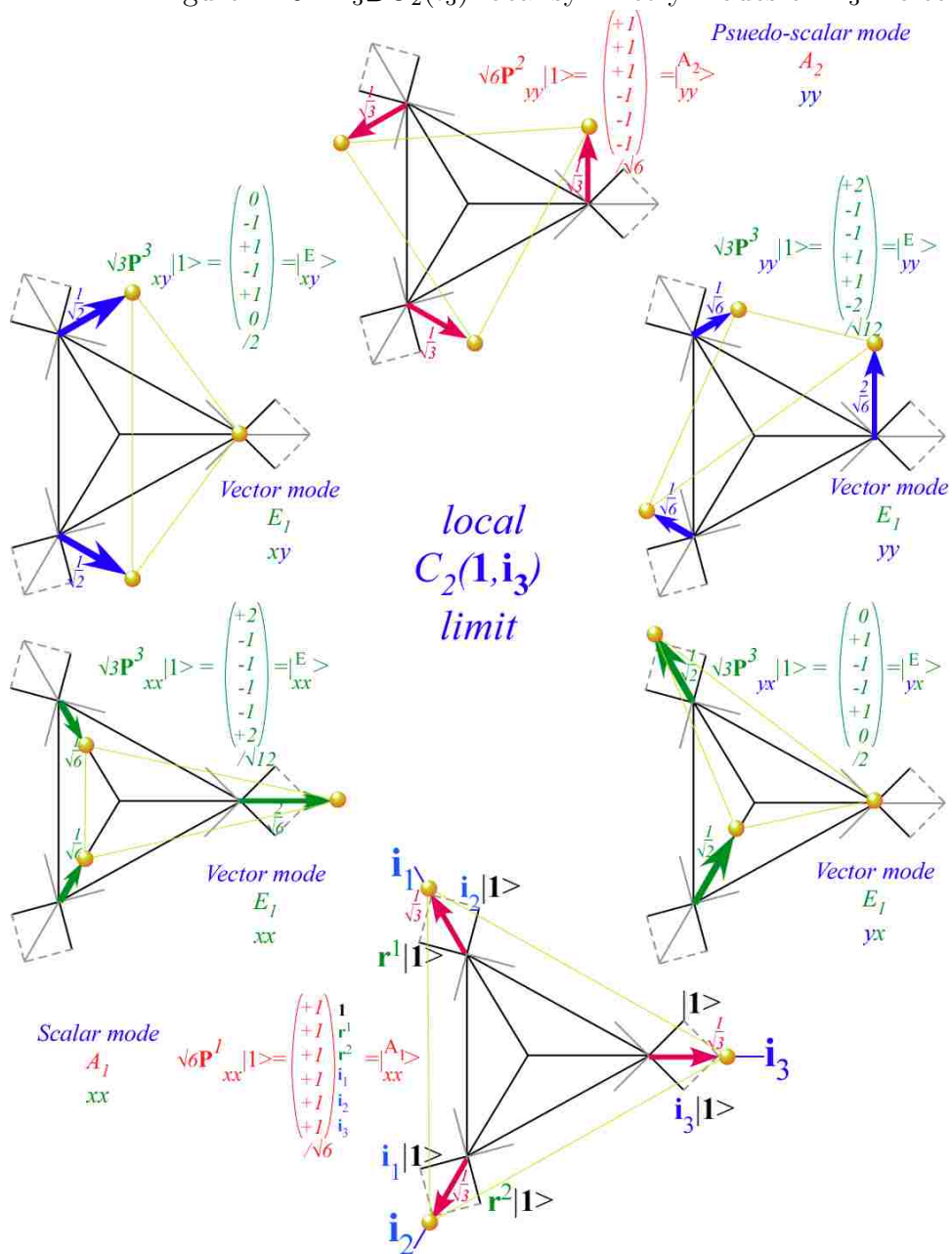
This exposes easy derivations of  $E$ -irrep  $D_{jk}^{E_1}(\mathbf{g}) = \langle j|\mathbf{g}|k\rangle$  in (4.48). Irreps in (4.46) such as  $D_{jk}^{E_1}(\mathbf{r})$  for  $120^\circ$ -rotation  $\mathbf{r}$  simply contain direction cosines  $\langle j|\mathbf{r}|k\rangle = \hat{\mathbf{e}}_j \bullet \hat{\mathbf{e}}_{r \cdot k}$  of rotated vectors  $[|\mathbf{r}|x\rangle, |\mathbf{r}|y\rangle]$  relative to original  $[|x\rangle, |y\rangle]$ .

$$\begin{aligned} \mathbf{r}|x\rangle &= -\frac{1}{2}|x\rangle + \frac{\sqrt{3}}{2}|y\rangle \\ \mathbf{r}|y\rangle &= -\frac{\sqrt{3}}{2}|x\rangle - \frac{1}{2}|y\rangle \end{aligned} \quad (4.76)$$

$$\text{implies: } \left\{ D^E(\mathbf{r}) = \begin{pmatrix} \langle x|\mathbf{r}|x\rangle & \langle x|\mathbf{r}|y\rangle \\ \langle y|\mathbf{r}|x\rangle & \langle y|\mathbf{r}|y\rangle \end{pmatrix} = \begin{pmatrix} -\frac{1}{2} & -\frac{\sqrt{3}}{2} \\ +\frac{\sqrt{3}}{2} & -\frac{1}{2} \end{pmatrix} \right.$$

This also fixes local transformations. Local  $x$ -vector modes  $|_{xx}^{E_1}\rangle$  and  $|_{yx}^{E_1}\rangle$  (lower  $E_1$  row in figure) “point” along local  $x$ -axes that are local *radial* lines while local  $y$ -vector modes  $|_{xy}^{E_1}\rangle$  and  $|_{yy}^{E_1}\rangle$  (upper  $E_1$  row) “point” along local  $y$ -axes that are local *angular* lines. If global symmetry meets local anti-symmetry as in  $|_{xy}^{E_1}\rangle$  (or *vice-versa* in  $|_{yx}^{E_1}\rangle$ ), a zero appears on the  $\mathbf{i}_3$ -axis in Fig. 4.10. Singlet modes  $|_{xx}^{A_1}\rangle$  and  $|_{yy}^{A_2}\rangle$  avoid

Figure 4.10:  $D_3 \supset C_2(i_3)$ -local symmetry modes of  $X_3$  molecule





such conflicts by being one or the other.

For group-defined cases like Fig. 4.10, symmetry arguments alone determine normal modes that usually require diagonalizing a  $K$ -matrix (below) just as tunneling states (Fig. 4.8) usually require diagonalizing an  $H$ -matrix.

### Comparing $K$ -Matrix and $H$ -matrix formulation

Classical modes are eigenvectors of force-field matrix  $K$  or operator  $\mathbf{K}$  that is a linear function of spring constants ( $k_0$ , *etc.* in Fig. 4.11) for a harmonic approximate potential  $V(\mathbf{x})$  that is a quadratic  $K$ -form of coordinates  $x_a$  based on six  $D_3$ -labeled axes  $\hat{\mathbf{x}}^a$  or  $|a\rangle$  shown in Fig. 4.10. Each  $\mathbf{K}$  component  $K_{ab} = \langle a | \mathbf{K} | b \rangle$  is a sum over spring  $k$ -constants that connect axis- $\mathbf{x}^a$  to axis- $\mathbf{x}^b$  multiplied by factor  $(\hat{\mathbf{k}}_a \bullet \hat{\mathbf{x}}^a)(\hat{\mathbf{k}}_b \bullet \hat{\mathbf{x}}^b)$  for projecting spring  $k$ 's end vectors  $\hat{\mathbf{k}}_a$  and  $\hat{\mathbf{k}}_b$  onto  $\hat{\mathbf{x}}^a$  and  $\hat{\mathbf{x}}^b$  at respective connections. (A straight-line spring has equal  $\hat{\mathbf{k}}_a = \hat{\mathbf{k}}_b$ . Curvilinear springs must only have  $\hat{\mathbf{k}}$ -ends with equal sense ( $\rightarrow\rightarrow$ ) or ( $\leftarrow\leftarrow$ ) of spring direction. Either direction gives the same  $K_{ab}$ .)

$$\begin{aligned}
 V(x) &= \sum_{(k)} \frac{1}{2} \langle x | \mathbf{K} | x \rangle \quad \text{where: } |x\rangle = \sum_a x^a |a\rangle, \quad (a, b) = (1, r^1, r^2, i_1, i_2, i_3) \\
 &= \frac{1}{2} \sum_{a,b} K_{ab} x_a x_b \quad \text{where: } K_{ab} = \begin{cases} \sum_{(k)} \frac{k}{2} (\hat{\mathbf{k}}_a \bullet \hat{\mathbf{x}}^a)^2 & \text{if } : a = b \\ - \sum_{(k)} k (\hat{\mathbf{k}}_a \bullet \hat{\mathbf{x}}^a)(\hat{\mathbf{k}}_b \bullet \hat{\mathbf{x}}^b) & \text{if } : a \neq b \end{cases}
 \end{aligned} \tag{4.77}$$

This sum of harmonic Hooke ( $kx^2/2$ )-potentials has diagonal  $K_{aa}$  terms followed by off-diagonal terms ( $K_{ab} = K_{ba}$ ).

$$\begin{aligned}
 V(x) &= \sum_{(k)} \frac{k}{2} (\Delta \ell_k)^2 = \sum_{(k)} \frac{k}{2} \sum_{a,b} (\hat{\mathbf{k}}_a \bullet \mathbf{x}^a - \hat{\mathbf{k}}_b \bullet \mathbf{x}^b)^2 \\
 &= \sum_{(k)} \frac{k}{2} \sum_a (\hat{\mathbf{k}}_a \bullet \hat{\mathbf{x}}^a)^2 x_a^2 - \sum_{(k)} k \sum_{a \neq b} (\hat{\mathbf{k}}_a \bullet \hat{\mathbf{x}}^a)(\hat{\mathbf{k}}_b \bullet \hat{\mathbf{x}}^b) x_a x_b
 \end{aligned} \tag{4.78}$$

The classical equation of coupled harmonic motion is a Newtonian  $\mathbf{F} = \mathbf{M} \cdot \mathbf{a}$  relation of a  $n$ -dimensional force vector  $\mathbf{F}$ , acceleration vector  $\mathbf{a}$ , and mass operator  $\mathbf{M}$ . The latter is a unit-matrix-multiple  $M \cdot \mathbf{1}$  for the  $D_3$ -symmetric case treated here. Driving force  $\mathbf{F}$  is a (-)derivative of potential (4.77) that becomes a  $\mathbf{K}$ -matrix expression.

$$-M\partial_t^2 x^a = \frac{\partial V}{\partial x^a} = \sum_b K_{ab}x^b \quad (4.79)$$

It is instructive to compare this classical equation of motion to that of Schrodinger's equation for quantum motion.

$$i\hbar\partial_t\psi^a = \sum_b H_{ab}\psi^b \quad (4.80)$$

Squaring quantum time generator  $i\hbar\partial_t = \mathbf{H}$  yields equations having classical form (4.79) with  $K = H^2$  and  $M = \hbar^2$ .

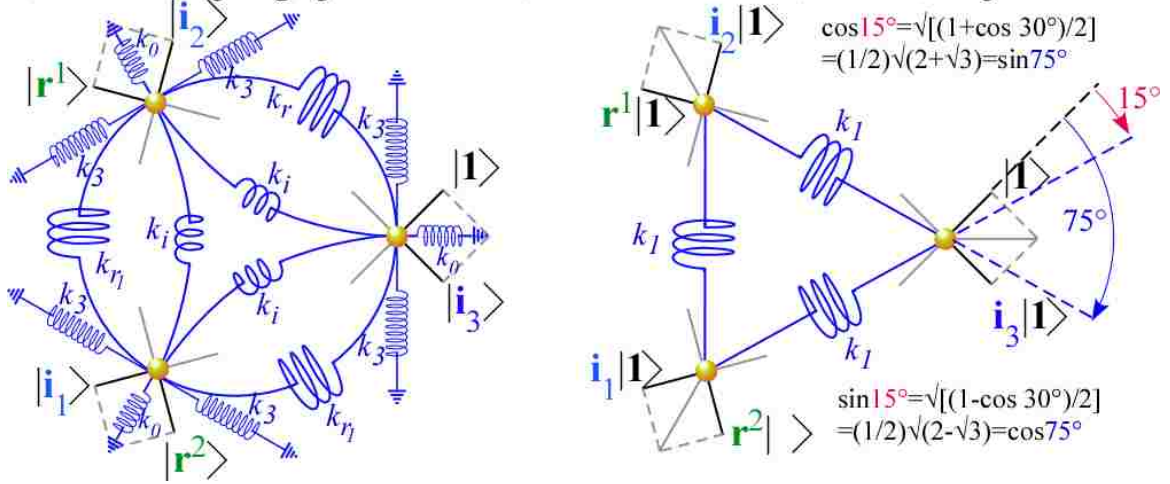
$$-\hbar^2\partial_t^2\psi^a = \sum_b K_{ab}\psi^b \text{ where: } K = H^2 \quad (4.81)$$

The  $(\mathbf{H}/\hbar)$ -eigenvalues are quantum angular frequencies  $\epsilon_m/\hbar = \omega_m$ . The  $(\mathbf{K}/M)$ -eigenvalues are classical *squared* angular frequencies  $k_m/M = \omega_m^2$ . The former is Planck's oscillator frequency relation  $\epsilon = \hbar\omega$ . The latter is Hooke's relation  $k/M = \omega^2$ . Apart from normalization, eigenvectors of quantum  $H$  are identical to those of classical  $K$  and either eigenvalue set corresponds to the respective energy spectrum.

### Comparing $K$ -Matrix and $H$ -matrix eigensolutions for local $D_3 \supset C_2(i_3)$

The preceding relates eigensolutions (4.51) and (4.52) of quantum Hamiltonian  $H$ -matrix in (4.30) with those of a classical  $K$ -matrix. In particular, eigenvectors of  $H$  found using  $D$ -matrices in (4.48) or (??) also serve as mode-eigenkets in Fig. 4.10 that diagonalize a  $D_3 \supset C_2(i_3)$ -locally-symmetric  $K$ -matrix. With this symmetry,  $K$

Figure 4.11:  $X_3$  spring models with local symmetry: (a)  $D_3 \supset C_2(i_3)$  (b) Mixed



cannot couple radial (local- $x$ ) and angular (local- $y$ ) modes and is left with just four independent real group-based parameters  $g_a = r_0, r_1, i_{12},$  and  $i_3$  allowed for  $D_3 \supset C_2(i_3)$ -symmetric  $H$  in (4.52). These relate to four spring  $k_h$ -constants in Fig. 4.11(a).

Only 1<sup>st</sup>-row parameters  $g_b = \langle \mathbf{1} | \mathbf{K} | \mathbf{g}_b \rangle = K_{1b}$  of the force matrix  $K_{ab}$  are needed for the spring model in Fig. 4.11(a). That model includes  $k_r$ (angular) and  $k_i$ (radial) constants for internal connections between masses. The  $k_3$ (angular) and  $k_0$ (radial) constants represent external connections between each mass and an outside lab frame.

Generic group parameters  $g_b = H_{1b}$ , labeled  $[r_0, r_1, r_2, i_1, i_2, i_3]$  for the  $H$ -matrix in (4.30), are now applied to  $g_b = K_{1b}$ . The  $g_b$  are to be related to spring-constants  $k_j$  using coordinate-spring projection cosine factors  $(\hat{\mathbf{k}}_1 \bullet \hat{\mathbf{x}}^1)(\hat{\mathbf{k}}_b \bullet \hat{\mathbf{x}}^b)$  in (4.77) and (4.78). The usual harmonic limit assumes small vibrational amplitudes ( $x_b \ll 1$ ) for which direction of spring end vectors  $\hat{\mathbf{k}}^1$  or  $\hat{\mathbf{k}}^b$  do not vary to 1<sup>st</sup>-order, and so, for lab-fixed  $\hat{\mathbf{x}}^a$  the

$K_{ab}$  are constants.

$$\begin{array}{c|cccccc}
|g_b\rangle & |\mathbf{1}\rangle & |\mathbf{r}^1\rangle & |\mathbf{r}^2\rangle & |\mathbf{i}_1\rangle & |\mathbf{i}_2\rangle & |\mathbf{i}_3\rangle \\
\hline
\langle \mathbf{1} | \mathbf{K} | g_b \rangle = & k_i/2 & k_i/2 & k_i/2 & k_i/2 & k_i/2 & k_i/2 \\
& +k_r & -k_r/2 & -k_r/2 & +k_r/2 & +k_r/2 & -k_r \\
& +k_3 & +0 & +0 & +0 & +0 & -k_3 \\
& +k_0/2 & +0 & +0 & +0 & +0 & +k_0/2
\end{array} \quad (4.82)$$

One may visualize each  $-K_{1b}$  as the acceleration of  $x_1$  due to setting a (tiny) unit  $x_b$  in (4.79). Diagonal  $-K_{11}$  must be negative or else  $x_1$  blows up. Higher order *anharmonic* terms are needed to describe effects of rotating  $\hat{\mathbf{k}}^b$  or  $\hat{\mathbf{x}}^b$  and such models are likely to suffer from classical stochastic (chaotic) motion.

Substitution of generic  $g_a$  from (4.82) into reduced  $D_3 \supset C_2(i_3)$ -symmetric  $H$ -matrix in (4.51) or (4.52) gives  $K$ -matrix eigenvalues  $K_{\ell\ell}^\alpha$  due to each spring  $k_i$ ,  $k_r$ ,  $k_3$ , or  $k_0$  in Fig. 4.11(a) separately or together. Modes in Fig. 4.10 remain *eigenmodes* for all values of four spring constants  $k_i$ ,  $k_r$ ,  $k_3$ , and  $k_0$  since none can mix local  $x$ -and- $y$ -symmetry.

$$\begin{aligned}
K_{xx}^{A_1} &= r_0 + r_1 + r_1^* + i_1 + i_2 + i_3 = k_0 + 3k_i \\
K_{yy}^{A_2} &= r_0 + r_1 + r_1^* - i_1 - i_2 - i_3 = 3k_3 \\
\begin{pmatrix} K_{xx}^E & K_{xy}^E \\ K_{yx}^E & K_{yy}^E \end{pmatrix} &= \frac{1}{2} \begin{pmatrix} 2r_0 - r_1 - r_1^* - i_1 - i_2 + 2i_3 & \sqrt{3}(-r_1 + r_1^* - i_1 + i_2) \\ \sqrt{3}(-r_1^* + r_1 - i_1 + i_2) & 2r_0 - r_1 - r_1^* + i_1 + i_2 - 2i_3 \end{pmatrix} \\
&= \begin{pmatrix} k_0 & 0 \\ 0 & k_3 + 2k_r \end{pmatrix}
\end{aligned} \quad (4.83)$$

Any set of four  $K$ -matrix eigenvalues  $k^{A_1}$ ,  $k^{A_2}$ ,  $k_x^E$ , and  $k_y^E$  is arithmetically possible by adjusting the four spring constants. However, their arrangement in Fig. 4.10 (This was drawn to match tunneling states in Fig. 4.8.) is impossible without negative

$k$ -values that would give classical instability. As shown below, free ring molecules often have  $A_1$ -stretching modes among the highest frequencies. In contrast, tunneling amplitudes are often negative so their  $A_1$  states lie low. As a rule, fewer quantum nodes imply lower energy.

### **$K$ -Matrix eigensolutions for broken local symmetry**

In some ways the direct- $k_1$ -connection spring model of Fig. 4.11(b) is quite the opposite of the  $D_3 \supset C_2(i_3)$  model just treated since it involves maximal (50-50) mixing of  $x$  and  $y$  local symmetry. Below are recalculated generic  $g_b = \langle \mathbf{1} | \mathbf{K} | g_b \rangle$  in terms of direct spring-constants  $k_1$  using (4.78) with projection cosines listed in Fig. 4.11(b).

$ g_b\rangle$	$ \mathbf{1}\rangle$	$ \mathbf{r}^1\rangle$	$ \mathbf{r}^2\rangle$	$ \mathbf{i}_1\rangle$	$ \mathbf{i}_2\rangle$	$ \mathbf{i}_3\rangle$
$\langle \mathbf{1}   \mathbf{K}   g_b \rangle =$	$k_1(\cos^2 75^\circ$	$k_1 \cos 75^\circ$	$k_1 \cos 15^\circ$	$k_1 \cos 15^\circ$	$k_1 \cos 75^\circ$	$k_1(\cos^2 75^\circ$
	$+ \cos^2 15^\circ)$	$\cdot \cos 15^\circ$	$\cdot \cos 75^\circ$	$\cdot \cos 15^\circ$	$\cdot \cos 75^\circ$	$- \cos^2 15^\circ)$
	$= k_1$	$= \frac{k_1}{4}$	$= \frac{k_1}{4}$	$= \frac{k_1(2 - \sqrt{3})}{4}$	$= \frac{k_1(2 + \sqrt{3})}{4}$	$= \frac{k_1}{2}$

(4.84)

Again, a substitution of generic  $g_a$  from (4.84) into reduced  $H$ -matrix (4.52) gives a reduced  $K$ -matrix like (4.83), but now the  $E$ -symmetry submatrix is not diagonal.

$$\begin{aligned}
 K_{xx}^{A_1} &= 3k_1 \\
 K_{yy}^{A_2} &= 0 \\
 \begin{pmatrix} K_{xx}^E & K_{xy}^E \\ K_{yx}^E & K_{yy}^E \end{pmatrix} &= \begin{pmatrix} \frac{3k_1}{4} & \frac{3k_1}{4} \\ \frac{3k_1}{4} & \frac{3k_1}{4} \end{pmatrix}
 \end{aligned}
 \tag{4.85}$$

Eigenvectors of the  $E$ -submatrix are symmetric (+) and antisymmetric (-) mixtures of  $x$  and  $y$  local symmetry states.

$$\begin{aligned} \mathbf{K} \begin{vmatrix} E \\ g(-) \end{vmatrix} &= \mathbf{K} \left( \begin{vmatrix} E \\ gx \end{vmatrix} - \begin{vmatrix} E \\ gy \end{vmatrix} \right) \frac{1}{\sqrt{2}} = \frac{3k_1}{2} \begin{vmatrix} E \\ g(-) \end{vmatrix}, \\ \mathbf{K} \begin{vmatrix} E \\ g(+) \end{vmatrix} &= \mathbf{K} \left( \begin{vmatrix} E \\ gx \end{vmatrix} + \begin{vmatrix} E \\ gy \end{vmatrix} \right) \frac{1}{\sqrt{2}} = 0 \begin{vmatrix} E \\ g(+) \end{vmatrix}, \quad g = (x, y). \end{aligned} \quad (4.86)$$

Fig. 4.12 shows (50-50  $\pm$ )-mixing due to  $k_1$ . It distinguishes genuine vector modes ( $|^E_{x,(-)}\rangle$  or  $|^E_{y,(-)}\rangle$ ) and the scalar breathing mode ( $|^{A_1}_{x,x}\rangle$ ) from non-genuine (low or zero-frequency) vector modes of pure  $x$  or  $y$ -translation ( $|^E_{x,(+)}\rangle$  or  $|^E_{y,(+)}\rangle$ ) and rigid rotation (pseudo-scalar  $|^{A_2}_{y,y}\rangle$ ). The  $i_3$ -local symmetry is wiped out by direct connection- $k_1$ .

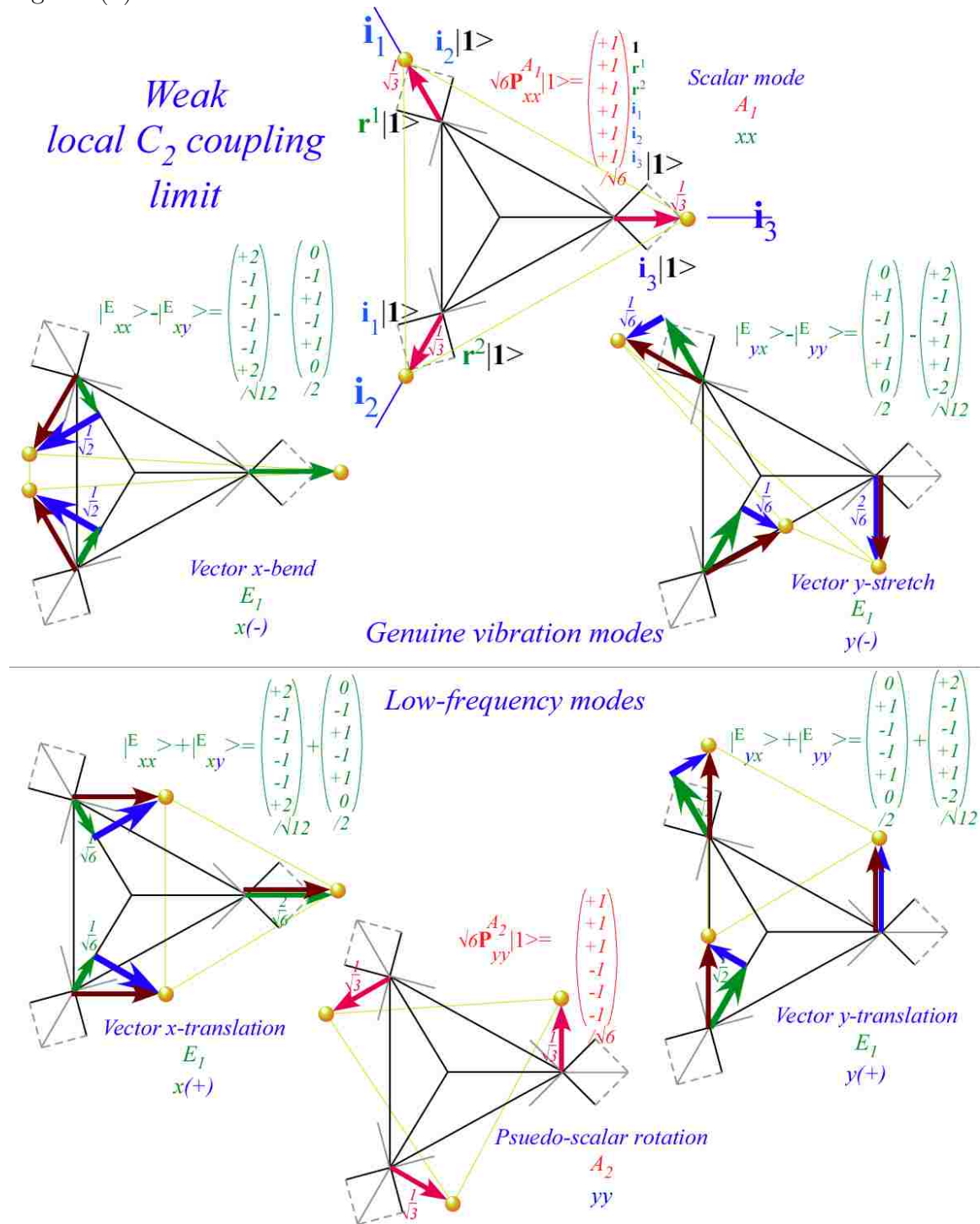
In order to reestablish approximate  $D_3 \supset C_2(i_3)$ -local-symmetry there needs to be a  $C_2(i_3)$ -“*locale*” provided by lab-grounded potential springs such as those with constants  $k_3$  and  $k_0$  in Fig. 4.11(a). Adding these in the form of (4.83) to (4.85) causes a transition between the two extremes. If the difference ( $k_3 + 2k_r - k_0$ ) between eigenvalues (4.83) begins to dominate the off-diagonal component ( $3k_1/4$ ) of (4.85), then mixed  $E$ -modes of Fig. 4.12 begin to recover  $D_3 \supset C_2(i_3)$  locality seen in Fig. 4.10 .

Meanwhile the constant  $k_3$  that determines eigenvalue  $k_{y,y}^{A_2}$  does not affect locality for either of the singlet  $A_1$  or  $A_2$  modes. Singlet eigenvectors are non-negotiable as long as master symmetry  $D_3$  holds.

### **$K$ -Matrix eigensolutions for $D_3 \supset C_3$ symmetry**

Another choice for  $D_3$  local symmetry is the  $C_3$  subgroup of Eq (4.38) corresponding to a strong chiral perturbation by internal rotation, spin, or  $B$ -field. The  $E$ -submatrix in (4.83) with zero generic reflection parameters ( $i_1=i_2=i_3=0$ ) may take a purely chiral  $C_3$  form if the generic rotation parameters  $r_1$  and  $r_2=r_1^*$  are purely imaginary corresponding to velocity dependent force. ( $r_1=ir$  and  $r_2=-ir$ . Here  $K$  is assumed

Figure 4.12: Mixed-local symmetry modes of direct- $k_1$ -coupled  $X_3$  model in Fig.4.11(b).



Hermitian self-conjugate as was  $H$ .)

$$\begin{aligned}
K_{xx}^{A_1} &= r_0 \\
K_{yy}^{A_2} &= r_0 \\
\begin{pmatrix} K_{xx}^E & K_{xy}^E \\ K_{yx}^E & K_{yy}^E \end{pmatrix} &= \begin{pmatrix} r_0 & -ir\sqrt{3} \\ +ir\sqrt{3} & r_0 \end{pmatrix} \quad r_1 = ir = -r_2^* \\
& \quad i_1 = i_2 = i_3 = 0
\end{aligned} \tag{4.87}$$

$C_3$   $E$ -eigenvectors have local  $x \pm iy = (\pm 1)_3$  combinations that exhibit purely circular right  $R = (+1)_3$  and left  $L = (-1)_3$  polarization orbits of  $C_3$  symmetry shown in Fig. 4.13. (Recall  $C_3$  splitting in Eq (4.38).)

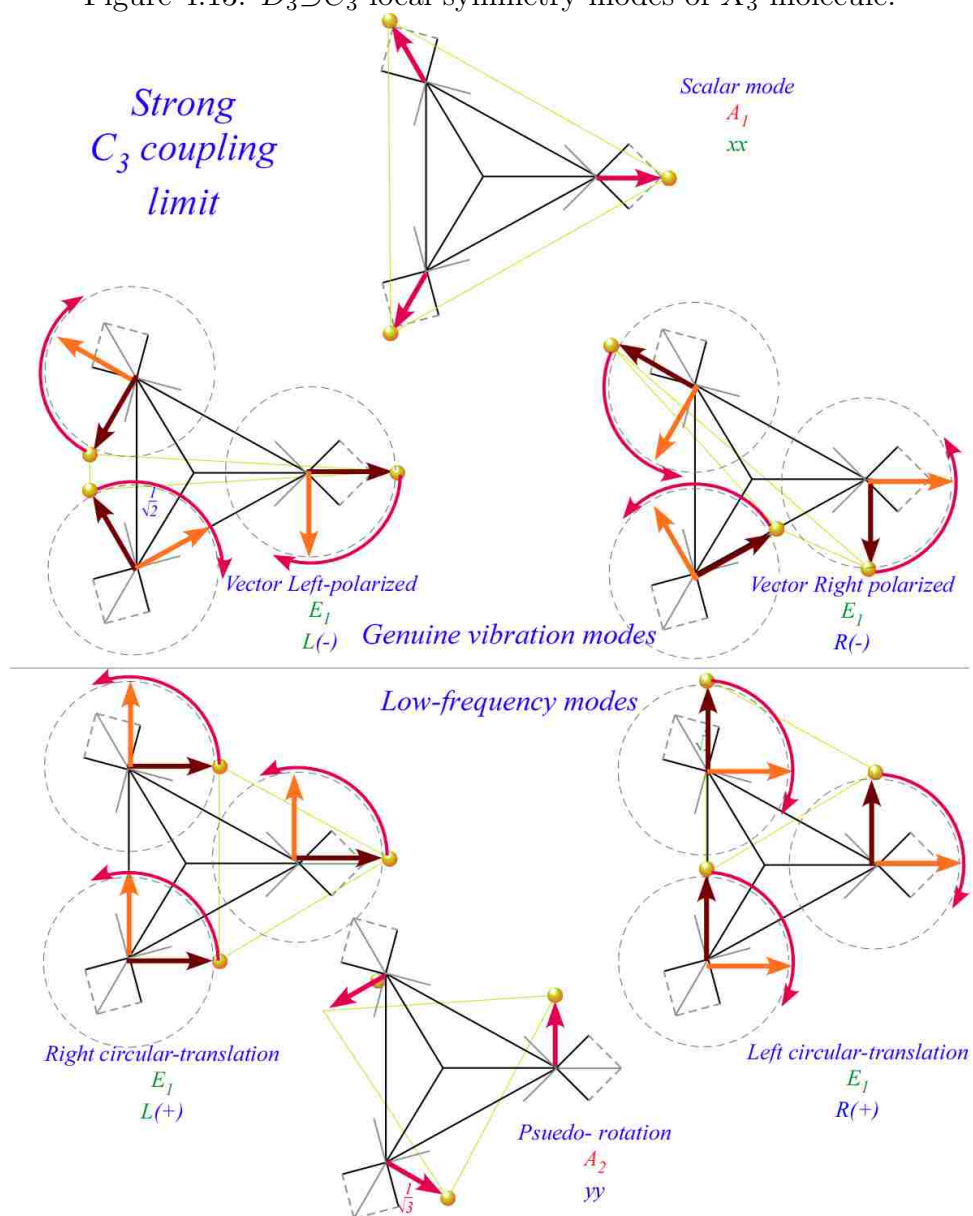
$$\begin{aligned}
\mathbf{K} \begin{vmatrix} E \\ g(+1)_3 \end{vmatrix} &= \mathbf{K} \left( \begin{vmatrix} E \\ gx \end{vmatrix} + i \begin{vmatrix} E \\ gy \end{vmatrix} \right) \frac{1}{\sqrt{2}} = +r\sqrt{3} \begin{vmatrix} E \\ g(+1)_3 \end{vmatrix}, \\
\mathbf{K} \begin{vmatrix} E \\ g(-1)_3 \end{vmatrix} &= \mathbf{K} \left( \begin{vmatrix} E \\ gx \end{vmatrix} - i \begin{vmatrix} E \\ gy \end{vmatrix} \right) \frac{1}{\sqrt{2}} = -r\sqrt{3} \begin{vmatrix} E \\ g(-1)_3 \end{vmatrix}, \quad g = (x, y).
\end{aligned} \tag{4.88}$$

Pure  $C_3$  symmetry is a normal subgroup and restricts  $k_{x,x}^{A_1}$  and  $k_{y,y}^{A_2}$  to become degenerate. Both the scalar  $|_{0_3,0_3}^{A_1}\rangle$  and pseudoscalar  $|_{0_3,0_3}^{A_2}\rangle$  state are both labeled equally by  $(0)_3$  symmetry. Local symmetry effectively goes global in the pure  $C_3$ -case where all internal coupling is zero.

Any internal or external parameters may split the  $A_1$ - $A_2$  degeneracy and mix the  $C_3$  states to form elliptical polarization orbits. This is most efficiently calculated using  $SU(2)$  analysis.



Figure 4.13:  $D_3 \supset C_3$ -local symmetry modes of  $X_3$  molecule.



## Chapter 5

### Local Symmetry Tunneling In Octahedral Molecules

## 5.1 Chapter Summary

This chapter uses the developments of Chapter 4 and applies them to octahedral spherical-top molecules. Particular care is taken with local symmetry subduction to parameterize all possible splittings of rotational clusters (superfine structure). This parameterization can form a basis from which both tunneling splittings and tunneling strengths may be evaluated. Local symmetries  $C_2$ ,  $C_3$  and  $C_4$  introduced in chapter 3 are detailed.

The power of this process is demonstrated for the  $C_2$  local-symmetry clusters possible in octahedral spherical-top molecules. Though this cluster has more degeneracy, the choice of  $C_2$  is convenient as the formulae describing its behavior are more compact. Moreover, this formalism, while easiest for the  $C_2$  cluster is exceedingly difficult to parameterize using other methods.

## 5.2 Octahedral symmetry analysis

Octahedral-cubic rotational symmetry  $O$  operations are modeled in Fig. 5.1. Rotation inversion symmetry  $O_h=O\times C_i$  operations are modeled in Fig. 5.2. In each case the larger  $\mathbf{g}$ -symbols label position ket states  $|\mathbf{g}\rangle=\mathbf{g}|1\rangle$  while smaller  $\mathbf{g}$ -symbols label axes of rotation in  $O$  or planes of reflection in  $O_h$ . Three Cartesian  $C_4$  axes of anti-clockwise  $90^\circ$  rotations  $\mathbf{R}_x$ ,  $\mathbf{R}_y$ , and  $\mathbf{R}_z$  define directions  $[100]$ ,  $[010]$ , and  $[001]$ , respectively. Their inverses  $\tilde{\mathbf{R}}_x=\mathbf{R}_x^3$ ,  $\tilde{\mathbf{R}}_y=\mathbf{R}_y^3$ , and  $\tilde{\mathbf{R}}_z=\mathbf{R}_z^3$  are also  $90^\circ$  rotations but around negative axes  $[\bar{1}00]$ ,  $[0\bar{1}0]$ , and  $[00\bar{1}]$ . A shorthand notation for  $180^\circ$  Cartesian rotations is  $\rho_x=\mathbf{R}_x^2$ ,  $\rho_y=\mathbf{R}_y^2$ , and  $\rho_z=\mathbf{R}_z^2$ . Trigonal  $C_3$  axes of anti-clockwise  $120^\circ$  rotations  $\mathbf{r}_1$ ,  $\mathbf{r}_2$ ,  $\mathbf{r}_3$ , and  $\mathbf{r}_4$  lie along  $[111]$ ,  $[\bar{1}\bar{1}1]$ ,  $[\bar{1}1\bar{1}]$ , and  $[\bar{1}\bar{1}\bar{1}]$ , respectively, while axes of inverses  $\tilde{\mathbf{r}}_1=\mathbf{r}_1^2$ ,  $\tilde{\mathbf{r}}_2=\mathbf{r}_2^2$ ,  $\tilde{\mathbf{r}}_3=\mathbf{r}_3^2$ , and  $\tilde{\mathbf{r}}_4=\mathbf{r}_4^2$  lie along the opposite directions  $[\bar{1}\bar{1}\bar{1}]$ ,  $[11\bar{1}]$ ,  $[1\bar{1}\bar{1}]$ , and  $[1\bar{1}1]$ , respectively.

There are six  $C_2$  axes of  $180^\circ$  rotations  $\mathbf{i}_1$ ,  $\mathbf{i}_2$ ,  $\mathbf{i}_3$ ,  $\mathbf{i}_4$ ,  $\mathbf{i}_5$ , and  $\mathbf{i}_6$  located along  $[101]$ ,  $[\bar{1}01]$ ,  $[110]$ ,  $[\bar{1}10]$ ,  $[011]$ , and  $[0\bar{1}1]$ , respectively. This completes the five classes of  $O$ :

$[\mathbf{1}]$ ,  $[\mathbf{r}_{1..4}, \tilde{\mathbf{r}}_{1..4}]$ ,  $[\rho_{xyz}]$ ,  $[\mathbf{R}_{xyz}, \tilde{\mathbf{R}}_{xyz}]$ , and  $[\mathbf{i}_{1..6}]$ . Including the rotations with inversion  $\mathbf{I}$  yields five more classes of  $O_h$ :  $[\mathbf{I}]$ ,  $[\mathbf{s}_{1..4}, \tilde{\mathbf{s}}_{1..4}]$ ,  $[\rho_{xyz}]$ ,  $[\mathbf{S}_{xyz}, \tilde{\mathbf{S}}_{xyz}]$ , and  $[\sigma_{1..6}]$  where  $\mathbf{s}_{1..4}=\mathbf{I} \cdot \mathbf{r}_{1..4}$ ,  $[\sigma_{xyz}]=[\mathbf{I} \cdot \rho_{xyz}]$ ,  $[\mathbf{S}_{xyz}]=[\mathbf{I} \cdot \mathbf{R}_{xyz}]$ , and  $[\sigma_{1..6}]=[\mathbf{I} \cdot \mathbf{i}_{1..6}]$ .  $\sigma$ 's are mirror-plane reflections in Fig. 5.2.

Fig. 5.1 and Fig. 5.2 are useful for quickly evaluating group products and for identifying local symmetry subgroups and their cosets. Three of the largest cyclic subgroups of  $O$  are tetragonal  $C_4$  such as  $C_4=[\mathbf{1}, \mathbf{R}_z, \mathbf{R}_z^2=\rho_z, \mathbf{R}_z^3=\tilde{\mathbf{R}}_z]$  displayed on the  $\mathbf{R}_z$ -face of the cube in Fig. 5.1. In Fig. 5.2 the same face displays local symmetry  $C_{4v}=[\mathbf{1}, \rho_z, \mathbf{R}_z, \tilde{\mathbf{R}}_z, \sigma_4, \sigma_x, \sigma_3, \sigma_y]$  that contains  $C_4$  plus pairs of diagonal mirror reflections  $[\sigma_4=\mathbf{I} \cdot \mathbf{i}_4, \sigma_3=\mathbf{I} \cdot \mathbf{i}_3]$  and Cartesian mirror reflections  $[\sigma_x=\mathbf{I} \cdot \rho_x, \sigma_y=\mathbf{I} \cdot \rho_y]$ . Each pair  $[\sigma_x, \sigma_y]$  and  $[\sigma_3, \sigma_4]$  is a  $C_{4v}$  class as is rotation pair  $[\mathbf{R}_z, \tilde{\mathbf{R}}_z]$  or, singly,  $\mathbf{1}$  and  $\rho_z$ . The other five cube faces display cosets of the tetragonal subgroups  $C_{4v} \supset C_4$  of  $O_h \supset O$ .

Fig. 5.1 shows six  $O$ -cosets  $\mathbf{g} \cdot C_4$  of  $C_4=[\mathbf{1}, \mathbf{R}_z, \rho_z, \tilde{\mathbf{R}}_z]$ . Opposite  $\rho_x$ -face has coset  $\rho_x \cdot C_4=[\rho_x, \mathbf{i}_4, \rho_y, \mathbf{i}_3]$  in that order. The  $\mathbf{r}_1$ -face shows coset  $\mathbf{r}_1 \cdot C_4=[\mathbf{r}_1, \mathbf{i}_1, \mathbf{r}_4, \mathbf{R}_y]$  in upper right of Fig. 5.1, and the opposite  $\mathbf{r}_2$ -face has coset  $\mathbf{r}_2 \cdot C_4=[\mathbf{r}_2, \mathbf{i}_2, \mathbf{r}_3, \tilde{\mathbf{R}}_y]$ . Top and bottom faces have cosets  $\tilde{\mathbf{r}}_1 \cdot C_4=[\tilde{\mathbf{r}}_1, \tilde{\mathbf{R}}_x, \tilde{\mathbf{r}}_3, \mathbf{i}_6]$  and  $\tilde{\mathbf{r}}_2 \cdot C_4=[\tilde{\mathbf{r}}_2, \mathbf{R}_x, \tilde{\mathbf{r}}_4, \mathbf{i}_5]$ .

Each  $\mathbf{g} \cdot C_4$ -coset element  $\mathbf{g} \cdot \mathbf{R}_z^p$  ( $p = 0..3$ ) transforms the  $\mathbf{1}$ -face to the same  $\mathbf{g}$ -face and orients it according to a  $C_4$  element  $\mathbf{R}_z^p$  as it permutes the list of its elements accordingly. Each face may be labeled by any element  $\mathbf{g} \cdot \mathbf{R}_z^p$  in its coset. An  $\mathbf{i}$ -class labeling by  $\mathbf{1}$ ,  $\mathbf{i}_3$ (or  $\mathbf{i}_4$ ),  $\mathbf{i}_1$ ,  $\mathbf{i}_2$ ,  $\mathbf{i}_6$ , and  $\mathbf{i}_5$  of  $C_4$  cosets in Fig. 5.1 is as good as any other.

Fig. 5.2 shows six  $O_h$ -cosets of  $C_{4v}$  (counting  $C_{4v}$  itself) in a geometric display that also shows eight trigonal cosets of  $C_{3v} \supset C_3$ -[111] and twelve dihedral cosets of  $C_{2v} \supset C_2$ -[101]. Fig. 5.3 shows three symmetry points of Fig. 5.2 forming a triangular cell with sides that are on reflection planes.

An order-8 axial symmetry  $C_{4v}$  lies on the tetragonal- $z$ -[001]-axis of a cube face or octahedral vertex. An order-6  $C_{3v}$  lies on the trigonal-[111]-axis of a cube vertex or octahedral face. Finally, there is a dihedral- $C_{2v}$  [110]-axis of a cube or octahedral

Figure 5.1:  $O$  operators distributed in cosets of  $C_4 \supset C_2$

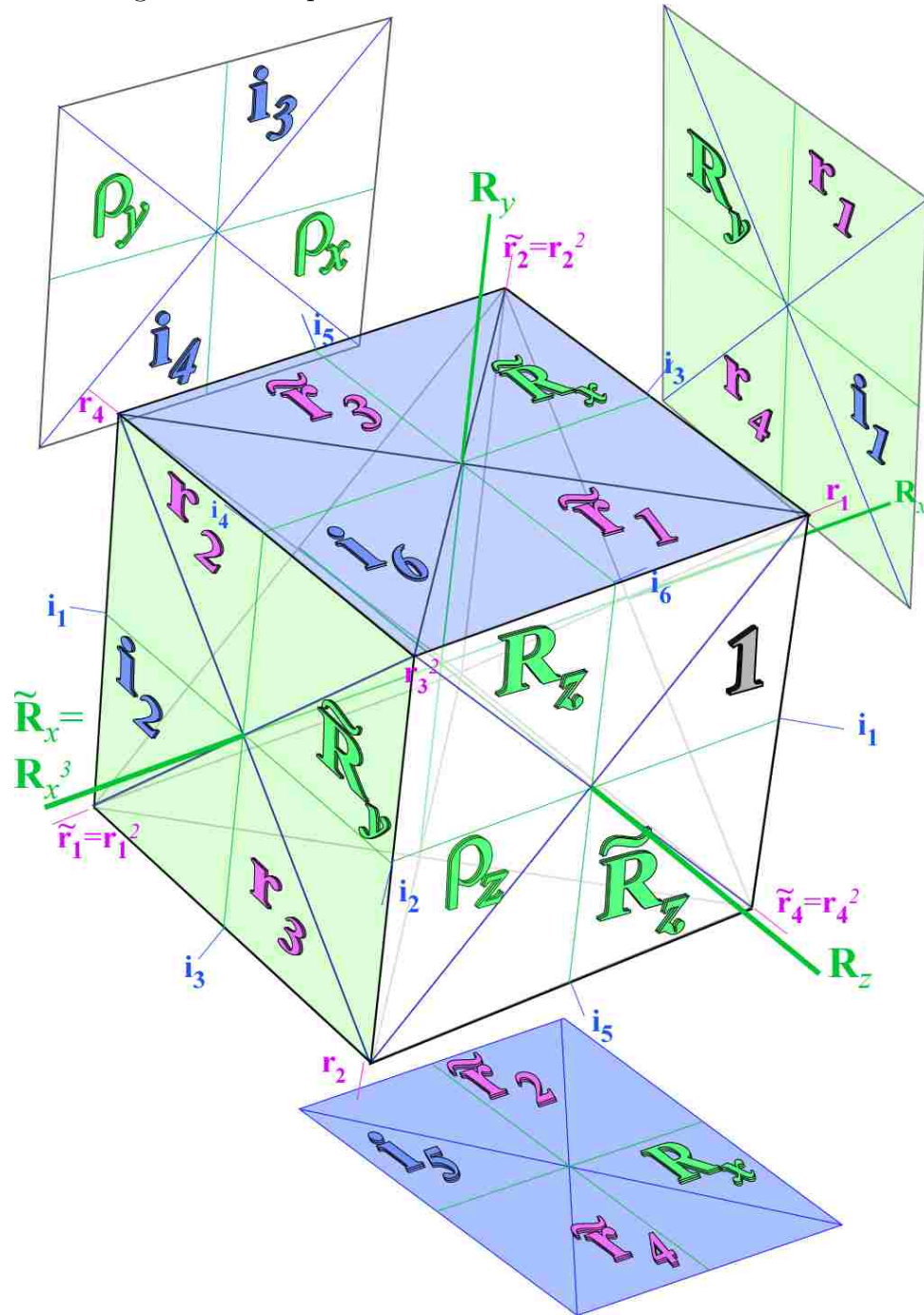
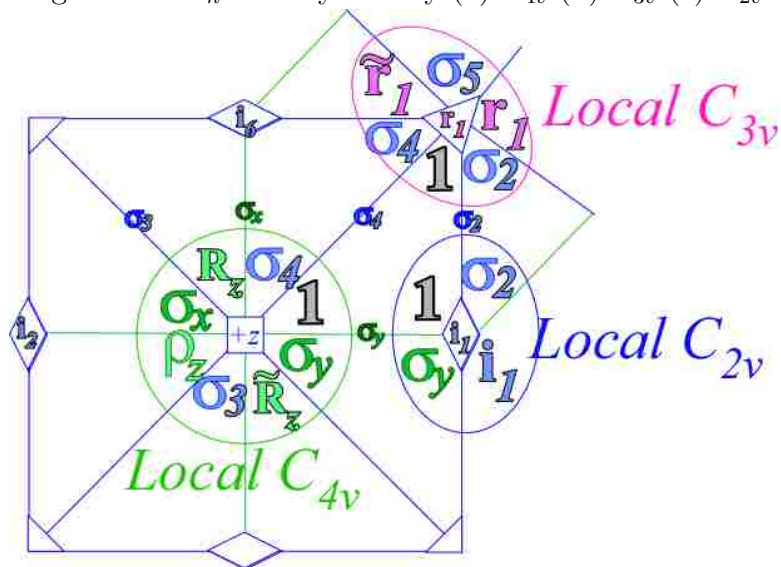




Figure 5.3:  $O_h$  local symmetry (a)  $C_{4v}$  (b)  $C_{3v}$  (c)  $C_{2v}$



edge. Lines between the axes have bilateral local reflection symmetry  $C_v(y)=[\mathbf{1}, \sigma_y]$ ,  $C_v(2)=[\mathbf{1}, \sigma_2]$ , or  $C_v(4)=[\mathbf{1}, \sigma_4]$ , fundamental symmetry operations whose products generate all others.

Each subgroup spawns a coset space and a set of induced representations of full  $O_h$  symmetry that generalize the  $C_{3v}$  induced representations in (4.74) and base kets sketched in Fig. 4.9. Correlation tables between  $O$  or  $O_h$  and its subgroups  $\mathcal{H} \subset \mathcal{G}$  tell which  $O$  or  $O_h$  irreps, states, and energy levels arise from each coset space. Lesser local symmetry order  ${}^\circ L$  implies greater coset dimension  $d_{\mathcal{H}} = {}^\circ \mathcal{G}/{}^\circ \mathcal{H}$  and more irreps or levels in  $\mathcal{H} \uparrow \mathcal{G}$ -induced representations, as in Eq 3.5. The correlation tables between the octahedral molecular symmetry group and local subgroups was mentioned in chapter 3 in Eq 3.1 and are repeated in Eq 5.2.

### 5.2.1 Octahedral characters and subgroup correlations

Spectral resolution of  $O$  classes in Fig. 5.1 is similar to that of  $D_3$  classes in (4.34) and gives character array in (5.1). Detailed derivation is available in many group theory

texts[1, 2].

<i>O</i> group $\chi_{\kappa_g}^\alpha$	$g = 1$	$r_{1-4}$ $\tilde{r}_{1-4}$	$\rho_{xyz}$	$R_{xyz}$ $\tilde{R}_{xyz}$	$i_{1-6}$
$\alpha = A_1$	1	1	1	1	1
$A_2$	1	1	1	-1	-1
$E$	2	-1	2	0	0
$T_1$	3	0	-1	1	-1
$T_2$	3	0	-1	-1	1

(5.1)

Cyclic subgroup  $C_4(\mathbf{R}_z^p)$ ,  $C_3(\mathbf{r}_1^p)$ , and  $C_2$  characters correlate with those of  $O$  according to arrays in (5.2).

$O \supset C_4$	$0_4$	$1_4$	$2_4$	$3_4$	$O \supset C_3$	$0_3$	$1_3$	$2_3$
$A_1 \downarrow C_4$	1	·	·	·	$A_1 \downarrow C_3$	1	·	·
$A_2 \downarrow C_4$	·	·	1	·	$A_2 \downarrow C_3$	1	·	·
$E \downarrow C_4$	1	·	1	·	$E \downarrow C_3$	·	1	1
$T_1 \downarrow C_4$	1	1	·	1	$T_1 \downarrow C_3$	1	1	1
$T_2 \downarrow C_4$	·	1	1	1	$T_2 \downarrow C_3$	1	1	1

$O \supset C_2(\mathbf{i}_1)$	$0_2$	$1_2$	$O \supset C_2(\rho_z)$	$0_2$	$1_2$
$A_1 \downarrow C_2$	1	·	$A_1 \downarrow C_2$	1	·
$A_2 \downarrow C_2$	·	1	$A_2 \downarrow C_2$	1	·
$E \downarrow C_2$	1	1	$E \downarrow C_2$	2	·
$T_1 \downarrow C_2$	1	2	$T_1 \downarrow C_2$	1	2
$T_2 \downarrow C_2$	2	1	$T_2 \downarrow C_2$	1	2

(5.2)

Equivalent subgroup correlations  $O \supset H$  and  $O \supset \mathbf{g}H\mathbf{g}^{-1}$  share elements in the same  $O$ -classes and have one correlation array. Thus all three  $C_4$  local symmetries have



$$\begin{aligned}
O\text{-centrum: } k(O) &= \sum_{\alpha} (\ell^{\alpha})^0 = 5 && \text{number of classes} \\
O\text{-rank: } \rho(O) &= \sum_{\alpha} (\ell^{\alpha})^1 = 10 \\
O\text{-order: } {}^{\circ}O &= \sum_{\alpha} (\ell^{\alpha})^2 = 24
\end{aligned}$$

Table 5.1: Key commutation number for group  $O$  are listed using Eq 4.43.

one correlation table in (5.2), as do all four  $C_3$  subgroups. However,  $O \supset C_2(\rho_z)$  and  $O \supset C_2(\mathbf{i}_1)$  correlations differ since  $\mathbf{i}_1$  and  $\rho_z$  have different  $O$ -class and characters in (5.1).

Projectors  $\mathbf{P}_{jk}^{\alpha}$  and irreps  $D_{jk}^{\alpha}$  of  $O$  depend on choice of local symmetry just as  $D_3$  projector splitting in (4.37) or (4.38) depends on choice of correlation  $D_3 \supset C_2$  in (4.63) or  $D_3 \supset C_3$  in (4.62), respectively. Sub-labels  $(j, k)$  range over  $C_2$  values  $[0_2, 1_2]$  or else  $C_3$  values  $[0_3, 1_3, 2_3]$  while a tetragonal correlation  $O \supset C_4$  will use sub-labels  $(j, k) = [0_4, 1_4, 2_4, 3_4]$ .

The  $m_4$  or else  $m_3$  unambiguously define all  $O$  states since no  $O \supset C_4$  or  $O \supset C_3$  correlation numbers in (5.2) exceed unity. However,  $O \supset C_2(\mathbf{i}_1)$  correlations cannot distinguish all three sub-levels of  $T_1$  or  $T_2$  wherever a number 2 appears, and the  $O \supset C_2(\rho_z)$  correlation leaves the  $E$  sub-levels unresolved, as well. A full  $O_h$  labeling resolves the first ambiguity as shown below, but we consider the unambiguous  $O \supset C_4$  case first. ( $C_4$  also resolves  $C_2(\rho_z)$  ambiguities.)

### **Resolving commuting $O \supset C_4$ local symmetry subalgebra: rank= $\rho(O) = 10$**

The  $C_4$  correlation table in (5.2) shows how invariant class projectors  $\mathbf{P}^{\alpha}$  (expanded below in terms of  $O$  characters  $\chi_{\kappa_g}^{\alpha}$  in table shown in Eq (5.1)) will split into irrep projectors  $\mathbf{P}_{m_4 m_4}^{\alpha}$  when hit by by  $C_4$  local symmetry projectors  $\mathbf{p}_{m_4}$ . The latter  $\mathbf{p}_m$  are expanded in terms of  $C_4$  operators  $\mathbf{R}_z^p$  weighted by character eigenvalues  $\phi_p^{m_4} = (\chi_p^{m_4})^*$

using Eqs (4.16) and (4.18). Since rank is  $\rho(O) = 10$  there are 10 results.

$$\begin{aligned}
\mathbf{1} \cdot \mathbf{P}^\alpha &= \overline{(\mathbf{p}_{0_4} \quad +\mathbf{p}_{1_4} \quad +\mathbf{p}_{2_4} \quad +\mathbf{p}_{3_4})} \cdot \mathbf{P}^\alpha \\
\mathbf{1} \cdot \mathbf{P}^{A_1} &= \mathbf{P}_{0_4 0_4}^{A_1} \quad +0 \quad +0 \quad +0 \\
\mathbf{1} \cdot \mathbf{P}^{A_2} &= 0 \quad +0 \quad +\mathbf{P}_{2_4 2_4}^{A_2} \quad +0 \\
\mathbf{1} \cdot \mathbf{P}^E &= \mathbf{P}_{0_4 0_4}^E \quad +0 \quad +\mathbf{P}_{2_4 2_4}^E \quad +0 \\
\mathbf{1} \cdot \mathbf{P}^{T_1} &= \mathbf{P}_{0_4 0_4}^{T_1} \quad +\mathbf{P}_{1_4 1_4}^{T_1} \quad +0 \quad +\mathbf{P}_{3_4 3_4}^{T_1} \\
\mathbf{1} \cdot \mathbf{P}^{T_2} &= 0 \quad +\mathbf{P}_{1_4 1_4}^{T_2} \quad +\mathbf{P}_{2_4 2_4}^{T_2} \quad +\mathbf{P}_{3_4 3_4}^{T_2}
\end{aligned} \tag{5.3}$$

The five class projectors  $\mathbf{P}^\alpha$  are  $O$ -invariant and commute with all twenty-four  $O$ -operators  $(\mathbf{1}, \mathbf{r}_1, \mathbf{r}_2, \dots, \mathbf{i}_5, \mathbf{i}_6)$ . So do the five class operators  $(\kappa_0, \kappa_{r_k}, \kappa_{\rho_k}, \kappa_{R_k}, \kappa_{i_k})$  in which each  $\mathbf{P}^\alpha$  is expanded as follows. (Recall  $D_3$  classes in Eq (4.34).)

$$\begin{aligned}
\mathbf{P}^\alpha &= \frac{\ell^\alpha}{\circ O} \sum_{k=0}^5 \chi_k^\alpha \kappa_k = \quad \text{where: } \alpha = A_1, A_2, E, T_1, \text{ or } T_2 \\
&= \frac{\ell^\alpha}{24} \left[ \chi_0^\alpha \mathbf{1} + \chi_{\kappa_r}^\alpha (\mathbf{r}_1 + \mathbf{r}_2 + \dots + \tilde{\mathbf{r}}_4) + \chi_{\kappa_\rho}^\alpha (\rho_x + \rho_y + \rho_z) \right. \\
&\quad \left. + \chi_{\kappa_R}^\alpha (\mathbf{R}_x + \mathbf{R}_y + \dots + \tilde{\mathbf{R}}_z) + \chi_{\kappa_i}^\alpha (\mathbf{i}_1 + \mathbf{i}_2 + \dots + \mathbf{i}_6) \right]
\end{aligned} \tag{5.4}$$

Each of the  $\ell^\alpha$  irrep projectors  $\mathbf{P}_{n_4 n_4}^\alpha$  is obtained from its invariant  $\mathbf{P}^\alpha$  by product  $\mathbf{P}^\alpha \mathbf{p}_{n_4} = \mathbf{p}_{n_4} \mathbf{P}^\alpha$  following (5.3) with each of four  $C_4$  local symmetry projector  $\mathbf{p}_{m_4}$ .

$$\mathbf{p}_{m_4} = \sum_{p=0}^3 \frac{e^{2\pi i m \cdot p/4}}{4} \mathbf{R}_z^p = \begin{cases} \mathbf{p}_{0_4} = (\mathbf{1} + \mathbf{R}_z + \rho_z + \tilde{\mathbf{R}}_z)/4 \\ \mathbf{p}_{1_4} = (\mathbf{1} + i\mathbf{R}_z - \rho_z - i\tilde{\mathbf{R}}_z)/4 \\ \mathbf{p}_{2_4} = (\mathbf{1} - \mathbf{R}_z + \rho_z - \tilde{\mathbf{R}}_z)/4 \\ \mathbf{p}_{3_4} = (\mathbf{1} - i\mathbf{R}_z - \rho_z + i\tilde{\mathbf{R}}_z)/4 \end{cases} \tag{5.5}$$

As the five ( $O$ -*centrum*=5) projectors  $\mathbf{P}^\alpha$  split into ten ( $O$ -*rank*=10) sub-projectors

$\mathbf{P}_{n_4 n_4}^\alpha$ , the five  $O$  class sums  $\kappa_g$  split into ten  $C_4$ -invariant sub-class sums  $\mathbf{c}_k$  ( $k=1..10$ ).

$$\frac{\circ O}{\ell^\alpha} \cdot \mathbf{P}_{n_4 n_4}^\alpha = \sum_{k=0}^{10} D_{n_4 n_4}^{\alpha*}(g_k) \mathbf{c}_k$$

$$\text{where: } D_{n_4 n_4}^\alpha(g_k) = D_{n_4 n_4}^\alpha(R_z^{p\dagger} g_k R_z^p) \quad (5.6)$$

The resulting ten products  $\frac{\circ O}{\ell^\alpha} \mathbf{P}_{n_4 n_4}^\alpha$  are listed in (5.7) of diagonal irrep coefficients  $D_{n_4 n_4}^\alpha(g_k)$  in terms of twenty-four group elements  $g_k$  that have been sorted into ten *sub-classes* that have  $C_4(z)$  local symmetry. The ten irrep projectors  $\mathbf{P}_{n_4 n_4}^\alpha$  are  $C_4$  local-invariant, that is, they commute with four  $C_4$ -operators ( $\mathbf{1}, \mathbf{R}_z, \mathbf{R}_z^2 = \rho_z, \mathbf{R}_z^3 = \tilde{R}_z$ ) but not the whole  $O$  group like the  $\mathbf{P}^\alpha$  do. The ten sub-class-sum operators  $\mathbf{c}_k$ , into which each  $\mathbf{P}_{n_4 n_4}^\alpha$  is expanded in (5.7), are each individually invariant to  $\mathbf{R}_z^p$ , that is  $\mathbf{R}_z^p \mathbf{c}_k = \mathbf{c}_k \mathbf{R}_z^p$ , and  $D_{n_4 n_4}^\alpha(g_k)$  is the same for all  $g_k$  in sub-class  $c_k$ . Note that a sum of  $\ell^\alpha$  rows belonging to  $\mathbf{P}_{n_4 n_4}^\alpha$  between horizontal lines in (5.7) yields corresponding character values  $\chi_k^\alpha = \text{trace} D^\alpha(g_k)$  in  $O$ -character array (5.1) and effectively “unsplits”

the sub-classes. For example  $\{\rho_x, \rho_y, \rho_z\}$  “unplits” into  $\{(\rho_x, \rho_y)\rho_z\}$ .

$\mathbf{P}_{n_4 n_4}^{(\alpha)} (O \supset C_4)$	$\mathbf{1}$	$\frac{r_1 r_2}{\tilde{r}_3 \tilde{r}_4}$	$\frac{\tilde{r}_1 \tilde{r}_2}{r_3 r_4}$	$\rho_x \rho_y$	$\rho_z$	$\frac{R_x \tilde{R}_x}{R_y \tilde{R}_y}$	$R_z$	$\tilde{R}_z$	$i_1 i_2 i_5 i_6$	$i_3 i_4$
$24 \cdot \mathbf{P}_{0_4 0_4}^{A_1}$	1	1	1	1	1	1	1	1	1	1
$24 \cdot \mathbf{P}_{2_4 2_4}^{A_2}$	1	1	1	1	1	-1	-1	-1	-1	-1
$12 \cdot \mathbf{P}_{0_4 0_4}^E$	1	$-\frac{1}{2}$	$-\frac{1}{2}$	1	1	$-\frac{1}{2}$	1	1	$-\frac{1}{2}$	1
$12 \cdot \mathbf{P}_{2_4 2_4}^E$	1	$-\frac{1}{2}$	$-\frac{1}{2}$	1	1	$+\frac{1}{2}$	-1	-1	$+\frac{1}{2}$	-1
$8 \cdot \mathbf{P}_{1_4 1_4}^{T_1}$	1	$-\frac{i}{2}$	$+\frac{i}{2}$	0	-1	$+\frac{1}{2}$	$-i$	$+i$	$-\frac{1}{2}$	0
$8 \cdot \mathbf{P}_{3_4 3_4}^{T_1}$	1	$+\frac{i}{2}$	$-\frac{i}{2}$	0	-1	$+\frac{1}{2}$	$+i$	$-i$	$-\frac{1}{2}$	0
$8 \cdot \mathbf{P}_{0_4 0_4}^{T_1}$	1	0	0	-1	1	0	1	1	0	-1
$8 \cdot \mathbf{P}_{1_4 1_4}^{T_2}$	1	$+\frac{i}{2}$	$-\frac{i}{2}$	0	-1	$-\frac{1}{2}$	$-i$	$+i$	$+\frac{1}{2}$	0
$8 \cdot \mathbf{P}_{3_4 3_4}^{T_2}$	1	$-\frac{i}{2}$	$+\frac{i}{2}$	0	-1	$-\frac{1}{2}$	$+i$	$-i$	$+\frac{1}{2}$	0
$8 \cdot \mathbf{P}_{2_4 2_4}^{T_2}$	1	0	0	-1	1	0	-1	-1	0	1

(5.7)

Without evaluating (5.7), one may find ten  $O \supset C_4$  sub-classes by simply inspecting Fig. 5.1 for operations in each  $O$ -class that transform into each other by  $C_4$  operations  $\mathbf{R}_z^p$  only. The  $O$ -class of eight  $120^\circ$  rotations  $\mathbf{r}_k$  split into two sub-classes, one  $[r_1, r_2, \tilde{r}_3, \tilde{r}_4]$  whose axes intersect four corners of the  $+z$  front square, and the other  $[\tilde{r}_1, \tilde{r}_2, r_3, r_4]$  whose axes similarly frame the  $-z$  back square. The class of six diagonal  $180^\circ$  rotations  $\mathbf{i}_k$  split into a sub-class  $[i_1, i_2, i_5, i_6]$  whose two-sided axes bisect edges of the  $z$  squares, and sub-class  $[i_3, i_4]$  whose axes are perpendicular to  $z$ -axis and bisect edges of  $xy$  side squares. The  $180^\circ$  rotational class  $[\rho_x, \rho_y, \rho_z]$  splits similarly into sub-classes  $[\rho_x, \rho_y]$  and  $[\rho_z]$  with axes perpendicular and along, respectively, the  $\mathbf{R}_z$  axis. The  $90^\circ$  class splits, as indicated in the top row of (5.7), into a sub-class of four perpendicular  $xy$ -axial rotations and separate sub-classes for  $R_z$  and  $\tilde{R}_z$ .

The inverse to (5.6) expresses the ten subclasses in terms of the ten diagonal irrep projectors using the same (albeit, conjugated) array of  $D_{n_4 n_4}^\alpha(g_k)$ . However, column

and row labels must switch and acquire different coefficients.

$$\frac{\mathbf{c}_k}{\circ C_k} = \sum_{k=0}^{10} D_{n_4 n_4}^\alpha(g_k) \mathbf{P}_{n_4 n_4}^\alpha = \sum_{k=0}^{10} \frac{D_{n_4 n_4}^\alpha(\mathbf{c}_k)}{\circ C_k} \mathbf{P}_{n_4 n_4}^\alpha \quad (5.8)$$

### Resolving D-matrices with $C_4$ local symmetry

Off-diagonal  $D_{m_4 n_4}^\alpha(g_k)$  matrices derive from products of diagonal irrep projectors in (5.7) using (4.41b) repeated here.

$$\mathbf{P}_{j,j}^\alpha \cdot \mathbf{g} \cdot \mathbf{P}_{k,k}^\alpha = D_{j,k}^\alpha(g) \mathbf{P}_{j,k}^\alpha \quad (5.9)$$

Scalar  $A_1$  and pseudo-scalar  $A_2$  are given first then  $E$ ,  $T_1$ , and  $T_2$  irrep matrices for the fundamental  $\mathbf{i}_k$ -class of  $O$ .

$$\begin{aligned} D_{0_4 0_4}^{A_1}(i_k \mathbf{i}_k) &= i_1 + i_2 + i_3 + i_4 + i_5 + i_6 \\ D_{2_4 2_4}^{A_2}(i_k \mathbf{i}_k) &= -(i_1 + i_2 + i_3 + i_4 + i_5 + i_6) \end{aligned} \quad (5.10)$$

$$D^E(i_k \mathbf{i}_k) = \begin{array}{c|cc|c} & & 0_4 & 2_4 & \\ \hline 0_4 & & -\frac{1}{2}(i_1 + i_2 + i_5 + i_6) + i_3 + i_4 & \frac{\sqrt{3}}{2}(i_1 + i_2 - i_5 - i_6) & \\ 2_4 & & h.c. & \frac{1}{2}(i_1 + i_2 + i_5 + i_6) - i_3 - i_4 & \\ \hline & & & & \end{array} \quad (5.11)$$

$D^{T_1^*}(i_k \mathbf{i}_k)$	$1_4$	$3_4$	$0_4$
$1_4$	$-\frac{1}{2}(i_1 + i_2 + i_5 + i_6)$	$-\frac{1}{2}(i_1 + i_2 - i_5 - i_6)$ $-i(i_3 - i_4)$	$-\frac{1}{\sqrt{2}}(i_1 - i_2) + \frac{i}{\sqrt{2}}(i_5 - i_6)$
$3_4$	<i>h.c.</i>	$-\frac{1}{2}(i_1 + i_2 + i_5 + i_6)$	$+\frac{1}{\sqrt{2}}(i_1 - i_2) + \frac{i}{\sqrt{2}}(i_5 - i_6)$
$0_4$	<i>h.c.</i>	<i>h.c.</i>	$-(i_3 + i_4)$

$D^{T_2^*}(i_k \mathbf{i}_k)$	$1_4$	$3_4$	$2_4$
$1_4$	$+\frac{1}{2}(i_1 + i_2 + i_5 + i_6)$	$+\frac{1}{2}(i_1 + i_2 - i_5 - i_6)$ $-i(i_3 - i_4)$	$+\frac{1}{\sqrt{2}}(i_1 - i_2) + \frac{i}{\sqrt{2}}(i_5 - i_6)$
$3_4$	<i>h.c.</i>	$+\frac{1}{2}(i_1 + i_2 + i_5 + i_6)$	$-\frac{1}{\sqrt{2}}(i_1 - i_2) + \frac{i}{\sqrt{2}}(i_5 - i_6)$
$0_4$	<i>h.c.</i>	<i>h.c.</i>	$+(i_3 + i_4)$

(5.12)

Symmetry of  $C_4 \subset O$  subclass  $[i_1, i_2, i_5, i_6]$  and  $[i_3, i_4]$  would demand equality of parameters for each.

$$i_1 = i_2 = i_5 = i_6 \equiv i_{1256} \equiv i_I, \quad \text{and}, \quad i_3 = i_4 \equiv i_{34} \equiv i_{II} \quad (5.13)$$

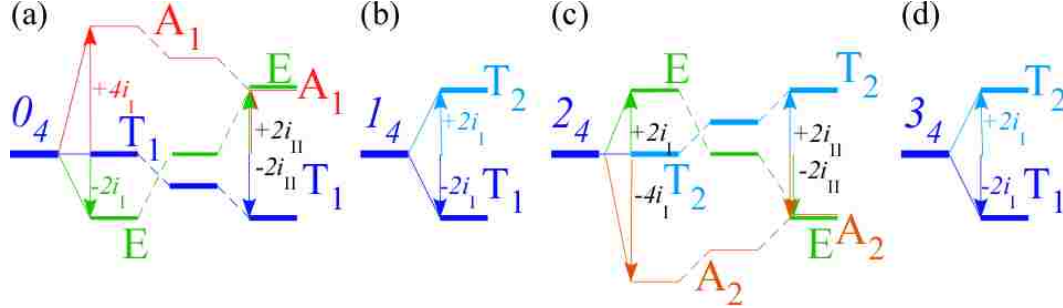
Setting each parameter to the inverse of its sub-class order ( $i_k = 1/(\circ c_{i_k})$ ) reduces each matrix to diagonal form and gives the diagonal  $D_{n_4 n_4}^\alpha(g_k)$  given in (5.7). Classes  $r, \rho, R$  behave similarly.

### Resolving Hamiltonians with $C_4$ local symmetry

An octahedral Hamiltonian  $\mathbf{H} = \sum_{k=1}^{24} g_k \bar{\mathbf{g}}_k$  with local  $C_4(z)$  symmetry is resolved by sorting  $g_k$  into its  $C_4(z)$  sub-classes  $c_k$  and then into  $\mathbf{P}_{n_4 n_4}^\alpha$  whose coefficients are the desired  $\mathbf{H}$  eigenvalues  $\epsilon_{n_4}^\alpha$ . Zero off-diagonal  $H_{m_4 n_4}^\alpha = 0$  and  $C_4$ -local symmetry conditions shown in (5.13) arise from (5.7) consistent with Fig. 5.1. Tunneling parameter  $i_{1256} = i_I$  from  $+z$ -axis to its 1<sup>st</sup>-neighbor  $\pm x$  or  $\pm y$  axes may dominate flip-tunneling  $i_{34} = i_{II}$  to 2<sup>nd</sup> neighbor- $z$ -axis. The  $i$ -columns of Eq (5.7) (or matrix diagonals in Eqs (5.10)-(5.12)) give  $i_I$  and  $i_{II}$  contributions to eigenvalues  $\epsilon_{n_4}^\alpha$  listed in

Table 5.2: Splittings of  $O \supset C_4$  given sub-class structure.

$O \supset C_4$	$0^\circ$	$r_n 120^\circ$	$\rho_n 180^\circ$	$R_n 90^\circ$	$i_n 180^\circ$
$0_4$	.	$r_I = \text{Re } r_{1234}$ $m_I = \text{Im } r_{1234}$	.	$R_z = \text{Re } R_z$ $I_z = \text{Im } R_z$	$i_I = i_{1256}$ $i_{II} = i_{34}$
$\epsilon_{0_4}^{A_1} =$	$g_0$	$+8r_I$	$+2\rho_{xy} + \rho_z$	$+4R_{xy} + 2R_z$	$+4i_I + 2i_{II}$
$\epsilon_{0_4}^{T_1}$	$g_0$	0	$-2\rho_{xy} + \rho_z$	$+2R_z$	$-2i_{II}$
$\epsilon_{0_4}^E$	$g_0$	$-2r_I$	$+2\rho_{xy} + \rho_z$	$-2R_{xy} - R_z$	$-2i_I + 2i_{II}$
$1_4$	.	.	.	.	.
$\epsilon_{1_4}^{T_2}$	$g_0$	$+2m_I$	$-\rho_z$	$-R_{xy} - 2I_z$	$+2i_I$
$\epsilon_{1_4}^{T_1}$	$g_0$	$-2m_I$	$-\rho_z$	$+R_{xy} - 2I_z$	$-2i_I$
$2_4$	.	.	.	.	.
$\epsilon_{2_4}^E$	$g_0$	$-2r_I$	$+2\rho_{xy} + \rho_z$	$+2R_{xy} - R_z$	$+2i_I - 2i_{II}$
$\epsilon_{2_4}^{T_2}$	$g_0$	0	$-2\rho_{xy} + \rho_z$	$-2R_z$	$+2i_{II}$
$\epsilon_{2_4}^{A_2}$	$g_0$	$+8r_I$	$+2\rho_{xy} + \rho_z$	$-4R_{xy} - 2R_z$	$-4i_I - 2i_{II}$
$3_4$	.	.	.	.	.
$\epsilon_{3_4}^{T_2}$	$g_0$	$-2m_I$	$-\rho_z$	$-R_{xy} + 2I_z$	$+2i_I$
$\epsilon_{3_4}^{T_1}$	$g_0$	$+2m_I$	$-\rho_z$	$+R_{xy} + 2I_z$	$-2i_I$

 Figure 5.4:  $O$   $i$ -class level clusters of  $C_4$  local symmetry (a)  $0_4$  (b)  $1_4$  (c)  $2_4$  (d)  $3_4$ 


the  $i_n$ -column of Table 5.2. Clusters  $(\epsilon_{0_4}^{A_1}, \epsilon_{0_4}^{T_1}, \epsilon_{0_4}^E)$  thru  $(\epsilon_{3_4}^{T_2}, \epsilon_{3_4}^{T_1})$  are plotted in Fig. 5.4 for select values of parameters  $i_I = i_{1256}$  and  $i_{II} = i_{34}$ .

One expects the parameter  $i_{II}$  for  $2^{nd}$ -neighbor tunneling to be exponentially smaller than  $i_I$  for adjacent tunneling so the  $(i_{II} = 0)$ -cases are drawn first in Fig. 5.4. While the  $i$ -class operations are most fundamental (all operations are generated by products of  $\mathbf{i}_k$ ) other operations also generate  $1^{st}$ -neighbor transformation. Three class parameters  $R_{xy}(90^\circ)$ ,  $r_I(120^\circ)$ , and  $i_I(180^\circ)$  label  $1^{st}$ -neighbor inter- $C_4$  axial tunneling paths that have the same  $i_I$ -level patterns and splitting ratios as  $(i_{II}=0)$ -cases in Fig. 5.4 but with differing sign. (Signs differ since each sub-class eigenvalue set must

be orthogonal to all others as shown below.) Level patterns in Fig. 5.4 are reflected in *spectral* patterns of Fig. 5.5 if both ground and excited vib-rotor states have similar RES-shape. However, only  $C_{4z}$  sub-class  $i_I(180^\circ)$  patterns (with  $i_I < 0$ ) exhibit spectral ordering  $(A_1T_1E)(T_2T_1)(ET_2A_2)(T_2T_1)$  on the left hand side of Fig. 5.5 that is maintained even as levels re-cluster into patterns  $(T_1ET_2)(T_1ET_2)(A_2T_2T_1A_1)$  of  $C_{3[111]}$  local symmetry across the separatrix break on the right-hand side of Fig. 5.5 as analyzed below [3, 4].  $O$ -crystal-field wavefunctions for either case tend to follow a Bohr-orbital progression  $s(A_1), p(T_1), d(E, T_2), f(T_1, A_2, T_2), g(E, T_1, T_2, A_1), \dots$ . In general, ordering is sensitive to RES-shape and tensor rank as discussed later.

For an isolated three-level  $(ATE)$ -cluster of local symmetry  $0_4$  or else  $2_4$  the splitting pattern requires only two parameters. This could be either the  $180^\circ(i_I, i_{II})$  or the  $90^\circ(R_{xy}, R_z)$  class pair in Table 5.2. The  $120^\circ$ -class, lacking  $180^\circ$  flips, has just one real parameter  $r_I$ . Parameters  $i_I$ ,  $R_{xy}$ , and  $r_I$  each split  $(ATE)$  by 2:1 ratio but differ in sign.

Local symmetry  $1_4$  and  $3_4$  each have two-level  $(TT)$  clusters that require just one splitting parameter, say  $i_I$ , or else  $R_{xy}$ . Complex parameters  $R_z$  and  $I_z$  of the  $90^\circ R_n$ -class and the  $\rho_n(180^\circ)$ -class in Table 5.2 may play minor roles in most  $C_4$  clusters but are necessary in order that the whole set be orthonormal and complete.

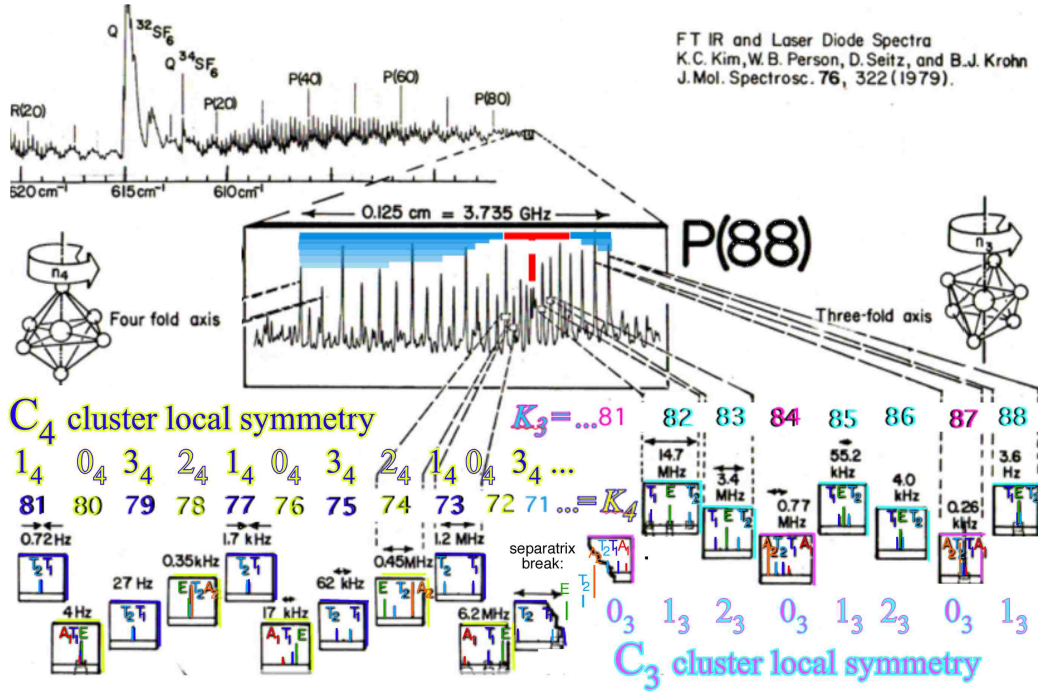
### Orthogonality-completeness of local symmetry parameters

Eq (5.7) expands  $\mathbf{P}_{nn}^{(\alpha)}$  by Eq (4.42) in group operators  $(\mathbf{1}, \mathbf{r}_1, \mathbf{r}_2, \dots, \mathbf{i}_6)$ . It acts on  $|\mathbf{1}\rangle$  to give  $|\frac{(\alpha)}{n_4 n_4}\rangle$  eigenkets in (5.14).

$$\begin{aligned} |\frac{(\alpha)}{nn}\rangle &= \mathbf{P}_{nn}^{(\alpha)} |\mathbf{1}\rangle \sqrt{\frac{\circ G}{\ell^\alpha}} = \sqrt{\frac{\ell^\alpha}{\circ G}} \sum_{b=1}^{\circ G} D_{nm}^{(\alpha)*}(g_b) \mathbf{g}_b |\mathbf{1}\rangle \\ &= \sqrt{\frac{\ell^\alpha}{\circ G}} \sum_{b=1}^{\circ G} D_{nm}^{(\alpha)*}(g_b) |g_b\rangle \end{aligned} \quad (5.14)$$



Figure 5.5: Tiny excerpt of  $SF_6 \nu_4 P(88)$  superfine spectral cluster structure in  $16\mu m$  region



An  $O$ -symmetric  $\mathbf{H}$  matrix is a sum of *dual* operators  $(\bar{\mathbf{1}}, \bar{\mathbf{r}}_1, \bar{\mathbf{r}}_2, \dots, \bar{\mathbf{i}}_6)$  with coefficients  $g_a = \epsilon_0, r_1, r_2, \dots, i_6$ . Local symmetry  $C_4$  or  $C_3$  reduces the sum to  $\rho_G = 10$  sub-class terms  $\bar{\mathbf{c}}_a = \bar{\mathbf{g}}_a + \bar{\mathbf{g}}'_a + \dots$  each sharing a coefficient  $g_a = g'_a \dots$

$$\mathbf{H} = \sum_{a=1}^{\rho_G} g_a \bar{\mathbf{g}}_a = \sum_{a=1}^{\rho_G} g_a \bar{\mathbf{c}}_a \quad (5.15)$$

From these arise expansions like Table 5.2 of  $\mathbf{H}$  eigenvalues  $\epsilon_{n_4}^\alpha$  in terms of its coefficients  $g_a$ . Dual commutation  $\mathbf{g}_j \bar{\mathbf{g}}_k = \bar{\mathbf{g}}_k \mathbf{g}_j$  makes  $\mathbf{P}_{nn}^{(\alpha)}$  and  $\mathbf{H}$  commute. Duality relation in (4.53) leads to a  $D^{\alpha*}$ -weighted sum of  $g_a$  analogous to sum in (5.14) of

$|g_a\rangle$ .

$$\begin{aligned}
\varepsilon_n^\alpha &= \langle {}^{(\alpha)}_{nn} | \mathbf{H} | {}^{(\alpha)}_{nn} \rangle = \langle \mathbf{1} | \mathbf{P}_{nn}^{(\alpha)} \mathbf{H} \mathbf{P}_{nn}^{(\alpha)} | \mathbf{1} \rangle \frac{{}^\circ G}{\ell^\alpha} = \langle \mathbf{1} | \mathbf{H} \mathbf{P}_{nn}^{(\alpha)} | \mathbf{1} \rangle \frac{{}^\circ G}{\ell^\alpha} \\
&= \langle \mathbf{1} | \sum_{a=0}^{\circ G} g_a \bar{\mathbf{g}}_a \sum_{b=0}^{\circ G} D_{nn}^{(\alpha)*}(g_b) \mathbf{g}_b | \mathbf{1} \rangle = \langle \mathbf{1} | \sum_{a=0}^{\circ G} g_a \sum_{b=0}^{\circ G} D_{nn}^{(\alpha)*}(g_b) \mathbf{g}_b \mathbf{g}_a^{-1} | \mathbf{1} \rangle \\
&= \sum_{a=0}^{\circ G} g_a D_{nn}^{(\alpha)*}(g_a) = \sum_{a=1}^{\rho_G} D_{nn}^{(\alpha)*}(g_a) {}^\circ c_a g_a
\end{aligned} \tag{5.16}$$

Each  $C_4$  sub-class of order  ${}^\circ c_a$  has  ${}^\circ c_a$  equal terms  $g_a D_{nn}^{(\alpha)*}(g_a) = g'_a D_{nn}^{(\alpha)*}(g'_a) = \dots$  expanding eigenvalue  $\varepsilon_{n_4}^\alpha$ . Rank-of-group  $\rho_G = 10$  is the number of eigenvalues and of expansion terms  ${}^\circ c_a g_a D_{nn}^{(\alpha)*}(g_a)$  in (5.16) or Table 5.2. Each of ten eigenvalues  $\varepsilon_{n_4}^\alpha = (\varepsilon^{A_1}, \varepsilon^{A_2}, \dots, \varepsilon_{3_4}^{T_2})$  expand to ten  $C_4$ -local tunneling parameters  $g_a = (\varepsilon_0, r_I, r_{II}, \dots, i_{II})$  and *vice-versa*.

$$\begin{aligned}
g_a &= \langle \mathbf{1} | \mathbf{H} | g_a \rangle = \langle \mathbf{1} | \mathbf{H} \mathbf{g}_a | \mathbf{1} \rangle = \sum_{\alpha} \sum_j^{\ell^\alpha} \sum_k^{\ell^\alpha} D_{jk}^{(\alpha)}(g_a) \langle \mathbf{1} | \mathbf{H} \mathbf{P}_{jk}^\alpha | \mathbf{1} \rangle \\
&= \sum_{\alpha} \sum_n^{\ell^\alpha} D_{nn}^{(\alpha)}(g_a) \langle \mathbf{1} | \mathbf{H} \mathbf{P}_{nn}^\alpha | \mathbf{1} \rangle = \sum_{\alpha} \sum_n^{\ell^\alpha} D_{nn}^{(\alpha)}(g_a) \frac{\ell^\alpha}{{}^\circ G} \varepsilon_n^\alpha
\end{aligned} \tag{5.17}$$

One might count twelve real parameters in Table 5.2 since both pairs  $(r_I, \tilde{r}_I)$  and  $(R_z, \tilde{R}_z)$  are complex unlike  $R_I = \tilde{R}_I$  which are real. If  $H$  is a Hermitian array ( $H = H^\dagger$ ) it should only require ten, the rank of  $O$ , for its ten distinct real eigenvalues and the parameter pairs must be complex conjugates.

With no conjugation symmetry, such as for a *unitary*  $O \supset C_4$ -symmetric matrix, the  $R$  and  $r$  parameters may be complex and unrelated to  $\tilde{R}$  and  $\tilde{r}$ , and resulting extra real parameters are then needed. Symmetry parameter dimension matches eigen-solution dimension for each local symmetry as shown in Fig. 5.7. The formulas (5.16) and (5.17) are generalizations of projective character formulas such as Eq (4.34) that involves classes  $k$  and irreps  $(\alpha)$ . These former involve split classes and irreps like the character coefficients  $\chi_k^\alpha$  of the latter and have class-to-class transformations that are quasi-unitary.

Table 5.3: Splittings of  $O \supset C_3$  given sub-class structure.

$O \supset C_3$	$0^\circ$	$r_n 120^\circ$	$\rho_n 180^\circ$	$R_n 90^\circ$	$i_n 180^\circ$
$0_3$	.	$r_I = Re(r_1) \quad i_I = Im(r_1)$ $r_{II} = Re(r_{234}) \quad i_{II} = Im(r_{234})$	$\rho = \rho_{xyz}$	$R_n = Re(R_{xyz})$ $I_n = Im(R_{xyz})$	$i_I = i_{136}$ $i_{II} = i_{245}$
$\varepsilon_{0_3}^{A_1}$	$g_0$	$2r_I + 6r_{II}$	$3\rho$	$6R_n$	$3i_I + 3i_{II}$
$\varepsilon_{0_3}^{A_2}$	$g_0$	$2r_I + 6r_{II}$	$3\rho$	$-6R_n$	$-3i_I - 3i_{II}$
$\varepsilon_{0_3}^{T_1}$	$g_0$	$2r_I - 2r_{II}$	$-\rho$	$2R_n$	$i_I - 3i_{II}$
$\varepsilon_{0_3}^{T_2}$	$g_0$	$2r_I - 2r_{II}$	$-\rho$	$-2R_n$	$-i_I + 3i_{II}$
$1_3$					
$\varepsilon_{1_3}^E$	$g_0$	$-r_I + \sqrt{3}i_I - 3r_{II} + 3\sqrt{3}i_{II}$	$3\rho$	0	0
$\varepsilon_{1_3}^{T_1}$	$g_0$	$-r_I + \sqrt{3}i_I + r_{II} - \sqrt{3}i_{II}$	$-\rho$	$2R_n + 2\sqrt{3}I_n$	$-2i_I$
$\varepsilon_{1_3}^{T_2}$	$g_0$	$-r_I + \sqrt{3}i_I + r_{II} - \sqrt{3}i_{II}$	$-\rho$	$-2R_n - 2\sqrt{3}I_n$	$2i_I$
$2_3$					
$\varepsilon_{2_3}^E$	$g_0$	$-r_I - \sqrt{3}i_I - 3r_{II} - 3\sqrt{3}i_{II}$	$3\rho$	0	0
$\varepsilon_{2_3}^{T_1}$	$g_0$	$-r_I - \sqrt{3}i_I + r_{II} + \sqrt{3}i_{II}$	$-\rho$	$2R_n - 2\sqrt{3}I_n$	$-2i_I$
$\varepsilon_{2_3}^{T_2}$	$g_0$	$-r_I - \sqrt{3}i_I + r_{II} + \sqrt{3}i_{II}$	$-\rho$	$-2R_n + 2\sqrt{3}I_n$	$2i_I$

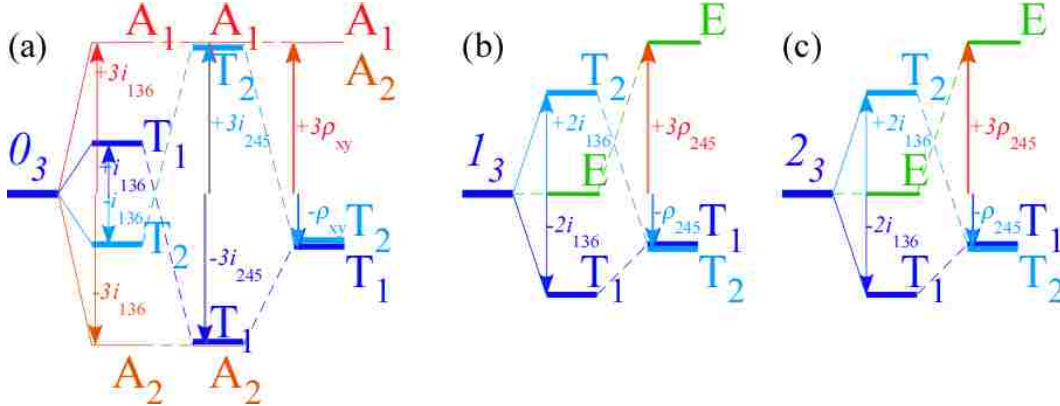
### Resolving Hamiltonians with $C_3$ local symmetry

The previous two sections have detailed of symmetry-based level clustering and cluster splitting for  $C_4$ . In Fig. 5.5 these are the lower energy clusters of  $SF_6$  for  $\nu_4 P(88)$ . Given the previous two sections, it is possible to find the splittings of the  $C_3$  sub-group quickly. Starting with (5.2) and (5.3) one can build the irreducible representations necessary to create the  $\mathbf{P}_{n_3 n_3}^\alpha$  for the new sub-group. At this point, one can create a table analogous to Table 5.2. Such a table for  $C_3$  is shown in Table 5.3. The  $C_3$  clustering fits patterns of  $(A_1, A_2, T_2, T_2)$  and two of  $(E, T_1, T_2)$ , each with a total degeneracy of 8. As before in Fig. 5.4, the splittings in  $C_3$  make different patterns depending on which tunneling parameters are active. This is demonstrated in Fig. 5.6.

### Octahedral splitting for a range of local symmetry $C_1 \subset C_2 \dots \subset O$

As the order  $^\circ L$  of local symmetry  $L \subset G$  decreases there are proportionally fewer types of local symmetry irrep  $d^\lambda(L)$  and hence fewer types of energy level cluster since each cluster is defined by its induced representation  $d^\lambda(L) \uparrow G$ . There is a proportional increase in total number  $\ell^{\lambda \uparrow G} = (\ell^\lambda)^\circ G / ^\circ L$  of levels in each eigenvalue cluster. How-

Figure 5.6:  $O$   $i$ -class and  $\rho$ -class level clusters of  $C_3$  local symmetry given different tunneling parameters



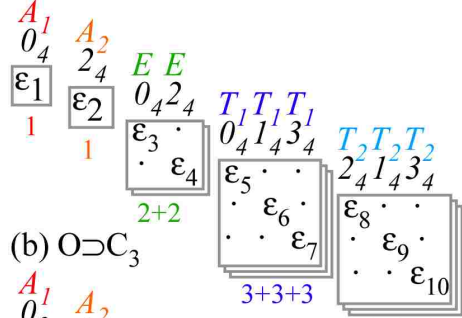
ever,  $G$ -symmetry degeneracy limits the total number of *distinct* eigenvalues from all clusters to be global rank  $\rho(G)$  or less, no matter what local symmetry is in effect. Octahedral rank is  $\rho(O)=10=\ell^{A_1}+\ell^{A_2}+\ell^E+\ell^{T_1}+\ell^{T_2}$  where  $\ell^\alpha$  gives both the global degeneracy of each level type and the number of times it appears.

The number of  $H$ -matrix parameters equals the number of distinct eigenvalues as long as all *eigenvectors* are determined by global-local symmetry, that is, each entry is 0 or 1 in the  $G \supset L$  correlation array. Diagonal eigenmatrix forms are shown in Fig. 5.7(a-b) for  $C_4 \subset O$  and  $C_3 \subset O$  for which all bases states are distinctly labeled. Multiple correlation ( $\geq 2$ ) occurs if  $L$ -symmetry is too small to determine some of the  ${}^\circ G$  eigenbases. Then the  $H$ -matrix must have extra parameters that fix vectors thru diagonalization. This happens for the  $C_2(\mathbf{i}_1) \subset O$  symmetry whose correlation array in (5.2) assigns the same  $C_2$  label to two bases of  $T_1$  and of  $T_2$ . (Two  $C_2$  symmetries  $0_2$  and  $1_2$  cannot distinctly label three bases.) Fig. 5.1 shows  $C_2(\mathbf{i}_1)$  splits  $O$  into fourteen sub-classes:  $(\mathbf{1})$ ,  $(\mathbf{r}_1\tilde{\mathbf{r}}_4)$ ,  $(\mathbf{r}_2\tilde{\mathbf{r}}_2)$ ,  $(\mathbf{r}_3\tilde{\mathbf{r}}_3)$ ,  $(\mathbf{r}_4\tilde{\mathbf{r}}_1)$ ,  $(\rho_x\rho_z)$ ,  $(\rho_y)$ ,  $(\mathbf{R}_x\mathbf{R}_z)$ ,  $(\tilde{\mathbf{R}}_x\tilde{\mathbf{R}}_z)$ ,  $(\mathbf{R}_y\tilde{\mathbf{R}}_y)$ ,  $(\mathbf{i}_1)$ ,  $(\mathbf{i}_2)$ ,  $(\mathbf{i}_3\mathbf{i}_5)$ ,  $(\mathbf{i}_4\mathbf{i}_6)$ . The  $C_2 \subset O$  sub-classes form a non-commutative algebra and cannot be resolved so easily as  $C_3 \subset O$  or  $C_4 \subset O$  into commuting idempotent combinations like (5.8).

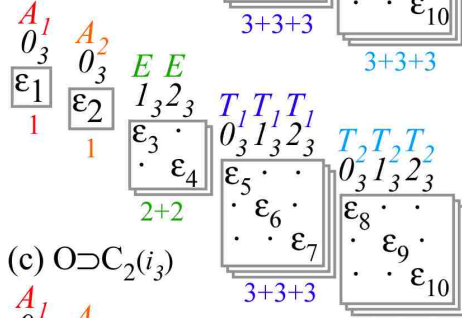
Spectral resolution of fourteen  $C_2(\mathbf{i}_1) \subset O$  sub-classes requires more than rank number  $\rho(O)=10$  of diagonal commuting  $O$  idempotents  $\mathbf{P}_{nn}^\alpha$ . To fully determine  $C_2$  basis,

Figure 5.7:  $O \subset L$ -local symmetry eigenmatrix parameters (a-e)  $L=C_4, \dots, C_1$  (f-j)  $L=O, D_4, \dots, D_2$

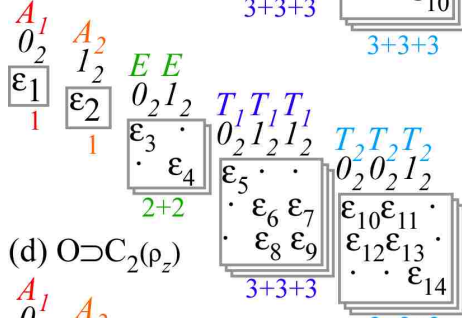
(a)  $O^{\text{global}} * O^{\text{local}} \supset O^{\text{global}} * C_4^{\text{local}}$



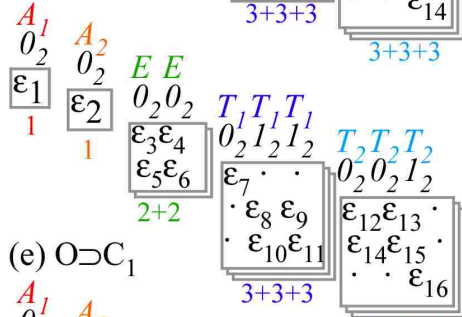
(b)  $O \supset C_3$



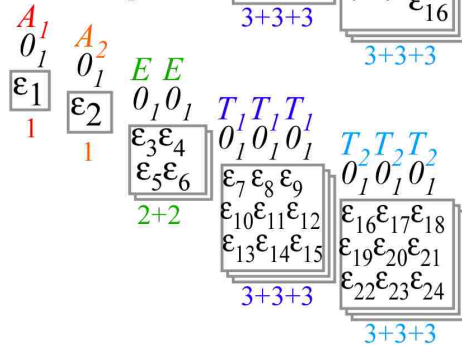
(c)  $O \supset C_2(i_3)$



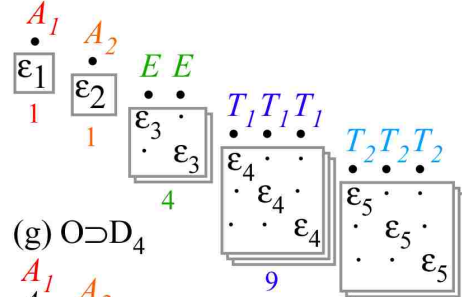
(d)  $O \supset C_2(\rho_z)$



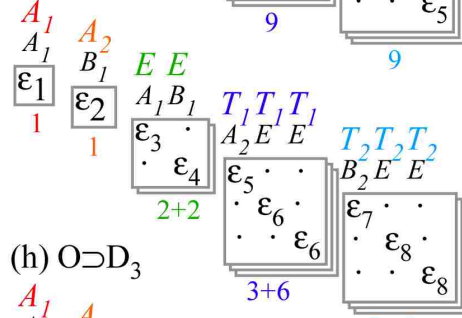
(e)  $O \supset C_1$



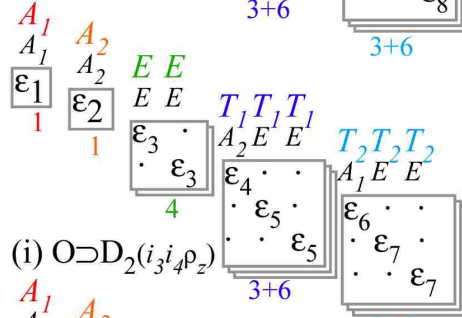
(f)  $O^{\text{global}} * O^{\text{local}}$



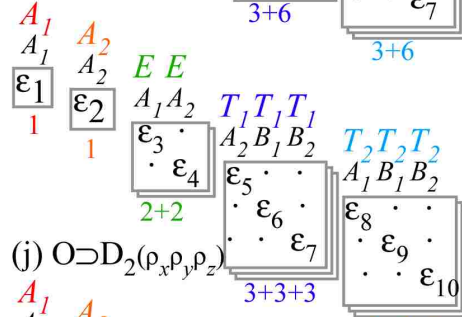
(g)  $O \supset D_4$



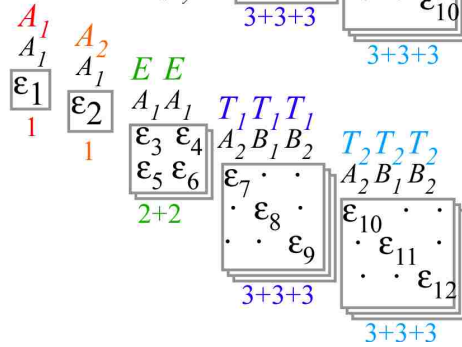
(h)  $O \supset D_3$



(i)  $O \supset D_2(i_3, \rho_z)$



(j)  $O \supset D_2(\rho_x, \rho_y, \rho_z)$



two off-diagonal pairs  $\mathbf{P}_{ab}^{T_1}=\mathbf{P}_{ba}^{T_1\dagger}$  and  $\mathbf{P}_{ab}^{T_2}=\mathbf{P}_{ba}^{T_2\dagger}$  of non-commuting nilpotent projectors are needed to finish  $C_2$ -labeling of  $T$ -triplets. Adding these four gives fourteen projectors with their fourteen parameter coefficients  $\epsilon_\ell$  shown in Fig. 5.7(c) to fully define general  $C_2(\mathbf{i}_1)\subset O$   $H$ -operators. (However, only twelve of the fourteen parameters are independent for Hermitian  $H_{a,b}=H_{b,a}^*$ .)

The other class of  $C_2$  symmetry has similar problems. Local  $C_2(\rho_z)\subset O$  symmetry requires projector pairs  $\mathbf{P}_{ab}^{T_1}=\mathbf{P}_{ba}^{T_1\dagger}$  and  $\mathbf{P}_{ab}^{T_2}=\mathbf{P}_{ba}^{T_2\dagger}$ , too, but then another nilpotent pair  $\mathbf{P}_{ab}^E=\mathbf{P}_{ba}^{E\dagger}$  must be added to label repeated  $E$  bases in array (5.2). This gives sixteen  $C_2(\rho_z)$  sub-classes to resolve and sixteen parameters sketched in Fig. 5.7(d). (Hermitian  $H=H^\dagger$  matrices for  $C_2(\rho_z)\subset O$  have thirteen free parameters.)

For the lowest local symmetry  $C_1=[\mathbf{1}]$  (*i.e.*, no local symmetry) sub-classes are completely split since every  $O$ -operator is invariant to  $\mathbf{1}$  as  $C_1$  provides no distinguishing labeling, and all twenty-four  $O$ -projectors ( $\Sigma_\alpha(\ell^\alpha)^2=24$ ) are active in its resolution. The 24-parameter  $H$ -matrix resolution is sketched in Fig. 5.7(e). Each parameter  $\epsilon_a$  for  $a=1, \dots, 24$  is a combination of 24 products  $D_{j,k}^{\alpha*}(g_p)g_p$  ( $p=1, \dots, 24$ ) of irrep and group element coefficient  $g_p$  as given in (4.49) or (5.16). (If  $H$  is Hermitian the number of free parameters reduces to  $\Sigma_\alpha \ell^\alpha(\ell^\alpha+1)=17$ .)

For  $O$ 's highest local symmetry, namely  $O$  itself, there is no splitting of the  $\Sigma_\alpha(\ell^\alpha)^0=5$  invariant idempotents  $\mathbf{P}^\alpha$  that resolve the five  $O$  classes. Then  $H$  has five independent parameters and five eigenvalues of degeneracy  $(\ell^\alpha)^2$ . This 5-parameter resolution is sketched in Fig. 5.7(f). Total level degeneracy for sub-matrix eigenvalues are listed below each one, and show less splitting than Abelian cases listed in Fig. 5.7(a-e).

Any non-Abelian local symmetry such as  $L = D_4$  also fails to split  $\mathbf{P}^\alpha$  into a full number  $\ell^\alpha$  of components  $\mathbf{P}_{nn}^\alpha$  if  $O$  irrep- $(\alpha)$  correlates with multi-dimensional  $L$ -irreps. By splitting out less than the full rank number  $\rho(O)=10$  of idempotent projectors  $\mathbf{P}_{nn}^\alpha$ , the resulting number of independent  $H$  matrix parameters reduces

accordingly. The 8-parameter resolution for an  $H$ -matrix with  $D_4 \subset O$  is sketched in Fig. 5.7(g) and similarly for  $D_3 \subset O$  in Fig. 5.7(h). Two kinds of  $D_2 \subset O$  in Fig. 5.7(i-j) share degeneracy sums with the Abelian cases.

Each matrix display lists *exact* degeneracy  $\ell^\alpha$  due to *global* symmetry  $O$  but not the cluster *quasi*-degeneracy  $\ell^{\lambda \uparrow G}$  due to *local* symmetry induced representation  $d^\lambda(L) \uparrow G$ . The latter is found by summing global degeneracy  $\ell^\alpha$  of all states  $|\alpha_{a,\lambda}\rangle$  with the same local symmetry  $\lambda$  as per Frobenius reciprocity in (4.65). The result is integer  $\ell^{\lambda \uparrow G} = (\ell^\lambda)^\circ G / {}^\circ L$  mentioned above.

### 5.3 Spectral resolution of full $O_h$ symmetry

Including inversion  $\mathbf{I}$  and reflection operations  $\sigma_n$  allows parity correlations between even- $g$  (*gerade*) and odd- $u$  (*ungerade*) states. Two classes of  $C_2$  subgroups lie in  $O$  and appear in separate  $C_2$ -correlations in (5.2). In the following  $O_h$  correlations, Eq (5.18), the two types of  $C_{2v}$  subgroups have separate tables. The first subgroup  $C_{2v}^i = [\mathbf{1}, \sigma_y, \mathbf{i}_1, \sigma_2]$  is the one of the three local symmetries shown in Fig 5.7 while the second  $C_{2v}^z = [\mathbf{1}, \rho_z, \sigma_y, \sigma_x]$  is just a subgroup of local symmetry  $C_{4v}$  as would be

$$C_{2v}^{34} = [\mathbf{1}, \rho_z, \sigma_3, \sigma_4].$$

$O_h \downarrow C_{4v}$	$A'$	$B'$	$A''$	$B''$	$E$	$C_{3v}$	$A'$	$A''$	$E$	
$A_{1g} \downarrow C_{4v}$	1	·	·	·	·	$A_{1g}$	1	·	·	
$A_{2g} \downarrow C_{4v}$	·	1	·	·	·	$A_{2g}$	·	1	·	
$E_g \downarrow C_{4v}$	1	1	·	·	·	$E_g$	·	·	1	
$T_{1g} \downarrow C_{4v}$	·	·	1	·	1	$T_{1g}$	·	1	1	
$T_{2g} \downarrow C_{4v}$	·	·	·	1	1	$T_{2g}$	1	·	1	,
$A_{1u} \downarrow C_{4v}$	·	·	1	·	·	$A_{1u}$	·	1	·	
$A_{2u} \downarrow C_{4v}$	·	·	·	1	·	$A_{2u}$	1	·	·	
$E_u \downarrow C_{4v}$	·	·	1	1	·	$E_u$	·	·	1	
$T_{1u} \downarrow C_{4v}$	1	·	·	·	1	$T_{1u}$	1	·	1	
$T_{2u} \downarrow C_{4v}$	·	1	·	·	1	$T_{2u}$	·	1	1	
$C_{2v}^i$	$A'$	$B'$	$A''$	$B''$		$C_{2v}^z$	$A'$	$B'$	$A''$	$B''$
$A_{1g}$	1	·	·	·		$A_{1g}$	1	·	·	·
$A_{2g}$	·	1	·	·		$A_{2g}$	1	·	·	·
$E_g$	1	1	·	·		$E_g$	2	·	·	·
$T_{1g}$	·	1	1	1		$T_{1g}$	·	1	1	1
$T_{2g}$	1	·	1	1	,	$T_{2g}$	·	1	1	1
$A_{1u}$	·	·	1	·		$A_{1u}$	·	·	1	·
$A_{2u}$	·	·	·	1		$A_{2u}$	·	·	1	·
$E_u$	·	·	1	1		$E_u$	·	·	2	·
$T_{1u}$	1	1	·	1		$T_{1u}$	1	1	·	1
$T_{2u}$	1	1	1	·		$T_{2u}$	1	1	·	1

(5.18)

The local symmetry  $C_{2v}^i \subset O_h$  unambiguously defines all states in its correlation array while the other  $C_{2v}$  symmetries fail to split the  $E_g$  and  $E_u$  sub-species. The former lead to complete eigenvalue formulae. The latter may not.



Table 5.4: Splittings of  $O \supset C_2(i_4)$  given sub-class structure.

$O \supset D_4$ $\supset C_2(i_4)$	$0^\circ$	$r_n 120^\circ$	$\rho_n 180^\circ$	$R_n 90^\circ$	$i_n 180^\circ$
$0_2$					
$\varepsilon_{0_2}^{A_1}$	$g_0$	$4r_{12} + 4r_{34}$	$2\rho_{xy} + \rho_z$	$4R_{xy} + 2R_z$	$4i_{1256} + i_3 + i_4$
$\varepsilon_{0_2}^E$	$g_0$	$-2r_{12} - 2r_{34}$	$2\rho_{xy} + \rho_z$	$-2R_{xy} + 2R_z$	$-2i_{1256} + i_3 + i_4$
$\varepsilon_{0_2}^{T_1}$	$g_0$	$-2r_{12} + 2r_{34}$	$-\rho_z$	$2R_{xy}$	$-2i_{1256} - i_3 + i_4$
$\varepsilon_{0_2}^{T_2E}$	$g_0$	$2r_{12} - 2r_{34}$	$-\rho_z$	$-2R_{xy}$	$2i_{1256} - i_3 + i_4$
$\varepsilon_{0_2}^{T_2A_1}$	$g_0$	0	$-2\rho_{xy} + \rho_z$	$-2R_z$	$i_3 + i_4$
$1_2$					
$\varepsilon_{1_2}^{A_2}$	$g_0$	$4r_{12} + 4r_{34}$	$2\rho_{xy} + \rho_z$	$-4R_{xy} - 2R_z$	$-4i_{1256} - i_3 - i_4$
$\varepsilon_{1_2}^E$	$g_0$	$-2r_{12} - 2r_{34}$	$2\rho_{xy} + \rho_z$	$2R_{xy} - 2R_z$	$2i_{1256} - i_3 - i_4$
$\varepsilon_{1_2}^{T_1E}$	$g_0$	$2r_{12} - 2r_{34}$	$-\rho_z$	$2R_z$	$-2i_{1256} + i_3 - i_4$
$\varepsilon_{1_2}^{T_1A_2}$	$g_0$	0	$-2\rho_{xy} + \rho_z$	$-2R_z$	$-i_3 - i_4$
$\varepsilon_{1_2}^{T_2E}$	$g_0$	$-2r_{12} + 2r_{34}$	$-\rho_z$	$-2R_{xy}$	$2i_{1256} + i_3 - i_4$

### 5.3.1 Resolving Hamiltonians with $C_{2v}$ local symmetry

As the order of the local sub-group symmetry goes down, the degeneracy and complexity of the rotational cluster must increase.  $O_h \supset C_{2v}$  clusters are 12 fold degenerate and come in 4 cluster species. Matrices describing this system are larger, but  $O \supset C_2$  will show many of the same effects. To actually resolve the doubled  $T_1$  or  $T_2$  triplets of  $O \supset C_2$  requires distinguishing the  $u$  and  $g$  versions of each. The  $C_2$  clusters are 12 fold degenerate, but they are also easily displayed.

As mentioned earlier, the  $O \supset D_3 \supset C_2$  and  $O \supset D_4 \supset C_2$  local symmetries give identical cluster degeneracies and groupings, but with cluster splittings and structure dependent on the sub-group chain. Though it neglects inversion, Fig. 5.7 indicates that there are several different types of  $O \supset C_2$  (and, thus  $O_h \supset C_{2v}$  local sub-group symmetries). Examples given here involve the  $O \supset D_4 \supset C_2(i_4)$  sub-group chain.

Compared to  $O \supset C_4$  and  $O \supset C_3$ , the splittings of  $O \supset C_2$  are relatively simple to calculate since the terms in (5.16) will be real. Creating splitting tables for  $C_2$  is done in the same way as for Tables 5.2 and 5.3. It is shown in Table 5.4.

Table 5.5: Matrix that converts tunneling strengths to cluster splitting energies

$0_2$	$\mathbf{1}$	$r_{12}, i_{1256}$	$r_{34}, R_{xy}$	$\rho_{xy}, R_z$	$\rho_z, i_3$
$\varepsilon_{0_2}^{A_1}$	1	4	4	2	1
$\varepsilon_{0_2}^E$	1	-2	-2	2	1
$\varepsilon_{0_2}^{T_1}$	1	-2	2	0	-1
$\varepsilon_{E,0_2}^{T_2}$	1	2	-2	0	-1
$\varepsilon_{A_1,0_2}^{T_2}$	1	0	0	-2	1

### Local sub-group tunneling matrices and their inverse

Table 5.4 can be further broken apart to demonstrate how a numerical program may automatically evaluate the tunneling splittings for  $O \supset C_2$  local-symmetry structures. This would require an invertible transformation between cluster-splitting energy and tunneling parameters whose inverse is easily defined.

Eq (5.16) produces Table 5.4, but even after combining splittings from each subclass, repetition exists. Two steps convert Table 5.4 into convenient, reduced transformation matrices. First we assume that only  $n_m$  levels may interact with themselves, e.g., that  $1_2$  and  $0_2$  clusters are decoupled. Second we recognize that only half of the subclasses are needed to fully define the possible splittings, the others simply repeat the same information. Table 5.4 shows this for the  $0_2$  cluster. Looking at the  $A_1$  level in the  $0_2$  cluster, one can see that the subclasses  $\mathbf{1}, r_n, \rho_n$  make a vector  $\{1, 4, 4, 2, 1\}$  while the  $R_n, i_n$  subclasses make a vector  $\{4, 2, 4, 1, 1\}$ . These vectors are reordered versions of each other. Thus only one is needed. The  $A_2$  level in the  $1_2$  cluster shows the same similarity, but the  $R_n, i_n$  now contain a negative sign.

By applying only five splitting parameters to a single cluster gives a condensed version of Table 5.4  $H$  transforms five select symmetry-based tunneling values into five energy levels reduced in the form of Eq (5.16). Such a table is shown in Table 5.5. Its inverse in Table 5.6 gives tunneling parameters for a given set of cluster energy splittings in the reduced form of Eq (5.17).

The following example demonstrates this process for a simple Hecht Hamilto-

Table 5.6: Matrix that converts cluster splitting energies to tunneling strengths

$0_2$	$\varepsilon_{0_2}^{A_1}$	$\varepsilon_{0_2}^E$	$\varepsilon_{0_2}^{T_1}$	$\varepsilon_{E,0_2}^{T_2}$	$\varepsilon_{A_1,0_2}^{T_2}$
$\mathbf{1}$	$\frac{1}{12}$	$\frac{1}{6}$	$\frac{1}{4}$	$\frac{1}{4}$	$\frac{1}{4}$
$r_{12}, i_{1256}$	$\frac{1}{12}$	$-\frac{1}{12}$	$-\frac{1}{8}$	$\frac{1}{8}$	0
$r_{34}, R_{xy}$	$\frac{1}{12}$	$-\frac{1}{12}$	$\frac{1}{8}$	$-\frac{1}{8}$	0
$\rho_{xy}, R_z$	$\frac{1}{12}$	$\frac{1}{6}$	0	0	$-\frac{1}{4}$
$\rho_z, i_3$	$\frac{1}{12}$	$\frac{1}{6}$	$-\frac{1}{4}$	$-\frac{1}{4}$	$\frac{1}{4}$

nian written for an octahedral floppy spherical-top molecule of varying spectroscopic parameters. The specific Hamiltonian used is (5.19). The terms  $T^{[4]}$  and  $T^{[6]}$  are rotational distortions written in an octahedral basis and are fourth and sixth order respectively in  $J$ . The parameter  $\theta$  is varied to explore the different relative contributions of  $T^{[4]}$  and  $T^{[6]}$  while keeping them normalized. Because  $T^{[4]}$  and  $T^{[6]}$  are derived from octahedral operators, (5.19) (a repeat of Eq (3.3)) represents all possible octahedral pure rotational Hamiltonians up to sixth order.

$$H = BJ^2 + \cos(\theta)T^{[4]} + \sin(\theta)T^{[6]} \quad (5.19)$$

It was noted in Fig 3.4 that both the cluster structure location and the RES shape will change significantly as the Hamiltonian parameters change in (5.19). As such, the tunneling parameters and cluster splittings must also change. Fig. 5.8 plots the rotational energy levels of (5.19) for changing  $\theta$  and shows the corresponding RES for several points along the parameter-space. RES plots in the figure demonstrate how the phase-space changes with the Hamiltonian fitting terms.

RES diagrams in Fig. 5.8 along with the cluster degeneracy indicate where in the parameter-space  $C_2$  clusters exist. The lowest cluster in Fig. 5.8 in the range  $\theta \simeq 18^\circ - 132^\circ$  is  $C_2$  symmetric. This cluster is magnified nearly 100 times and displayed in Fig. 5.9. In Fig. 5.9 the inside plot shows the  $C_2$  cluster only and the levels have been adjusted to only show level splittings, not the shifting of the cluster. This is done by subtracting a  $\theta$ -dependent shift from all rotational levels.

Figure 5.8:  $J=30$  Energy levels and RES plots for  $T^{[4,6]}$  vs.  $[4,6]$  mix-angle  $\theta$  with  $T^{[4]}$  levels above  $\phi=0^\circ$  (extreme left),  $T^{[6]}$  levels at  $\theta=90^\circ$  (center), and  $-T^{[4]}$  levels at  $\theta=180^\circ$  (extreme right).  $C_4$  local symmetry and 6-fold level clusters dominate at  $\theta=17^\circ$  while  $C_3$  type 8-fold level clusters dominate at  $\theta=132^\circ$ . In between these extremes are  $C_2$  type 12-fold level clusters particularly around  $\theta=80^\circ$  where a  $C_3 - C_4$  level-cluster-crossing of the top 14 levels occurs.

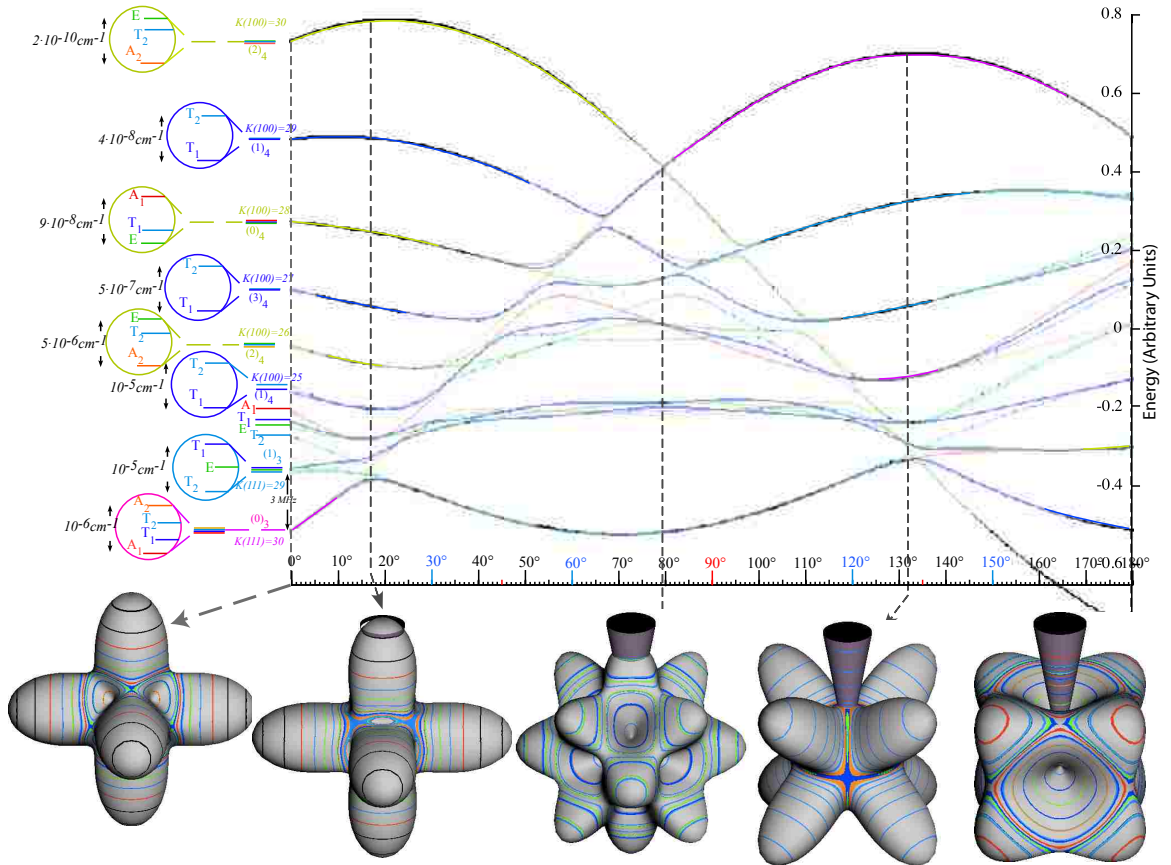
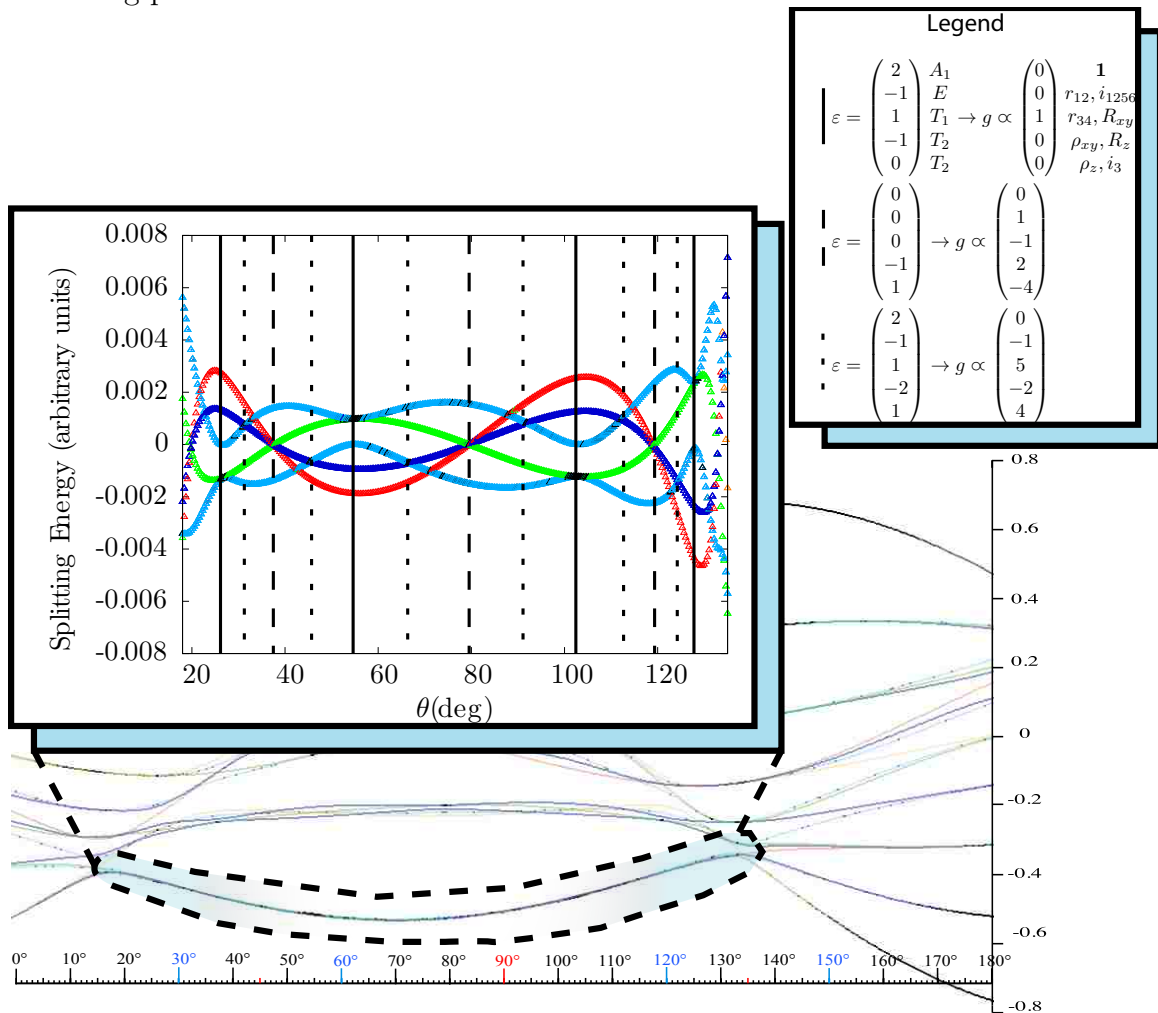


Figure 5.9: The plot focuses on the lowest cluster in the previous energy plot (Fig. 5.8) of the  $T^{[4,6]}$  Hecht Hamiltonian for  $J = 30$ . The inside plot has been magnified 100 times. The inside diagram also centers the levels around their center of mass, showing only the splittings and ignoring the shifts of the cluster. As before, color indicates the symmetry of each level. The vertical lines on inside plot draw attention to specific clustering patterns described in the text.



There are repeated points of coincidence in Fig. 5.9 including degeneracy between levels of different symmetry or notable splitting patterns. These are included in Fig. 5.9 by the vertical dashed, dotted and solid lines corresponding to  $(A_1, E, T_1, T_2, T_2)$  splitting patterns of  $(0, 0, 0, 1, -1)$ ,  $(2, -1, 1, 1, -1)$  and  $(2, -1, 1, 0, -1)$  respectively.

The transformation in Table 5.6 converts each splitting pattern marked in Fig. 5.9 into a vector of tunneling amplitudes for each of several values of the fitting parameter  $\theta$  used in the Hecht Hamiltonian (5.19). The tunneling for these cases is shown in the inset legend of Fig. 5.9 and is consistent with the notation of Tables 5.6 and 5.5.

Particularly surprising are three cases of dashed lines consisting of a triple crossing of  $(A_1, T_1, E)$  lying between a pair of  $T_2$  levels. (Two additional such cases appear outside of the  $18^\circ$  to  $132^\circ$  range.) This  $(T_2[A_1, T_1, E]T_2)$  cluster belongs to  $O \supset C_2$ , induction  $0_2(C_2) \uparrow O$ . One normally sees  $(A_1, T_1, E)$  clusters present in the  $\nu_3$  spectra of  $\text{CH}_4$  taken by Pine[5] and assigned to be a  $C_4$ -type cluster[6], though its band location was close to the  $C_2$  separatrix region.

The relationship between the more common  $(A_1, T_1, E)$   $C_4$  methane clusters and this extraordinary cluster-within-cluster  $(T_2[A_1, E, T_1]T_2)$   $O \supset C_2$  cluster shown here is not yet understood. Despite this, students of group theory may not be amazed to see a connection between  $T \supset C_4$  and  $O \supset C_4 \supset C_2$  as the tetrahedral and octahedral groups are isomorphic. Moreover the  $O \supset C_4 \supset C_2$  subgroup chain must contain the  $T \supset C_4$  chain. Continuing the subduction from  $C_4$  to  $C_2$  entails further splitting of the  $C_4$  clusters. This does not explain the  $(A_1, T_1, E)$   $C_4$  pattern, but does show a route to its origin.

## 5.4 Conclusion

Using the developments of Chapter 4, it is possible to use group operator based parameters to construct and solve Hamiltonians in a more complete and rigorous manner than was previously possible using only nearest-neighbor coupling amplitudes.

This more general approach accounts for changes in phase of eigenvector components, a common point of difficulty and confusion for nearest-neighbor models.

Parameterization based on local symmetry of rotational eigenstates greatly reduces the number of possible tunneling parameters by showing equivalency between them, leading to condensed forms such as Table 5.2 or Table 5.5. This derives possible cluster splitting patterns for a particular molecular symmetry group subduction.

The use of such a basis is shown explicitly in Fig 5.9. In this figure, the splittings are labeled in terms of the basis created by the body-frame operations. This ortho-complete transformation between energy splittings and tunneling parameters is a computationally simple process embodied by Eqs (5.5) and (5.6) and more able to be automated for use in more complex spectral analyses, such as the disentanglement of polyadic rovibrational bands discussed in chapter 6.

## Bibliography

- [1] William G. Harter. *Principles of symmetry, dynamics, and spectroscopy*. J. Wiley, 1993.
- [2] Volker Heine. *Group Theory in Quantum Mechanics*. Number 9 in International Series of Monographs in Pure and Applied Mathematics. The MacMillan Company, 60 Fifth Avenue, New York 11, NY, 1960.
- [3] K. C. Kim, W. B. Person, D. Seitz, and B. J. Krohn. Analysis of the  $\nu_4$  ( $615\text{ cm}^{-1}$ ) region of the fourier transform and diode laser spectra of  $\text{SF}_6$ . *Journal of Molecular Spectroscopy*, 76(1-3):322 – 340, 1979.
- [4] William G. Harter. Theory of hyperfine and superfine levels in symmetric polyatomic molecules. ii. elementary cases in octahedral hexafluoride molecules. *Physical Review A*, 24(1):192–263, July 1981.

- [5] A. S Pine. High-resolution methane  $\nu_3$ -band spectra using a stabilized tunable difference-frequency laser system. *Journal of the Optical Society of America*, 66(2):97, 1976.
- [6] William G. Harter and Chris W. Patterson. Asymptotic eigensolutions of fourth and sixth rank octahedral tensor operators. *Journal of Mathematical Physics*, 20(7):1453–1459, July 1979.



## Chapter 6

### Rotational Energy Surfaces Analysis for the $\nu_3/2\nu_4$ Polyad of $\text{CF}_4$

## 6.1 Chapter Summary

CF<sub>4</sub> has spectroscopic interest because, like CH<sub>4</sub>, it is a known greenhouse gas and one that requires more detailed study. Experimental data for the  $\nu_3/2\nu_4$  polyad band exist[1], but has recently been expanded[2]. Of the spherical tops, CH<sub>4</sub> is one whose vibrational structure contains the most anomalously resonant anharmonic and Coriolis interactions. Its heavier cousin, CF<sub>4</sub>, also has strong Coriolis interactions. Moreover, its higher inertia means much higher  $J$  values in standard temperature spectroscopy and more opportunity to investigate rovibronic quantum mechanics.

This chapter is an attempt to offer theoretical insight to the experimental and calculated spectrum of CF<sub>4</sub> using semi-classical RES methods. The treatment done here can be extrapolated to help study other molecules of similar symmetry including the very fluxional CH<sub>4</sub> and P<sub>4</sub>.

Semi-classical or semi-quantum solutions often provide a qualitative understanding that would be more obscure by purely quantum mechanical or numerical means. Rotational Energy Surface (RES) analysis is one such technique. This study uses Rotational Energy Surface analysis to provide such understanding to rotational level clusters found in the  $\nu_3/2\nu_4$  polyad of CF<sub>4</sub>.

Previous chapters required only a single RES to show rotational behavior given a vibrational singlet or ground state. The inclusion of a vibrational polyad removes this simplification, requiring a combination of interacting Rotational Energy Eigenvalue Surfaces (REES). The surfaces plotted each represent parts of multiply connected phase-space surfaces. As such they are useful in locating possible tunneling paths and clustering patterns.

## 6.2 Polyad Formalism

The polyad model is a method for classifying molecular vibrational interactions in which vibrational states which may interact with each other as well as with rotational

states. This implies that vibrational interactions may be anharmonic, non-linear and may break the Born-Oppenheimer Approximation between molecular rotation and vibration.

Once a polyad is defined in terms of its vibrational interaction, the rovibrational Hamiltonian becomes an outer product of anharmonic rotational and vibrational parts. The polyad model is a particularly convenient tool used to evaluate spherical-top molecules for which polynomials of rotational and vibrational terms may be computationally inexpensive to calculate and are based on parameters of the molecular symmetry group. Ref [3, 4] describes how formulations of anharmonic rovibrational Hamiltonians may be rewritten using the polyad model.

A polyad Hamiltonian is one that has been transformed into the form of Eq (6.1). In this form,  $P_0$  is the vibrational ground state (GS) while  $P_k$  ( $k = 0, \dots, n$ ) are various vibrationally excited interactions.  $P_{\{1\}}$  refers to a single vibration or monad.  $P_{\{2\}}$  refers to two coupled vibrations or a dyad. The dyad  $\nu_3/2\nu_4$  is the focus of Sec 6.5.

$$H = H_{\{P_0=GS\}} + H_{\{P_1\}} + \dots + H_{\{P_k\}} + \dots + H_{\{P_{n-1}\}} + H_{\{P_n\}} \quad (6.1)$$

The specific case shown in this chapter is a semi-classical treatment of the  $\nu_3/2\nu_4$  polyad (dyad) band of  $\text{CF}_4$ . The  $\nu_3/2\nu_4$  is an interaction of the  $\nu_3$  vibrational triplet and the harmonic of the  $\nu_4$  vibrational triplet. The  $\nu_3/2\nu_4$  exists because of the coincidence in energy of these two vibrations ( $\nu_3 = 1283.460\text{cm}^{-1}$  and  $\nu_4 = 631.059\text{cm}^{-1}$ ). The Hamiltonian used here includes  $P_0 = GS$ ,  $P_1 = \nu_3$  and  $P_2 = \nu_3/2\nu_4$ .

The polyad formalism is convenient for both theoretical and computational scientists for several reasons. It strictly uses parameters derived from group operations. This creates computational conveniences and it offers a coherent language to describe various spectroscopic effects and features. Similar formulation can be used to calculate electric dipole moments and spectral intensities as well as energy levels. Once

enough spectroscopic data exists to create fitting parameters, a synthetic spectrum can be generated including spectral linewidth, energy and intensity.

Once a specific vibrational and rotational Hamiltonian operators are created, they may be reused for other molecules of the same symmetry. Thus, changes between similar molecules of the same symmetry may only require a change in fitting parameters.

Terms  $H_{P_k}$  also have no matrix elements with  $P_{k' > k}$  terms, making the continuation of an expansion. Expanding to higher order terms uses previously generated operators in this formalism as higher order (or higher polyad) terms are simply added to the Hamiltonian.

### 6.3 Development

The rewritten polyad Hamiltonian is expressed as an outer product of molecular-symmetry-based rotation and vibration operators as shown in Eq (6.2). The sum in Eq (6.2) is over all possible rotation and vibration operators while the  $t_{\{\gamma_1\}\{\gamma_2\}}^{\Omega(K,n\Gamma)\Gamma_1\Gamma_2}$  coefficients are fitting parameters found for a particular set of operators and a particular molecular species and transition.

The operator  $V_{\gamma_1\gamma_2}^{\Gamma_1\Gamma_2(\Gamma_\nu)}$  is a vibrational operator for coupling between mode  $\gamma_1$  (of symmetry  $\Gamma_1$ ) and  $\gamma_2$  (of symmetry  $\Gamma_2$ ). The term  $\Gamma_\nu$  is the symmetry of the combined  $\Gamma_1 \otimes \Gamma_2$  operator.

Rotation operator  $R^{\Omega(K,n\Gamma_r)}$  is similar to the rotational Hamiltonian operators found in chapter 3. The term  $\Omega$  defines the order,  $K$  defines the rank and  $\Gamma_r$  defines the tetrahedral symmetry of the operator. The term  $n$  in the rotation operator helps distinguish operators which may have the same tetrahedral symmetry. These operators are not shown explicitly here, but may be found in ref [3].

The term  $\beta$  is a numerical coefficient defined as  $\beta = \sqrt{[\Gamma_1]}(-\sqrt{3}/4)^{\Omega/2}$ , unless  $(K, n\Gamma) = (0, 0A_1)$  when  $\beta = 1$ . Thus it is also dependent on the vibrational and rotational operators used, though it is independent of molecular species. The specific

fitting parameters used here can be found in ref [2].

$$H = \sum_{\{\gamma_1\}\{\gamma_2\}} t_r^{\Omega(K,n\Gamma)\Gamma_1\Gamma_2} \beta(R^{\Omega(K,n\Gamma_r)} \otimes^\epsilon V_{\gamma_1\gamma_2}^{\Gamma_1\Gamma_2(\Gamma_\nu)})^{A_1} \quad (6.2)$$

Individual matrix elements are formed as Eq (6.3). Such a Hamiltonian is fully quantum mechanical. Reduced matrix elements, normalization factors, generalized  $3J$  symbols and isoscalar factors are all discussed in depth in ref [3, 5, 6]. Many of these terms are easily calculated by easily available software packages[7, 8, 9]. To make this a semi-quantum Hamiltonian, the rotation operators must be classical functions of body-frame angles  $\theta$  and  $\phi$ . This changes the form of the matrix elements into the simpler Eq (6.4), forcing a basis of vibrational components only since the rotation is now classical.

$$\begin{aligned} & \left\langle J n_r C_r; \{\nu_s\} C_\nu; C \left| (R^{\Omega(K,n,\Gamma)} \times^\epsilon V_{\gamma_1\gamma_2}^{\Gamma_1\Gamma_2(\Gamma)})^{A_1} \right| J n'_r C'_r; \{\nu'_s\} C'_v; C' \right\rangle \quad (6.3) \\ & = (-1)^{J+K} K \begin{pmatrix} K & J & J \\ n\Gamma & n'_r C'_r & n_r C_r \end{pmatrix} (-1)^{\Gamma+C+C'_r+C_v} \begin{pmatrix} C'_v & C'_r & C \\ C_r & C_v & \Gamma \end{pmatrix} \sqrt{\frac{1}{[\Gamma]}} \\ & \times \langle J \| R^{\Omega(K)} \| J \rangle \langle \{\nu_s\} C_\nu \|^\epsilon V_{\gamma_1\gamma_2}^{\Gamma_1\Gamma_2(\Gamma)} \| \{\nu'_s\} C'_v \rangle \delta_{CC'} \end{aligned}$$

$$\begin{aligned} & \left\langle \{\nu_s\} C_\nu \sigma \left| (R^{\Omega(K,n\Gamma)} \times^\epsilon V_{\gamma_1\gamma_2}^{\Gamma_1\Gamma_2(\Gamma)})^{A_1} \right| \{\nu'_s\} C'_\nu \sigma' \right\rangle \quad (6.4) \\ & = \frac{1}{N} \begin{pmatrix} \Gamma & \Gamma & A_1 \\ \sigma_1 & \sigma_2 & \end{pmatrix} \begin{pmatrix} C' & \Gamma & C \\ \sigma_\nu & \sigma & \sigma'_{nu} \end{pmatrix} R^{\Omega(K,n\Gamma)} \langle \{\nu_s\} C_\nu \|^\epsilon V_{\gamma_1\gamma_2}^{\Gamma_1\Gamma_2(\Gamma)} \| \{\nu'_s\} C'_\nu \rangle \end{aligned}$$

While several studies have generalized the RES for cases involving vibration[10, 11, 12] or torsion, some being totally classical [13], the present treatment keeps vibration a quantum operator. In this way the total molecular Hamiltonian can be thought



Figure 6.1: All 9 interacting Rotational Energy Eigenvalue Surfaces for  $\nu_3/2\nu_4$  of  $CF_4$  with  $J = 60$ . Minimum uncertainty cone is also shown for this value of  $J$ . Surfaces are also dissected show those of lower energy beneath. Outer RES also tend to be more spherical, making contours challenging and causing them to be slightly dappled.

of as a vibrational Hamiltonian matrix which has elements made up of classical rotational terms. This total molecular Hamiltonian is then numerically diagonalized, giving several interacting Rotational Energy Eigenvalue Surfaces (REES). In the fully classical description there is a single surface existing in a higher dimensional space. The diagonalization prevents surfaces from crossing one another.

Figure 6.1 shows the 9 interacting surfaces describing the  $\nu_3/2\nu_4$ ,  $J = 60$  manifold of  $CF_4$ . Taken as such a large group they are of limited utility. Following sections show how these nested surfaces can be used for to analyze this  $\nu_3/2\nu_4$  polyad.

#### 6.4 3D Oscillator Example

Though polyad formalism is well known in molecular spectroscopy, it is less familiar to the broader physics community. As a means of introduction, a short example is given, showing behavior familiar to physicists. More details on a similar problem can be found in ref [10]. Further examples of rovibrational and multi-rotor RES are included

in appendix 6.A.

The simplest polyad is that of a single vibrational excitation (monad). This monad band is formed by the interaction between rotational modes and a single vibrational mode. Using a minimum number of terms, such a rovibrational spectrum may be modeled as an uncoupled vibrational term, a rotational term and a Coriolis term. In this case, the Hamiltonian could have the form found in Eq (6.5).

$$H = \nu_3 + BJ^2 + B\zeta \vec{J} \cdot \vec{v}_3 \quad (6.5)$$

This simplified case keeps the notation and parameterization of tetrahedrally symmetric molecules ( $XY_4$ ). The vibration  $\nu_3$  is chosen because it is the lowest vibrational state that has a non-zero Coriolis interaction. For an  $XY_4$  molecule,  $\nu_3$  is a three-dimensional oscillator of symmetry  $F_2$ .

Using the notation of Eq (6.2) the Hamiltonian terms used in this example are the following. The pure rotational term is  $B(R^{2(0,A_1)} \otimes \mathbf{1})$ . This is also the  $H_{\{P_0\}}$ , the vibrational ground state term which allows molecular rotations. The next two terms are a part of  $H_{\{P_1\}}$  since they include a contribution from the vibration  $\nu_3$ . The pure vibrational term is  $\nu_3(R^{0(0,A_1)} \otimes V_3^{F_2 F_2(A_1)})$ . The Coriolis term is written as  $B\zeta(R^{1(1,F_1)} \otimes V_3^{F_2, F_2(F_1)})$ , coupling rotational and vibrational operators.

While estimates of the Coriolis coupling term can be calculated[14], that is not the process this example is intended to show. In fact, the coupling term is often taken as a fitting parameter, as it is done here.

To demonstrate the similarity between effects in molecular spectroscopy and the atomic splittings better known to physicists, Fig 6.2(a) plots the splitting of the vibrational band with increasing  $J$ . The plot is of reduced energy, subtracting the  $BJ(J+1)$  shift from each point, showing only the shift. The example assumes the following parameters:  $\nu_3 = 1000 \text{ cm}^{-1}$ ,  $B = 1 \text{ cm}^{-1}$ ,  $B\zeta = 0.1 \text{ cm}^{-1}$ .

This behavior is analogous to that of  $\vec{l} \cdot \vec{s}$  coupling. The vibrational angular mo-

momentum of the triplet  $\nu_3$  will split the rotational sub-levels into three distinct bands just as  $l$  and  $s$  will form two bands in  $J$ . For  $\vec{l} \cdot \vec{s}$  coupling,  $J = l \pm 1/2$  are possible values. Here, splittings happen in the same fashion, but from vibrational angular momentum  $\nu_3$ .

Other types of splitting are possible in this context as well. The distinct bands formed in Fig 6.2(a) can be split into constituent  $J$  sub-levels by rotational anharmonicity. Such a term is introduced to form Fig 6.2(b). The term added here is forth-order in  $J$  and splits the bands, showing the  $J$  sub-levels underneath. The exact term is shown in Eq (6.6) with  $D = 10^{-7}\text{cm}^{-1}$ . Though the constant in the term is small, it quickly becomes large for high values of  $J$ .

$$R^{4(4,A_1)} = D (J_x^4 + J_y^4 + J_z^4 - 3J_y^2 J_z^2 - 3J_x^2 (J_y^2 + J_z^2)) \quad (6.6)$$

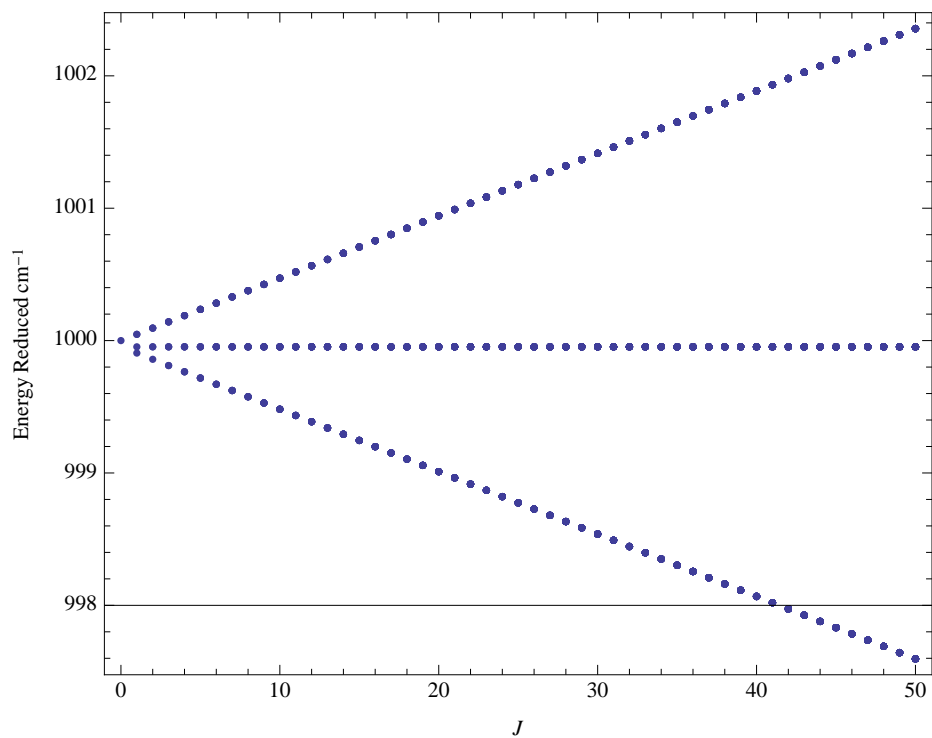
This short example has shown the effect of two different operators inside a single polyad, one that split degeneracies by rotation and one that did so by rotation-vibration interaction. In treating the  $\text{CF}_4$   $\nu_3/2\nu_4$  dyad, both types of operators are active and both types will couple to a second vibration. The key distinction between this simplified example and the following dyad is this coupling between separate vibrational modes. That is, the distinction between monad and dyad.

## 6.5 Analysis

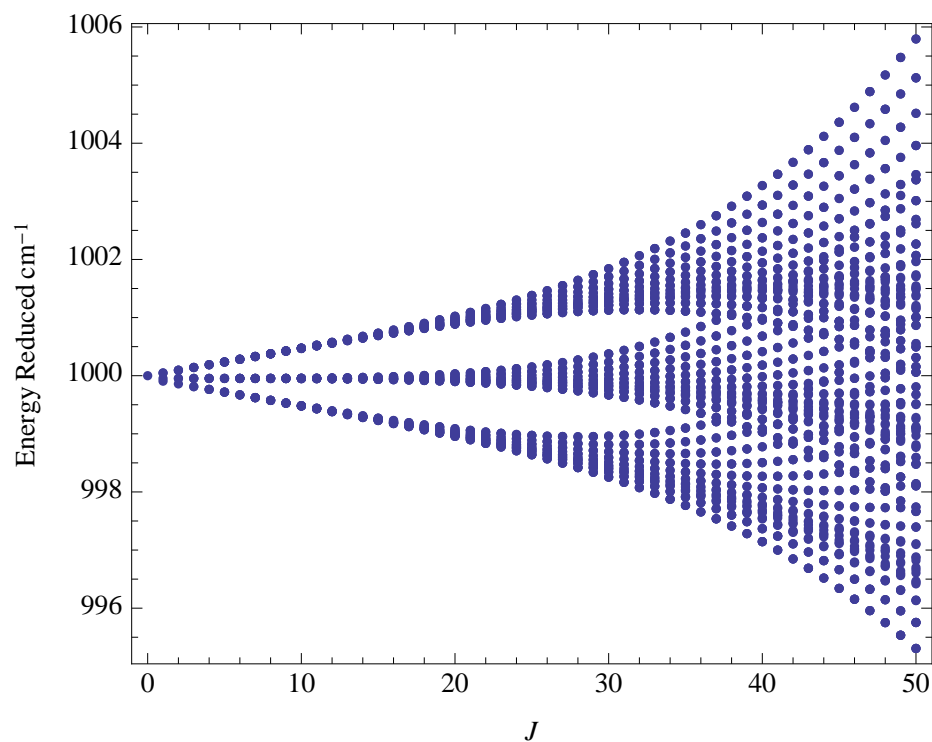
### 6.5.1 Experimental and Computational Details

The spectrum of  $\text{CF}_4$  was measured by Fourier transform infrared (FTIR) methods at a resolution of  $0.003\text{cm}^{-1}$  both at room temperature and by supersonic expansion jet at at temperature of nearly 15 K. The experimental work was done by Maul and coworkers[2] in Braunschweig, Germany. A synthetic linelist of this spectrum was extrapolated Boudon and coworkers[2] and included in the HITRAN 2008[15] and





(a) Reduced Energy plots shows the energy splitting while removing  $BJ^2$  term. This figure demonstrates splittings from a monad of a vibrational triplet state.



(b) Including anharmonic rotational terms may split the bands formed by the Coriolis interaction.

Figure 6.2: Reduced Energy plots may show different types of interactions depending on the model Hamiltonian used.

GEISA 2009 databases. The fitting parameters associated with this experimental fit and synthetic spectrum were used in this analysis.

### 6.5.2 Rotational Band Boundaries

This section evaluates the  $\nu_3/2\nu_4$  polyad band of  $\text{CF}_4$ , explaining rotational clusters in terms of symmetry reduction and explaining the boundaries of the rotational bands for a given angular momentum. Each REES represents a band of rotational energy levels. The bands may interact with each other through phase-space tunneling, though the effect is small. The minimum and maximum of the REES represent classical bounds to the quantum band. Quantum levels outside the classical boundaries represents a breakdown of the semi-quantum treatment. Fig 6.3 plots quantum rovibrational energy with changing  $J$  along with the height of the  $C_4$ ,  $C_3$  and  $C_2$  axes for each REES in the  $\nu_3/2\nu_4$  polyad. Evaluating the height (energy) of these subgroup axes allows for great computational simplicity. A numerical search for maxima and minima would be computationally expensive and unnecessary because, by definition, a global maxima or minima for an object of symmetry  $\mathcal{G}$  must exist only on axes of subgroup  $\mathcal{H}$ .

It is possible for the  $C_1$  axis to provide a maximum or minimum, but since the axis moves, its height is significantly more challenging to calculate and would require a numerical search. Though rare, these  $C_1$  structures do occasionally exist in  $\nu_3/2\nu_4$ . Fig 6.4 shows an REES which includes evidence of  $C_1$  local structure. While they have been shown to exist, their effect is small. As such, we do not track them, though they could be a small source of error, particularly at even higher values of  $J$ .

Correspondence between the classical band boundaries and the quantum levels is clear for most of Fig 6.3. Regions of Fig 6.3 which diverge the most are in the range of  $J > 50$  on the third vibrational band. The fifth band near  $J = 60$  has a single cluster which is out of the semi-quantum boundaries. Closer inspection shows this band to be build of an REES with  $C_1$  clusters as global maxima, which is shown in Fig 6.4.

Though the  $C_1$  maxima extends past the band boundaries, the highest cluster is still beyond the semi-classical approximation.

Clusters do fit more tightly in low  $J$  portions of Fig 6.3. Slight disagreement found at low  $J$  is thought to be of different origin from those at high  $J$ . Lack of correspondence at low  $J$  can be easily thought of as a difference between classical and quantum rotational operators. This is distinct from the lack of correspondence at higher  $J$  which is likely from the simplification of the outer product of the rotational and vibrational Hamiltonians in the semi-quantum approximation. Thus, this difference can be considered a type of Born-Oppenheimer breakdown.

### 6.5.3 Rotational Level Clustering

While taken all at once, the nine rotational energy surfaces, as shown in Fig 6.1, are of limited utility. Taken individually they offer an explanation as to the origin of rotational level clusters seen in the  $\nu_3/2\nu_4$  band.

Individual RES plots are shown in Fig 6.5. The plots are taken of the  $J = 60$  rotational energy surfaces, starting with the fourth rotational band and increasing to the sixth of nine. These were chosen because they are of high enough  $J$  to have a significant number of rotational clusters (REES contours) on each surface. They each show local regions of very different subgroup symmetry while still showing clear global octahedral symmetry.

There are several noteworthy features in Fig 6.5. All REES plots show excellent agreement between the minimum uncertainty cone and accompanying level cluster. Fig 6.5(d) makes this slightly less obvious since this cluster is found along the  $C_2$  axis and is deformed into an ellipse. Figs 6.5(c) and 6.5(d) also show clusters matching this cone, but placed along the  $C_3$  axis. Some clusters do not match intersections with uncertainty cones. While this is common near separatrix regions, as one would expect given the shift in local subgroup symmetry, it occasionally happens for higher  $J_z$  cones as  $J$  increases.

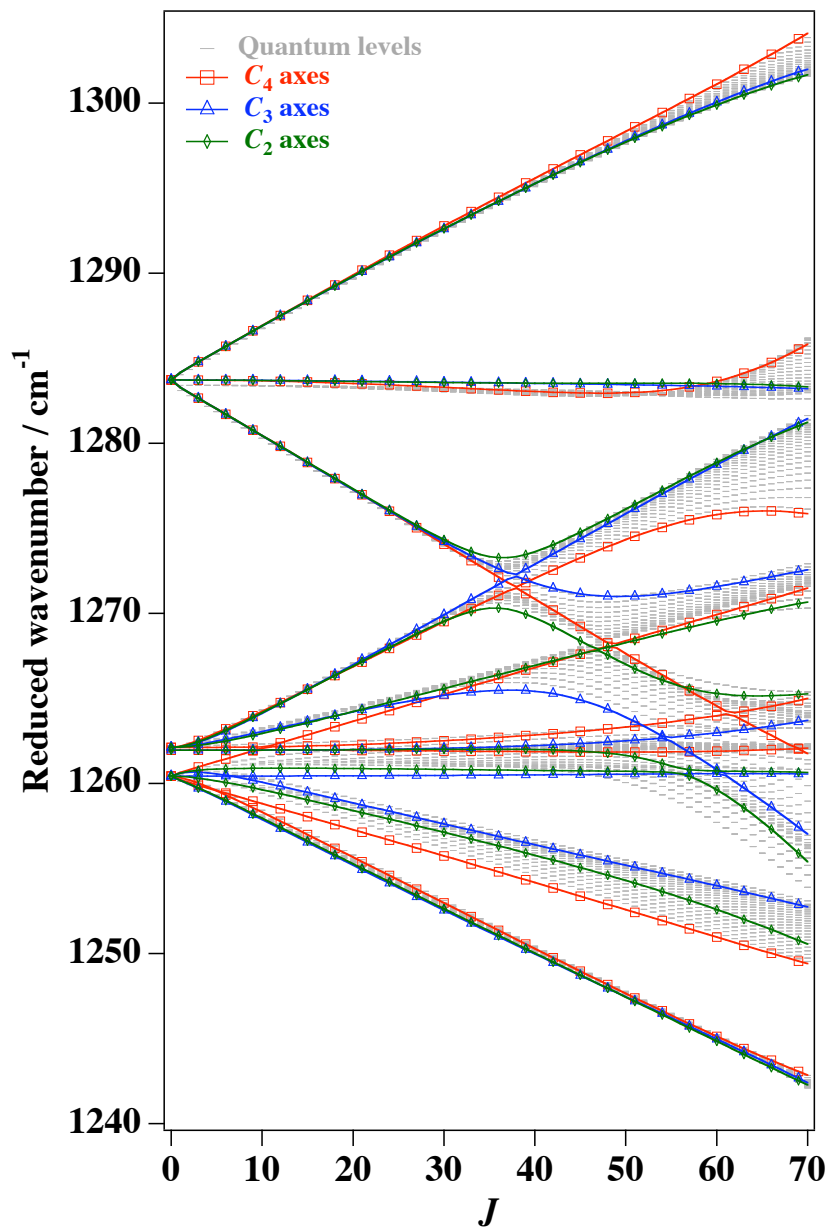


Figure 6.3: Semi-quantum outlines show band boundaries for the rotational levels of  $\nu_3/2\nu_4$ . Reduced energy is defined as the quantum energy subtracted by all scalar fully rotational terms. In this way, the reduced energy shows the energy splittings without the energy shifts related only to increasing  $J$ .

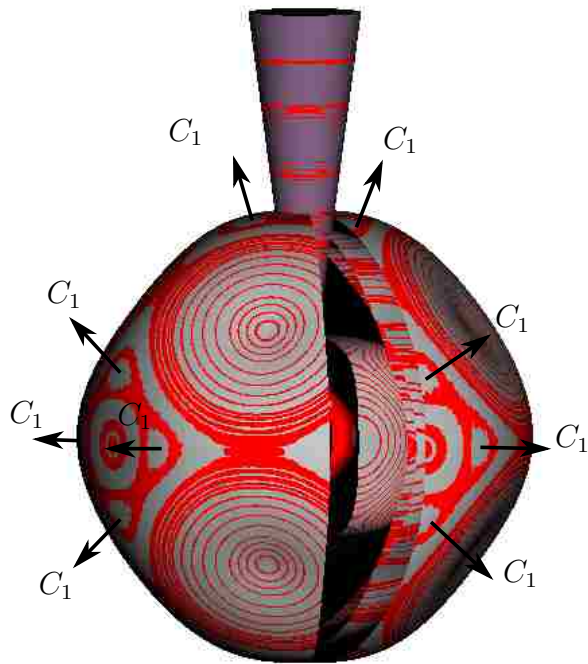


Figure 6.4:  $C_1$  local symmetry structures are rare, but we see some at  $J = 57$  on the fifth surface from the bottom. Others do exist, but this one is amongst the clearest at this range of  $J$ .

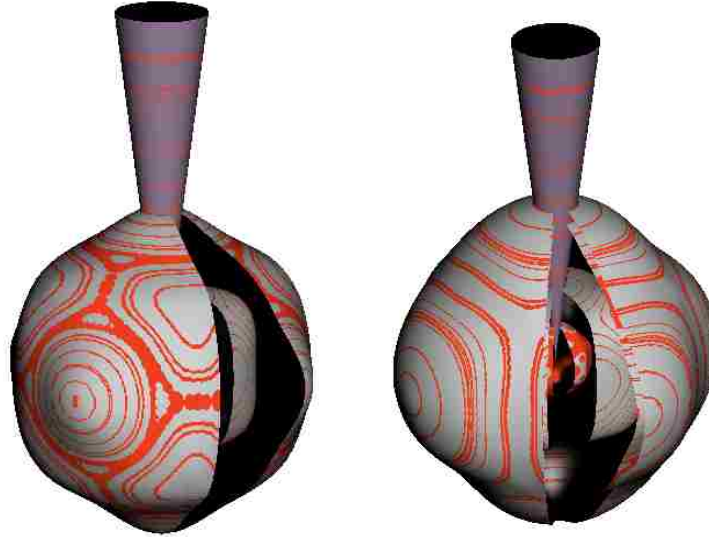
Importantly, clusters placed on each region do show the internal symmetry and degeneracy expected of the given local symmetry region. The only notable exception to this is when neighboring REES plots overlap in range. Though the surfaces cannot cross, the maxima of one may extend above the minima of the next. In such cases an REES may show a contour that belong to a different REES. This is easiest to spot when the improperly placed cluster either shows the clustering related to one REES and not the other or when the cluster obeys the angular momentum uncertainty for one REES and not the other.

## 6.6 Conclusion

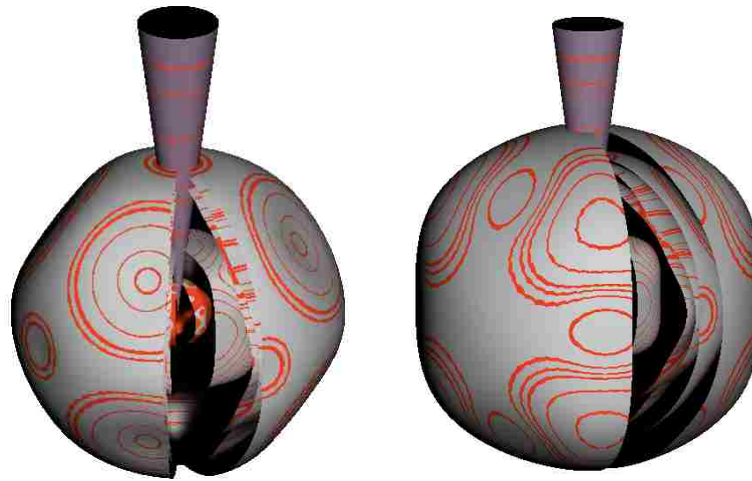
Semi-quantum Rotational Energy Eigenvalue Surface plots can predict several important spectral features for the  $\nu_3/2\nu_4$  polyad band of  $\text{CF}_4$ . The semi-classical tools of angular momentum uncertainty cones works with some success in this sort of system. While for vibrational singlets it is highly predictive, for this polyad system the technique can lose precision as  $J$  increases. As in the case of vibrational singlets, angular momentum uncertainty cones are most accurate at predicting cluster energies of clusters that are more localized to a single axis, thus showing less  $K$  mixing.

The REES are effective at finding the boundaries of the rotational bands for a given angular momentum,  $J$ . The REES are perhaps the most useful in predicting the rotational clusters that originate from symmetry reduction from the global molecular symmetry to the local subgroup symmetry regions of the REES. This is typically done for REES for vibrational singlets. For polyads it is more efficiently done with an energy plot using semi-quantum outlines as in Fig 6.3. The semi-quantum outlines help diagnose which of the possible local symmetry regions can produced symmetry reduced clusters.

While some of this analysis has been done in previously for monads, this work shows that semi-classical theory can be extended to a system with significant rotation-



(a)  $J = 60$  3rd surface has  $C_4$  and  $C_3$  local symmetry. (b)  $J = 60$  4th surface has  $C_4$  local symmetry.



(c)  $J = 60$  5th surface has  $C_4$  local symmetry. (d)  $J = 60$  6th surface has  $C_3$  and  $C_2$  local symmetry.

Figure 6.5:  $CF_4 \nu_3/2\nu_4$  REES plots. Surfaces are labeled starting from the center going out. Looking at surfaces one by one shows their individual geometry and indicates how the level clusters (contours) must arrange themselves. We include only 4 surfaces as examples, but many are examined in the analysis.

vibration coupling which also requires many REES.

## Bibliography

- [1] T. Gabard, G. Pierre, and M. Takami. Study of the  $\nu_3$  and  $2\nu_4$  interacting states of  $^{12}\text{CF}_4$ . *Molecular Physics*, 85(4):735–744, 1995.
- [2] V. Boudon, J. Mitchell, A. Domanskyaya, C. Maul, R. Georges, A. Benidar, and W. G. Harter. High-resolution spectroscopy and analysis of the  $\nu_3/2\nu_4$  dyad of  $\text{CF}_4$ . *Molecular Physics*, submitted, 2011.
- [3] J.-P. Champion and M. Loëte. *Spectroscopy of the Earth's atmosphere and interstellar medium*, chapter Spherical top spectra, pages 399–422. Academic Press, 1992.
- [4] Jacques Moret-Bailly. Introduction au calcul de l'énergie de vibration-rotation des molécules à symétrie sphérique. *Cahiers de physique*, 13:476, 1967.
- [5] J. P. Champion, G. Pierre, F. Michelot, and J. Moret-Bailly. Composantes cubiques normales des tenseurs spheriques. *Canadian Journal of Physics*, 55:512–520, 1977.
- [6] G. Poussigue, E. Pascaud, J. P. Champion, and G. Pierre. Rotational analysis of vibrational polyads in tetrahedral molecules. *Journal of Molecular Spectroscopy*, 93:351–380, 1982.
- [7] Ch. Wenger, V. Boudon, J.-P. Champion, and G. Pierre. Highly-spherical top data system (HTDS) software for spectrum simulation of octahedral  $\text{XY}_6$  molecules. *Journal of Quantitative Spectroscopy and Radiative Transfer*, 66:1–16, 2000.



- [8] M. Rey, V. Boudon, Ch. Wenger, G. Pierre, and B. Sartakov. Orientation of  $O(3)$  and  $SU(2) \otimes C_i$  representation in cubic point groups ( $O_h, T_d$ ) for application to molecular spectroscopy. *Journal of Molecular Spectroscopy*, 219:313–325, 2003.
- [9] Ch. Wenger, V. Boudon, M. Rotger, M. Sanzharov, and J.-P. Champion. XTDS and SPVIEW: Graphical tools for the analysis and simulation of high-resolution molecular spectra. *Journal of Molecular Spectroscopy*, 251:102–113, 2008.
- [10] William G. Harter, Chris W. Patterson, and Harold W. Galbraith. Centrifugal and coriolis effects on level cluster patterns for  $T(\nu_3)$  rovibrational bands in spherical top molecules. *Journal of Chemical Physics*, 69:4896, 1978.
- [11] William G. Harter, Harold W. Galbraith, and Chris W. Patterson. Energy level cluster analysis for  $e(\nu_2)$  vibration rotation spectrum of spherical top molecules. *Journal of Chemical Physics*, 69:4888, 1978.
- [12] G. Dhont, D. Sadovskii, B. Zhilinski, and V. Boudon. Analysis of the "unusual" vibrational components of triply degenerate vibrational mode  $\nu_6$  of  $\text{Mo}(\text{CO})_6$  based on the classical interpretation of the effective rotation-vibration hamiltonian. *Journal of Molecular Spectroscopy*, 201:95–108, 2000.
- [13] D. A. Sadovskii and B. I. Zhilinski. Group-theoretical and topological analysis of localized rotation-vibration states. *Physical Review A*, 47(4):2653, April 1993.
- [14] Philip R. Bunker and Per Jensen. *Molecular Symmetry and Spectroscopy*. NRC Research Press, 2 edition, 1998.
- [15] L. S. Rothman, I. Gordon, A. Barbe, D. Benner, P. Bernath, M. Birk, and et al. The HITRAN 2008 molecular spectroscopic database. *Journal of Quantitative Spectroscopy and Radiative Transfer*, 110:533–572, 2009.

## Appendix 6.A Multiple Rotors and Rotor-2D Vibration Hamiltonians

Fluxional rotor molecular systems as well as polyad states are areas of considerable spectroscopic interest. Molecules demonstrating this behavior are known to be greenhouse gasses and many exist astronomically. This appendix demonstrates the simplest possible Rotational Energy Surfaces for such states. A more detailed explanation is found in ref [1].

### 6.A.1 Constrained Molecular Double Rotators

Common composite rotors are molecules which are a rigid rotor, but with an attached methyl ( $\text{CH}_3$ ) pinwheel. Both the main rotor angular momentum,  $R$ , and methyl rotor angular momentum,  $S$ , must be considered in this case. Moreover,  $R$  and  $S$  will add to make total angular momentum  $\vec{J} = \vec{R} + \vec{S}$ .

When treated numerically, these rotor-rotor interaction are treated with a torsional potential as in Eq (6.7). In the simplified case here, the secondary rotor or gyro,  $S$  is constrained to exist in a fixed body-frame axis.

$$H_{R+S} = H_{\text{rotor},R} + H_{\text{gyro},S} + V_{RS} \quad (6.7)$$

Given that  $S$  is constrained, it does no work and need not contribute to the Hamiltonian. This should be rewritten to incorporate the fact that  $\text{vec}R = \vec{J} - \vec{S}$ . For a main rotor that is an asymmetric top, the Eq(6.7) can be written as Eq (6.8).

$$\begin{aligned} H_{R+S,\text{fixed}} &= A(\mathbf{J}_x - \mathbf{S}_x)^2 + B(\mathbf{J}_y - \mathbf{S}_y)^2 + C(\mathbf{J}_z - \mathbf{S}_z)^2 + H_{\text{gyro},S} \\ &= A\mathbf{J}_x^2 + B\mathbf{J}_y^2 + C\mathbf{J}_z^2 - 2A\mathbf{J}_x\mathbf{S}_x - 2B\mathbf{J}_y\mathbf{S}_y - 2C\mathbf{J}_z\mathbf{S}_z + H_{\text{gyro},S} \end{aligned} \quad (6.8)$$

For a spherical top, Eq(6.8) condenses into (6.9).

$$H = BJ^2 - 2\mathbf{S} \cdot \mathbf{J} + H_{\text{gyro},S} \quad (6.9)$$

If  $S$  is treated as classical and constant, then Eq (6.9) simplifies, forcing  $H_{\text{gyro},S}=\text{const.}$  which may be removed from the total Hamiltonian, as in (6.10).

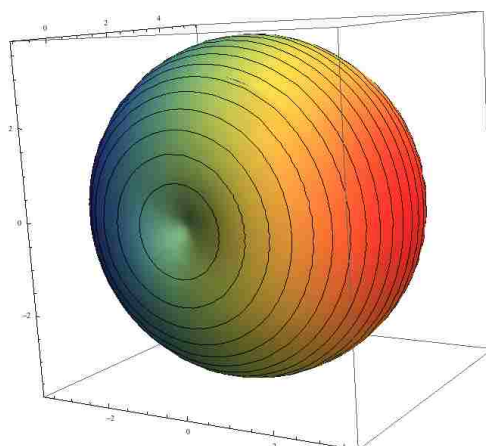
$$H_{R+S,\text{fixed}} = A\mathbf{J}_x^2 + B\mathbf{J}_y^2 + C\mathbf{J}_z^2 - 2AS_x\mathbf{J}_x - 2BS_y\mathbf{J}_y - 2CS_z\mathbf{J}_z \quad (6.10)$$

By converting components  $J_x$ ,  $J_y$  and  $J_z$  into  $T_q^k$  form, as described in chapter 1, the Hamiltonian Eq (6.10) may be plotted as an RES. Fig 6.6 shows RES plots for various values of rotor  $A$ ,  $B$ , and  $C$  coefficients. Fig 6.6(a) is formed from a spherical top with a gyro  $S$  vector pointing along the body-frame  $x$  axis. This create a cardioid-like surface that has been pushed away from the origin by the  $S$  vector.

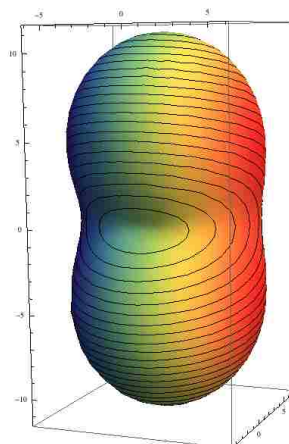
Figs 6.6(b) and 6.6(c) are similarly formed, but from prolate and oblate tops respectively. Both prolate and oblate versions contain a separatrix while Fig 6.6(a) did not.

### 6.A.2 2D Oscillation - 3D Rotation Analogy

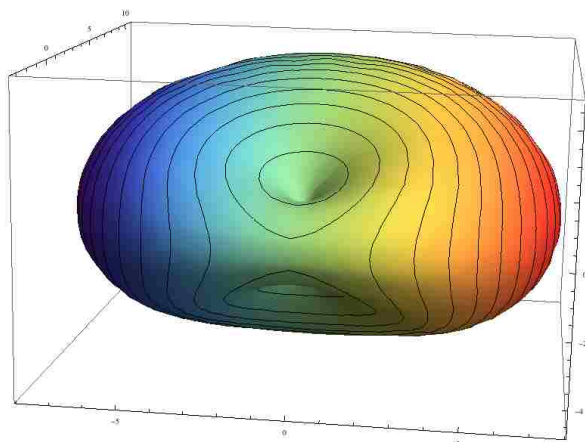
RES plots identical to those in Fig 6.6(c) may also be created for an analogous system: one with a rotor fixed to a vibrational angular momentum[1]. In the same way 2D electric field polarization may be plotted as a vector in a three dimensional Stokes-space, any 2D vibration (or two 1D oscillations) may be plotted as such a 3D vector using either Pauli spinors or Hamilton quaternions[2, 3]. The Hamiltonian will have



(a) Spherical-top with gyro



(b) Prolate rotor with gyro on the body- $x$  axis



(c) Oblate rotor with gyro on the body- $x$  axis

Figure 6.6: Multi-rotor RES formed from different types of rotors will make RES with varying topographies. Unlike other RES, the contours here do not indicate quantum energies. They exist only to show changes in topography.

the form of Eq (6.11).

$$\begin{aligned}
 H &= \begin{pmatrix} A & B - iC \\ B + iC & D \end{pmatrix} \\
 &= \frac{A + D}{2} \sigma_0 + \frac{A - D}{2} \sigma_A + B \sigma_B + C \sigma_C
 \end{aligned} \tag{6.11}$$

where

$$\begin{aligned}
 \sigma_0 &= \begin{pmatrix} 1 & 0 \\ 0 & 1 \end{pmatrix} & \sigma_A &= \begin{pmatrix} 1 & 0 \\ 0 & -1 \end{pmatrix} \\
 \sigma_B &= \begin{pmatrix} 0 & 1 \\ 1 & 0 \end{pmatrix} & \sigma_C &= \begin{pmatrix} 0 & -i \\ i & 0 \end{pmatrix}
 \end{aligned}$$

The constants  $A, B, C$  and  $D$  should not be confused for the rotational constants or inverse moments of inertia. The labels  $\frac{A-D}{2}$  (asymmetric diagonal),  $B$  (bilateral) and  $C$  (Coriolis or circular) are mnemonics for the Pauli spinors. In this way, the rovibrational Hamiltonian is converted to Eq (6.12).

$$H = S_0 J_0 + S \cdot \mathbf{J} \tag{6.12}$$

where

$$J_0 = \sigma_0, \quad J_A = \frac{\sigma_A}{2}, \quad J_B = \frac{\sigma_B}{2}, \quad J_C = \frac{\sigma_C}{2}$$

and

$$S_0 = \frac{A + D}{2}, \quad S_A = (A - D), \quad S_B = 2B, \quad S_C = 2C$$

In this Stokes analogy, what was an RES is now a deformed Stokes sphere. The directions  $x, y$  and  $z$  correspond to linear x, y and circular polarization of the 2D oscillator. The radius of the surface now indicates the amplitude of oscillation. Given the total angular momentum is constant, neither the vibrational angular momentum nor the rotor angular momentum need be, so long as the sum is.

B-type Hamiltonians  $H_B$ , built of  $\sigma_B$  operators, angular momentum  $J$  must precess about the  $x$  axis symmetrically as in Figs 6.6(a) and 6.6(b). Eigenvectors of these Hamiltonians are linearly polarized oscillators. The difference between the two figures is in the contribution of a rotational  $T_0^2$  operator, but not in  $\sigma_\alpha$  contributions. Fig 6.6(c) includes a B-type and also an A-type term to the rovibrational Hamiltonian, forming eigenvectors at two points that are still in the linear x,y plane, but not along either an x (B) or y (A) axis.

### 6.A.3 Rovibrational Multi-surface RES Plots

Rovibrational Hamiltonians may also be plotted a second way. This involves treating the single-rotor rotation classically (though of fixed magnitude) and the vibration quantum mechanically. This is the method used in chapter 6 to analyze the  $\nu_3/2\nu_4$  dyad band of  $\text{CF}_4$ . The simplest possible example of this is to include the RES of a classical rotation coupled to a quantum mechanical spin. For this rotor-spin example, the  $2 \times 2$  Hamiltonian must be diagonalized, creating two surfaces[4].

Converting Eq (6.8) to quantize spin  $S$  creates Eq (6.13).

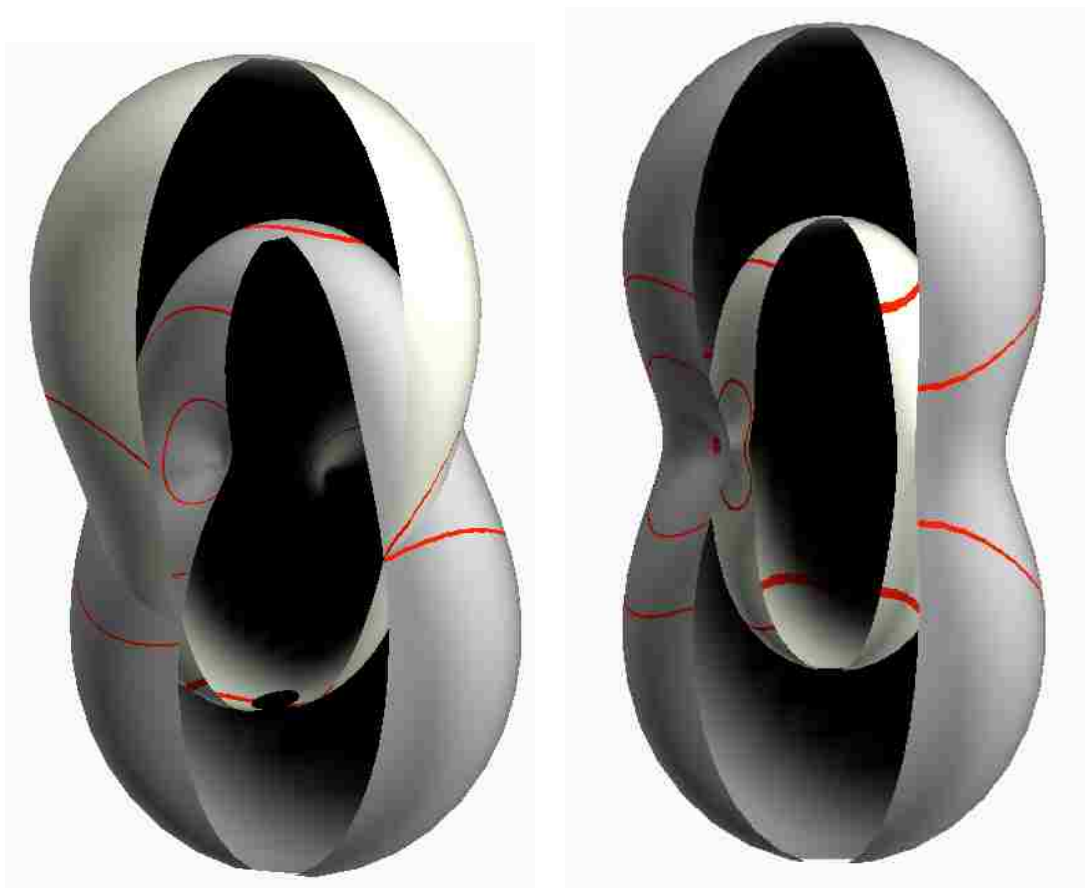
$$\begin{aligned}
 H &= M_0 J^2 + Q_{xx} J_x^2 + Q_{yy} J_y^2 + Q_{zz} J_z^2 \\
 &\quad + D_x |S| \sigma_x J_x + D_y |S| \sigma_y J_y + D_z |S| \sigma_z J_z \\
 &= \begin{pmatrix} h(J) + D_z |S| J_z & |S| (D_x J_x - i D_y J_y) \\ |S| (D_x J_x + i D_y J_y) & h(J) - D_z |S| J_z \end{pmatrix}
 \end{aligned} \tag{6.13}$$

where

$$h(J) = M_0 J^2 + Q_{xx} J_x^2 + Q_{yy} J_y^2 + Q_{zz} J_z^2$$

and

$$\begin{aligned}
 d_\alpha &= D_\alpha |S| |J| & M_0 &= A + B + C \\
 D_\alpha &= -2AS_\alpha & Q_{zz} &= \frac{2C - A - B}{6}
 \end{aligned}$$



(a) Classical plot creates intersecting surfaces (b) Quantum plot creates nested surfaces that avoid each other.

Figure 6.7: Classical and quantum spin treatment will result in different RES. Contours show topography and do not indicate quantum energy. Surfaces are sliced open to show the surface inside.

If treated quantum mechanically, this matrix must be diagonalized, giving the double surface Rotational Energy Eigenvalue Surface (REES) plot shown in Fig 6.7(b). To compare to classical behavior, Fig 6.7(a) plots the same, but with the off diagonal terms ignored. This classical case still contains two surfaces, but they may intersect while the quantum surfaces are forced to avoid each other. Behavior at the top and bottom (away from the intersection) is nearly identical for both plots in Fig 6.7, mirroring much of the classical-quantum agreement shown in chapter 2.



## Bibliography

- [1] W. G. Harter. *Handbook of Atomic, Molecular and Optical Physics*, chapter 32, page 501. Springer, 2006.
- [2] William G. Harter. *Principles of symmetry, dynamics, and spectroscopy*. J. Wiley, 1993.
- [3] William G. Harter. SU(2) coordinate geometry for semiclassical theory of rotors and oscillators. *Journal of Chemical Physics*, 85(10):5560, 1986.
- [4] Juan Ortigoso and Jon T. Hougen. Rotational energy surfaces of molecules exhibiting internal rotation. *Journal of Chemical Physics*, 101(4):2710–2719, August 1994.

## Chapter 7

### Conclusions

Despite a history nearly as long as quantum mechanics itself, quantum molecular spectroscopy remains a dynamic field. Computational and experimental tools have transformed the study, but new theoretical work is still needed to interpret these results. Spectroscopists have proven themselves invaluable to analytical chemists, astronomers, atmospheric scientists and remote sensing experts. Current advancements in molecular theory are exploring the boundaries of physics, even exploring supersymmetric string theory[1].

This work is an attempt to add to the qualitative toolset of molecular theorists. We have introduced tools of quantitative approximations, but the goal is to allow theorists to better explain the sea of experimental and computational data now being created.

To that end, this dissertation demonstrates several tools. Chapter 2 describes approximation methods for symmetric and asymmetric-top molecules. This is done by using the connection between unitary multipole operators and Legendre functions to make a semiclassical approximation, also demonstrating the breakdown of this approximation with increasing rank of the Hamiltonian parameter (multipole operator).

This work is continued in chapter 3 to increase the parameter space for which octahedral spherical-top molecules have been explored by RES analysis. These regions of the parameter space show a new type of rotational level clustering consistent with the symmetry subduction from  $O$  to  $C_1$ .

The enormous degeneracy of both the rotational level cluster and the local-symmetry axes require a different type of analysis to explain the tunneling splitting of the clusters. This is the motivation for the work of chapters 4 and 5. Chapter 4 describes

how Hamiltonians may be written in terms of lab-frame and body-frame operators to better parametrize tunneling. This technique was carried out in chapter 5 using  $C_2$  rotational clusters in octahedral molecules as an example.

While previous cases of RES analysis shown here were for vibrational singlets or ground states, chapter 6 expands this work to a vibrational polyad involving the nine interacting vibrational modes in the  $\nu_3/2\nu_4$  dyad of  $\text{CF}_4$ . This required nine interacting, nested REES plots. Similar work has been done with triplet states as well as fully classical analysis. Shown here is the connection between rotational energy clustering and polyad REES plots. These are predictive of the synthetic spectra for most cases. Errors between our analysis and the computed spectra are likely a result of our semiclassical approximations as discussed in chapter 6.

## Bibliography

- [1] A. E. Leanhardt, J. L. Bohn, H. Loh, P. Maletinsky, E. R. Meyer, L. C. Sinclair, R. P. Stutz, and E. A. Cornell. On measuring the electron electric dipole moment in trapped molecular ions. Technical Report arXiv:1008.2997, August 2010.